IMPACT OF CLIMATE VARIABILITY ON GLACIER MASS BALANCE IN REGIONAL, BASINAL AND LOCAL SCALE

Ph.D. THESIS

by

AKANSHA PATEL

CENTRE OF EXCELLENCE IN DISASTER MITIGATION AND MANAGEMENT

INDIAN INSTITUTE OF TECHNOLOGY ROORKEE

ROORKEE-247667 (INDIA)

APRIL, 2022

IMPACT OF CLIMATE VARIABILITY ON GLACIER MASS BALANCE IN REGIONAL, BASINAL AND LOCAL SCALE

A THESIS

Submitted in partial fulfilment of the
requirements for the award of the degree

of

DOCTOR OF PHILOSOPHY

in

DISASTER MITIGATION AND MANAGEMENT

by

AKANSHA PATEL

CENTRE OF EXCELLENCE IN DISASTER MITIGATION AND MANAGEMENT

INDIAN INSTITUTE OF TECHNOLOGY ROORKEE

ROORKEE-247667 (INDIA)

APRIL, 2022

INDIAN INSTITUTE OF TECHNOLOGY ROORKEE

STUDENT'S DECLARATION

I hereby certify that the work presented in the thesis entitled "**IMPACT OF CLIMATE VARIABILITY ON GLACIER MASS BALANCE IN REGIONAL, BASINAL AND LOCAL SCALE"** is my own work carried out during a period from December, 2017 to April, 2022 under the supervision of Dr. Ajanta Goswami, Associate Professor, Centre of Excellence in Disaster Mitigation and Management, Indian Institute of Technology Roorkee, Roorkee and Dr. Thamban Meloth, Scientist G and Group Director, Polar Sciences, National Centre for Polar and Ocean Research, Goa.

The matter presented in this thesis has not been submitted for the award of any other degree of this or any other Institution.

Dated: April 18, 2022 **Signature of the Student**

(AKANSHA PATEL)

SUPERVISOR'S DECLARATION

This is to certify that the work mentioned above is carried out under our supervision.

Signature of Supervisor
(THAMBAN MELOTH)

Signature of Supervisor
(AJANTA GOSWAMI)

Dated: April 18, 2022

ABSTRACT

Glacier Mass Balance (MB) is essential in order to understand the response of glaciers with changing climate system. The warming climate may lead to a shift in the hydrological regime of the glacier in terms of snow-fed runoff timing and snow-fed to rainfall-dominated hydrological regimes. Apart, the changing glacier mass can modify the hydrological cycle and river flow, which also creates concerns about the sustainability of streamflow in the summer season. Therefore, reliable estimation of MB and its interaction with climate are important to quantify the response of glacier change with future climatic variability. The mountains of the Himalayan region hold the largest ice masses outside the polar regions, even several major rivers originated from these mountains, and its downstream regions are densely populated. However, the Himalayan mountains are characterized by data scarcity due to their complex topography and varying climatic conditions, limiting the continuous monitoring of glacier changes using in-situ observation. In a changing climatic boundary condition, an appropriate model for MB estimation and glacier characterization are required that can represent the key controlling mechanism. Due to the lack of continuous glaciological and meteorological observations, the monitoring and modelling of the MB over the Himalayan glaciers are a major challenge. To overcome this limitation, the utility of remote sensing data presented a great advantage for MB estimation in time and space.

In this thesis, we use Gravimetric twin satellite data for regional surface mass change measurement over the glaciers of the Karakoram and Himalayan (KH) region. The spatio-temporal mass change distribution and its trends are estimated in order to assess the hotspot/coldspot region of mass variation and their further influence on streamflow in the near future. The regional mass change estimation is important because it provides us insight into what is exactly happening in the KH region other than glacier mass loss. During the study of regional-scale mass variation, we have also established an interconnection between the mass change and climatic (former) variables as well as with the other influential (impacted/latter) variables.

After analyzing the regional mass change and influence of forcing variables, we selected the Chandra basin (western Himalayas) for the basinal scale glacier MB estimation. This basin is mainly considered due to the higher mass loss (observed from the regional-based mass variation); therefore, a detailed investigation is needed. A spatially distributed mass balance model has been developed for the basinal scale to ensure that all the necessary physical variables and processes are correctly incorporated into the model. A new multi-step physical-based Energy Balance Model (EBM) has been carried out by parameterizing the energy balance components and also

modelled the air temperature at the spatial extent. To test the model, a calibration/validation has been performed using the in-situ observation of the Himansh station (located within the basin) and with the published MB. The model observations suggested that the spatially distributed EBM at the catchment scale can bridge the gap between regional observation-based mass change and point-scale-based studies.

The results of basinal MB demonstrated that the Batal glacier shows a significant loss in its mass than the nearby glaciers, i.e., Sutri Dhaka glacier (showing a considerable mass loss) over the observational period. These two glaciers have similar climatic conditions and orientations, despite having varying melt conditions by controlling debris thickness over the glacier surface. Therefore, we have selected the Batal and Sutri Dhaka glaciers for locale-scale glacier MB estimation. Over these two selected glaciers, the glacier feature classification and shift in isotherm have been quantified to monitor temporal glacier variation. Then, the glacier surface velocity, modelled ice thickness, and total stored volume are estimated against the remote sensing data. The associated uncertainties of the modelled ice thickness and surface velocity are measured to test the reliability of the observations. Despite this, the locale scale MB has been calculated by the difference between different Digital Elevation Models (DEMs) and compared the results with the reported MB. The model finding of locale MB illustrated that the Batal glacier experienced more mass loss due to the presence of debris that contributes to a higher rate of melting than the Sutri Dhaka glacier.

To derive the MB from regional to local, we have used a hierarchical methodology to connect the changes of MB with the spatial extent and also with the climatic interaction. With this methodology, we have not required in-situ observations for modelling the MB; however, it uses field observation for calibration and validation of the obtained results. The overall varying climatic variables and their relationship with water availability are presented in objective-1. The regional scale mass changes and contribution of hydro-meteorological variables are discussed in objective-2, and the model developed in objective-3. Finally, a detailed mass balance analysis and glacier characterization are mentioned in objective-4.

Overall, the obtained results and developed model are likely to be important for the research community of glaciologists, hydrologists, decision-makers, water resource managers, and civil engineers (for understanding the streamflow under the summer season at the time of dam construction). This thesis can also be a benchmark for modellers in the high-altitude region and facing the problem of data scarcity to evaluate their experimental approaches. In a broader

context, the results of this thesis can be used for predicting the river runoff and water stress/water availability in both upstream and downstream regions.

Keywords: Glacier mass balance; Energy balance; Remote sensing; Karakoram and Himalayan region; Model development.

ACKNOWLEDGEMENT

It is my indeed pleasure to acknowledge the role of several individuals for helping me make this thesis possible. I would first like to express my deepest gratitude to my research supervisors Dr. Ajanta Goswami, Associate Professor, Centre of Excellence in Disaster Mitigation and Management, Indian Institute of Technology, Roorkee and Dr. Thamban Meloth, Scientist G and Group Director, Polar Sciences, National Centre for Polar and Ocean Research, Goa, for his continuous support, motivation, immense knowledge, impeccable advise for solving a problem and also by providing excellent research environment. They act as a compass to me in providing directions for my research work and then for publication also. As per my opinion, both the supervisors are a great combination for my development and thesis completion. The timely supervision and encouragement helped me a lot in the successful execution of the thesis work.

Apart from my guide, I take this opportunity to my deep and profound sense of respect and heartfelt thanks to Prof. Sumit Sen, Head of the Centre, and Prof. Mahua Mukherjee, Former Head of the Centre, for providing the necessary facilities to carry out the work in a pleasant environment. I would also like to thank the Indian Indian Technology, Roorkee, National Centre for Polar and Ocean Research, Goa and Space Application Centre (SAC), ISRO, Ahmedabad for providing research grants that allowed this research to be completed. A special thanks to my research committee member Prof. Ravi Kumar, Prof. Sudip Roy, Prof. J. D. Das and Dr. L. N. Thakural for their valuable comments and suggestion for enhancing the quality of work at various stages. In addition, I would also like to thank Prof. A. K. Sen and Prof. P. Pati for providing the knowledge to take this journey. I would like to thank Dr. Parmanand Sharma, National Centre for Polar and Ocean Research, Goa, for their valuable support and advice during my research work. I am also thankful to the non-technical staff of the centre, and a special thank you to Mr. Tahir for their time to time guidance for the official work.

I sincerely acknowledge NASA and other data-providing agencies for their free data policy and dissemination, allowing me to use it for my research work.

I am eternally thankful to all my fellow lab mates that directly or indirectly contribute to research work. Especially, I would like to thank Dr. Pir Mohammad for providing me with good advice and suggestion that motivate me to work in a continuous manner. Apart, I would like to thank Dr. Anugya Shukla, Dr. Rituraj Nath, Mr. Nani Das, Mr. Abhishek Kumar, Mr. Atul Kumar, Mr. Lucky Shukla, and many others who helped me in a possible way to carry out this research work.

My thesis wouldn't be productive for the research community without my husband, Jaydeo K. Dharpure. His unconditional support and contribution to my research work make it possible to complete my thesis with good publications.

Last but not least, I would like to thank my beloved parents, sister, and my in-laws for their love, support, cooperation, and understanding during my work. It was beyond my capacity to express my indebtedness towards them.

Finally, I would like to thank god for showing the light of this day in my life.

Dated: April 18, 2022

Signature of the Student
(AKANSHA PATEL)

TABLE OF CONTENTS

LIST OF FIGURES

CHAPTER - 3

CHAPTER - 4

CHAPTER - 5

LIST OF TABLES

CHAPTER 1

INTRODUCTION

1.1. BACKGROUND

Retreating the mountainous glacier is a sensitive indicator for potential climate change and poses a serious concern for millions of people who rely primarily on river water. The glacier response to changes in atmospheric conditions is slow enough to filter out the high-frequency climatic variability; however, it is fast enough for providing an understanding related to systematic changes in the environment (Marzeion et al. 2017). With regards to the hydrological role of glaciers and their future evolution of potential glacier hazards, monitoring of both glaciers growing and shrinking is essential to regulate the seasonal water availability (Bolch et al. 2012; Kääb et al. 2018; Hock et al. 2019a). A global glacier area distribution across 19 regions of the world is shown in Figure 1.1.

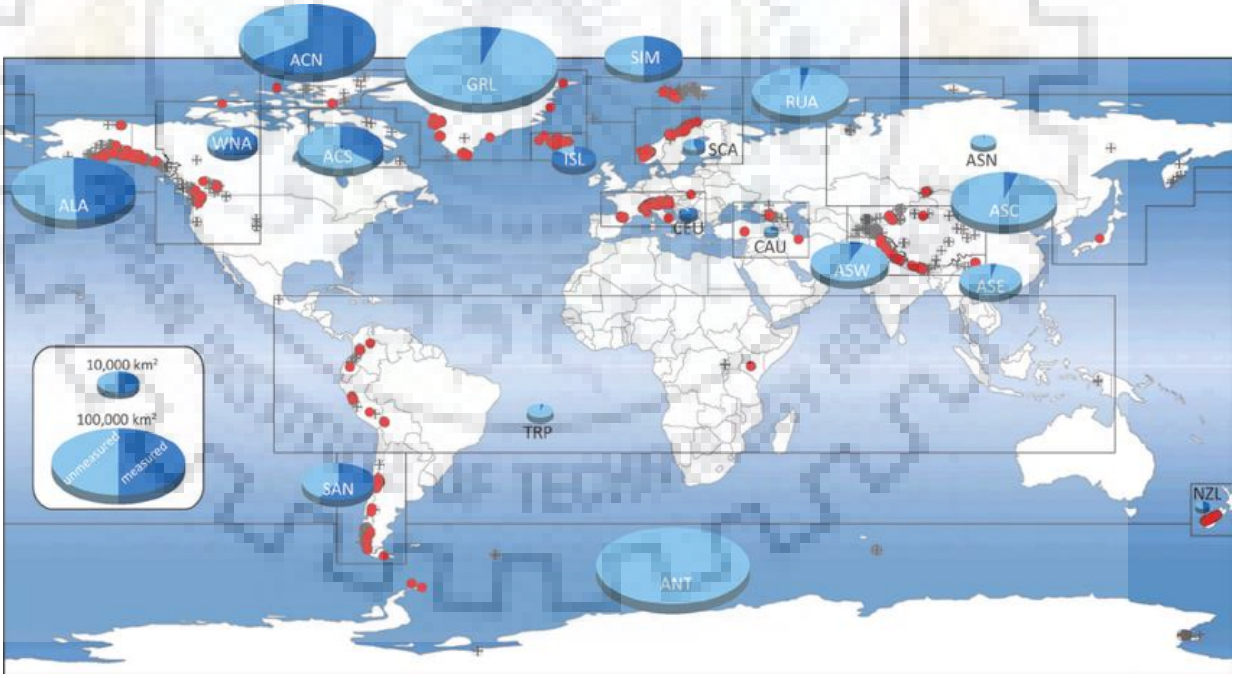

Figure 1.1. Global glacier area distribution and their fluctuation. The pie chart indicates the glacier area and the fraction covered by the observations. Red and black dots represent the continued and interruption location data. Note: Alaska (ALA); Western North America (WNA); Arctic Canada North (ACN); Arctic Canada South (ACS); Greenland (GRL); Iceland (ISL); Svalbard and Jan Mayen (SJM); Scandinavia (SCA); Russian Arctic (RUA); Asia

North (ASN); Central Europe (CEU); Caucasus and Middle East (CAU); Asia Central (ASC); Asia South East (ASE); Asia South West (ASW); Low Latitudes (TRP); Southern Andes (SAN); New Zealand (NZL); Antarctica and Sub Antarctic Islands (ANT) (Source: Zemp et al., (2015)).

According to the International Panel on Climate Change (IPCC) 5th Assessment Report (AR5), it was concluded that "Because nearly all glaciers are too large for equilibrium with the present climate, there is a committed water resource change during much of the 21st century, and changes beyond the committed change are expected due to continued warming; in glacier-fed rivers, total meltwater yields from stored glacier ice will increase in many regions during the next decades but decrease thereafter" (IPCC 2014). Additionally, Ragettli et al. (2016) have highlighted that this increase in meltwater will occur in some regions, whereas others will directly face a reduction in freshwater availability. Therefore, the changing pattern of glaciers and their impact on hydrological processes are currently a key concern for public and scientific debate.

1.2. IMPORTANCE OF THE HIMALAYAN REGION

The Himalayas, one of the youngest and loftiest mountain ranges, have the largest glacier concentration outside the polar region. This region, aptly called the 'Water Tower of Asia' provides around 8.6×10^6 m^3 of water annually, thus contributing significantly to supplement the snow and rainwater and provide the interannual stability in streamflow for irrigation and hydropower generation (Dyurgerov and Meier 1997; Singh and Bengtsson 2004; Immerzeel et al. 2010; Bolch et al. 2012). The availability of water is under threat due to the rapid increase in population, which places a greater demand for water resources (Cosgrove and Loucks 2015). Similarly, climate change also affects water availability all over the major basins and beyond (Zhu and Ringler 2012). A map of the Hindu-Kush Himalayan region, river, and glacierized region is shown in Figure 1.2.

Glaciers are an important aspect of the world's hydrological cycle. About one-third of the world's population depends upon the largest freshwater reservoirs on the Earth (Brown et al. 2010). It also influences the Earth's dynamics in terms of climatologically and hydrologically. Glacier ice and snow cover can exert a substantial influence on climate by interacting with the atmosphere through a range of feedback mechanisms (Hock 2005).

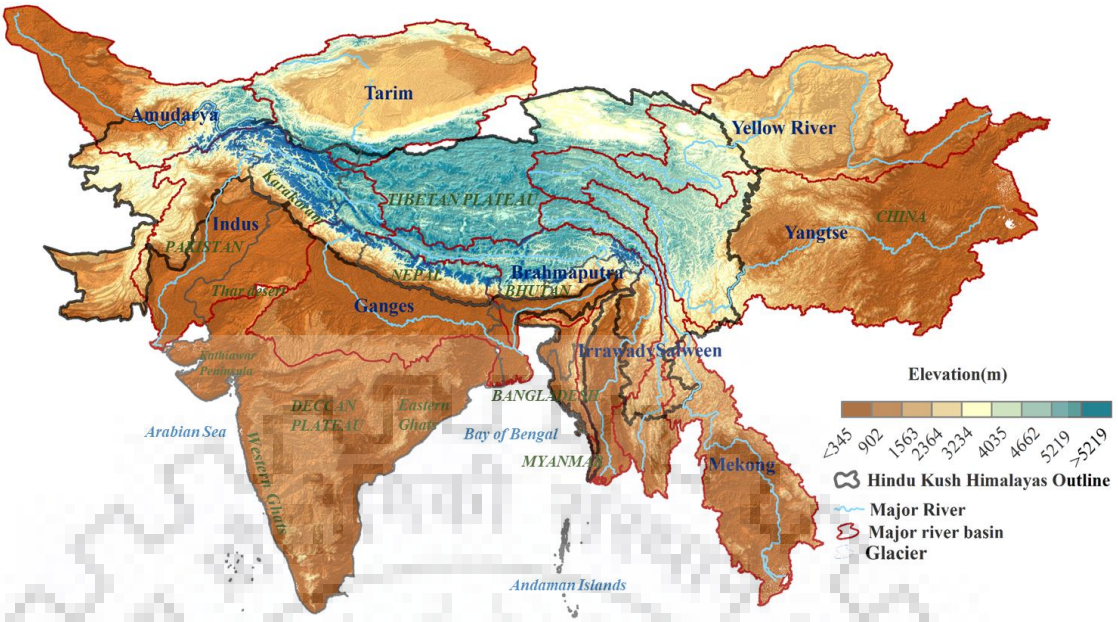

Figure 1.2. Map of the Hindu-Kush Himalayan region with all major river and basin.

1.3. GLACIER MASS BALANCE AND ITS IMPORTANCE

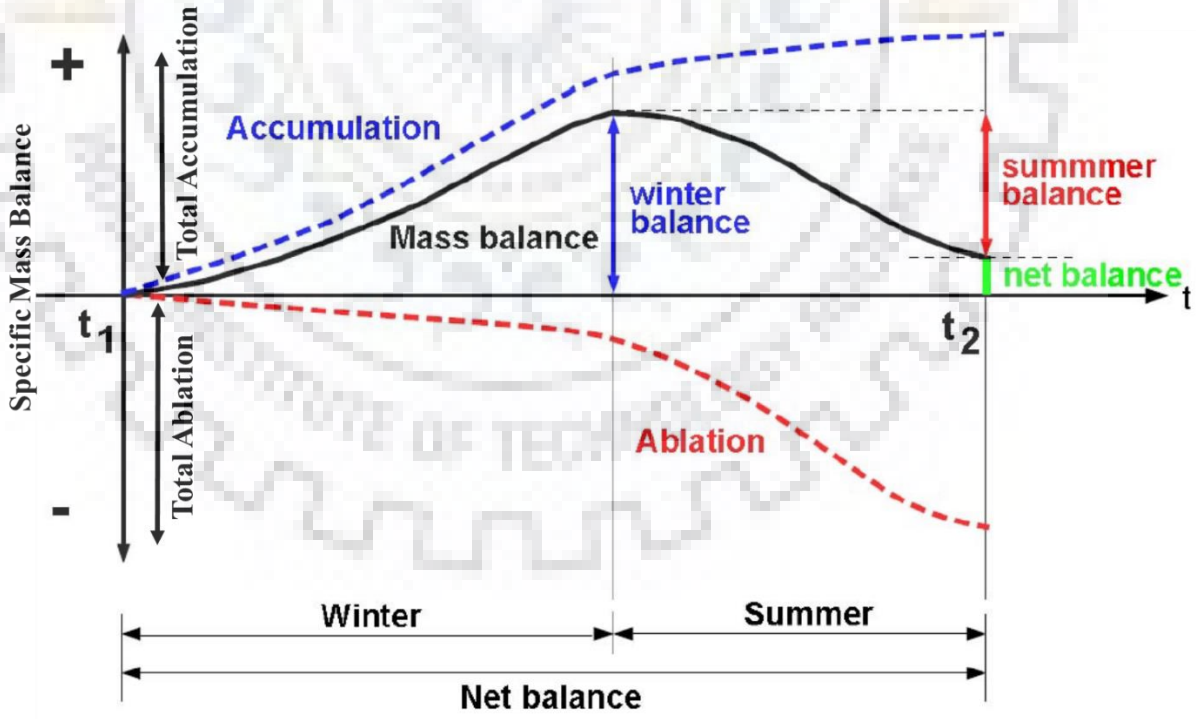

Figure 1.3. Schematic diagram of glacier mass balance at the annual time scale.

Glacier Mass Balance (MB) is an essential parameter for assessing glacier health and the impact of climate change. MB is the difference between amounts of accumulation and ablation of the

glacier. It gives the net change in the volume of a glacier over a specific period. Annual MB is a hydrological budget, which measures the difference between accumulation and ablation of a glacier during a hydrologic year (Hock et al. 2019a; Ramsankaran et al. 2019). It depends on accumulation and ablation parameters so that MB can be positive, negative, or zero. Glacier showing positive MB is found to be growing, negative MB indicates glacier is shrinking, and the glacier with zero MB shows steady-state and no volume change (Manatsa et al. 2008). A schematic diagram of annual MB estimation is drawn to understand the basic pattern of glacier mass distribution (Figure 1.3)

The aim of glacier MB is to represent glacier health and its response to climate change. MB methods investigate the mass change of a glacier and the distribution of these changes with respect to space and time (Cuffey and Paterson 2010) vertically relative to the glacier surface (Oerlemans 2001). The study of glacier MB results in long-term assessment of streamflow change and glacier-related hazards (Hock et al. 2007; O'Neel et al. 2014; Nie et al. 2021).

1.4. GLACIER MASS BALANCE METHODS

Five methods are widely used for glacier MB estimation over the different locations of the Karakoram and Himalayan (KH) region. These include direct glaciological (Dobhal et al. 2013; Sharma et al. 2016; Soheb et al. 2020; Mandal et al. 2020), Surface Energy Balance (SEB) (Zhang et al. 2013; Azam et al. 2014a; Li et al. 2018a), hydrological method (Bhutiyani 1999), gravimetric (Moiwo et al. 2011; Wouters et al. 2019) and remote sensing (Vijay and Braun 2016; Bolch et al. 2017; Lin et al. 2017; Tawde et al. 2017; Maurer et al. 2019; Muhammad et al. 2019) based methods.

The compilation of ground-based MB records is an integral part of the World Glacier Monitoring Service (WGMS) for worldwide glaciers (Zemp et al. 2009). In the Indian Himalaya, there are only two glaciers (Chhota Shigri and Hamtah) for which partial MB records are available from (WGMS 2020) (www.wgms.ch), and most of the other records are published in reports of the Geological Survey of India (GSI, Govt of India). Dyurgerov and Meier (2005) compiled MB data of eight Indian Himalayan glaciers (Shaune Garang- 9 years, Gor Garang- 8 years, Changme Khangpu- 6 years, Dunagiri- 5 years, Nehnar- 5 years, Tipra- 3 years, Kolahoi- 1 years and Shishram- 1 years) with the globally available MB series. Recent studies have also reported MB observations for Dokriani, Chorabari, and Chhota Shigri glaciers in the Indian Himalaya, showing overall cumulative negative mass balance (Wagnon et al. 2007; Dobhal and Thayyen 2008; Azam et al. 2012; Dobhal et al. 2013). Studies by the (Bolch et al. 2012; DST 2012)

analyzed the mean specific MB of the Indian Himalayan glaciers and found that most MB series is negative. However, the global glacier MB record for the Indian Himalaya remains incomplete and requires updates. This is necessary to strengthen the global glacier database used for climate interpretations and sea-level-rise assessment (Dyurgerov and Meier 1997; Zemp et al. 2009).

Table 1.1. Glacier mass balance method wise consideration, advantage and their limitation

Techniques	Requirement	Advantages	Limitation
Glaciological measurement	• Site Accessibility • Stake Installation on the glacier bed (high-density network of stake) • Minimum one field survey.	• High accuracy (sub-meter or Sub-centimeter (By the use of DGPS) • Point measurement	• Intense manual labor • High manpower cost • Time-consuming • Limited accessibility in rugged glacierized terrain.
Energy balance method	• Automatic Weather Station (AWS) installation • Meteorological parameter for estimation • >1 field visit	• Hourly temporal data available • Use for understanding physical process on a glacier. • Less manpower oriented	• Point glacier melt measurement (AWS location) • Spatial coverage.
Geodetic method	• Digital elevation models (DEMs) of two different time frames for thickness calculation	• Multi annual measurement • Average of specific mass change(areal-average thickness) over time-span.	• Lack of information about the seasonal correction • Wide time span
Area Accumulation Ratio(AAR)	• Equilibrium Line Altitude (ELA) estimation • Ancillary data, i.e., temperature, precipitation, etc.	• Glacier-scale spatial coverage • Higher precision as compared to Geodetic mass balance method	• Revisit the period of imagery. • Cloud covered on optical imagery. • Depend upon visual interpretation.
Hydrological method	• AWS Installation and meteorological data. • Discharge data (total runoff)	• Indirect glacier mass balance estimation. • Basin-wide analysis	• For a short period of time (weekly or daily) • Difficult in the storage of water in glaciers.

Several methods have been employed to explore the link between glacier MB and climatic variables, ranging from local (glacier wise) to regional scale across a large part of the Karakoram and Himalayan (KH) region (Barrand and Murray 2006; Gardner et al. 2013; Mandal et al. 2020). The regional MB was a simpler method for estimating glacier mass gain/loss covering a larger

spatial extent than the basinal and local scale methods (Rupper and Roe 2008; Scherler et al. 2011; Zemp et al. 2019). It provides significant glacier mass change information at intra- and inter-annual spatio-temporal scales. However, this simplified method neglects the contribution from other non-ice components (Wouters et al. 2019) as well as micro-climatic and topographic variation (Pelto and Riedel 2001). Therefore, a detailed investigation of glacier MB at various spatial scales ranging from regional to basinal and from basinal to local scale are needed to understand the hotspot/coldspot region of MB and their associated influential variables.

1.5. RESEARCH QUESTIONS

- **How does the Himalayan glacier behave in response to concerning climatic variability?** Is the Himalayan glacier retreating or advancing? What are the contributing variables responsible for the glacier mass loss? How has the glacier extent of the Himalayan region changed from ~2000 to the present?
- **How is mapping the glacier at a varying spatial scale possible with a remote sensing-based approach?** What is the hotspot/coldspot region of glacier mass change? Are detailed studies on the identified hotspot/coldspot carried at a basinal scale? What are the possible models available for glacier MB estimation over the whole basin? What is the need for a new model for MB estimation at a basinal scale?
- **What are the influential variables that impacted the glacier mass loss?** What is the forcing mechanism, and how do its varying patterns affect the MB of the glaciers? Is the glacier mass loss highly dependent upon the climatic variables or radiative forcing?
- **What is the fractional contribution of glacier meltwater to summer season streamflow?** What is the associated risk with the change in glacier MB? What adaptation plan and measures need to be considered by the stakeholder for managing the water resource at upstream and downstream regions?

1.6. RESEARCH AIM AND OBJECTIVES

This thesis aims to quantify the distribution, driving force, and mechanisms of MB in the KH glaciers and its variability in regional-basinal and local spatial scales. It also includes developing a new basinal scale glacier MB estimation model that improved the estimation by parameterizing the radiative forcing and its impact on glacier surface melt. Additionally, the present thesis builds up a detailed investigation of glacier MB from the hotspot region on a regional scale to a basinal scale and then on a locale scale. For this, we have addressed the following research objectives:

1. Analyzing the precipitation and temperature hotspots/coldspot region for understanding the influence of driving factors on glaciers
2. Mapping and monitoring of regional mass anomaly using remote sensing-based analysis *(Regional scale)*
3. Developing a glacier MB model using satellite and *in situ* measurement by incorporating the energy balance components *(Basinal scale)*
4. Monitoring glacier retreat/advance by the geodetic MB method and its implication on glacier health *(Local/Glacial scale)*

1.7. THESIS STRUCTURE

This thesis is organized into six chapters to achieve the overall aim of the objective. A brief description of each chapter is summarized below:

Chapter 1: This chapter comprises a brief description of glacier mass balance, background, and their importance globally. It also added knowledge related to the research gap in glacier mass balance estimation, objectives, and thesis structure.

Chapter 2: This chapter includes the spatio-temporal distribution of rainfall and its trend at annual and seasonal scales. The variation of rainfall intensity and days; analyzed the hotspot/coldspot regions in the Indian major river basins and assessed the influence of water storage change in a warming scenario.

Chapter 3: This chapter comprises the regional scale glacier mass balance study over the Karakoram and Himalayan region. The monthly variation of mass balance at spatial and temporal scales, pixel-wise volume change, and the contributing hydro-climatic variables and radiative fluxes are assessed to establish the linkage between the glacier mass variation and climate sensitivity. This chapter also includes the associated uncertainty and sensitivity analysis of each influential variable is also monitored.

Chapter 4: In this chapter, a 2-dimensional glacier mass balance model is developed by parameterizing the climatic variables and energy fluxes over the Chandra basin glaciers, western Himalayas. The validation of the model is tested with the *in situ* data. The radiation and heat fluxes are explained at different altitude ranges. Also, assess the model uncertainties and sensitivity of each contributing variable.

Chapter 5: This chapter comprises the varying mass balance patterns and glacier characteristics of the Sutri Dhaka and Batal glaciers (Chandra basin, western Himalaya). This chapter discusses the spatial and temporal change in glacier feature classification, a shift in isotherms, surface velocity, ice thickness, and mass balance.

Chapter 6: This chapter summarizes the research contribution from this thesis to glacier mass balance studies and conclusion from Chapters 2 to 5. this section also includes the new insight of future research related to this work and the implication of glacier mass balance change on managing the water resources.

CHAPTER 2

ANALYZING THE PRECIPITATION AND TEMPERATURE HOTSPOTS/COLDSPOT REGION FOR UNDERSTANDING THE INFLUENCE OF DRIVING FACTORS ON GLACIERS

2.1. INTRODUCTION

The Indus, Ganga, and Brahmaputra (IGB) river basins played a significant role in managing the water resource (Hasson et al. 2014). The headwater of the IGB basins supports more than 700 million people living in the downstream as well as mountainous regions (Shrestha et al. 2015). A significant proportion of the population (~830 million) depends on the regional hydrology for agriculture, forestry, fisheries, and livestock for their livelihood. However, the warming climate and increase in population density emerge as a serious concern towards the water resources of these river systems as they may become vulnerable to water stress (Shrestha et al. 2012). According to Lutz et al. (2014), under the warming scenario, the total runoff will likely be changed by −5% to +12% for the Upper Indus basin; however, it will be increased by 1–27% for the Upper Ganga basin and 0–13% for the Upper Brahmaputra basin by 2050. This significant change in precipitation pattern and rising temperature can alter the hydrological regime through factors such as rainfall amount, an extreme event caused by rainfall, seasonal rainfall onset changes, rainfall intensity, and duration (Rosenzweig et al. 2001; Berger et al. 2019).

Many studies have focused on the annual and seasonal rainfall change over different parts of the world (Brunetti et al. 2012; García-Barrón et al. 2015; Latif et al. 2017; Machiwal et al. 2017). For instance, Nepal and Shrestha (2015) have assessed the rainfall trends and extremes in the Indus basin, showing an insignificant trend with a slight increase in rainfall. Similarly, several studies in the Ganga basin have highlighted heavy precipitation during the monsoon period, with extended periods of no precipitation during the winter months (Mittal et al. 2014; Pechlivanidis et al. 2017). A few studies have also indicated that the rainfall intensity decreased, and the rainy days remained constant in the Brahmaputra basin (Hirabayashi et al. 2010). Moreover, the spatio-temporal patterns of daily and monthly rainfall concentration have been studied worldwide (Brunetti et al. 2012; Benhamrouche et al. 2015; Yeşilırmak and Atatanır 2016). Many studies have focused on the amount of rainfall (in terms of minimum, maximum, and mean) and trends in specific locations (Kumar and Jain 2010; Jamandre and Narisma 2013; Bharti et al. 2016). In the IGB basins, the annual rainfall shows an enormous change in precipitation (Shrestha et al.

2015). Therefore, the impact of spatio-temporal variation of rainfall on the water availability over the IGB basins needs further investigation.

2.2. RESEARCH QUESTIONS

- **What are the rainfall characteristics in the IGB river basins?** How has the rainfall distribution changed from monthly to seasonal and seasonal to annual? Is there any shift in the onset of the rainfall observed?
- **What are the contributing factors responsible for rainfall variability**? What is the forcing mechanism that causes perturbations in regional-scale rainfall signals? Can certain variables play a direct or indirect role in controlling the seasonal variability over the region?
- **What role do the topography and climatic condition of a region play**? How important is the topographic and climatic information supporting the rainfall across the IGB basins? Does the change in topographic and climatic variables play a significant role in varying spatial patterns of rainfall?

2.3. OBJECTIVES

- Analyzing the spatio-temporal pattern of rainfall and its trend using satellite remote sensing data
- Quantification of hotspot/coldspot region and rainfall characteristics over the IGB river basins
- Assessing the impact of climatic variables on the availability of water across the study area

2.4. STUDY AREA

The study area extends over the Indus, Ganga, and Brahmaputra river basins, covering an area of about 112×10^4, 108.7×10^4 and 54.3×10^4 km^2 respectively (Shrestha et al. 2015). The total area of the basins is about 275×10^4 km^2 out of which 143×10^4 km^2 is distributed over India. The geographical location varies from 21°–37° N latitude and 66°–97° E longitude, spread across five countries, i.e., India, Nepal, Pakistan, Bhutan, and Bangladesh (Figure 2.1). The Indus River flows into the Arabian Sea, which forms a delta of about 16,000 square miles (41,440 km^2). The Brahmaputra River joins with the Ganga River in Bangladesh and then falls into the Bay of Bengal. The study area elevation varies from 271 to 8527 m above sea level (a.s.l.) with a mean altitude of 1600 m a.s.l. (based on Shuttle Radar Topographic Mission (SRTM) DEM).

The complex topography of the terrain gives rise to altitude-dependent climatic variability ranging from semi-tropical to semi-arctic in the Himalayas (Bahadur 1993).

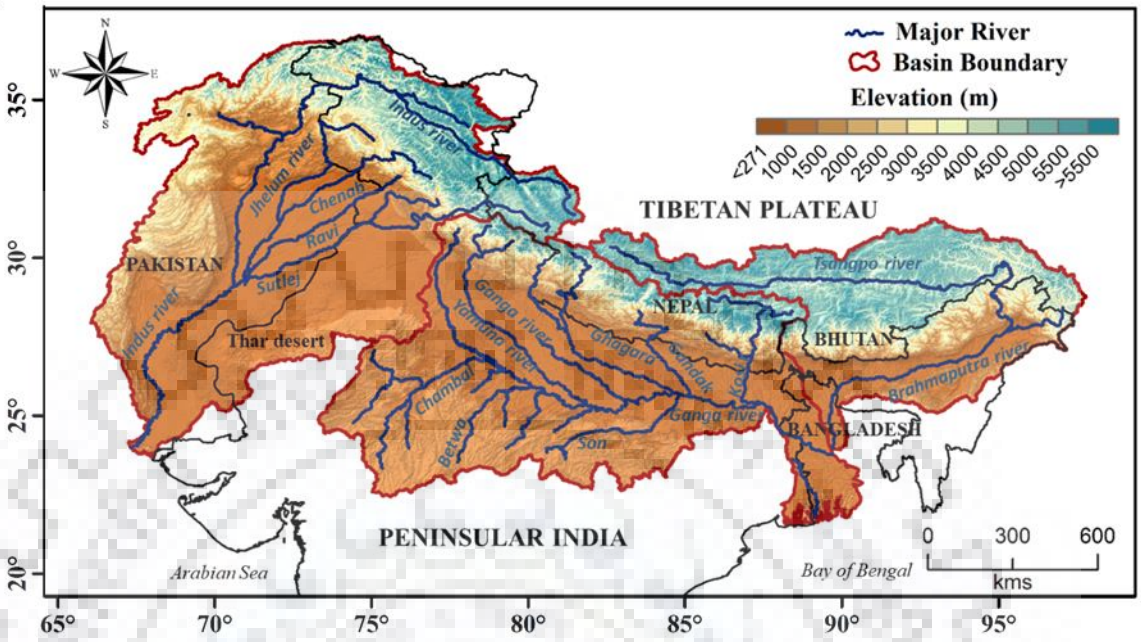

Figure 2.1. Topographic map of the Indus, Ganga, and Brahmaputra (IGB) river basins and their tributaries along the region.

2.5. DATA USED

2.5.1. TROPICAL RAINFALL MEASURING MISSION (TRMM) DATA

The Tropical Rainfall Measuring Mission (TRMM 3B42 v7) data is available at 0.25° × 0.25° grid resolution and is widely used for analyzing rainfall variability in climatological studies (Immerzeel et al. 2009; Bookhagen and Burbank 2010), hydrological modeling (Artan et al. 2007; Stisen and Sandholt 2010), rainfall erosivity estimation (Vrieling et al. 2010), soil erosion estimation (Sanchez-Moreno et al. 2014) and soil moisture prediction (Gupta et al. 2014). The TRMM satellite is equipped with various sensors such as the precipitation radar TRMM Microwave Imager (TMI), Lightning Imaging Sensor (LIS), and Visible and Infrared Sensor (VIRS). The TRMM Multi-satellite Precipitation Analysis (TMPA) algorithm contains precipitation estimates from various Passive Microwave (PMW) sensors, microwave-adjusted merged geo-IR, and monthly Global Precipitation Climatology Centre (GPCC) products (Huffman et al. 2007). There are two successive versions of the research quality estimate, i.e., version-6 (3B42V6) and the latest version-7 (3B42V7). The near-real-time data is provided very rapidly but less accurately for monitoring rainfall variability, whereas research quality data is more precise and appropriate for research (Himanshu et al. 2017). This data is freely available

on the National Aeronautics and Space Administration (NASA) (https://search.earthdata.nasa.gov). For this study, we utilize daily TRMM data for the IGB basins over 1998–2017.

2.5.2. APHRODITE DATA

The Asian Precipitation Highly Resolved Observational Data Integration Towards Evaluation (APHRODITE) gridded time series data of daily temperature and precipitation were available during 1961–2015 and 1951–2015, respectively, with a grid resolution of 0.25° × 0.25°. This data was substantially improved for temperature and precipitation observations over Asia (Yatagai et al. 2012). Also, the accuracy of APHRODITE data is closely comparable with the India Meteorological Department (IMD) gridded data (Rajeevan and Bhate 2008; Rajendran et al. 2012). This study utilizes a daily air temperature during 2003–2015 to analyze their association with rainfall and water availability. The precipitation data are used to assess the correlation with TRMM data during 1998–2015 (Figure 2.2). The spatial distribution of Pearson's correlation coefficient illustrates that the TRMM data is highly correlated with the APHRODITE data except for the upper reaches of the IGB basins and the lower west part of the Indus basin. The weak correlation may have occurred due to the availability of lesser rain-gauge stations installed in the upper reaches of the Himalayan region (https://climatedataguide.ucar.edu/climate-data/aphrodite-asian-precipitation-highly-resolved-observational-data-integration-towards).

2.5.3. GRAVITY RECOVERY AND CLIMATE EXPERIMENT (GRACE) DATA

The Jet Propulsion Laboratory (JPL) RL06 GRACE mascon solutions available at a grid resolution of 0.5° × 0.5° are used from January 2003 to December 2016 for analyzing the influence of changing climatic variables on total water storage. Rodell and Houser (2004) have reported the importance of GRACE Terrestrial Water Storage Anomaly (TWSA) data for understanding the impact of climate change, agriculture productivity, flooding, drought, and other natural hazards. This data employs a Coastal Resolution Improvement (CRI) filter that reduces the leakage errors across the coastlines (Wiese et al. 2016). A detailed description of data and their processing steps were given by Watkins *et al.* (2015)**.** However, a few images were found missing and replaced by the averaging of available pre and post-image of the missing dataset (Long et al. 2015) during the observational period.

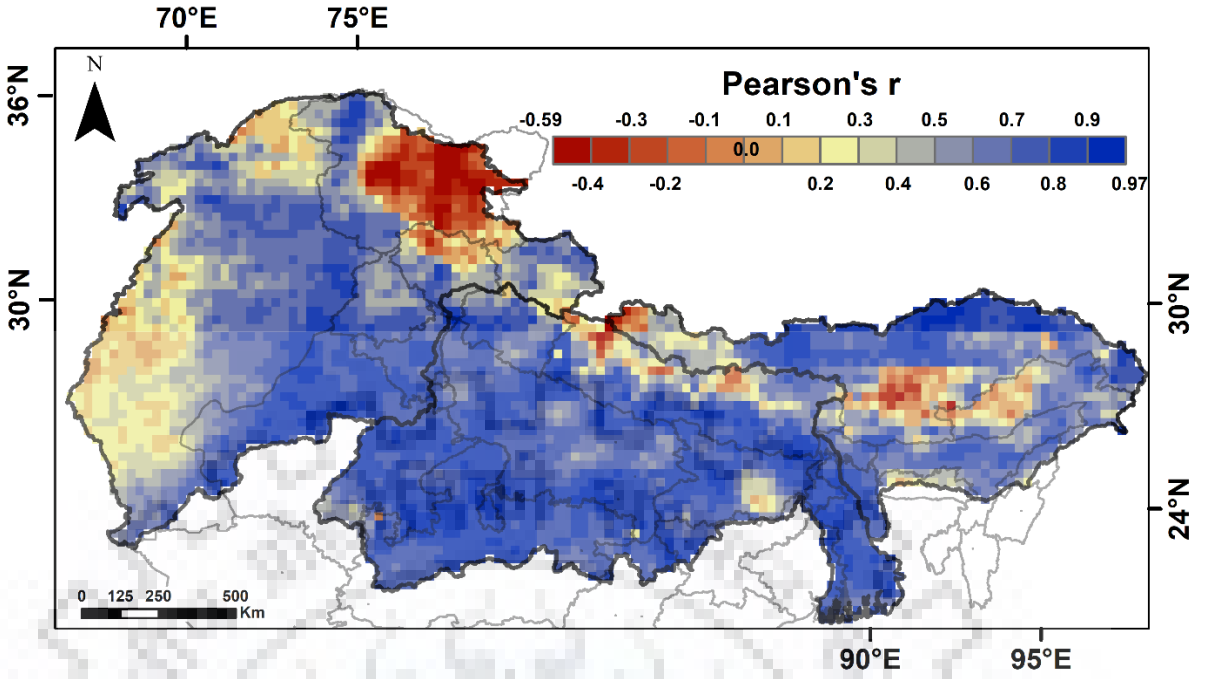

Figure 2.2. Spatial variation of Pearson's correlation coefficient measured between satellite-based TRMM and station-based rainfall (APHRODITE) data in the IGB river basins from 1998 to 2015.

2.6. METHODOLOGY

2.6.1. RAINFALL ANALYSIS

2.6.1.1. Precipitation Concentration Index (PCI)

The PCI shows the monthly rainfall distribution (heterogeneity) proposed by Oliver (1980). The equation employed for the calculation of PCI is as follows, expressed by Equation 2.1:

$$PCI = \frac{\sum_{i=1}^{12} P_i^2}{(\sum_{i=1}^{12} P_i)^2} * 100 \qquad \textbf{Eq. 2.1}$$

where P_i is the monthly precipitation in the i^{th} month (1 to 12 months). According to Oliver (1980), the PCI values below 10 represent an evenly distributed precipitation, values between 11 and 15 indicate a moderate precipitation concentration, values from 16 to 20 show an irregular precipitation distribution, and above 20 indicate a significantly uneven precipitation concentration.

2.6.1.2. Spatial Seasonality Index (SSI)

The SSI is used to measure precipitation distribution throughout the seasonal cycle, which can further classify the different rainfall regimes. Also, their long-term change will explain the shift in seasonal rainfall. This index was proposed by Feng *et al.* (2013). The monthly distribution of rainfall is denoted by $r_{k,m}$, for each hydrological year (k). The mean monthly rainfall climatology for the hydrological year was calculated using the following equation (Livada and Asimakopoulos 2005):

$$\overline{r_m} = \frac{1}{k}\sum_{k=1}^{20} r_{k,m} \qquad \textbf{Eq. 2.2}$$

The mean annual rainfall for the specific location is calculated by $\bar{R} = \sum_{m=1}^{12} \overline{r_m}$, and its monthly probability distribution is denoted by $\overline{p_m} = \overline{r_m} / \bar{R}$. The relative entropy for each pixel is calculated as $\bar{D} = \sum_{m=1}^{12} \overline{p_m} \log_2(\overline{p_m} / q_m)$, where q_m is the uniform distribution where each month has a value of 1/12. The dimensionless long-term seasonality index S_i is calculated by the following equation:

$$S_i = \bar{D} * \frac{\bar{R}}{\overline{R_{max}}}, \qquad \textbf{Eq 2.3}$$

where S_i is 0 when $\bar{R}$ is distributed uniformly throughout the year and maximized (at $\log_2 12$ = 3.585) when $\overline{R_{max}}$ is concentrated in a single month.

2.6.2. STATISTICAL ANALYSIS

For the statistical analysis, the simple linear regression trend, as well as the non-parametric Sen's slope (Sen, 1968) and Mann-Kendall (MK) (Mann, 1945; Kendall, 1975) trend test methods, are applied over monthly, seasonal, and annual time scale. Sen's slope estimator provides the magnitude of the trend in the time series data. In contrast, the MK test checks whether the trend is monotonically increasing or decreasing in the defined confidence interval. This method is widely used for determining the magnitude of a trend in hydro-meteorological time series data (Lettenmaier et al. 1994; Yue and Hashino 2003; Partal and Kahya 2006).

Several researchers have employed the MK trend test to ascertain the presence of statistically significant trends in hydrological, climatic variables, such as temperature, precipitation, and streamflow, concerning climate change (Burton et al. 2004; Kumar et al. 2010; Yu et al. 2016).

If the MK Z-statistics value indicates a significant trend if |Z| > 1.645, |Z| > 1.96, and |Z| > 2.576 at a significance level of 10%, 5%, and 1%, respectively then the null hypothesis is rejected.

2.7. RESULTS AND DISCUSSION

2.7.1. TEMPORAL RAINFALL VARIABILITY

The mean seasonal and annual rainfall variability over the IGB basins are analyzed using daily TRMM data from 1998 to 2017 (Figure 2.3). For seasonal analysis, we categorize each year into four seasons based on Rathore et al. (2013), i.e., pre-monsoon (March to May), monsoon (June to September), post-monsoon (October to December), and winter (January and February). Results demonstrate that the maximum and minimum rainfall are estimated in the monsoon and winter seasons, respectively.

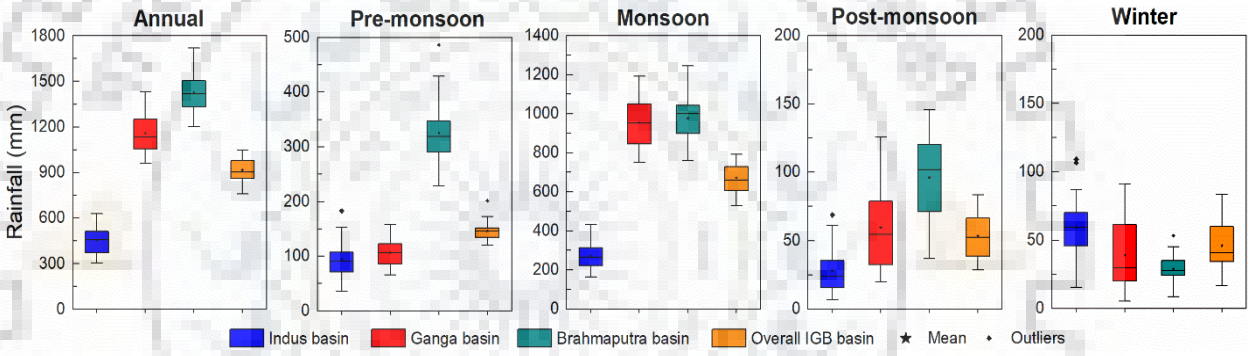

Figure 2.3. Boxplots of mean annual and seasonal rainfall over the Indus, Ganga, Brahmaputra, and whole basin from 1998 to 2017.

However, the monsoon period observes the highest rainfall in the Brahmaputra, followed by the Ganga and the Indus river basin. Also, the mean annual rainfall ranges from 114.3 mm to 5291.3 mm, with a mean value of 914.1 mm. The minimum rainfall is observed in the Indus basin and the maximum in the Brahmaputra basin. Overall, it is found that the Brahmaputra basin attains higher rainfall variability and maximum yearly as well as monsoonal rainfall, whereas the Indus basin receives lower rainfall during the study period.

Numerous studies reveal that the Indian Summer Monsoon (ISM) forms by the collision with humid air masses, orographic barriers, and heavy convection that leads to high rainfall amounts in the Eastern and Central Himalayas (Barros et al. 2000; Bookhagen et al. 2005; Bookhagen and Burbank 2010). The Western Himalayas receives rainfall from both the circulations, i.e., ISM and mid-latitude westerly (Bhowmik et al. 2005; Bookhagen et al. 2005; Pattanaik et al. 2005).

The inter-annual variation of mean annual rainfall and its linear trends are analyzed (Figure 2.4). This indicates that the Brahmaputra and Ganga basins show a decreasing trend, whereas the increasing trend is observed in the Indus basin. A similar increasing trend of rainfall in the Indus basin was highlighted by several authors (Hartmann and Buchanan 2014; Shrestha et al. 2015). Krakauer *et al.* (2019) revealed that the Indus basin experienced an increasing rainfall trend from 1891 to 2016. In contrast, Bera (2017) carried out a study on the 236 districts in the entire Ganga basin during 1901–2000, highlighting that half of the district showed a decreasing trend in rainfall. Also, Deka et al. (2013) revealed that the Brahmaputra and Barak basin showed a decreasing trend of precipitation during 1901–2010. The overall trend of the entire IGB basin shows a decreasing pattern over the study period.

The mean monthly rainfall pattern was observed over the IGB basins during 1998–2017 (Figure 2.5). The result of mean monthly rainfall shows that the minimum, maximum, and mean monthly rainfall was found in December (6.9 mm), July (220.1 mm), and annual (76.2 mm), respectively. The Indus, Ganga, and Brahmaputra basin received the maximum mean monthly rainfall in July (92.3 mm), July (327.4 mm), and July (289.0 mm), respectively, while the minimum rainfall was observed in November (6.4 mm), December (4.3 mm), and December (5.2 mm), respectively.

2.7.2. SPATIAL RAINFALL VARIABILITY

The spatial variability of seasonal and annual rainfall is analyzed using a non-parametric MK test, and its strength is determined through Sen's slope method (Figure 2.6). Results demonstrate that a lower value of annual rainfall is observed in the upper reaches (leeward side) of high mountains and the southwest part of the IGB basins (especially in the Ganga and Indus basins). On the other hand, a higher rainfall is observed in the southeast region of the IGB basins, particularly in the Brahmaputra and the Ganga basin. The statistical analysis indicates a significant decreasing trend in the upper part of the Ganga and the lower part of the Brahmaputra basins. The increasing trend was observed in the southwest part of the Indus basin. Several authors have reported a similar rainfall pattern in this region (Bandyopadhyay 1995; Cooper 2010). Overall, the mean annual rainfall of the IGB basins shows a heterogeneous pattern at varying locations. The spatial distribution of seasonal rainfall indicates that the IGB basins cover 73.2% of the mean annual rainfall in the monsoon period. It is also noted that the rainfall trend in the eastern part of the basin (the Brahmaputra and the Ganga) is significantly decreasing, and in the western part of the basin is increasing (the Indus). Several authors have reported that the substantial portion of the Brahmaputra and the Ganga basins indicates a progressively decreasing

rainfall trend in the monsoon period (Kelkar et al. 2008; Immerzeel et al. 2009; Gain and Giupponi 2015).

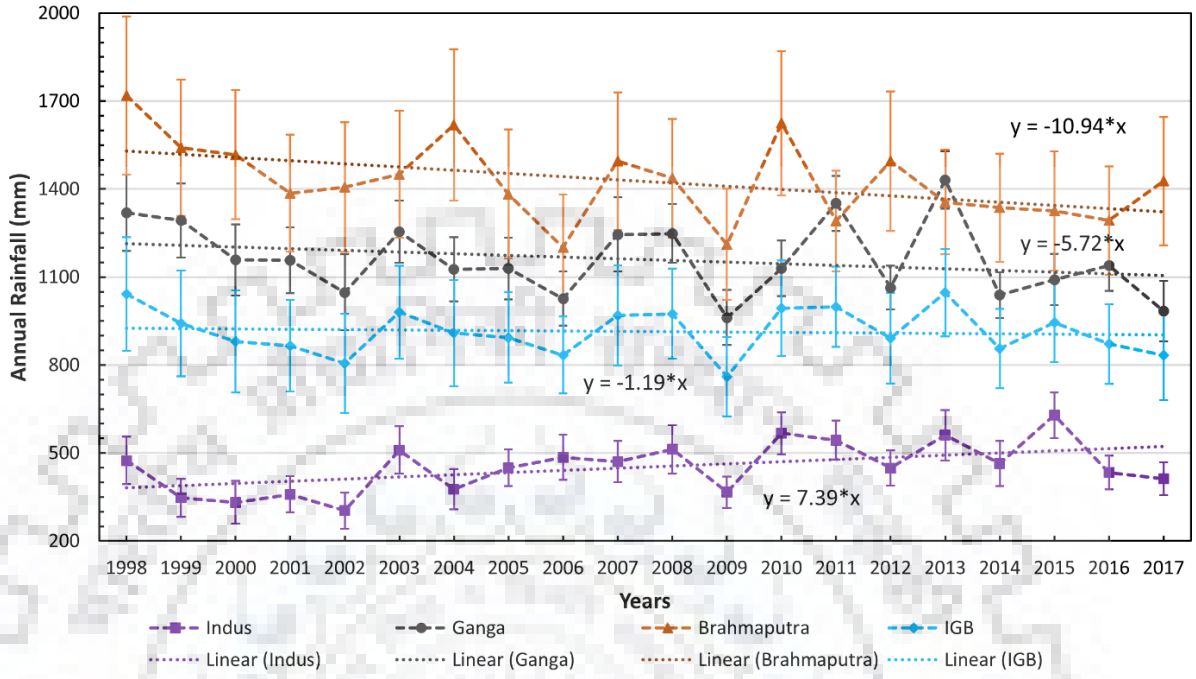

Figure 2.4. Annual rainfall with its linear trend of the Indus, Ganga, Brahmaputra, and the whole IGB river basins from 1998 to 2017.

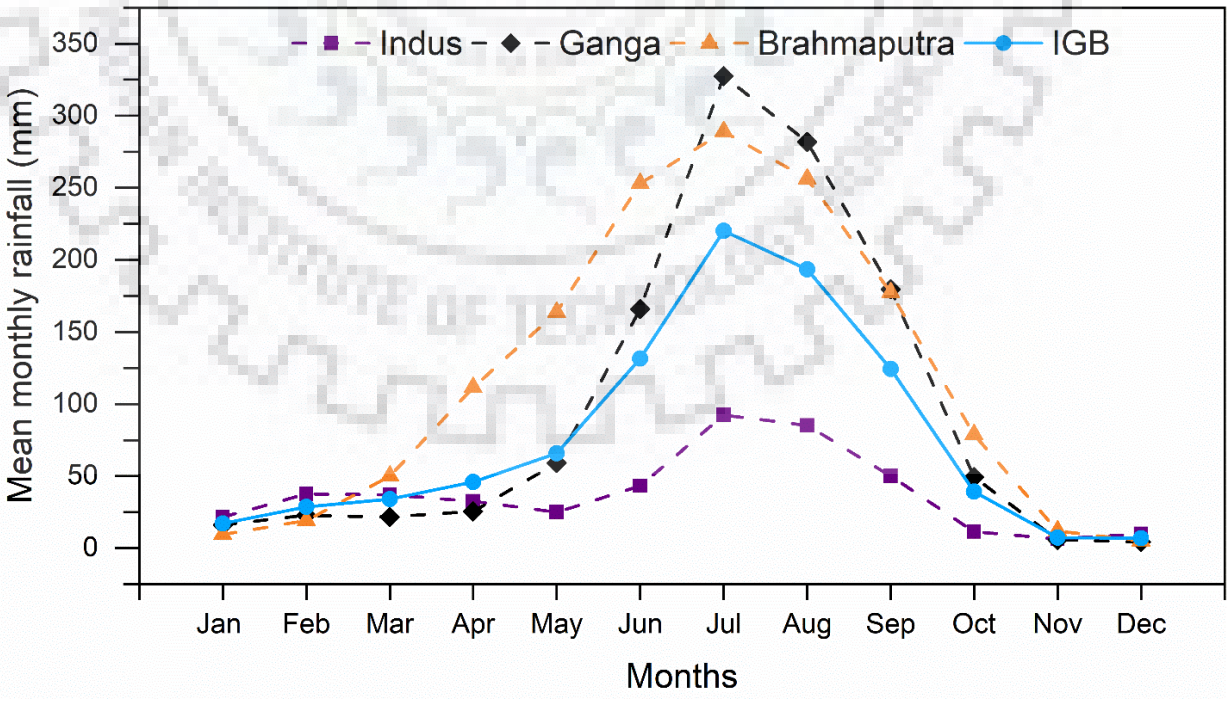

Figure 2.5. Mean monthly rainfall of the Indus, Ganga, Brahmaputra, and whole IGB river basins from January 1998 to December 2017.

The mean rainfall in the winter season ranges from 0.9 to 137.3 mm, with a slope of –3.89 to 11.29 mm yr^{-1}. No significant trend is found in the substantial part of the basin for the winter period. For the pre-monsoon season, the mean rainfall varies from 2.6 to 381.9 mm, with an inter-annual variability rate from −5.04 to 9.99 mm yr^{-1}. A significant increasing trend was observed in the western part of the basin for the pre-monsoon season. Similarly, the average post-monsoon rainfall varies from 0.9 to 102.7 mm, with a trend ranging from –4.30 to 7.42 mm yr^{-1} which is insignificant. The result of seasonal analysis follows a similar pattern a to that of Deka et al. (2013). Results also demonstrate that the rainfall pattern decreases while moving from east to west over the study area. This may occur due to the orographic distribution (Alpert 1986; Anders et al. 2006) and the rain shadow zone of the Himalayas (other side of the basin) (Bookhagen and Strecker 2008). Therefore, a very less amount of rainfall is observed in the southern part of the Indus basin during the monsoon period. The maximum rainfall in the Indus basin is received due to western disturbance rather than Indian Summer Monsoon (Shekhar et al. 2010). On the other hand, the upper-middle portion of the IGB basins shows a significant increasing trend during the monsoon season. Thayyen et al. (2013) found that this region frequently experiences cloud-burst events.

The seasonal analysis suggests that annual rainfall distribution follows an almost similar pattern as the monsoon season over the northeast part of the IGB basins (as shown in Figure 2.6). Therefore, the month-wise study of the monsoon season (June to September) are analyzed to understand the changing pattern in monthly rainfall and its shift with time (Figure 2.7). The negative trend of rainfall is higher in July and lower in September. Naidu et al. (2009) highlighted that the monsoon rainfall decreased over the Brahmaputra and some parts of the Ganga basin from 1871 to 2005. These decreasing trends may occur due to the delay of the ISM over the northeastern part of India. Many authors reported that the monsoonal precipitation was delayed over the Northeastern region (Kripalani and Kulkarni 2001; Kripalani and Kumar 2004).

The standardized annual rainfall anomalies are measured for 1998–2017, which demonstrates that the Indus basin received a higher positive value (above-normal rainfall) in 1998, 1999, 2003, 2008, 2010, 2011, 2013, and 2015 (Figure 2.8). In comparison, the maximum rainfall was observed in 2013 over the southwestern part of the Ganga basin. This higher rainfall may be due to the occurrence of the Kedarnath disaster in June 2013. The disaster happened because of excessive rain over a short span of time (Ziegler et al. 2014), which may be responsible for filling up the Chorabari lake and further leading to breaching of the moraine-dam lake (Dobhal et al. 2013; Das et al. 2015).

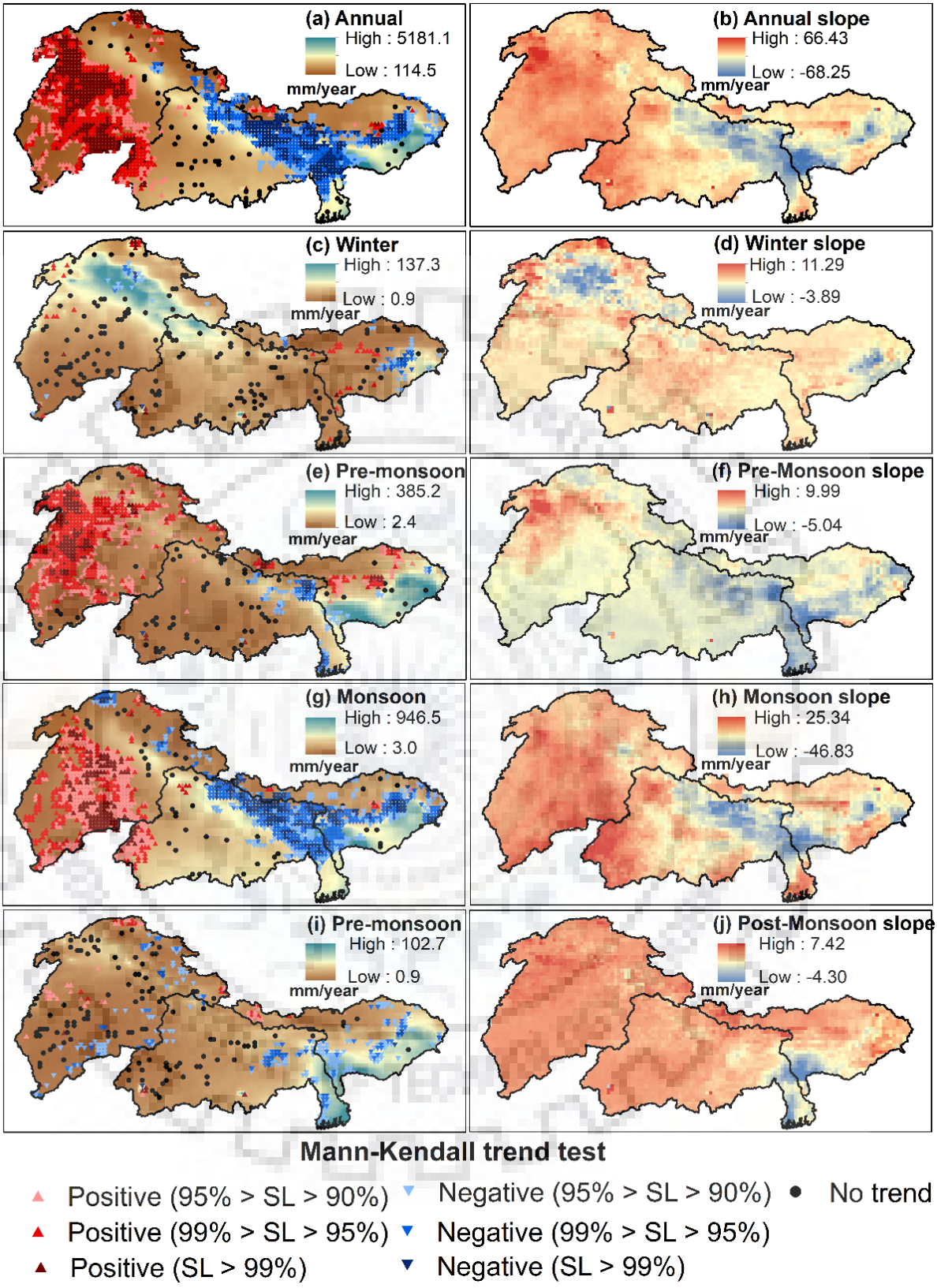

Figure 2.6. The spatial distribution of annual and seasonal rainfall (a, c, e, g, i), and trends (b, d, f, h, j) across the IGB river basins based on Sen's slope and Mann-Kendall trend test from 1998 to 2017.

Other than that, the spatial rainfall anomalies experienced a varying drought magnitude during all the other years. The anomalies comprise the drought occurrences (below-average rainfall) in 2000, 2001, 2002, 2004, 2005, 2006, 2007, 2009, 2012, 2014, 2016, and 2015 for the Ganga and Brahmaputra basin and 2017 across the IGB basins. According to the Indian Institute of Tropical Meteorology (IITM), Pune, a total number of 26 significant drought years were observed based on All-India Summer Monsoon months (June to September) Rainfall (AISMR) anomalies during 1871–2015 (Kothawale and Rajeevan 2016).

2.7.3. RAINFALL INDEX ANALYSIS

2.7.3.1. Precipitation Concentration Index (PCI)

The monthly rainfall distribution is examined using the PCI over the study area. It varies from 9.1 to 28.5, with a mean value of 16.8 (Figure 2.9). A higher value of PCI is observed in the southern part of the Ganga and Indus basin. The monthly change in PCI is investigated using Sen's slope, highlighting an insignificant trend in most of the region. However, it tends to decrease significantly in the upper part of the Indus basin.

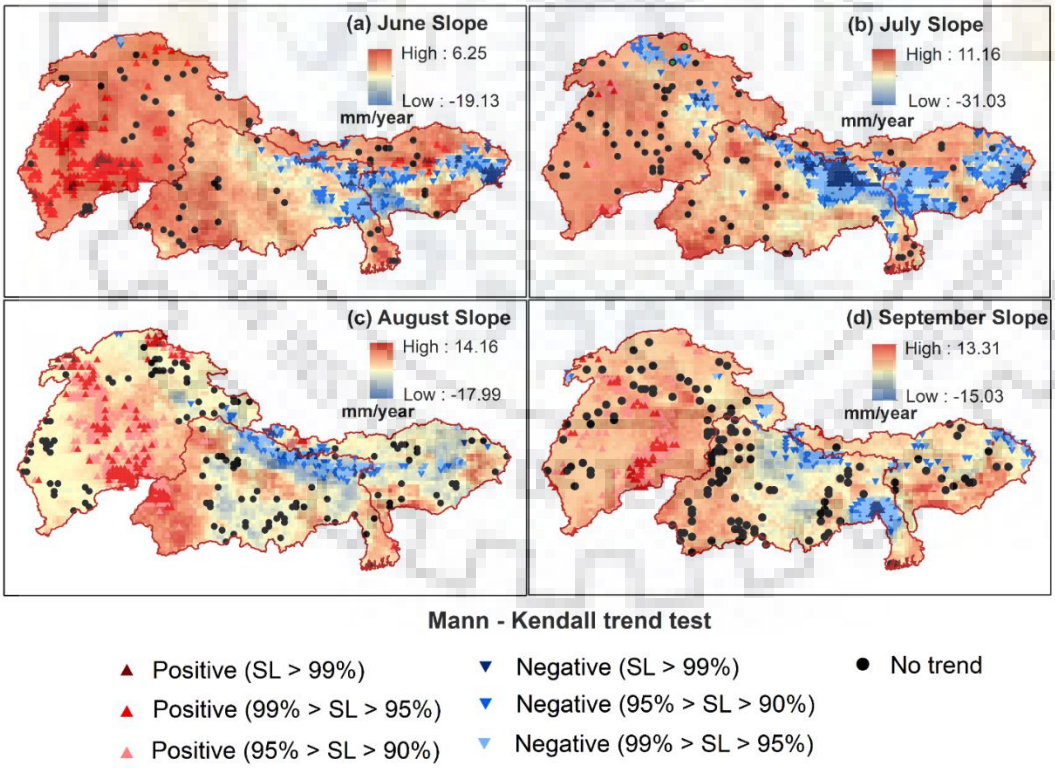

Figure 2.7. Spatial pattern of rainfall trend and its significant level during the monsoon months: a) June, b) July, c) August, and d) September over the IGB river basins.

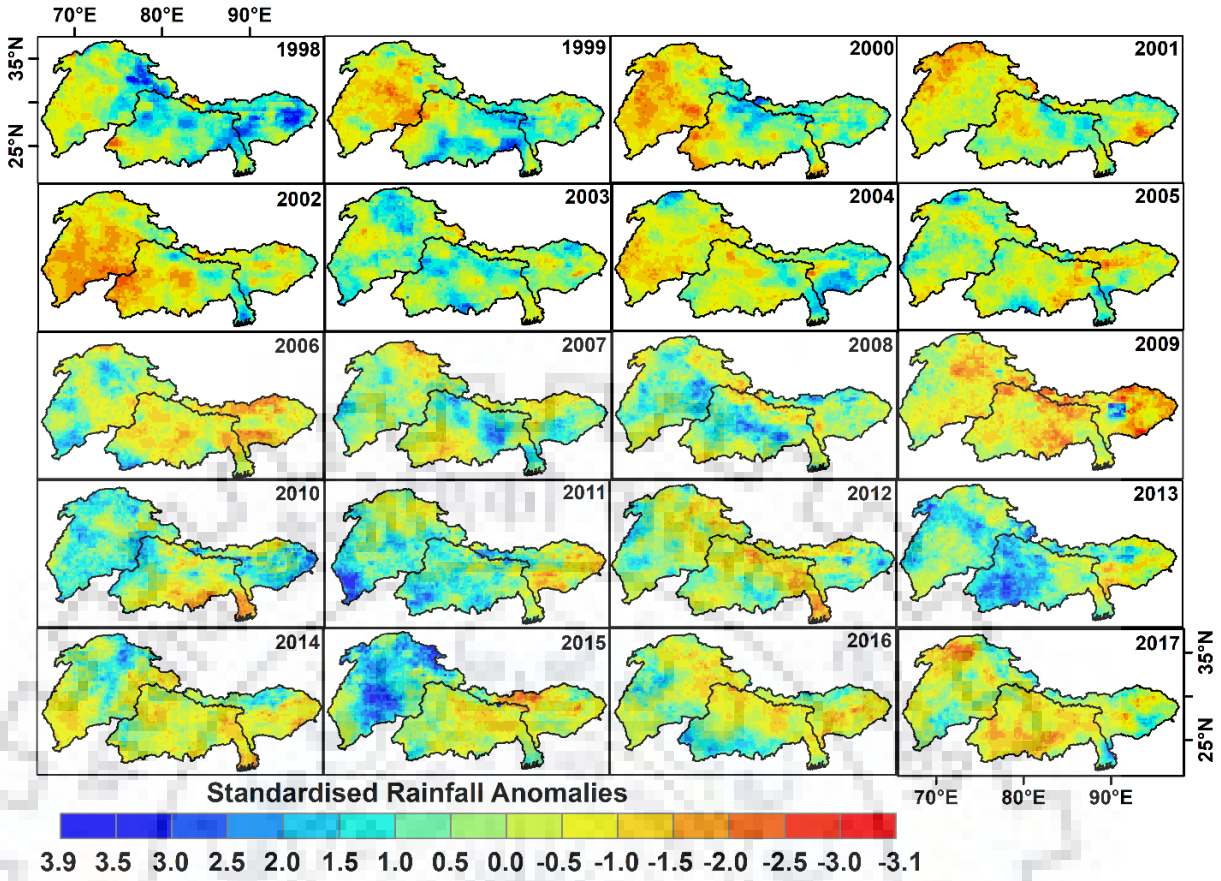

Figure 2.8. Standardized annual rainfall anomalies in the IGB basins, indicating the magnitude of departure using the long-term mean rainfall (1998–2017) data. Negative values include below the normal rainfall that shows the drought events, whereas the positive values (above-normal rainfall) are associated with the flood events.

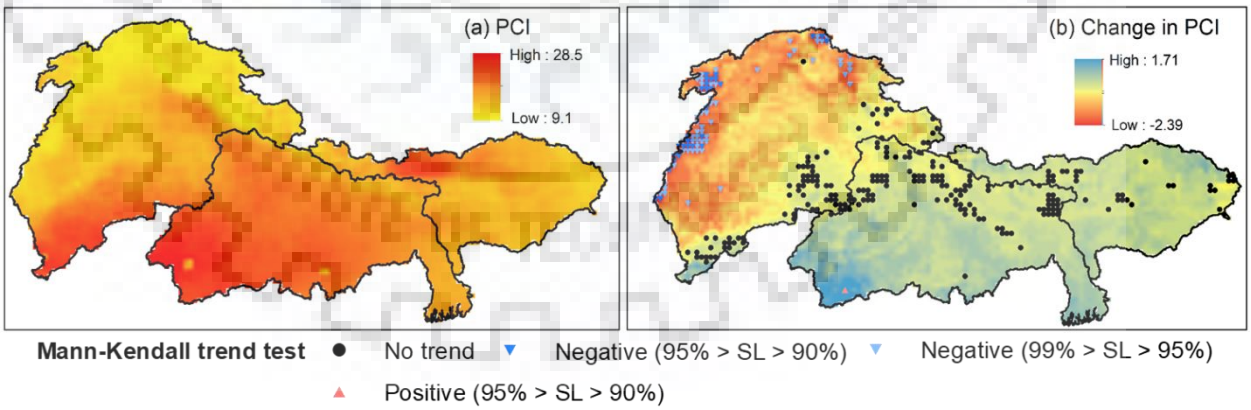

Figure 2.9. Spatial monthly distribution of PCI (a) and its trend (b) across the IGB basins.

The PCI values are categorized into four classes based on Oliver (1980). The percentages of area covered in each category, i.e., uniform (below 10), moderate rainfall (from 11 to 15), irregular precipitation (16–20), and significantly irregular precipitation (above 20) are found to be 0.9%, 32.1%, 40.0%, and 27.0% respectively.

2.7.3.2. Seasonality Index (SI)

The rainfall seasonality and its inter-annual distribution are assessed using the seasonality index across the IGB basins, which ranged from 0.9 to 1.0, with a mean of 0.94 (Figure 2.10). Results demonstrate that most of the IGB region comes under a high mean value of SI, suggesting that the seasonality of rainfall shows a heterogeneous distribution. While, the lower value of SI was attained in the southern part of the Indus basin. It is also noted that the positive/negative trend of SI is scattered all across the IGB basins while no significant trends cover most of the region.

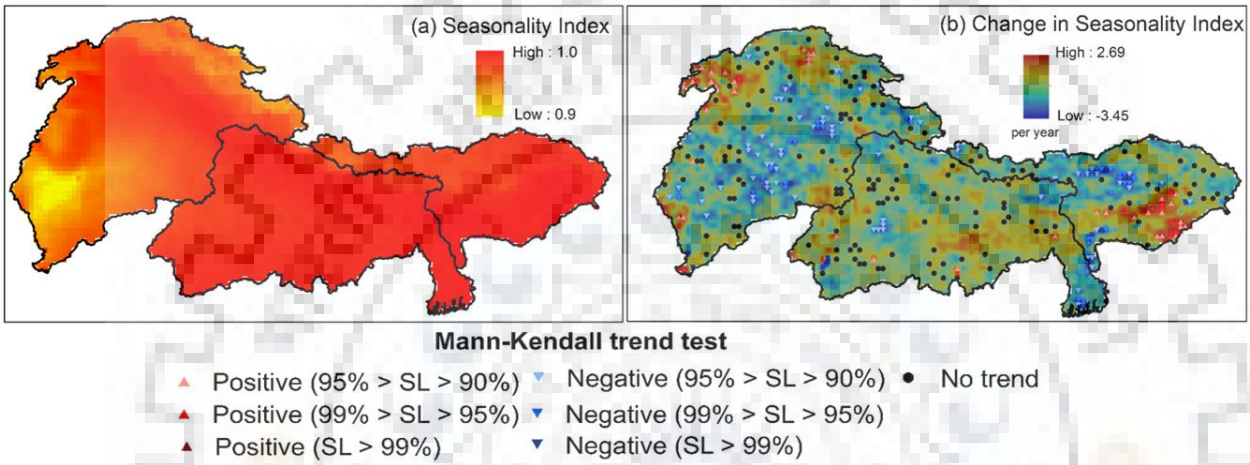

Figure 2.10. Spatial distribution of SI a) Seasonality Index and b) change in SI across the IGB river basins.

2.7.3.3. Coefficient of variation (CV)

The spatial variability of rainfall is estimated using Coefficient of Variation (CV). Majority of the area in the IGB basins is found less variable (< 20%) (Figure 2.11). In contrast, an extremely variable rainfall (> 60%) is found in the southwestern part of the basins. Higher variability of rainfall is observed in the Indus basin, which varies from 12 to 87.1%, with a mean of 35.6 %. In comparison, less variability is found in the Brahmaputra basin which ranges from 7.9 to 59.0%, with a mean value of 17.1%. Deka et al. (2013) noticed that the Brahmaputra basin attains a CV (10%) less than the Barak basin (13%). The Ganga basin represents an intermediate variability between these two basins and varies from 9.5 to 38.2%, with a mean value of 21.5%. Yu et al. (2013) demonstrated that the CV in the Ganga basin showed a value of 27% during 1951–2000. The overall CV of the IGB basins varies from 7.9 to 87.1, with a mean value of 26.8%.

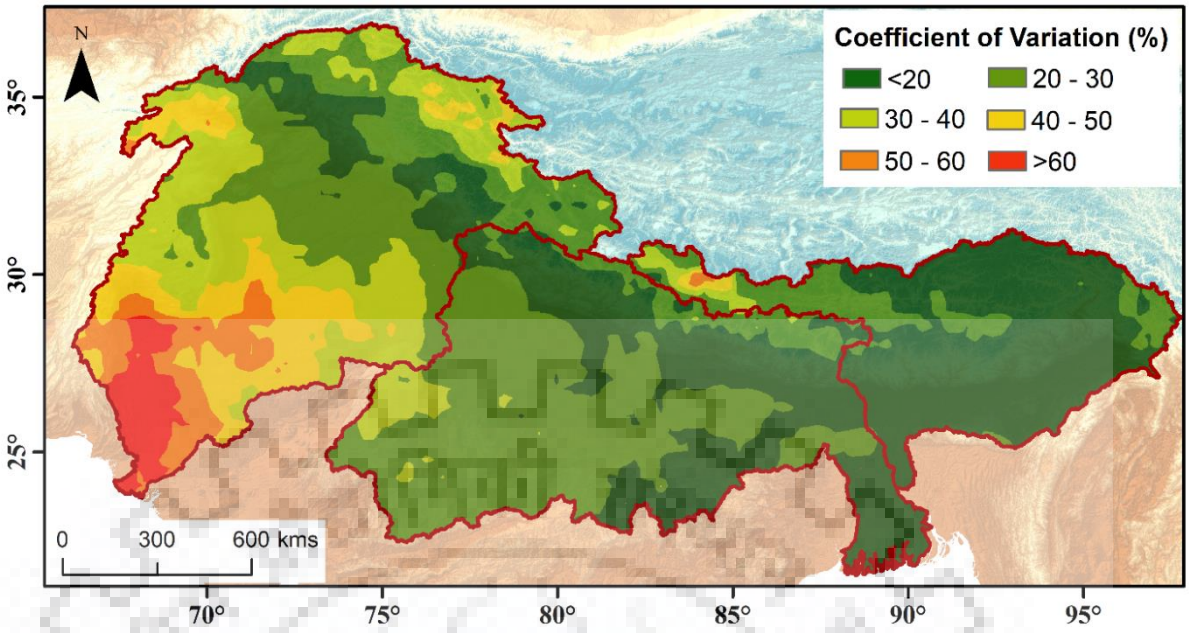

Figure 2.11. Coefficient of variation (in percentage) calculated by annual rainfall data from 1998 to 2017 over the IGB basins.

2.7.4. SPATIAL DISTRIBUTION OF RAINFALL FREQUENCY AND RATE

The daily rainfall data are used to examine the possible changes in the frequency of rainfall events in terms of their duration and intensity over the basins. It is observed that the rainfall intensity varies from 0.3 to 14.3 mm day^{-1} with a mean value of 2.5 mm day^{-1}. The higher rainfall intensity for a shorter time may be responsible for a flash flood (Varikoden et al. 2010; Kumar et al. 2018a). Light rain (< 2.0 mm day^{-1}) covers 47.8% of the IGB area, whereas extreme rainfall intensity (> 14.0 mm day^{-1}) only contributes about 1.0% over the study area (Figure 2.12a).

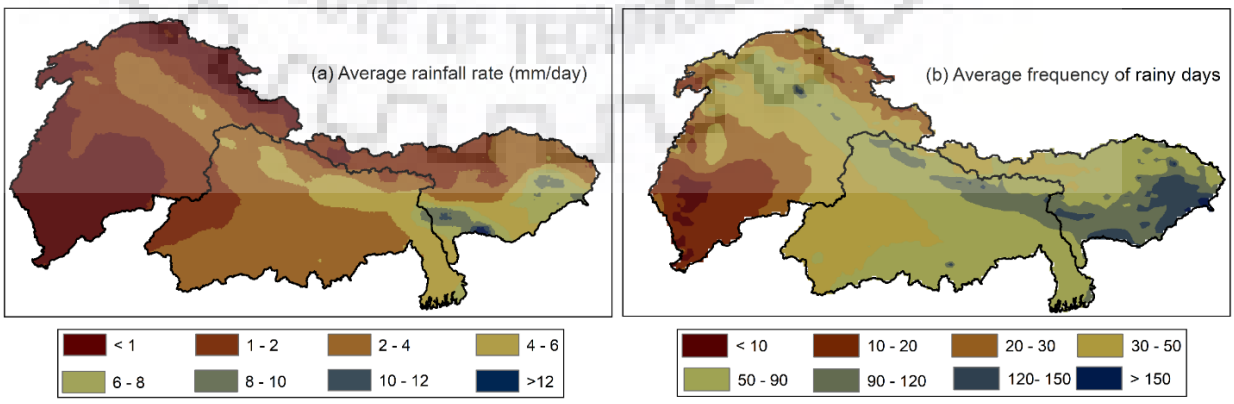

Figure 2.12. Spatial distribution of a) average rainfall rate (intensity) and b) average frequency (number of rainy days) over the IGB basins.

Overall, the mean rainfall intensity shows a declining trend during 1998–2017. The higher rainfall intensity occurs in the southern part of the Brahmaputra basin, while light rain occurs in the southwest region of the Indus basin.

The daily-accumulated rainfall data was considered for calculating the rainy days based on the amount of rainfall acquired in a single grid. If the amount of rain is greater than or equal to 2.5 mm, then it is considered as rainy day (marked as 1); otherwise, no rainfall (marked as 0) (Das et al. 2009). The frequency of rainy days was well related to the average annual rainfall (Figure 2.12b). A higher number of rainy days (88 ± 30 days) was observed in the Brahmaputra basin, followed by the Ganga (63 ± 19 days) and the Indus (33 ± 18 days) river basins. The mean rainfall days was about 55 ± 30 days and showed a declining trend over the whole IGB basins. A similar trend and pattern of rainy days was observed by many authors over the IGB basins

2.7.5. DISTRIBUTION OF OROGRAPHIC RAINFALL

The spatial distribution of rainfall is highly dependent on the meteorological variables and topography of the region (As-Syakur et al., 2011; Prasetia et al., 2013). Singh and Kumar (1997) stated that the windward side of the Himalayan range receives more rain as compared to the leeward side (rain shadow zone). Shrestha et al. (2000) studied the variability of rainfall related to altitude in different regions of the Himalayas. Therefore, a detailed investigation of rainfall variability against altitude is performed over the IGB basins for 1998–2017 (Figure 2.13).

For understanding the rainfall pattern relative to the topography, a transverse profile (AA') is drawn from west to east (AA') and three cross-section profiles (BB', CC', and DD') from lower to upper reaches in each basin (Figure 2.14). The cross-section profiles include the plain as well as mountainous regions. The mean annual rainfall progressively increases above a particular elevation and is also highly dependent upon the relief of a mountain. Kumar et al. (2018) revealed that most of the extreme rainfall events recorded in the Himalayas are orographically situated on the windward side. A higher amount of rainfall is highlighted in the cross-sectional profile of DD' followed by CC' and then BB'. The larger elevation variability is observed in the Indus basin cross profile and smaller in the Ganga basin profile. It is also noted that the cross-section profile of the Ganga basin majorly contains the part of the plain compared to the mountainous region. The transverse profile indicates that the rainfall starts decreasing while moving from east to west (A' to A). This may occur due to the ISM, which primarily affects the Brahmaputra basin and then move towards the Ganga and Indus basin; however, the strength of the precipitation may decrease (Miller et al. 2012; Kumar et al. 2018a).

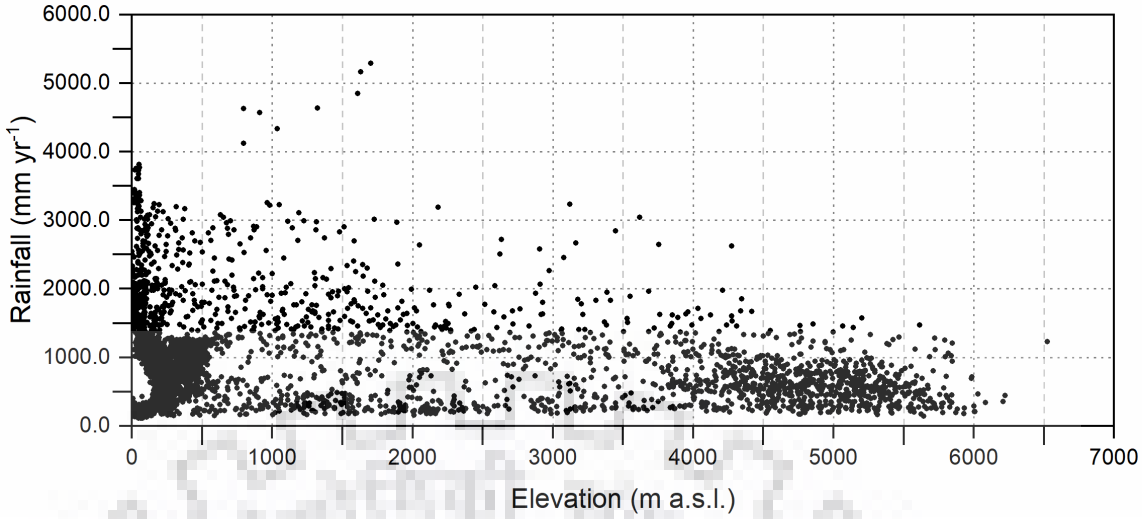

Figure 2.13. Mean annual rainfall distribution against elevation over the IGB basins.

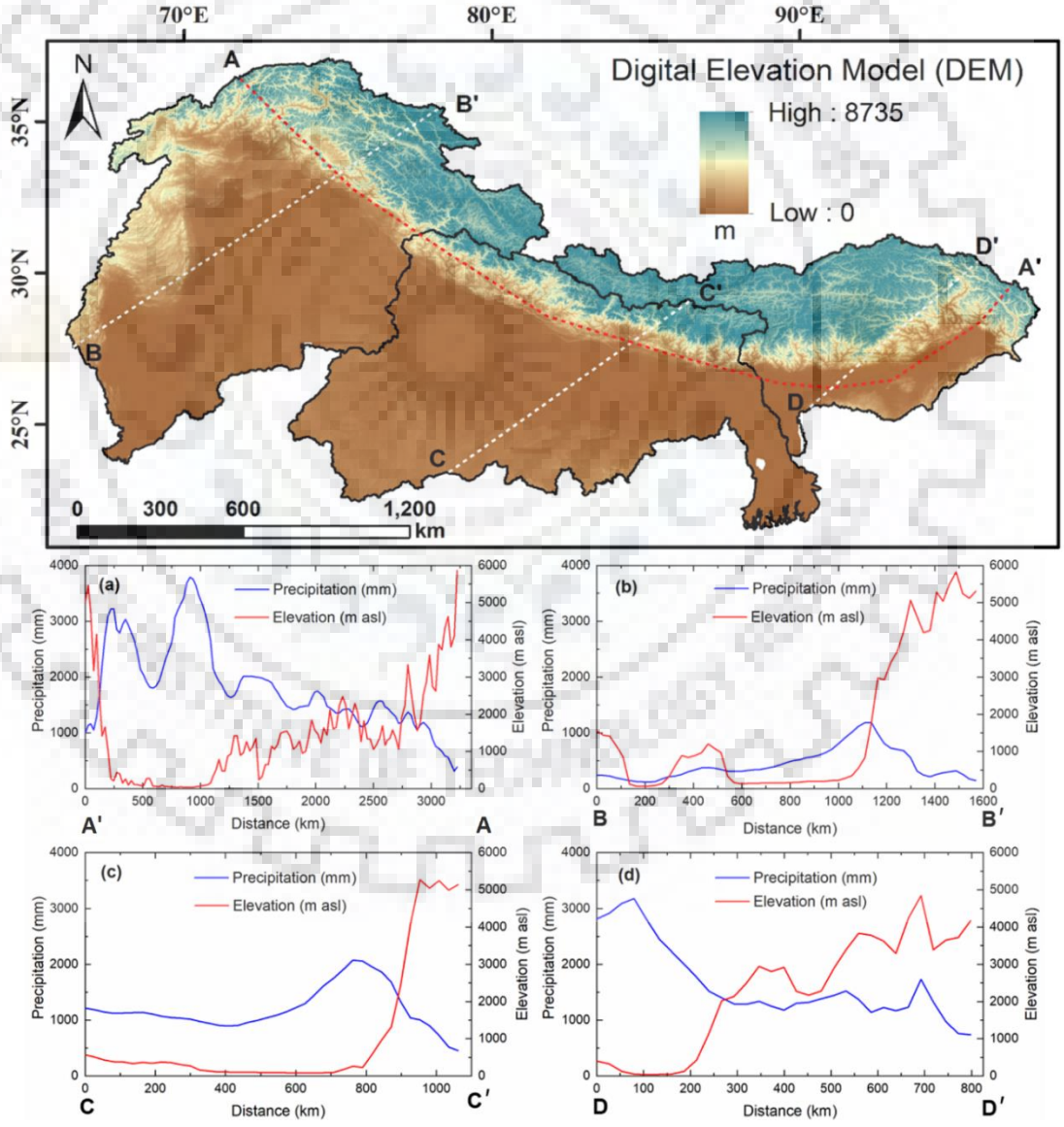

Figure 2.14. Relationship of rainfall with elevation extracted through profile drawn on the study area (a) Transverse profile AA' (b), (c) and (d) cross-sectional profile BB', CC' and DD', respectively.

2.7.6. CLIMATE VARIABILITY

The spatio-temporal distributions of rainfall and temperature are closely associated with the total availability of water (Barnett et al. 2005; Milly et al. 2005; Trenberth 2011). Therefore, understanding the climatic variables (rainfall and temperature) and their relation with water storage are significant to assess the level of water stress over the region. In this study, we analyze the trend of climatic variables and TWSA from 2003 to 2015 (Figure 2.15). Results reveal that the temperature shows an increasing trend that varies from –0.05 to 0.05 °C yr^{-1} with a mean value of 0.02 °C yr^{-1} . The increasing trend is mainly concentrated in entire basins except in the central part of the Ganga and upper reaches of the Indus basin. The spatial analysis also highlights that the upper part of the Ganga basin (part of Nepal and west Uttar Pradesh) shows a declining trend. These temperature changes occurr due to an increase in groundwater irrigation over the region (Cao and Roy 2020), which further leads to a decrease in water storage and may accelerate water stress over the area. According to Cao and Roy (2018), the upper portion of the Ganga basin experiences an intensification in well and tube-well irrigation, responsible for a decrease in TWSA. Baidya et al. (2008) have reported a significant decrease in temperature and precipitation based on observation data (location-based) over the Nepal region.

Other than that, the statistical analysis of TWSA shows a decreasing trend in most parts of the IGB basins and an increasing trend in the western part of the Indus and lower part of the Ganga basin. The TWSA shows a declining trend over the Brahmaputra basin, which is statistically significant. Additionally, a correlation test is performed between rainfall, TWSA, and temperature. The mean annual rainfall is positively correlated (r = 15.8) with TWSA, whereas temperature was negatively (r = –38.8) associated with rainfall. This correlation indicates that changes in rainfall were significantly impacted the TWSA.

Overall, it is observed that the middle-upper reaches of the basins indicate a higher temperature and precipitation and are characterized by higher TWSA, which indicates a low risk of water stress over the region. However, the south-eastern part of the Ganga basin shows more moderate rainfall with higher temperatures were characterized by lower TWSA, indicating a high probability of water stress. The results coincide with the finding of Kumar and Jain (2010). According to the World Resource Institute (WRI), this region comes under high and extremely high water stress (Wolf et al. 2003). Apart from this, some parts of the IGB basins show no trend in TWSA with a decrease in rainfall and temperature. These findings agreed with various field observation-based and simulation-based studies (Nepal and Shrestha 2015; Shrestha et al. 2015).

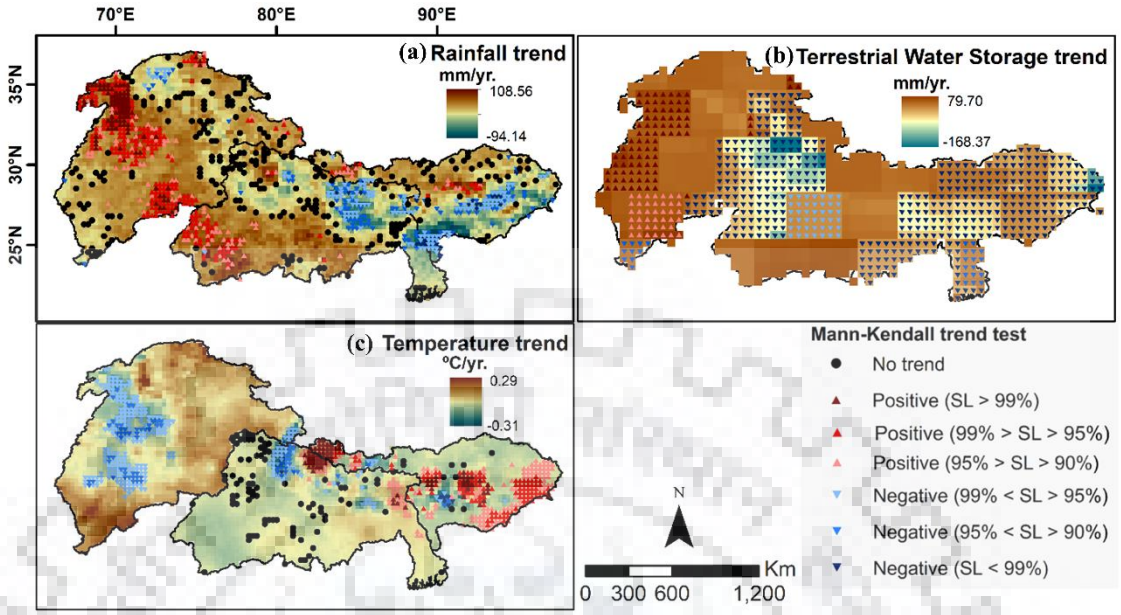

Figure 2.15. Spatial trends of annual a) rainfall; b) GRACE Terrestrial Water Storage Anomaly, and c) air temperature across the IGB basins during 2003–2015.

2.8. CONCLUSIONS

Rainfall distribution and its related trends play a significant role in managing the water resources and their demands. However, monitoring the spatio-temporal rainfall distribution using in-situ-based observation is highly difficult in the mountainous region of IGB basins due to rugged terrains and their broader spatial coverage. Therefore, we use daily TRMM data for reliable estimation of rainfall variability at spatial and temporal scales during 1998–2017. Results demonstrate that the mean annual rainfall in the IGB river basins was about 914.4 ± 675.2 mm with a maximum value (1425.4 ± 937.5 mm) in the Brahmaputra and minimum value (452.1 ± 292.2 mm) in the Indus river basins. The spatial seasonal and annual trend of rainfall shows a decreasing trend in the eastern part (the Brahmaputra basin) and an increasing trend in the western region (the Indus basin) which is statistically significant. It is observed that the major part (40%) of the basins come under the classification of irregular rainfall distribution. The seasonality of rainfall decreases over most parts of the basins. The maximum and minimum mean seasonal monsoon rainfall were observed in 2007 (791.4 mm) and 2009 (529.5 mm), respectively. The rainfall intensity was varied from 0.3 to 14.3 mm day^{-1} with a mean value of 2.5 mm day^{-1} and a higher number of rainfall days (88 ± 30 days) was observed in the Brahmaputra basin and lower value (33 ± 18 days) in the Indus basin.

Apart from this, the contribution of climatic variables (rainfall and temperature) are assessed to quantify the possible changes that occur in the vicinity of the basins and their association with water availability which may be further responsible for water stress. Results illustrate that the changing pattern of rainfall and temperature profoundly affected the total water storage of the basins. The upper-middle reaches of the basin experience a lower risk of water stress, and the south-eastern part of the Ganga basin indicates a high probability of water stress for the period 2003-2015. Overall, our study provides valuable knowledge about the change in rainfall and its impact on water storage across the basins. These findings will further contribute to the development of adaptation strategies and policy decisions to mitigate the adverse effect of climate change and extreme events. The outcomes are reliable for the extraction of rainfall trends and improvements in future research on hydrological extremes and enhance sustainable water resource management.

CHAPTER 3

MAPPING AND MONITORING OF REGIONAL MASS ANOMALY BY USING REMOTE SENSING-BASED ANALYSIS

3.1. INTRODUCTION

Mountain glaciers are losing mass worldwide, which directly or indirectly affects the Earth's inhabitants and contributes to sea-level rise (Zemp et al. 2019). The High Mountains of Asia (HMA) comprise the world's largest ice cover outside the polar regions, which lies at low-latitude and high-altitude (Bolch et al. 2012). Apart from this, the glaciers of HMA are considered a natural "climate meter" to understand the sensitivity of climate change (Davaze et al. 2020). In context to climate sensitivity, significant changes are likely to occur in the runoff during summer, which would modify the water resources and affect the water needs of millions of population in Asia (Immerzeel et al. 2010). Therefore, the study of HMA glaciers is essential not only to understand the impact of climate change on glaciers, but also to assess their contribution for the sustainable utilization of water resources.

Many studies carried out worldwide reveal that the glacier and ice caps are losing mass, leading to a sea-level rise of ~0.71 ± 0.08 mm yr^{-1} for the period 2003–2009 (Gardner et al. 2013), 0.92 ± 0.39 mm yr^{-1} during 2006–2016 (Zemp et al. 2019) and 1.85 ± 0.13 mm yr^{-1} between 2012 and 2016 (Bamber et al. 2018). During the early 21st century, the rapid ice loss over the Greenland and Antarctic ice sheets had increased into the near present day, which further contributes to global sea-level rise (Meredith et al. 2019). Also, numerous studies were conducted over the glaciers of the HMA and their total contribution to global sea-level rise (Huss and Hock 2015; Wang et al. 2019; Wouters et al. 2019).

Brun et al. (2017) observed that the HMA glaciers mass loss rate was –0.18 ± 0.04 mm yr^{-1} between 2000 and 2016. Similarly, Shean et al. (2020) have revealed that the regional mass change of HMA was –19.0 ± 2.5 Gt yr^{-1} between 2000 and 2018. De Kok et al. (2020) have also witnessed the glacier mass loss over western and southern HMA. Hock et al. (2019) have demonstrated that the regional mass variation of HMA was the least negative mass budget (–150 ± 110 kg $m^{-2}yr^{-1}$) for the period 2000–2016. The heterogeneity of glacier mass change in the HMA region highlights the importance of estimating the regional mass variation and their association with climate variables.

In the HMA, the field observation-based glacier mass balance fails due to the altitudinal variation and complex topography, which can be extrapolated to the vast unsampled area for regional variability (Brun et al. 2017). On the other hand, the geodetic method (Digital Elevation Model (DEM) differencing) may provide mass balance for a sub-regional scale, not representative for the larger region and for varying time-space. The above-mentioned scientific research questions were enabled by the recent development in flux/stress/slope related approaches for calculating the terrestrial water storage in terms of thickness change (Haeberli 2016). Therefore, the global coverage of Gravity Recovery and Climate Experiment (GRACE) based mass variation provides an excellent opportunity to understand the regional glacier mass change. Several authors have utilized the previous GRACE mission data for the mass budget of the HMA region over a different period (Chanard et al. 2014; Yi and Sun 2014; Reager et al. 2016). Therefore, we bridge the gap of temporal and regional mass balance for the Karakoram and Himalayan (KH) glacierized area.

3.2. RESEARCH QUESTIONS

- **What is the nature of regional glacier response in the KH region?** Are variations in glaciers from region to region caused due to climatic variability, topography or glacier sensitivity, or response time?
- **What are the climatic conditions required for glacier mass change?** What are the forcing (climatic or radiative) mechanisms responsible for glaciers advancing or retreating? And how do they respond to climate change in the near future?
- **What is the key environmental control of regional differentiation in glaciers?** Do the ice or non-ice hydrological components contribute to the regional scale mass variation? What are the likely impacts on the streamflow and water availability of the region?

3.3. OBJECTIVES

- Quantification of regional-scale glacier mass variation and its trend using the gravimetric approach
- Analyzing the influence of hydro-climatic drivers on glacier surface and their association with mass change
- Assessing the uncertainties and sensitivity of contributing variables on the glacier mass variation

3.4. STUDY AREA

The KH region lies between 72.4° – 95.5°E and 26.7° – 37.3°N, primarily known for its frozen freshwater reservoir in the form of snow cover and glacier ice. Consequently, the water stored in these regions glacier has a significant influence on the livelihood of the upstream and downstream population. The region records 32,399 glaciers, covering an area of 42,005 km2 (RGI Consortium 2017) out of the total area of ~7,13,907 km2. This region includes areas of India, Pakistan, Nepal, Bhutan, and China, as well as comprises many greatest mountain peaks in the world.

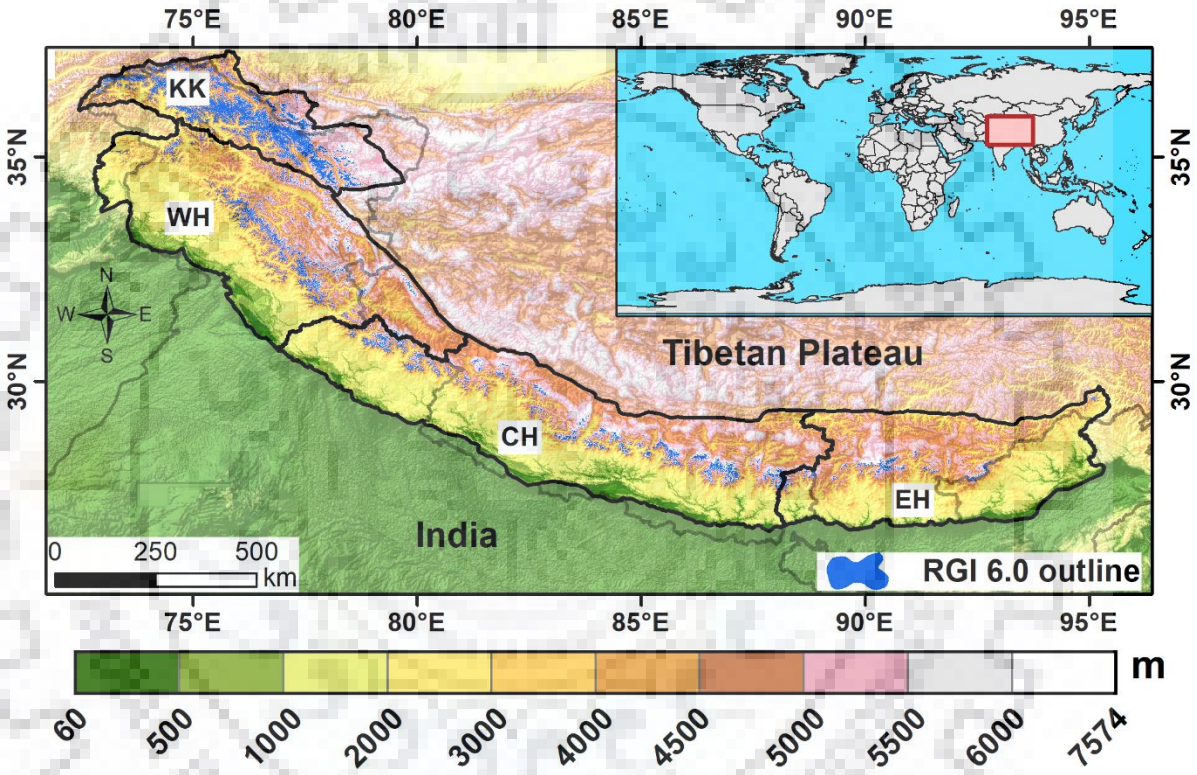

Figure 3.1. Location map of the Karakoram and Himalaya (KH) region and their sub-regions (KK: Karakoram, WH: Western Himalaya, CH: Central Himalaya, and EH: Eastern Himalaya) showing glacier outlines (RGI Consortium 2017), and orographic barrier (Shuttle Radar Topography Mission (SRTM) 90m digital elevation data version 3.0 available at https://earthexplorer.usgs.gov/).

Based on the climate and geographic location, the region is divided into four parts, i.e., the Karakoram (KK), Western (WH), Central (CH), and Eastern Himalaya (EH), as previously demarcated by Bolch et al. (2012) and is shown in Figure 3.1. The area of the glaciers in each selected region is estimated by Randolph Glacier Inventory (RGI) version 6.0 (RGI Consortium 2017). The KK, WH, CH, and EH regions cover an area of 21,683.5, 8,389.6, 8,947.9, and 2,983.6 km^2, respectively. These regions are characterized by the complex terrain and a

substantial influence of monsoon climate and global atmospheric circulation. Moreover, the glaciers are primarily nourished by the two precipitation systems, i.e., the Mid-Latitude Westerlies (MLW) and the Indian Summer Monsoon (ISM). The MLW precipitation greatly influences the KK and WH region during the winter and spring season, covering ~60–70% of the total precipitation annually (Shrestha et al. 2015). In comparison, the ISM has a dominant impact on the EH and CH region and partly on the WH during the summer. The monsoonal precipitation decreases from east to west of the Himalayan region with a mean annual precipitation of ~1071 mm in the EH (Brahmaputra basin) and ~423 mm in the WH (Indus basin) (Immerzeel et al. 2010). Any minor changes in these two precipitation intensities and frequency have significant consequences on its downstream water resource management.

3.5. DATA USED

3.5.1. GRACE MONTHLY TIME SCALE DATA

In this study, we have used the data from National Aeronautics and Space Administration (NASA) Jet Propulsion Laboratory (JPL) GRACE and GRACE Follow-On (GRACE-FO) TWSA version 02 release-6 (RL06) at 0.5º × 0.5º gridded monthly mass concentration (mascon) solutions (Wiese et al. 2016) from October 2002 to September 2019 (17 hydrological years) available at https://grace.jpl.nasa.gov/data/get-data/jpl_global_mascons/. This data employs Coastal Resolution Improvement (CRI) filter that reduces the leakage errors from the signal across the coastline (Watkins et al. 2015). The RL06 mascons have a significant advantage over the harmonics solution because it eliminates the empirical post-processing filter to remove the correlated errors in the gravity solution (Watkins et al. 2015).

The solutions provide monthly mass equivalent TWSA and uncertainty along with gain factors. The multiplicative gain factor is used to restore the TWS signal, attenuated by the use of filter helps in removing the systematic and random errors (Wiese et al. 2016; Banerjee and Kumar 2018). The monthly solutions of TWSA are multiplied by the spatially distributed gain factors, and then the scaled-TWSA is used to estimate the mass change over the KH region. We utilize 159 and 14 monthly solutions of GRACE and GRACE-FO, respectively. However, 29 and 2 monthly solutions were missing in each dataset during the observational period. The missing images are replaced by the mean value of sequent months (before and after) (Long et al. 2015; Yang et al. 2017).

3.5.2. GLDAS LSM OBSERVATIONAL DATA

The NASA Global Land Data Assimilation System (GLDAS) is an integration of satellite- and ground-based observation data, using advanced land surface modelling and data assimilation techniques, in order to generate optimal fields of land surface states and fluxes, with fine spatial and temporal resolution (Rodell et al. 2004). In this study, the latest monthly GLDAS NOAH land surface model (Version 2.1) is utilized from October 2002 to September 2019 with spatial resolution 0.25º × 0.25º (Rui and Beaudoing 2018) and retrieved from https://disc.gsfc.nasa.gov/datasets?keywords=GLDAS. The monthly GLDAS-derived Terrestrial Water Storage (TWS) was estimated by the combination of Soil Moisture Storage (SMS), Snow Water Equivalent (SWE), and Canopy Water Storage (CWS) variables over the KH region.

3.5.3. ERA5-LAND REANALYSIS DATA

ERA5-Land is a global reanalysis dataset that provides land-surface variables from 1981 onward at hourly and monthly time-scale. The grid resolution of the dataset is available at an enhanced resolution (9-km) compared to ERA5 (C3S 2019) (https://cds.climate.copernicus.eu/cdsapp#!/dataset/reanalysis-era5-land?tab=overview). Mahto and Mishra (2019) reported that the ERA5 variables, i.e., precipitation, temperature, evapotranspiration, and soil moisture, outperformed the other reanalysis dataset during the monsoon season over India. Likewise, Albergel et al. (2018) also revealed that ERA-5 has a consistent improvement over ERA-Interim products. In this study, we have used total precipitation, snowfall, air temperature, evaporation, total runoff, and energy flux components, i.e., net shortwave (SWN) and net longwave (LWN) radiations, to assess the varying pattern of these variables in relation with the mass change from October 2002 to September 2019 over the KH region.

3.5.4. ICESAT-1/GLAH14 SATELLITE DATA

The ICESat platform and Geoscience Laser Altimeter System (GLAS) instrument generated product Global Land Surface Altimetry data (GLAH14, version 34) is used from February 2003 to October 2009 over the HK region. This data comprises ellipsoid land elevation, laser footprint time, geolocation, and other parameters, which are used for geodetic, instrumental, and atmospheric corrections of the measured height. It is directly acquired from the NASA customize service provided by the EARTHDATA SEARCH engine (https://search.earthdata.nasa.gov/) in ASCII format. In this study, the data parameters at full 40Hz resolution are utilized that fall

within the ICESat land mask. Many authors previously used this data over the different regions of HMA (Kääb et al. 2015; Wang et al. 2017, 2021).

3.5.5. GLACIER MASS BALANCE RECORDS AND OTHER PUBLISHED DATA

The WGMS employs the direct glaciological measurement-based mass, volume, area, and length change of glaciers with respect to time (Jiao et al. 2020) (https://wgms.ch/data_databaseversions/). Also, the other published glacier mass balance information is utilized for comparison with GRACE-derived mass change. In this study, we have used 80 different glacier locations from the KH region, which have mass balance results that come under the period from 2002 to 2019.

3.5.6. RANDOLPH GLACIER INVENTORY (RGI)

In this study, the HMA RGI version 6.0 region was considered for retrieving the glacier mass change over the region (RGI Consortium 2017) (https://www.glims.org/RGI/rgi60_dl.html). In the KH region, 32372 out of 32399 glaciers have small glacier areas, i.e., <100 km2. However, the GRACE mascon signal is initially covered these glacier areas in one cell or more. This uncertainty in the signal is dominated by non-ice signals, which need to be considered (Wouters et al. 2019). Therefore, consider the grid covered by the glacier outline for mass change estimation over the KH region.

3.6. METHODOLOGY

3.6.1. GRACE-DERIVED GLACIERS MASS CHANGE

The GRACE TWSA includes the Ground Water Storage Anomaly (GWSA), Soil Moisture Storage Anomaly (SMSA), Canopy Water Storage Anomaly (CWSA), Snow Water Equivalent Anomaly (SWEA), and Surface Water Storage Anomaly (SWSA) (Thomas et al. 2017) is expressed by Equation 3.1.

$$GRACE_{TWSA} = GWSA + SMSA + CWSA + SWEA + SWSA \quad \textbf{Eq. 3.1}$$

The $GRACE_{TWSA}$ is resampled to 0.25º × 0.25º using a bilinear interpolation technique (Lillesand et al. 2015) to match the spatial resolution of GLDAS data. As the GLDAS dataset does not include the GWS and SWS components (Dai et al. 2003; Rodell et al. 2004), therefore, the monthly time-series of GLDAS data are used to estimate the mass change through subtracting with $GRACE_{TWSA}$. However, there might be a contribution of other sources of SWS (lakes, ponds,

and surface water, etc.), accounting for a relatively small proportion of TWS changes (Rodell et al. 2009), which can be ignored. For subtraction, the GLDAS-based dataset was converted into a monthly anomaly with the same consideration (mean of January 2004 to December 2009 image was subtracted from each month) of $GRACE_{TWSA}$. Several studies have neglected the SWSA for estimating the GWSA over a different part of the world (Rodell et al. 2007, 2009; Strassberg et al. 2007; Moiwo et al. 2009; Tiwari et al. 2009). The overall monthly mass change or GWSA was obtained by the following Equation 3.2.

$$GWSA = GRACE_{TWSA} - SMSA - SWEA - CWSA \quad \textbf{Eq. 3.2}$$

The obtained GWSA represents the mass change over the glaciers and nearby areas of the study region. A similar approach for glacier mass change estimation was adopted by Jiao et al. (2020) over Scandinavia using GRACE satellite data. For interannual analysis, we have added all months of each hydrological year (October to September). However, the solutions were continuously missing for ten months, from October 2017 to September 2018, making the mass change estimates unreliable. Thus, the data from 2017 to 2018 were excluded for estimating the annual mass change. The monthly volume change is calculated based on the GRACE-derived mass change in each pixel by multiplying the GRACE-resampled grid size (~27 km × 27 km) over the region. The total number of a grid in each region is 139, 230, 155, and 81 for the KK, WH, CH, and EH, respectively. The overall monthly volume is estimated by the summation of each grid volume over the region.

3.6.2. ICESAT-1 DERIVED THICKNESS CHANGE

The acquired ICESat data is used to compare the GRACE-derived mass change over the study area. For this, the preprocessing of ICESat data is required to obtain reliable land elevation data. The three quality control flags, i.e., FRir_qa_flg, elv_cloud_flg, elev_use_flg, and sat_corr_flg, are used to filter the outliers. We select these quality flags based on literature (Kumar et al. 2019a). These flags help retrieve the data attenuated by cloud, saturation, and the errors that occur during data acquisition. Originally the elevation data comes in Topex/Poseidon's (T/P) reference ellipsoidal; however, we have convert this projection into WGS84 height in the corrected elevation dataset by following Equation 3.3.

$$ICESat_{WGS84} = ICESat_{T/P} - ICESat_{geoid} - Delta_{ellipsoid} \quad \textbf{Eq. 3.3}$$

where, $ICESat_{T/P}$ is the measured elevation, $ICESat_{geoid}$ is the height of the geoid above the ellipsoid and $Delta_{ellipsoid}$ is the difference between T/P ellipsoid and WGS84 ellipsoid surface

elevation. All values are in meters. The description of the used parameters can be found in https://nsidc.org/data/glas/data-dictionary-glah14.

The thickness change (*dh*) of each footprint location is obtained by subtracting the ICESat elevation with Shuttle Radar Topography Mission (SRTM) digital elevation model data (DEM) (90m spatial resolution), which was bilinearly interpolated to match the footprint resolution, a similar approach was previously used by many authors (Gardner et al. 2013; Wang et al. 2021). Then, the *dh* is converted into mass change (m w.e.) by multiplying it with a density of 900 kg m^{-3} (Huss 2013).

3.6.3. UNCERTAINTY ANALYSIS

The monthly uncertainty in GWSA (derived from GRACE and GLDAS hydrological model) is computed using Equation 3.4 by assuming that the errors from each storage component are independent.

$$\sigma_{GWSA} = \sqrt{\sigma_{TWSA}^2 + \sigma_{SMSA}^2 + \sigma_{SWEA}^2 + \sigma_{CWSA}^2} \quad \textbf{Eq. 3.4}$$

where σ indicates the standard deviation of an individual variable. To quantify the TWSA uncertainty, we first compute the climatology of TWSA based on monthly time-series data by averaging the value of each month (e.g., all January in the 17 years data) (Thomas et al. 2017). Then, the monthly climatology is used to remove the annual and semi-annual cycles from TWSA. The residual of each month is obtained by subtracting the climatology from monthly TWSA, and it is expressed by σ_{TWSA}. Apart from this, we assume that the GLDAS hydrological variables do not contribute much uncertainty in the computed GWSA. Several studies have been carried out over different parts of the world that include different GLDAS hydrological models to estimate the uncertainty for the monthly time series data (Rodell and Famiglietti 2002; Shamsudduha et al. 2012; Richey et al. 2015; Wu et al. 2019). However, this study includes only a single NOAH model. Therefore, no monthly uncertainty can be obtained.

3.7. RESULTS

3.7.1. TIME-SERIES ANALYSIS OF GRACE DERIVED MASS CHANGE

3.7.1.1. Temporal mass change

The monthly, annual, and semi-annual signals of GRACE-derived mass variation were collectively used to compute the trend based on linear and non-parametric Mann Kendall (MK)

and Sen's slope test over the KH region for the period of 2002–2019. The mass change was assessed over 605 pixels (~32,399 glaciers) at 0.25º × 0.25º grid location lies under the different sub-regions of the KH, covering ~42,005 km2 total glacier area. Results of monthly and annual mass change of individually selected regions are shown in Figure 3.2.

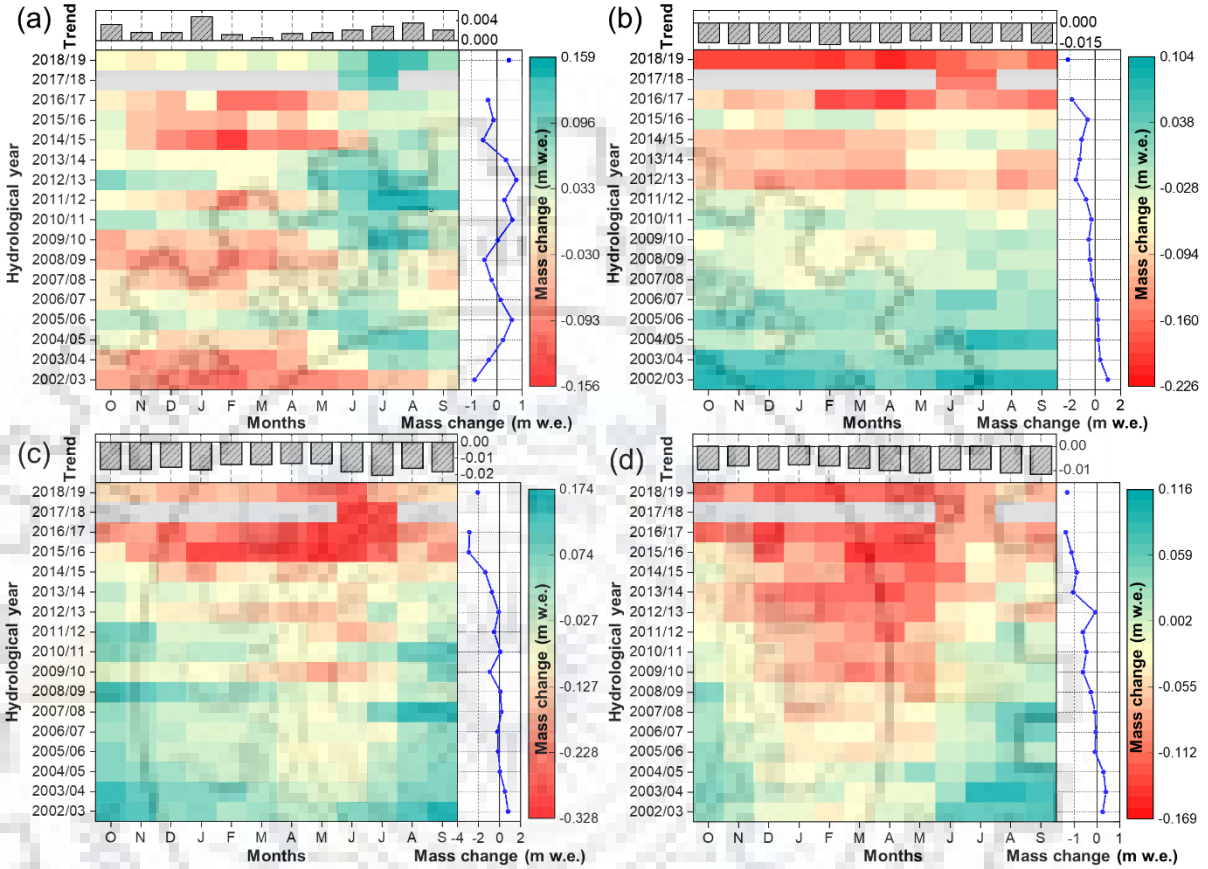

Figure 3.2. Monthly and yearly mass change over the a) Karakoram (KK), Western Himalaya (WH), c) Central Himalaya (CH), and Eastern Himalaya (EH). Sen's slope of mean monthly mass change indicates in the bar graph from 2002/03 to 2018/19. Grey color shows the data gap during the period 2017/18.

The temporal distribution of mass change suggests that the KK region follows a varying pattern, ranged from –0.88 to +0.76 m w.e. with an average of +0.04 ± 0.46 m w.e. (± standard deviation) for the study period (Figure 3.2a). It indicates a positive mass during 2004–2007, 2010–2014, and 2018/19 while a stable condition in 2009/10. The annual mass shows an increasing trend at the rate of +0.02 ± 0.05 m w.e. yr^{-1} (± standard error of linear trend at 95%). Gardelle et al. (2012) reported that the regional mass balance of glaciers over the central Karakoram region was positive (0.11 ± 0.22 m w.e. yr^{-1}) during 1999–2008. Farinotti et al. (2020) also observed a positive mass balance along with accelerating glacier flow over the Karakoram region. Besides, the glaciers of HMA (other than the Karakoram) are dominated by the higher retreating and mass

loss, which is contradictory to what has been observed over the Karakoram region. Thus, this stable or positive condition is denoted as "Karakoram anomaly".

Other than the KK, all the regions (WH, CH, and EH) undergo a negative mass change for the selected hydrological years. The overall monthly and annual time series demonstrates that the maximum mass change occurs in the CH, followed by WH and EH regions. We find a mean annual mass change of –0.62 ± 0.90, –0.80 ± 1.17, and –0.55 ± 0.60 m w.e. yr^{-1} for the WH, CH, and EH region, respectively. The annual mass change starts negative or nearly zero from 2007/08 onwards for WH (Figure 3.2b), 2005/06 onwards for CH and EH regions (Figure 3.2c, d). However, the overall mass change is continuously decreasing for the observational period in these three selected regions.

We find that the magnitude of monthly mass change trends for both the CH and WH are negative and nearly equal to each other. The annual mass change in the WH starts declining from 2012/13 onwards by a factor of 2.5 (from average), while that in CH and EH regions decrease by a factor of 3.6 and 2.1, respectively, from 2015/16 onwards. Maurer et al. (2019) found that the average mass loss rate was doubled across the Himalayas during 2000–2016 (–0.43 ± 0.14 m w.e. yr^{-1}) in comparison to 1975–2000 (–0.22 ± 0.13 m w.e. yr^{-1}). They also found that the mass-loss rate was increased by a factor of 3 in the Lahaul and Spiti region (WH) and 1.4 for west Nepal (CH). Apart from this, the monthly mass variation in the EH region shows that the positive mass months continuously decrease from 2009/10 onwards (Figure 3.2d).

Overall, a large temporal and linear variability in the mass change patterns is observed between different hydrological years. Nevertheless, a notable mass gain is observed in the KK region while strong declining trends are experienced over the other selected regions. Furthermore, a similar declining trend of the specific mass balance is observed (–0.21 ± 0.05 m w.e. yr^{-1}) by Kääb et al. (2012) over the entire Hindu Kush-Karakoram-Himalaya (HKKH) glaciers during 2003–2008.

3.7.1. 2. Spatial mass change

The spatial variation of mass balance estimation is crucial in order to understand the hydrological and atmospheric circulation over the KH region. For spatial analysis, we extract the GRACE-derived mass change grid (Figure 3.3) based on the RGI 6.0 glacier boundary. Then, the contribution of the glacier area in percentage ([glacier area/grid area]*100) is calculated to understand the variation and their contribution to mass change. This pixel-wise glacier contribution may help in providing an insight into the mass balance over the glacierized area at

a regional scale. The overall glacier trend and distribution are analyzed on each pixel based on MK and Sen's slope test. Based on the analyses, we select the four negative/positive clusters over the KH region to provide insights into the variability and duration of mass change for the observation period (2002–2019). Results demonstrate that the eastern part of the KK (Figure 3.3a) and middle portion of the CH region (Figure 3.3d) experience a positive mass change at the rate of +0.44 ± 0.06 and +0.02 ± 0.04 m w.e. yr^{-1}, respectively. However, at the junction of the WH (Figure 3.3b) and CH (Figure 3.3c) regions, an extreme negative mass change at the rate of –0.42 ± 0.04 and –0.89 ± 0.05 m w.e. yr^{-1}, respectively is observed. The monthly mass change trend declined from 2007 and 2006 onwards for the WH and CH cluster, respectively.

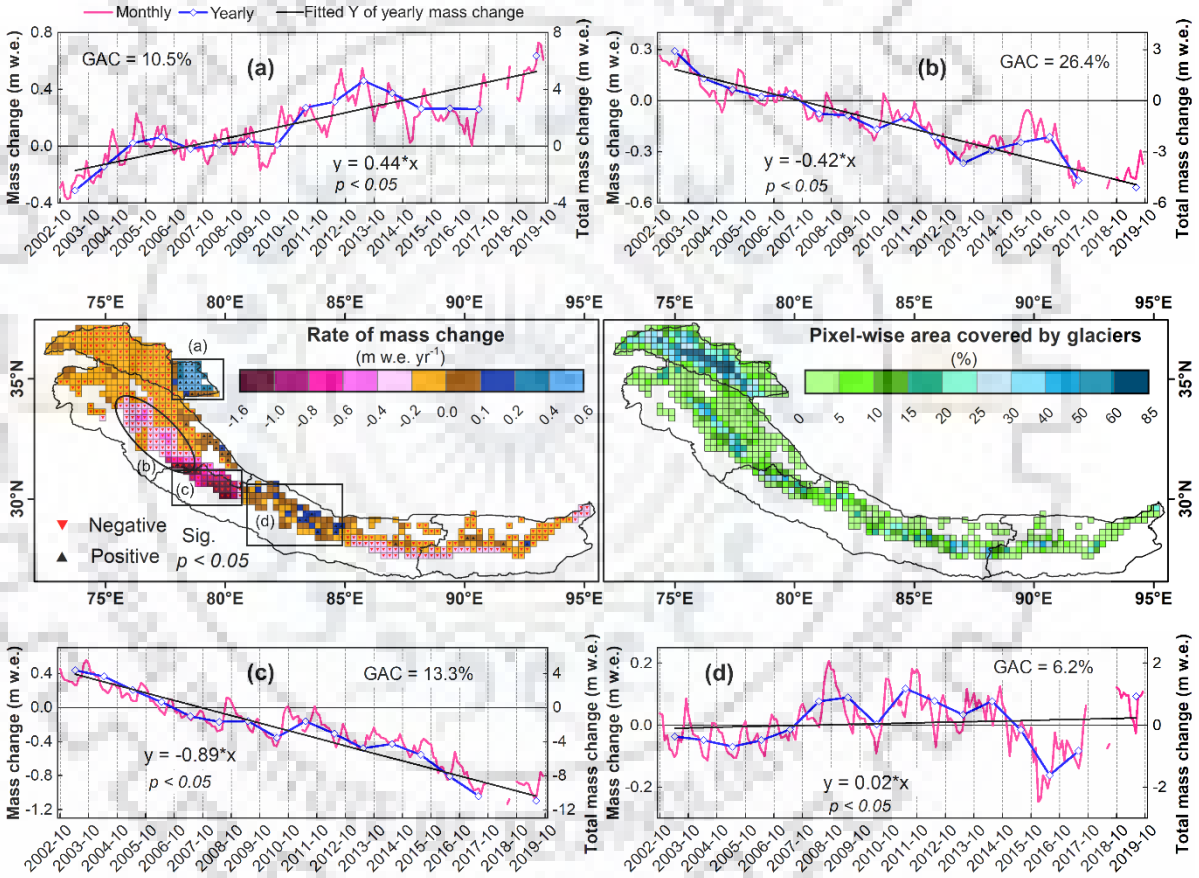

Figure 3.3. Spatial trend of annual mass change with a significant level at 5% for the period 2002−2019 (left) and pixel-wise area covered by glaciers ([glacier area/grid area]*100) (right) over the Karakoram-Himalayan (KH) region. (a-d) represents the monthly and annual mass change of the positive/negative clusters over the KH region.

This decreasing pattern of mass balance coincides with the findings of Pratap et al. (2016). They reported a higher mass loss (–4.40 × 10^6 m^3 m3 w.e.) over the Naradu glacier, Baspa valley of Himachal Pradesh (WH) based on the glaciological method between 2004 and 2010. A field-

based study was also conducted over the Chorabari glacier (CH), indicating an average mass loss of –4.20 m w.e. during 2000–2010 (Dobhal et al. 2013).

For the KK cluster, the yearly mass change increases from 2009 onwards for the observational period, while the contribution of the glacier area in this region is 10.5%. This indicates that the positive mass change can be contributed by other mass driving factors over the region. Muhammad et al. (2019) demonstrated that the glacier mass balance shows negligible mass loss over the western and central Karakoram while receded more mass in the eastern Karakoram. Also, Mukhopadhyay and Khan (2015) revealed that the Shyok basin (covering the eastern part of the Karakoram) shows continuous monthly volumetric contributions through baseflow while the snowmelt and glacier contribution was higher between May and September between 1973 and 2010. They also indicated that the higher contribution in the Shyok river basin was attributed by glacier-melt (50.10%), followed by snowmelt (26.81%) and baseflow (23.09%) on an annual scale. Likewise, Yu et al. (2013) observed the relative contribution of glacier-melt and snowmelt for the annual flow in the upper Indus sub-basins. They revealed that the ice melt was higher than the snowmelt over the Shyok basin. Ashraf and Batool (2019) observed that the number of glaciers and their volume decreased in the Shyok basin during 2001–2013. Negi et al. (2020) also experienced a mass loss over the east Karakoram from 1990 to 2014. Similarly, Gilany and Iqbal (2020) found that the Shyok basin comprises 66 glacier lakes, mainly concentrated over the northeastern part of the basin.

A positive mass change cluster is also observed in the middle of the CH, which indicates that the mass trend decreased for the entire observation period except for the period from 2007/08 to 2013/14. While this region only attains 6.2% of the average glacier-covered area for the selected grid locations. Several authors reported that the glaciers of the Nepal Himalaya show progressively declining mass for different periods (Fujita and Nuimura 2011; Gardelle et al. 2013; Bisset et al. 2020). Similarly, the spatio-temporal pattern of mass change was reported by Yi and Sun (2014) over the central and western Himalayas using GRACE CSR-RL05 data. Also, Khadka et al. (2018) demonstrated that the lakes originated from the glaciers over the Karnali sub-basins, western Nepal, showing a decadal expansion from 1987 to 2017. Therefore, the previous studies over the eastern KK and west Nepal (CH region) indicate that the positive mass change may be attributed to the increase in glacier-lakes rather than the glacier mass gain. This suggests a progressively increase in surface water through glacier-lakes that can contribute to the overall mass change.

3.7.2. COMPARISON OF GRACE-DERIVED MASS CHANGE

3.7.2.1. With published data

We compare the GRACE-derived annual mass change with the field-based glaciological mass balance records available at the WGMS database along with other published mass balance observations over the region (Figure 3.4a, b). Due to the potential sampling biases in these records (Wouters et al. 2019), this comparison may provide only qualitative views into the usefulness of the interannual variability captured by the GRACE analysis. A total of 80 different records of glaciers are selected that lies between 2002 and 2019. For comparison between GRACE and published mass balance (Figure 3.4c), we found that these two observations showed good consistency throughout the KH region with a positive correlation ($r = 0.77$, $p < 0.01$). Mostly, the maximum/minimum of GRACE corresponds to the positive/negative anomalies of published data. It is evident that the slow–melting years of glaciers correspond to the year with positive anomalies of GRACE-derived mass change and vice-versa. Similarly, Jiao et al. (2020) observed a significant correlation between GRACE and WGMS over the Scandinavian Mountain glaciers. The obtained relationship between GRACE mass change and WGMS in the KH region shows that the approach used in this study is relevant for regional mass change estimation over the glacierized region.

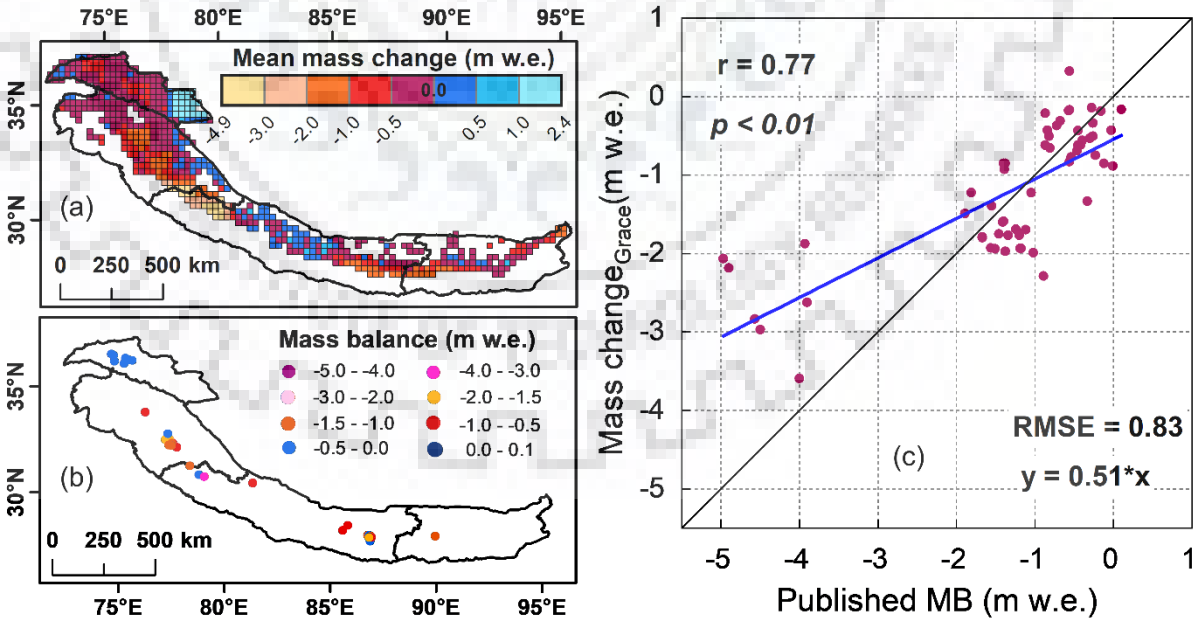

Figure 3.4. Comparison between the GRACE-derived mass change (a) and the published mass balance (b) along with (c) linear regression between these two variables for the period 2002–2019.

3.7.2.2. With remote sensing data

To ensure the accuracy of the GRACE-derived mass change, remote sensing (ICESat-1) data was employed over the KH region to quantify the mass change during 2003–2009. The ICESat captures data in radial orbit, which actively points to a footprint location. To compare GRACE-derived mass change and ICESat-1 footprint location-based mass change, we have averaged the mass of different footprints that come under the GRACE-grid resolution (0.25°) (Figure 3.5). The GRACE observation was previously compared with ICESat data across different parts of the world (Neckel et al. 2014; Jin et al. 2017; Wang et al. 2021). This analysis is carried out over the monthly and annual scale, suggesting that these two datasets are well matched with a correlation of 0.87 and 0.91, respectively, within the acceptable limits (Bezerra et al. 2015). Despite this, Gunter et al. (2008) found that the total mass loss computed by ICESat can be larger or smaller than the GRACE; however, they provide an insight mass balance over a larger area. Our obtained mass change and comparison result suggest that the GRACE obtained mass change over the KH region is reliable to understand the changing pattern of glacier mass over time.

3.7.3. GRACE-DERIVED ANNUAL VOLUME CHANGE

The pixel-wise mean annual volume change was calculated using the GRACE obtained mass distribution over the KH region for the study period (2002–2019) (Figure 3.6). Results demonstrated that the higher spatial variability of glacier volume was observed, ranging from –3.5 to +1.7 Gt yr^{-1} with an average of –0.31 ± 0.64 Gt yr^{-1}. The maximum positive volume is observed in the eastern KK, while negative values are noted between the junction of the WH and CH region. Similar ice mass loss over all the catchments of Uttrakhand (CH region) was demonstrated by Bandyopadhyay et al. (2019). They have revealed that the mass budget was –1.21 ± 0.11 Gt yr^{-1} for the study area during 2000–2014. Dobhal et al. (2013) have also suggested that the mass loss of the Chorabari glacier shows a greater magnitude (–4.4 × 10^6 m^3 w.e. yr^{-1}) than that of the other glaciers of Himalaya. Similarly, different studies are conducted using remote sensing data, suggesting that the glacier volume is declining on the Ganga sub-basins that lie in the uppermost region of the Uttarkhand (Bandyopadhyay et al. 2018; Sattar et al. 2019). Bhambri et al. (2017) have also identified that the volume of the eastern KK glaciers was increasing because of the surge-related impacts on the glaciers.

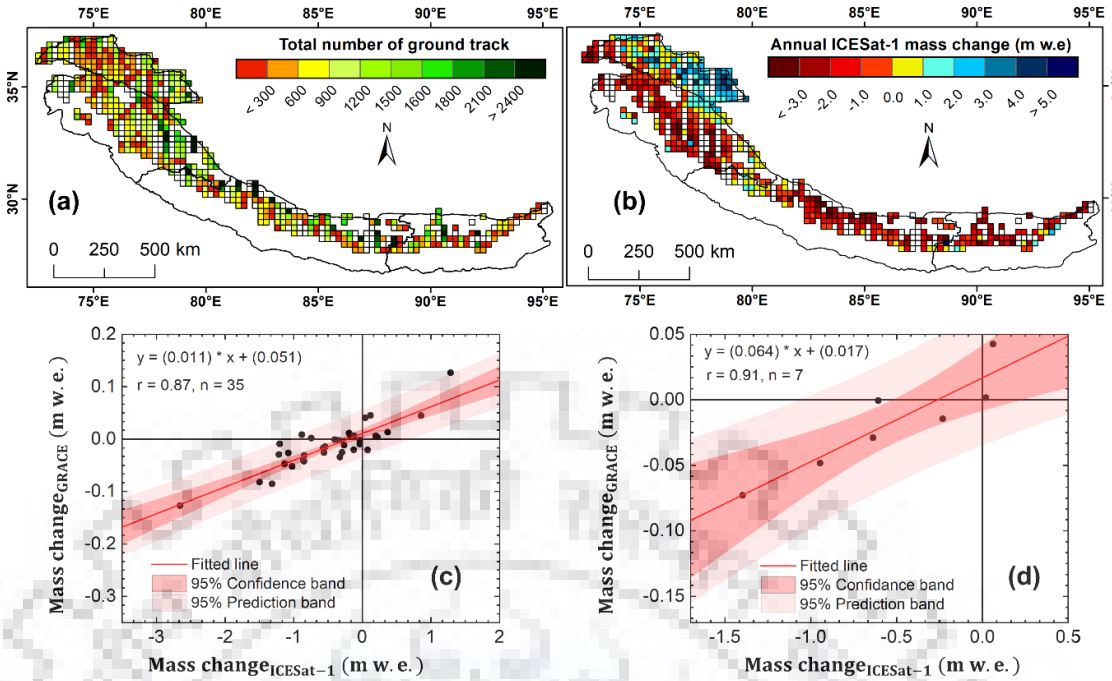

Figure 3.5. Grid-wise (a) total ground track footprint point and (b) Annual mass change as well as Scatter plot between GRACE-derived mass change and ICESat-1-derived mass change (c) Mean monthly from February 2003 to October 2009 and (d) Mean annual from 2003 to 2009 over the KH region.

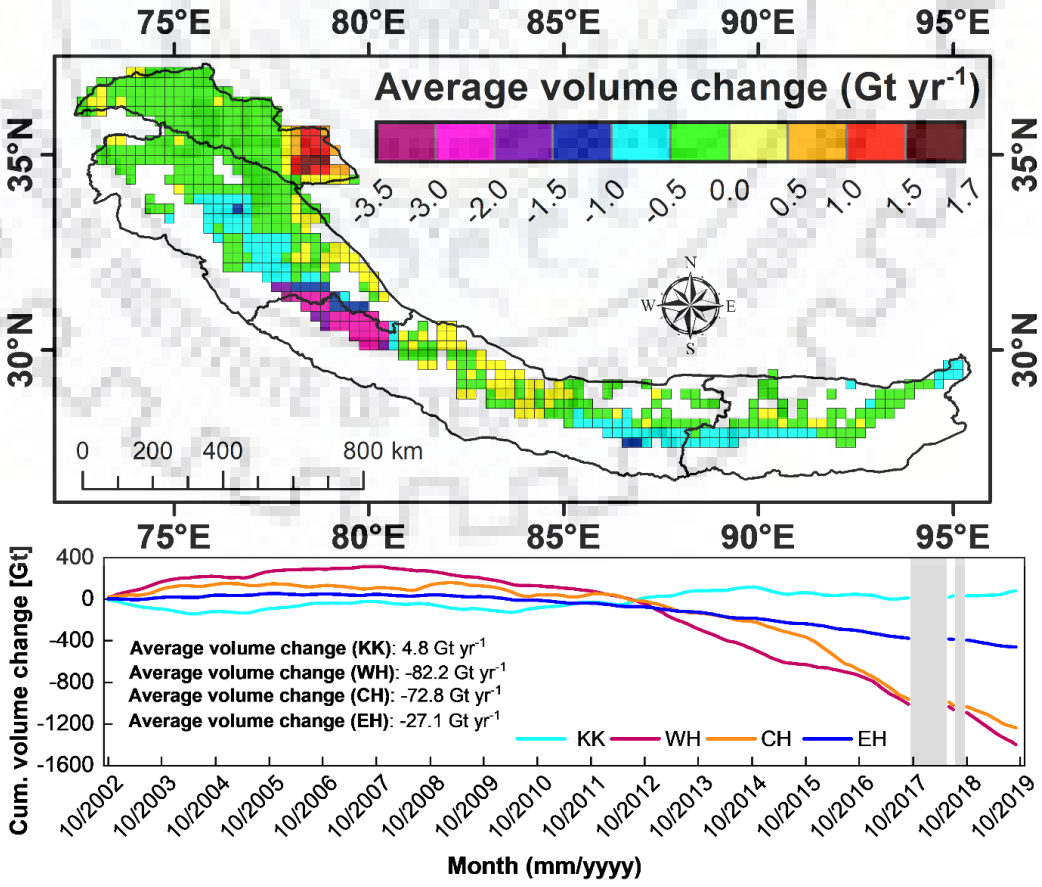

Figure 3.6. Grid-wise average volume change and its cumulative mass change over the KK, WH, CH, and EH regions for the period of 2002–2019.

The cumulative volume change of the KH shows an overall decreasing pattern over the WH, CH, and EH, while it was increasing in the KK region during the observational period. The maximum volume loss rate was attained over the WH (–27.5 ± 5.2 Gt yr^{-1}) followed by CH (–22.9 ± 6.0 Gt yr^{-1}) and then EH (–6.9 ± 0.7 Gt yr^{-1}), whereas it showed a mass gain in the KK (+2.2 ± 4.9 Gt yr^{-1}). Tayal and Sarkar (2019) have highlighted that the number of retreating glaciers and the extent of the retreat were higher in the western Himalayan glaciers than in the eastern Himalayas. However, Abdullah et al. (2020) have revealed that the KK region is experiencing a decreasing mass loss (–1.32 ± 3.8 Gt yr^{-1}) during 2000–2015 based on the geodetic method. This changing pattern of volume over the KK region is primarily attributed due to differences in the study period. Apart from this, they have only considered the glaciers with < 30% voids corresponding to the area. Our study (Figure 3.6) shows that the cumulative volume gain in the KK region starts from 2012 onwards. Farinotti et al. (2020b) have revealed that the volume changes were slightly positive over the KK and the nearby western Kun Lun region.

In our study, the overall volume loss is –55.0 ± 8.7 Gt yr^{-1}in the entire KH region. Similarly, Kääb et al. (2012) have also found a mass loss of –12.8 ± 3.5 Gt yr^{-1} during 2003–2008 over the HKKH glaciers. Gardner et al. (2013) reported that the glacier mass budget was –26 ± 12 Gt yr^{-1} over the HMA based on GRACE and ICESat data. Likewise, Matsuo and Heki (2010) have suggested that the ice mass loss rate for the HMA was –47 ± 12 Gt yr^{-1} during 2003–2009 using GRACE satellite data.

3.7.4. INFLUENCE OF HYDRO-CLIMATIC VARIABLES ON GLACIER MASS CHANGE

The spatial trend of hydro-climatic and radiative fluxes is investigated in order to understand their direct or indirect contribution towards the mass change (Figure 3.7). The teleconnection between these variables with GRACE-derived mass change was established over the KH region from 2002 to 2019. Results demonstrate that the mass change could be attributed to different hydro-climatic variables, and it also varies with location.

In eastern Karakoram, the increasing precipitation trend may directly impact the mass gain, whereas the snowfall and runoff showed a declining trend. Conversely, the air temperature, evaporation, and energy fluxes (SWN and LWN) are progressively increasing over the study area. This indicates that the region may comprise surface water storage in the form of lakes,

canals, dams, seepages, or glacier lakes. Negi et al. (2020) have illustrated that the temperature shows an increasing trend at a rate of 0.090 ºC yr^{-1} from 2000–2015 in eastern Karakoram.

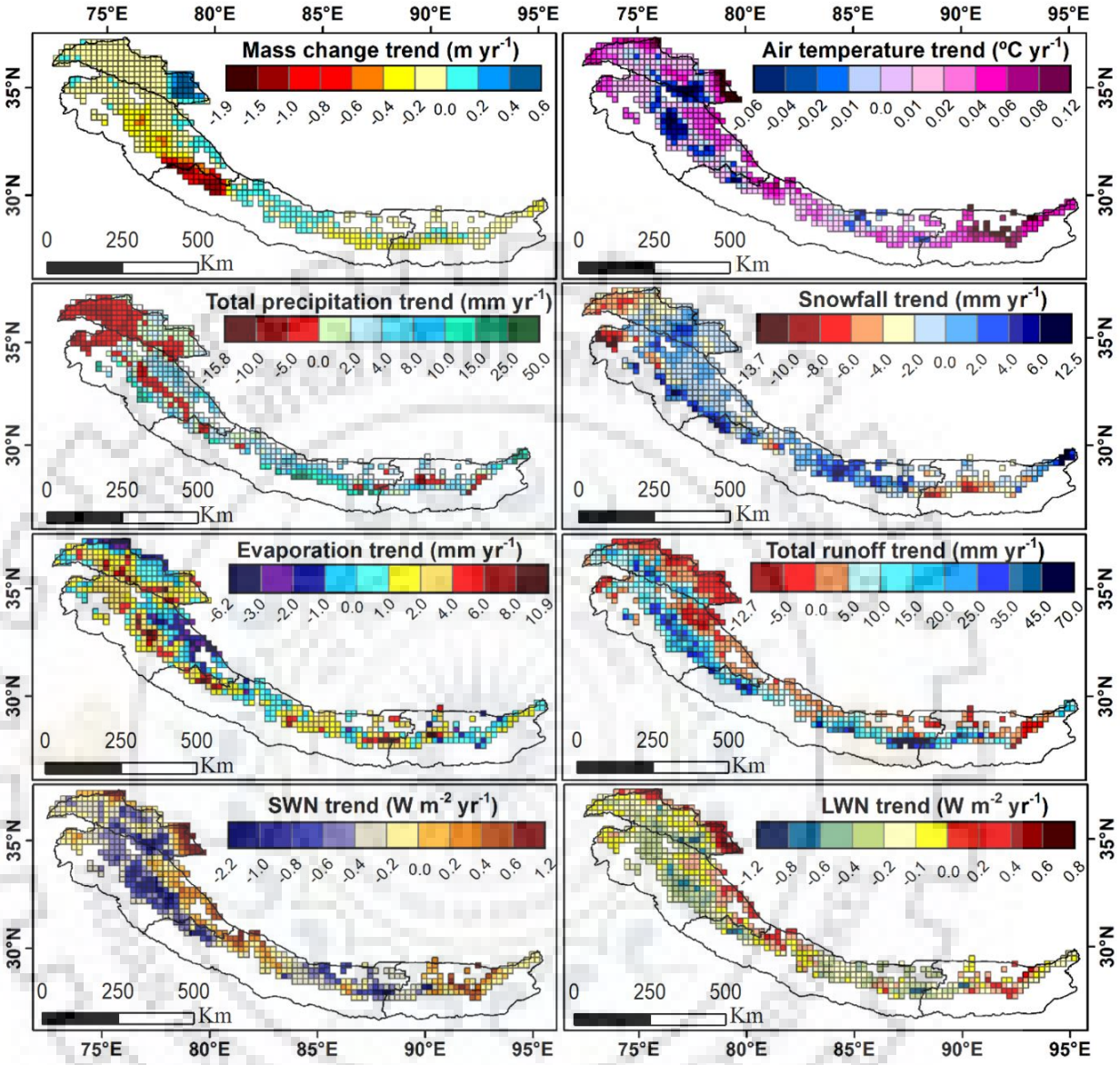

Figure 3.7. Spatial trend of mass change and different hydro-climatic variables along with radiative fluxes over the KH region for the period 2002–2019.

They have also revealed that the snowfall was decreased, while the rainfall shows an increasing trend of –22.01 mm yr^{-1} and 2.29 mm yr^{-1}, respectively, during 2000–2015. De Kok et al. (2018) have highlighted that the changing pattern of glacier accumulation and ablation are linked to increased evaporation. Similarly, Ashraf et al. (2012) revealed that the Shyok basin comprises several significant-end moraine-dammed lakes, which were identified as potential sites for dangerous Glacier Lake Outburst Flood (GLOF).

The negative mass change over the junction of WH and CH is mainly attributed by the increase of SWN that indirectly linked with the surface albedo and topographical variability (Reid and Brock 2010). In this cluster, the temperature, precipitation, evaporation, runoff, and SWN were progressively increasing while the LWN shows a decreasing trend. Also, the high negative mass cluster may be a part of high-intensity rainfall, resulting in increased runoff over the region. Raj (2014) reported that the Uttarkhand Himalayan glaciers experienced a receding trend with upward moving snowline, erratic rainfall, and temperature rise, further exaggerating the intensity and frequency of flash floods over the region. Ming et al. (2015) observed that the mean albedo trend decreased over the Lahaul-Spiti region (WH) for the period 2000–2011. This reduction in albedo can trap a large amount of energy, which further contributes to melting over the region. Mukherjee et al. (2018) also highlighted that the glaciers of the Lahaul-Spiti region were losing mass moderately (-0.07 ± 0.1 m w.e. yr^{-1}) from 1971 to 1999 while significantly increased after 2000 (-0.30 ± 0.1 m w.e. yr^{-1}). Tak and Keshari (2020) revealed that the Pravati Glacier lies in the WH showing a higher rate of mass loss -0.49 ± 0.11 m w.e. yr^{-1} with a total mass loss of 3.95 Gt over the period 1998–2016.

In the positive cluster of the CH region, all the hydro-climatic variables (precipitation, temperature, evaporation, and runoff) and energy fluxes (i.e., SWN) showed an increasing trend while the snowfall along with LWN was decreasing over the region. This varying pattern of different variables suggested that the amount of snowfall decreased, which can affect the surface albedo and easily trapped the radiation for melting. In addition, the increasing precipitation pattern may induce high runoff, and a rise in temperature resulted in high evaporation. Therefore, this mass gain may be attributed by the formation of glacier lakes or other water storage structures over the region. A similar spatial pattern of temperature, precipitation, and temporal discharge was demonstrated by Shrestha and Aryal (2011). Also, Kääb et al. (2012) illustrated that the west Nepal glaciers showed a negative mass trend for 2003–2009. National Research Council (2012) suggested that the rise in temperature and precipitation can increase evapotranspiration and greater snowmelt or icemelt over Nepal, leading to an increase in streamflow.

The temporal variability of hydro-climatic and energy fluxes were quantified with respect to mass change over the four selected positive/negative clusters (shown in Figure 3.3) in the KH region for the period 2002–2019 (Figure 3.8). Results demonstrated that the mass change has positively increased from 2004/05 onwards for the eastern KK region (Figure 3.8a). Over a similar period, total precipitation and snowfall were positively correlated with each other with a heterogeneous yearly pattern. Apart from this, the mass change was significantly increasing from 2010/11

onwards over the region, despite the total precipitation and snowfall were showing negative variation since 2010/11 except for 2014/15 and 2016/17. A similar pattern of total precipitation and snowfall was observed by Bilal et al. (2019) for the same period.

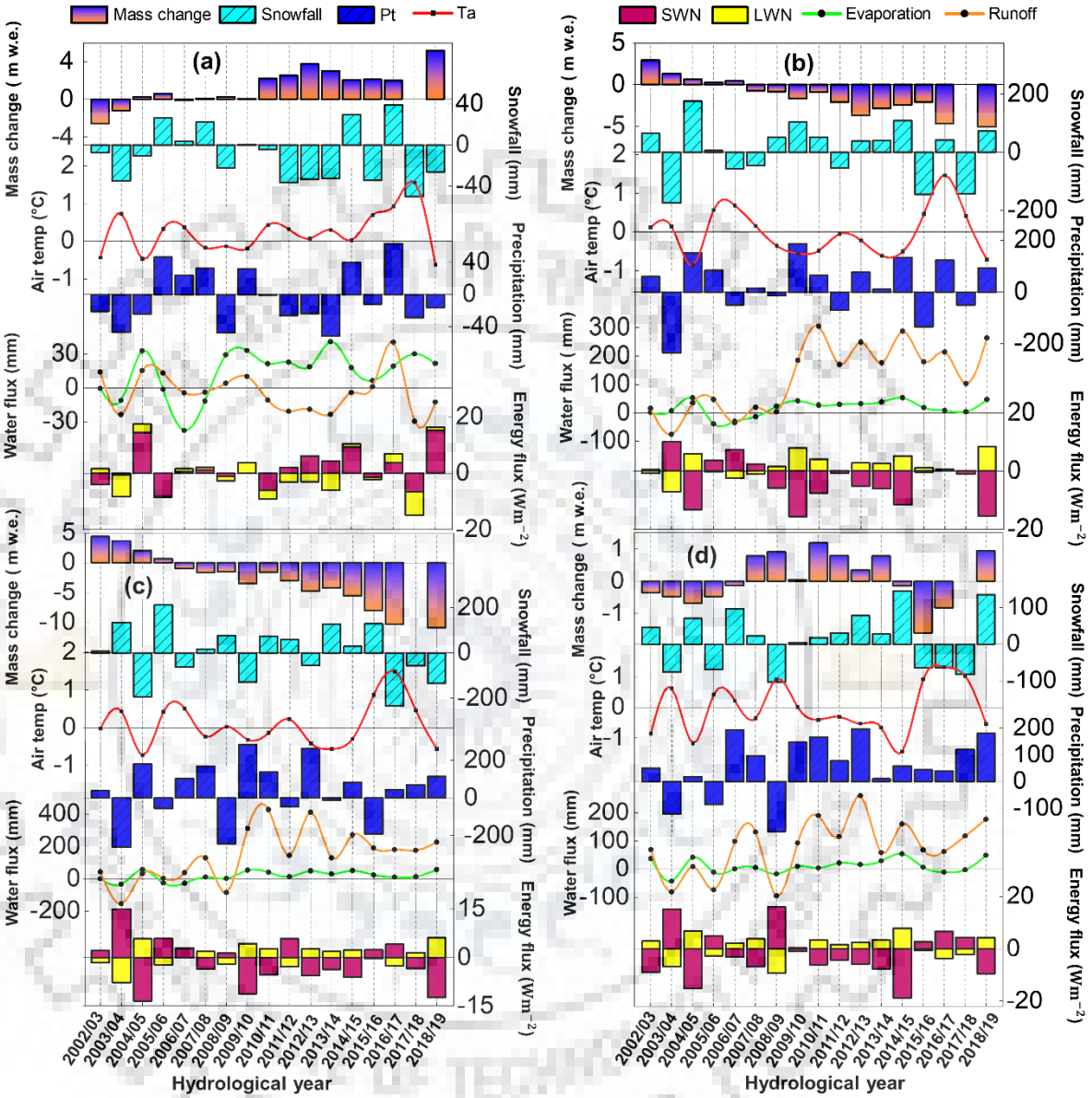

Figure 3.8. Temporal trend of mass change and different hydroclimatic variables along with radiative fluxes over the positive/negative cluster of the KH (a-d same cluster was considered of Figure 3.3) for the period 2002–2019.

The water flux components, i.e., evaporation and total runoff of this region, show a contradictory pattern; however, evaporation started increasing from 2007/08 with an interannual variation, while runoff was maximum in 2016/17. This analysis indicates that the total precipitation is sufficiently higher, which can be attributed to the increase in the amount of runoff. Yin et al. (2018) have illustrated a similar relation between precipitation and runoff. In contrast, the mass

change was positive over the region, which can be an effect of increasing potential ice-dammed glacier lakes from 2000 onwards (Bhambri et al. 2019).

On the other hand, the negative cluster over the CH and WH shows a decreasing mass from 2006/07 onwards for the selected region (Figure 3.8 b, c), while it obtains the maximum mass loss for the year 2018/19. For the same period, the snowfall also shows a decreasing pattern, while the total precipitation was positive for both regions. Guhathakurta and Rajeevan (2008) demonstrated that the rainfall showed a moderate increasing trend in 27 (out of 36) sub-divisions of India between 1901 and 2003. Krishnan et al. (2020) also illustrated that the rainfall was increased over India between 2018 and 2019. The decrease in snowfall may be trapped by the large amount of energy, which further induces the surface melting; therefore, the SWN was increasing for the period. Lin et al. (2020) have observed a similar decreasing albedo pattern. Additionally, this region was also controlled by the runoff, while the evaporation followed a similar pattern in both regions. Results suggested that the total runoff started increasing from 2008/09 onwards and peaked in 2010/11. SANDRP (2013) noticed an unprecedented disaster during September 2010 at downstream of the Tehri dam.

In the positive cluster of the CH region, the mass change was positive from 2007/08 to 2013/14 and attained a maximum in 2012/13, indicating that the positive mass was mainly concentrated during this period. A similar increase in precipitation was demonstrated by Karki et al. (2017) over western Nepal. They found that this period experienced an occurrence of extreme events over the Uttarakhand and bordered area of west Nepal. Even in continuation with this event, a major extreme precipitation event was identified during 14-16 August 2014 over western Nepal (Das et al. 2015). In the selected observation period, the precipitation and snowfall are positive for the whole period except for 2003/04, 2005/06, and 2008/09. The annual distribution of runoff is heterogeneous over the middle part of the CH region, while it is highest during 2012/13. The maximum runoff and precipitation over the same period suggested that the precipitation intensity was higher, which can further be contributed towards runoff rather than water storage. Several studies were conducted over western Nepal revealed that the rainfall intensity during the period was high (Karki et al. 2017; Krishnan et al. 2020; Stanley et al. 2020).

Overall, it is observed that the mass change was highly correlated with the total precipitation and snowfall variability over the spatiotemporal scale. In contrast, this correlation fails at the location where evaporation, runoff, and radiation were causing mass loss by trapping the energy over the surface. Also, the presence of artificial water structures, glacier lakes, canals, and seepage may contribute to the mass change, as a part of GRACE-based analysis that cannot eliminate the

surface water from the groundwater storage. Therefore, we can conclude that these variables, directly and indirectly, influence the mass change and further cause a change in water availability to the river system.

3.7.5. UNCERTAINTY ASSESSMENT

For uncertainty analysis, we calculate the mean and their standard deviation as well as linear trend and their standard error of GRACE-derived mass change, GRACE TWSA, GLDAS-derived TWSA, and GLDAS variables (i.e., SMSA, SWEA, CWSA) over the glaciers of the KH, summarized in Table 3.1.

Table 3.1. Statistical summary of the used variables for mass change analysis over the sub-regions of KH during 2002–2019.

Regions	Mean ± Std. (m w.e.)	Linear trend ± SE (m w.e. yr^{-1})
GRACE-derived mass change		
KK	0.04 ± 0.46	0.02 ± 0.05
WH	–0.53 ± 0.90	–0.16 ± 0.03
CH	–0.70 ± 1.17	–0.20 ± 0.06
EH	–0.50 ± 0.60	–0.12 ± 0.01
GRACE TWSA		
KK	0.17 ± 0.55	0.05 ± 0.05
WH	–0.62 ± 0.89	–0.16 ± 0.04
CH	–0.97 ± 1.33	–0.24 ± 0.06
EH	–0.69 ± 0.77	–0.15 ± 0.02
GLDAS TWSA		
KK	0.10 ± 0.32	0.03 ± 0.03
WH	–0.11 ± 0.30	–0.02 ± 0.03
CH	–0.28 ± 0.37	–0.07 ± 0.02
EH	–0.20 ± 0.24	–0.04 ± 0.01
GLDAS SWEA		
KK	–0.01 ± 0.24	0.00 ± 0.03
WH	–0.02 ± 0.17	–0.003 ± 0.02
CH	–0.17 ± 0.38	–0.03 ± 0.04
EH	–0.20 ± 0.55	–0.05 ± 0.05
GLDAS SMSA		
KK	0.11 ± 0.18	0.03 ± 0.01
WH	–0.09 ± 0.18	–0.02 ± 0.02
CH	–0.30 ± 0.37	–0.07 ± 0.01
EH	–0.19 ± 0.23	–0.04 ± 0.01
GLDAS CWSA		
KK	0.00 ± 0.00	0.00 ± 0.00
WH	0.00 ± 0.00	0.00 ± 0.00
CH	0.00 ± 0.00	0.00 ± 0.00
EH	0.00 ± 0.00	0.00 ± 0.00

Standard deviation is measured in the error of simple annual average mass change, while the standard error is associated with the fitted slope of simple linear regression at 95% confidence interval over the observational period. The average annual mass trend is–0.12 ± 0.04 m w.e. yr^{-1} over the KH region.

Results demonstrate that the maximum standard deviation associated with mean and standard error in the linear trend is observed in the CH region. This means the probability of error is higher in the CH, and future prediction of mass change is less reliable because of higher standard error over the region (Shamsudduha et al. 2012). The net change (increasing/decreasing) in the linear trend of annual mass is directly linked with SMSA, followed by SWEA, while no significant contribution of CWSA is observed in the entire KH glaciers region. It is concluded that the changing SMSA would not only influence the mass change; it is indirectly impacting the atmospheric and water flux components over the region, which further contributes to higher melting.

On the other hand, the SWEA attains a less negative trend over the KK while it shows a higher negative trend over the EH region. This may occur because of higher variability (declining rate) in solid precipitation over the region, while the overall mass change was less negative as compared to the CH and WH. It indicates that the EH region may be attributed to an increase in rainfall and by the formation of new glacier lakes along with its expansion over time, which balances the overall mass change. A similar pattern of these variables was observed by several authors (Bharti et al., 2016; King et al., 2019; Shukla et al., 2018; Wester et al., 2019).

3.7.6. SENSITIVITY ANALYSIS

To understand the sensitivity of the essential input climatic variables, i.e., temperature, snowfall, and precipitation on the glacier mass change, we quantify the primary drivers through the sensitivity test for the period 2002–2019. For this, the monthly precipitation and snowfall are changed by ±1.0 cm, while ±1ºC alters the temperature. When the precipitation and snowfall of the KH region were increased by 1.0 cm, then the value of mass balance was changed by 12.7% and 16.2%, respectively, from the reference mass balance. Similarly, the mass change is decreased by 23.5% when the temperature increases by +1ºC. The sensitivity analysis revealed that the snowfall and temperature have a strong influence on mass change response. The reason for the sensitivity is that the snowfall not only contributes to mass accumulation but it also has a strong effect on the overall SWN radiation through its control by surface albedo (Kumar et al., 2019). It is also noted that temperature plays a dominant role in controlling the glacier melt

(Azam et al. 2014b). It is more sensitive in the net longwave budget and sensible heat that indirectly correlated with the overall glacier mass loss (Ohmura 2001).

3.8. DISCUSSION

We use the GRACE solution to quantify the regional mass variation across all the glaciers in the KH region. Here, we aim to highlight the glacier contribution at the GRACE spatial scale, which will help to understand the association between mass change and the area covered by glaciers. Because the mass change over a large geographical extent may be dominated by other hydrological processes than glacier change. Wouters et al. (2019) highlighted that the GRACE signal with smaller glacier coverage will be dominated by non-ice hydrological components. They also revealed that the limit of 100 km^2 for GRACE signal considered based on the trade-off between completeness and an acceptable range of uncertainty of the estimates.

Numerous studies previously detected the mass change through GRACE signal over the High Mountain Asia region (Brun et al. 2017; Shean et al. 2020) and its sub-regions (De Kok et al. 2020). Our result on the glaciers of the KH region shows an overall positive trend in KK and strong declining trends in the other regions (WH, CH, and EH). Consistent with this study, Bonekamp et al. (2019) revealed that the Shimshal valley in the Karakoram shows a positive mass balance (+0.31 ± 0.06 m w.e. yr^{-1}) from 2011 to 2013. A similar positive mass gain was observed in the central Karakoram (+0.10 ± 0.16 m w.e. yr^{-1}) and western Pamir (+0.14 ± 0.13 m w.e. yr^{-1}) by a geodetic mass balance between 1999 and 2011 (Gardelle et al. 2013). A recent geodetic-based study revealed that the glaciers of the Shyok basin, East Karakoram experience mass loss with a rate of –0.10 ± 0.07 m w.e. yr^{-1} between 2000 and 2014 (Negi et al. 2020). Many studies reported similar results of both positive and negative mass balance over the sub-regions of Karakoram (Cogley 2011; Bolch et al. 2012; Kääb et al. 2015; Guo et al. 2016; Azam et al. 2018; Kumar et al. 2019a). Also, a recent geodetic-based study revealed that the glaciers of the Shyok basin, East Karakoram experiencing mass loss with a rate of –0.10 ± 0.07 m w.e. yr^{-1} between 2000 and 2014 (Negi et al. 2020).

The glaciers of the KK region are known to host numerous surge-type glaciers that characterize the alternation between short active phases involving rapid mass transfer from high to low elevations and longer quiescent phases of low mass fluxes (Barrand and Murray 2006; Hewitt 2007; Gardelle et al. 2012). It was also reported by Copland et al. (2011) that the surging type glaciers of the KK region doubled in number after 1990 (a total of 90 glaciers). In addition, this stability of the KK glacier may be due to heavy debris cover on the ablation zone because of

steep rock walls that surround them and intense avalanche activity (Bolch et al. 2012). The mean debris cover in the KK was about 10% of the total glacier area (Bolch et al. 2012), whereas it constitutes nearly 36% for the Central Himalaya (Scherler et al. 2011).

Other than this region, a notable negative mass balance was observed in the WH, CH, and EH region glaciers for the study period. Our findings were consistent with several studies (Brun et al. 2017; Shean et al. 2020). Similarly, Gaddam, Kulkarni, and Gupta (2016) demonstrated that the glaciers of the Baspa basin, western Himalaya experienced a negative mass balance during 1998–2014, while a few years of positive mass balance were observed for the Gara and Gor Garang glaciers before 2004. Also, Bonekamp et al. (2019) observed a similar negative mass balance in the Langtang catchment, central Himalaya, between 2011 and 2013. Similarly, Guo et al. (2016) have found a decreasing mass change (–20 mm yr^{-1}) over the middle Himalaya for the period 2003–2012. Yi et al. (2019) also revealed that the glaciers and snow region of the Brahmaputra basin (EH region) shows a negative mass balance from 2006 onwards.

In this study, the glacier mass variation was estimated and also have the potential to quantify the contribution of hydro-climatic variables on mass change. The former variables involved with mass change are total precipitation, snowfall, air temperature, SWN, and LWN, whereas the latter variables are evaporation and total runoff. A recent study suggested that the KH glaciers are sensitive to climatic variables and have dominant control on the mass balance (Kumar et al. 2019b). They also indicated that the snowfall was most sensitive to the mass balance rather than the local temperature. In contrast, several studies revealed that precipitation and temperature change cause a direct or indirect impact on glacier mass balance (Kumar et al., 2019; Mandal et al., 2020; Pratap et al., 2019; Tawde et al., 2017; Wang et al., 2019). Apart from this, several local scales to the global mass balance estimation methods suggest that the Himalayan glaciers are sensitive to climate change (temperature and precipitation) (Sakai et al. 2015; Azam et al. 2018).

By combining the published literature, our results present a comprehensive picture of glacier mass change at regional and sub-regional scales. These records of mass balance also indicate that the glaciers of the KK region experience a stable or positive trend, and other regions (WH, CH, and EH) find a negative trend of mass change at a temporal scale with a heterogeneous spatial pattern of mass change. Detailed future research will be needed on the KH region, which focuses on the effect of the non-hydrological component on mass change. This information could be helpful to quantify the contribution of different hydrological and non-hydrological components on water availability and sea-level rise.

3.9. CONCLUSIONS

In the Karakoram and Himalaya (KH) region, the availability of *in-situ* observation data is scarce, and their large spatial extent limits the field measured mass balance. We demonstrate that the use of GRACE-based mass change provides an unprecedented opportunity to quantify the mass variation at a regional scale. Our analysis reveals that the KH glaciers experience a continuous mass loss at an alarming rate. The rate of glacier mass change is maximum in the CH while it is stable or increasing over the KK region. Also, several locations are identified as hotspots of mass loss in the KH region. Results reveal that a positive or near zero mass balance is observed in the KK region, while a sharp declining trend of mass losses occurred in the WH, CH, and EH for 2002–2019.

A year-to-year variability of the mass change is observed and shows negative or nearly zero from 2007/08 onwards for WH, 2005/06 onwards for CH and EH regions. The spatial distribution of mass change revealed four positive/negative clusters of mass change over the KH region, suggesting that the eastern part of the KK and middle portion of the CH region were experienced a positive mass change while the junction of the WH and CH observed an extreme negative mass change. Moreover, the comparison between GRACE-derived mass balance with the published mass balance indicates a higher correlation (r = 0.77). On the other hand, the performance of the GRACE-derived mass change was compared with the ICESat-1-derived mass change over the region during 2003–2009, illustrating a correlation of 0.87 for monthly and 0.91 for annual scale. The pixel-wise average volume change was identified using the GRACE obtained mass distribution showed a higher spatial variability of glacier volume during 2002–2019, ranging from –3.5 to +1.7 Gt yr^{-1} with a mean of –0.31 ± 0.64 Gt yr^{-1} over the KH region.

Our study reveals that the variability in regional mass balance is predominantly driven by the hydro-climatic variables, i.e., air temperature, total precipitation, snowfall, evaporation, total runoff, as well as by the local radiative forcing. Results demonstrate that the mass change is highly correlated with total precipitation and snowfall over the spatiotemporal scale, while this correlation fails at the location where evaporation, runoff, and radiation were prominently influenced the mass loss. Uncertainties related to GRACE observation are assessed over the monthly and annual scale over the KH region. The average annual mass trend is –0.12 ± 0.04 m w.e. yr^{-1} over the entire KH region with the maximum standard error and deviation are observed in the CH region. A sensitivity test reveals that snowfall and temperature have a strong influence on the response of mass change. From a future perspective, our study on the regional scale mass change estimation will be useful for the socio-economic aspect, as it provides a better

understanding of future water supply in the downstream as well as the upstream region. Also, the utility of remote sensing-based GRACE data would overcome the data scarcity in the Himalayan region and understand the net impact of global warming on the glacier mass balance on the spatial and temporal scale. Lastly, this spatial mass change will help in the identification of the hotspot/coldspot region and future projection of the mass balance data. This study bridges the gap between the detailed local scale mass balance investigations to regional-scale change.

CHAPTER 4

DEVELOPING AN GLACIER MASS BALANCE MODEL USING SATELLITE AND INSITU MEASUREMENT BY INCORPORATING THE ENERGY BALANCE COMPONENTS

4.1. INTRODUCTION

Retreating glaciers all around the world is a concern for freshwater sustainability and management. These glaciers are an important regulator of seasonal water availability in many regions (Hock et al. 2019a). More importantly, the Himalayan glaciers are the source of numerous rivers that accommodate the water needs of millions of population in Asia (Immerzeel et al. 2013). In the Himalayan region, a majority of glaciers have been shrinking at an accelerated rate (Bolch et al. 2012; Sharma et al. 2016; Brun et al. 2017; Soheb et al. 2020; Mandal et al. 2020). In contrast, both advancement and shrinking of the glacier may cause several geohazards (Richardson and Reynolds 2000; Allen et al. 2016; Patel et al. 2017b; Kääb et al. 2018; Sattar et al. 2020) as well as transformation in the existing landscape (Haeberli et al. 2017).

Estimating the Himalayan glacier response towards future climatic change and their impacts on the regional population requires a reliable physical-based model for glacier mass balance. Numerous mass balance models have been developed by considering different assumptions and approaches (Braithwaite, 1995; Milner et al., 2017; Todd et al., 2019). The simplest mass balance model is established by regression analysis of mean summer temperature and snowfall (Greuell, 1992; Wallinga and Van de Wal, 1998). However, several authors have developed a model that can either use temperature index or empirical relation, ranging from zero-dimension to two-dimensional analysis (Klok and Oerlemans 2002; Hock 2003; Huss and Hock 2015; Tawde et al. 2017; Pratap et al. 2019). The temperature index model only covers the temperature and precipitation gradient, while the empirical model uses a statistical equation that was modeled for a specific location.

Over the past decades, only a few studies have been carried out for estimating the glacier mass balance using a two-dimensional model by incorporating the surface energy balance (SEB) components (Klok and Oerlemans 2002; Hock and Holmgren 2005; Paul and Kotlarski 2010; Huintjes et al. 2015). The energy balance models were found more efficient for glacier mass balance simulation all around the world, but it required detailed observational data for calibration and validation (Oerlemans et al. 1998; Hock 1999; Kayastha et al. 1999; Zhang et al. 2013).

Several authors have studied point-scale SEB based on meteorological variables (Automatic Weather Station (AWS) data) for the Himalayan glaciers (Wagnon et al. 2013; Azam et al. 2014b; Soheb et al. 2018, 2020; Mandal et al. 2020). However, the distributed SEB model over the Indian Himalayas is not yet available due to the extreme challenges for accessibility; only a limited number of locations are covered with in-situ observation for continuous monitoring of energy balance components.

Therefore, remote sensing data have a significant advantage for assessing the glacier mass balance over the larger basin. The remote sensing technique has been extensively used for geodetic and temperature index-based mass balance estimation (Moholdt et al. 2010; Tawde et al. 2017; Wastlhuber et al. 2017; Pratap et al. 2019). Apart, some recent studies have been made to estimate the regional mass balance using remote sensing data in different glaciers of the world (Jacob et al. 2012; Kumar et al. 2019b; Wouters et al. 2019; Sutterley et al. 2020).

4.2. RESEARCH QUESTIONS

- **What is the role of the radiation flux component in the glacier mass balance estimation?** Is the use of temperature index and enhanced temperature index model sufficient to model all possible physical conditions of glaciers? What is the feasibility of the physical-based model to the heterogeneous glacier with or without calibration/validation?
- **How can we improve the continuous monitoring and understanding of glaciers on a basinal scale in the Himalayas?** What is the spatial and temporal variation in mass balance over similar climatic condition glaciers? Are they related to climatic variability or with a topographic variation?
- **What circumstance is a Himalayan glacier able to sustain the glacier mass?** What factors influence the underlying mechanism? How do the ablation components dominate the basinal scale glacier mass loss?
- **What role do the topography and climatic condition of a region play**? Is the topographic and climatic information important in support of the glacier mass balance? Any change in topographic and climatic variables causes a significant change in mass balance?

4.3. OBJECTIVES

- Development of physical-based energy balance model at basinal scale, by parameterizing the energy fluxes and input climatic variables

- Quantify the main energy flux drivers and rate of ablation that influences the mass balance of the Himalayan glaciers
- Modeling the spatial distribution of air temperature and energy flux components over the mountain glaciers

4.4. STUDY AREA

The Chandra river basin (a major tributary of the Chenab river, part of the Indus River system) is located in the Lahaul and Spiti region of Himachal Pradesh (India) and covers an area of 2.44 $\times 10^3$ km^2 (Figure 4.1).

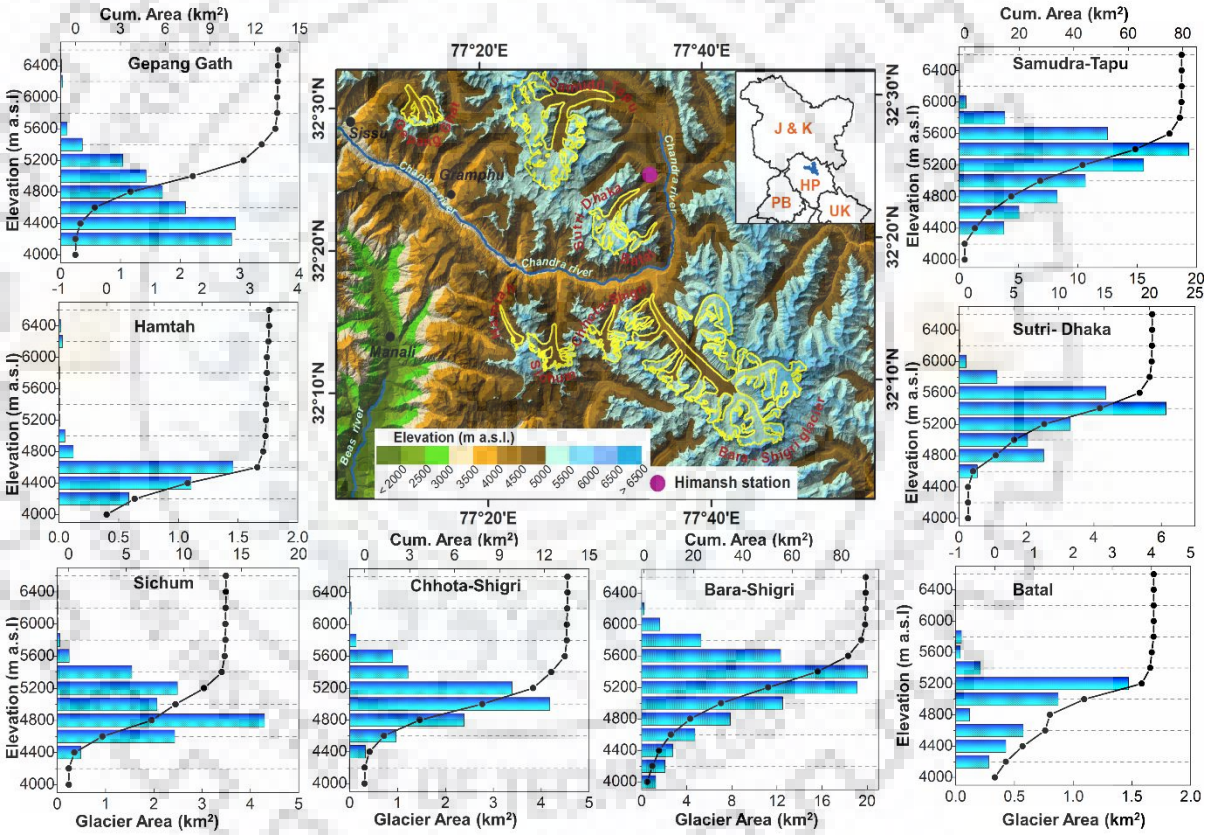

Figure 4.1. Location map of the selected glaciers in Chandra river basin, Lahaul-Spiti in Himachal Pradesh (India). The location of the Himansh meteorological station, orographic barrier (From SRTM DEM with hillshade effect), glacier outline (RGI Consortium 2017), as well as the hypsometry curve of each glacier.

This basin is widely covered with glaciers as there are 205 glaciers in the Chandra basin, covering an area of 703.6 km^2, which constitutes 29.5% of the total basin area (Sangewar and Shukla 2009). Therefore, we have classified this region into three categories based on their glacier area,

i.e., small glaciers (with an area < 5.0 km^2), large glaciers (between 5 and 50 km^2), and huge glaciers (with an area > 50.0 km^2) that account for 31.5%, 43.4%, and 25.0% of the total glacier area, respectively.

Based on this classification, we have selected eight different glaciers in the Chandra basin, i.e., Bara Shigri (131.0 km^2), Samudra Tapu (80.0 km^2), Sutri Dhaka (20.4 km^2), Chhota Shigri (16.8 km^2), Sichum (13.7 km^2), Gepang Gath (12.6 km^2), Batal (4.1 km^2), and Hamtah (3.4 km^2) for understanding the effectiveness of the proposed model. The glacier area was extracted from the Randolph Glacier Inventory (RGI) version 6 glacier boundary (RGI Consortium 2017). Among the selected glaciers, the Hamtah glacier has a minimum area, whereas the Bara Shigri glacier has a maximum size. The glaciers of this region received some amount of solid precipitation in summer (June–September) due to the Indian Summer Monsoon (ISM), while a significant amount of precipitation occurred in winter (November-March) due to the mid-latitude western disturbances (Dimri et al. 2016).

4.5. DATA DESCRIPTION

4.5.1. SATELLITE DATA

The Landsat-8 Operational Land Imager (OLI) images were acquired (Path-147 and Row-38) from the United States Geological Survey (USGS) Earth Explorer, which is available at a 30-m grid and 16-day temporal resolution. The optical bands of Landsat-8 were used for surface albedo (α) (Brock et al. 2000; Gurgiser et al. 2013; Pritchard et al. 2020), while a thermal infrared band was utilized for Land Surface Temperature (T_s) estimation based on the emissivity approach (Li et al. 2004; Mohamed et al. 2017; Sekertekin and Bonafoni 2020). However, cloud coverage produces a major difficulty while acquiring satellite data for monthly analysis. Therefore, we have selected 49 cloud-free imageries between October 2013 and September 2019, representing six hydrological years over the study area (Table 4.1).

4.5.2. METEOROLOGICAL DATA

The relative humidity (RH) and wind speed (u) were retrieved from the Meteorological and Oceanographic Satellite Data Archival Centre (MOSDAC), a data repository of the Indian Space Research Organization (ISRO), which comprises the Indian Meteorological Department (IMD) as well as ISRO AWS data for a particular year. For this, we have selected four meteorological stations located at Manali, Kullu, Keylong, and Kaza, around 20-50 km (aerial distance) from the Chandra basin glaciers.

Table 4.1. Details of the satellite data used for mass balance estimation from October 2013 to September 2019.

Hydrological Year	Date of image acquisition (DD/MM/YYYY)
2013-2014	25/09/2013; 27/10/2013; 28/11/2013; 15/01/2014; 16/02/2014; 20/03/2014; 21/04/2014; 08/06/2014; 10/07/2014; 28/09/2014
2014-2015	30/10/2014; 15/11/2014; 01/12/2014; 18/01/2015; 23/03/2015; 24/04/2015; 27/06/2015; 30/08/2015; 15/09/2015
2015-2016	01/10/2015; 02/11/2015; 04/12/2015; 05/01/2015; 22/02/2016; 26/04/2016; 12/05/2016; 13/06/2016; 25/09/2016
2016-2017	03/10/2016; 19/10/2016; 06/12/2016; 23/01/2017; 24/02/2017; 12/03/2017; 13/04/2017; 15/05/2017; 20/09/2017
2017-2018	06/10/2017; 22/10/2017; 07/11/2017; 09/12/2017; 26/01/2018; 31/03/2018; 02/05/2018; 03/06/2018; 22/08/2018
2018-2019	25/10/2018; 26/11/2018; 28/12/2018; 29/01/2019; 18/03/2019; 03/04/2019; 21/05/2019; 22/06/2019; 26/09/2019

Further, AWS measured data were collected from Himansh station (4052 m a.s.l.) maintained by National Centre for Polar and Ocean Research (NCPOR), lies at ~3.5 km (aerial distance) from the snout (4500 m a.s.l.) of the Sutri Dhaka Glacier (Pratap et al. 2019). In this study, we have used half-hourly climatic and meteorological variables, i.e., air temperature (T_a), RH, *u*, incoming shortwave radiation (SWI), outgoing shortwave radiation (SWO), incoming longwave radiation (LWI), and outgoing longwave radiation (LWO) for calibration/validation of the proposed model over two separate hydrological periods, i.e., October 2015 – October 2016 and October 2016 – October 2017.

4.5.3. DIGITAL ELEVATION MODEL DATA

Advanced Spaceborne Thermal Emission and Reflection Radiometer (ASTER) Global Digital Elevation Model Version 3 (GDEM 003) with a 30-m spatial resolution was obtained from National Aeronautics and Space Administration (NASA) Land Processes Distributed Active Archive Center (LP DAAC, https://lpdaac.usgs.gov/products/astgtmv003/) for topographic analysis. The accuracies of the ASTER GDEM are 20 meters for vertical and 30 meters for horizontal at 95% confidence (NASA 2009). Das et al. (2016) have also reported that the ASTER GDEM was found to be more accurate and consistent in terms of absolute accuracy than other existing DEMs over the Supin – Upper Tons Basin, Indian Himalayas.

4.5.4. ERA-5 REANALYSIS DATA

ERA5-Land is a global reanalysis dataset currently covering a period from 1981 to the present, available at 0.1º grid resolution with a monthly temporal scale (https://cds.climate.copernicus.eu/cdsapp#!/dataset/reanalysis-era5-land?tab=overview). For this study, the total precipitation (P_t) and snowfall were used for understanding the impact of snow accumulation/ablation on glacier mass balance over the region from 2013 to 2019.

4.6. METHODOLOGY

4.6.1. SPATIAL ENERGY BALANCE MODELING

The estimation of SEB at the spatio-temporal scale was carried out on the Chandra basin glaciers. The SEB includes the calculation of total energy fluxes available for melt. It is positive when directed towards the surface and negative when away from the surface, assuming a lack of horizontal energy flux transfer and cloud coverage for a unit of time. The surface energy balance of glacier can be expressed by the following Equation 4.1 (Oke 1987; Sicart et al. 2011):

$$F_M = R_N + H_S + H_l + H_G + P \qquad \textbf{Eq. 4.1}$$

Where F_M is the net heat flux available at the glacier surface, R_N is the surface net radiation (incoming – outgoing), H_S and H_l are the sensible and latent turbulent heat fluxes, respectively. H_G is the ground heat flux in the snow/ice, and P is the heat supplied by the precipitation, which is small enough to be neglected in glaciers. All energy fluxes are expressed in W m^{-2}. The calculation of each variable is discussed in the following sections.

4.6.1.1. Surface net radiation flux

For R_N calculation, the input variables like T_a, RH, *u*, sun elevation angle, declination angle, sun hour angle, were used to model the incoming and outgoing radiations at a basinal scale. Therefore, the instantaneous R_N radiation per unit area is calculated using Equation 4.2 (Bastiaanssen et al. 1998):

$$R_N = (1 - \alpha)\, SWI + LWI - LWO - (1 - \varepsilon_0)\, LWI \qquad \textbf{Eq. 4.2}$$

Where, ε_0 is the broadband surface thermal emissivity (dimensionless). All the radiation components expressed in$W\ m^{-2}$.

4.6.1.2. Surface albedo

Surface albedo (α) is the ratio of reflected electromagnetic radiation from the glacier surface to the incoming radiation. The maximum value of α attains during the snowfall and its exponential decay with snow aging (Paul et al. 2008). However, the measurement of α using the ground observation is not feasible over an extremely harsh glacier condition and extensive spatial coverage. To overcome this limitation, the α parameterization approach was performed based on reflectance in narrow bands of visible, near infrared, and shortwave infrared spectral bands of remote sensing data. The α is calculated from the following Equation 4.3 given by Bastiaanssen et al. (1998).

$$\alpha = \frac{\alpha_{TOA} - \alpha_{atm}}{\tau_{SW}^2} \quad \textbf{Eq. 4.3}$$

Where α_{TOA} is the broadband albedo at satellite sensor, α_{atm} is atmospheric corrected albedo and τ_{SW} is the two-way atmospheric transmittance. The value of α_{atm} lies between 0.025 and 0.040 (Allen et al. 2002). Therefore, an average value of 0.03 (0.025 and 0.040) was considered for the present study. Besides, the top of the atmosphere albedo (α_{TOA}) was calculated through a linear combination of the monochromatic reflectance (r_b) (calculated based on Equation 4.7) of the reflective bands of the satellite data, according to Equation 4.4:

$$\boldsymbol{\alpha_{TOA}} = \sum_{b=2}^{7} \boldsymbol{P_b} \times \boldsymbol{r_b} \quad \textbf{Eq. 4.4}$$

Where P_b is the weight of each band. For P_b estimation, it is necessary to estimate the solar constant ($k,\ W\ m^{-2}\mu m^{-1}$) associated with each reflective band of satellite data. The P_b of each spectral band was acquired by the ratio of k_b of that band to the summation of all the k_b obtained from each band using Equation 4.5 (Chander and Markham 2003).

$$\boldsymbol{k_b} = \frac{\boldsymbol{\pi L_b}}{\boldsymbol{r_b\ cosz d_r}} \quad \textbf{Eq. 4.5}$$

Where L_b is the radiance of each band in $W\ m^{-2} sr^{-1} \mu m^{-1}$. For the calculation of L_b, the additive ($Add_{rad,b}$) and multiplicative ($Mult_{rad,b}$) information on radiation was extracted from the metadata of each image, calculated according to Equation 4.6.

$$L_b = Add_{rad,b} + Mult_{rad,b}\ DN_b \quad \textbf{Eq. 4.6}$$

$$r_b = \frac{(Add_{ref,b} + Multi_{ref,b}\ DN_b)}{\cos z \times d_r} \quad \textbf{Eq. 4.7}$$

Where $Add_{ref,b}$ and $Multi_{ref,b}$ are represents the additive and multiplicative terms of each reflectance band extracted from the metadata of the image, respectively. Z is the Sun zenith angle, DN_b is the digital number of each pixel, b is the subscript representing each one of the six OLI band (2 to 7) and d_r is the correction of the eccentricity of the terrestrial orbit, expressed by Equation 4.8:

$$d_r = \left(\frac{1}{d_{ES}}\right)^2 \quad \textbf{Eq. 4.8}$$

Where d_{ES} is the Earth-to-Sun distance (astronomic unit) on the day of each image, also extracted from the metadata.

The τ_{SW} is calculated using Equation 4.9**,** described by ASCE–EWRI (2005).

$$\tau_{SW} = 0.35 + 0.627\, exp\left[\frac{-0.00146\, P}{K_t \times Cos\, z} - 0.075 \times \frac{W}{Cos\, z}^{0.4}\right] \quad \textbf{Eq. 4.9}$$

Where W is the water in the atmosphere (mm); K_t is the turbidity coefficient $0<K_t \leq 1.0$ (dimensionless), where K_t = 1.0 for clean air and K_t = 0.5 for extremely turbid, dusty, or polluted air (Allen 1996; Allen et al. 1998), and P is tshe atmospheric pressure (kPa) calculated using Equation 4.10.

$$P = 101.3\,(\frac{293-0.0065A}{293})^{5.26} \quad \textbf{Eq. 4.10}$$

Where constant 293 is a standard air temperature in K, and A is the altitude of the terrain in meter (m) above sea level (a.s.l.). W is calculated using measured or estimated near-surface vapor pressure from a representative weather station, according to Equation 4.11 (Garrison and Adler 1990).

$$W = 0.14\, e_a\, P + 2.1 \quad \textbf{Eq. 4.11}$$

Where e_a is a near-surface vapor pressure (kPa).

4.6.1.3. Incoming shortwave radiation

SWI is the direct and diffuse solar radiation flux that reaches the earth's surface. In this study, the clear sky conditions as an assumption were taken into account for the SWI estimation, calculated using Equation 4.12:

$$SWI = G_{SC} * cos\,\theta * d_r * \tau_{SW} \quad \textbf{Eq. 4.12}$$

Where G_{SC} is the solar constant (1367 $W\ m^{-2}$); $cos\ \theta$ is the cosine of the solar incidence angle; d_r is the inverse squared relative earth-sun distance (Equation 4.9); and τ_{SW} is the atmospheric transmissivity (Equation 4.10).

For a horizontal flat surface, θ is equivalent to the solar zenith angle (90º - Sun Elevation Angle). However, for the varying slope surface, θ must be calculated pixel-by-pixel based on the surface slope and aspect information, which is derived from a DEM by the following Equation 4.13 (Duffie and Beckman 1989)**:**

$$cos\ \theta = sin\ (\delta)\ sin\ (\emptyset)\ cos\ (s) - sin\ (\delta)\ cos\ (\emptyset)\ sin\ (s)\ cos\ (\gamma) + cos\ (\delta)\ cos\ (\emptyset)\ cos\ (s)\ cos\ (\omega) +\ cos\ (\delta)\ sin\ (\emptyset)\ sin\ (s)\ cos\ (\gamma)\ cos\ (\omega) + cos\ (\delta)\ sin(\gamma)\ sin\ (s)\ sin\ (\omega) \quad \textbf{Eq. 4.13}$$

Where, δ is the declination of the earth (Equation 4.14); $\emptyset$ is the altitude of the pixel obtained; s is the surface slope; γ is the surface aspect, and ω is the hour angle (Equation 4.15).

$$\delta = 0.409\ sin\ \left(\frac{2\pi}{365}J - 1.39\right) \quad \textbf{Eq. 4.14}$$

Where *J* is a Julian day of the year.

$$\omega =\ cos^{-1}[-\tan(\delta)\tan(\emptyset)] \quad \textbf{Eq. 4.15}$$

4.6.1.4. Modeling of air temperature

The measurement of T_a accounts for T_s and land surface variables such as Normalized Difference Vegetation Index (NDVI) (Prihodko and Goward 1997), α (Cristóbal et al. 2009), elevation (Lin et al. 2012), and solar zenith angle (Cresswell et al. 1999). For this, a multivariate statistical approach is used for the estimation of T_a. In general, the multivariate linear regression method can be acquired through multiple regressions using Equation 4.16:

$$T_a =\ b_0 + b_1\ \times\ X_1 +\ b_2\ \times\ X_2 + \cdots \ldots \ldots \ldots + b_n\ \times\ X_n \quad \textbf{Eq. 4.16}$$

Where b_0, b_1, b_2, ..., b_n are regression coefficients and X_1, X_2, ..., X_n are variables used to simulate T_a. In this study, the driving variables, i.e., T_s, NDVI, α, and RH, which are associated with air temperature, were used for T_a estimation. The unknown coefficients of input variables were determined based on the stepwise linear regression method.

4.6.1.5. Incoming longwave radiation

LWI is the thermal radiation flux originating from the atmosphere towards the surface and is traditionally calculated by the method of Swinbank (1963), which is physically substantiated. It can be obtained by Equation 4.17.

$$LWI = (9.2\ X\ 10^{-6})\ \sigma\ T_a^6 \qquad \textbf{Eq. 4.17}$$

Where T_a is the modeled air temperature (in Kelvin). According to past literature (Teodoro et al. 2018), the probable error for the *LWI* estimation is nearly less than 5.0 $W\ m^{-2}$.

4.6.1.6. Outgoing longwave radiation

LWO emitted from the surface is a function of surface temperature and broadband surface emissivity. It is computed using the Stefan-Boltzmann Equation 4.18:

$$LWO = \varepsilon_0\ \sigma\ T_s^4 \qquad \textbf{Eq. 4.18}$$

Where ε_0 is the broadband surface emissivity (dimensionless); σ is the Stefan-Boltzmann constant ($5.67\ X\ 10^{-8}\ W\ m^{-2}K^{-4}$) and T_s is the surface temperature in kelvin. The broadband emissivity is computed using the empirical Equation 4.19 (Tasumi 2005) based on the vegetative thermal spectral emissivity.

When NDVI >0;

$$\varepsilon_0 = 0.95 + 0.01\ LAI; \qquad for\ LAI < 3$$

$$\varepsilon_0 = 0.98; \qquad for\ LAI \geq 3 \qquad \textbf{Eq. 4.19}$$

For water; $NDVI < 0\ and\ \alpha < 0.47;\ \ \varepsilon_0 = 0.985$

For Snow/glacier; $NDVI < 0\ and\ \alpha \geq 0.47;\ \varepsilon_0 = 0.985$

Where LAI is the Leaf Area Index, a ratio of the total leaf area for the surface per unit ground area. It is used to estimate the biomass and canopy resistance to vapor flux. It is given by the following Equation 4.20:

$$LAI = -\frac{\ln[\frac{0.69 - SAVI}{0.59}]}{0.91} \qquad \textbf{Eq. 4.20}$$

Where SAVI is the Soil Adjusted Vegetation Index, the maximum value for LAI is 6.0, which corresponds to a maximum SAVI of 0.687. Beyond SAVI = 0.687, the value for SAVI 'saturates' with increasing LAI and does not change significantly. The SAVI index mainly used to minimize the background effect of soil from NDVI so that the soil wetness is reduced in the index. It can be calculated by Equation 4.21**.**

$$SAVI = \frac{(1+L)(NIR-RED)}{(L+NIR+Red)} \quad \textbf{Eq. 4.21}$$

Where L is a constant for SAVI. If L is zero, SAVI becomes equal to NDVI. A value of 0.5 is used in this study based on past literature.

The T_s is calculated with the following Equation 4.22.

$$T_s = \frac{T_b}{1+\left(\lambda*\frac{T_b}{\gamma}\right)*ln\,\varepsilon} \quad \textbf{Eq. 4.22}$$

Where T_b is the brightness temperature (in Celsius) obtained from the Landsat data based on Equation 4.23; λ is the average of limiting wavelengths (band 10) of Landsat-8 (λ = 10.895 μm) and ε is the surface emissivity value.

$$T_b = \frac{K_2}{\ln(\frac{K_1}{L_\lambda}+1)} - 273.15 \quad \textbf{Eq. 4.23}$$

Where K_1 and K_2 are calibration constants of Landsat-8, available in the metadata; L_λ is the spectral radiance ($Wm^{-2}sr^{-1}\mu m^{-1}$) calculated by the following Equation 4.24:

$$L_\lambda = M_L * Q_{cal} + A_L - O_i \quad \textbf{Eq. 4.24}$$

Where M_L represents the band-specific multiplicative rescaling factor; Q_{cal} is the Band 10 image, A_L is the band-specific additive rescaling factor, and O_i is the correction factor for Band 10.

4.6.1.7. Turbulent sensible and latent heat fluxes

The turbulent sensible (H_S) and latent (H_l) heat fluxes were estimated using the bulk aerodynamic method (Munro 1989). It can be calculated based on Monin-Obukhov theory, which uses a single level *u*, temperature, and RH, by the following Equation 4.25 (Oerlemans and Klok 2002):

$$H_S = \rho_a c_p C_H u\,(T_a - T_s) \quad \textbf{Eq. 4.25}$$

Where ρ_a is the air density; c_p is the specific heat capacity of air (1010 $JKg^{-1}K^{-1}$); C_H is the turbulent exchange coefficient of heat; u is the wind speed, T_a and T_s are the air and surface temperature, respectively. H_L can be calculated using Equation 4.26.

$$H_L = \rho_a L_v C_E u_z \left(\frac{0.622}{P}\right)(e_a - e_s) \quad \textbf{Eq. 4.26}$$

Where, L_v is the latent heat of vaporization (2.514×10^6 JKg^{-1}) and C_E is the turbulent exchange coefficients for vapour pressure. e_a and e_s are the actual and saturated vapor pressure, respectively, that estimated from T_a and dew point temperature. The turbulent exchange coefficients are computed by the method described by Hock (2005).

4.6.1.8. Ground heat flux

The H_G is the heat transfer rate trapped in soil and vegetation by the convection process. The amount of soil heat flux, vegetation index, and R_N were used to calculate the H_G. The relationship between the following variables as described by **Equation 34** (Bastiaanssen 2000).

$$G/_{R_N} = 0.05 + 0.18e^{-0.521 \times LAI}; \quad LAI > 0.5$$

$$G/_{R_N} = 1.8 \times \frac{T_s - 273.15}{R_N} + 0.084; \quad LAI < 0.5 \quad \textbf{Eq 4..27}$$

4.6.2. CALCULATION OF TOTAL MELT

An energy balance based approach was used to compute the pixel-wise glacier melt with the calculation of inward and outward energy fluxes on the glacier surface. The glacier surface revolved for melt when the surface temperature of the pixel is at $0°C$ and assumes that any surplus energy available will be converted into the melt. Additionally, the glacier surface layer turned into melt when the sublimation or re-sublimation process comes into consideration. According to Hock (2003), when F_M available is positive, then melt occurs; otherwise, negative is for loss of energy on the surface. The positively calculated energy can be converted into melt using the following Equation 4.28.

$$Melt\ (m\ w.e.) = \frac{F_M}{L_f \times \rho_w} \quad \textbf{Eq. 4.28}$$

Where, ρ_w is the density of water ($1000\ Kg\ m^{-3}$) and L_f is the latent heat of fusion/melt (L_f = $3.34 \times 10^5\ J\ Kg^{-1}$). F_M is the available energy on the surface and will produce melt only when

the surface temperature reaches 0°C. However, when the glacier surface is negative, then the sublimation process is derived using the latent heat of vaporization L_v based on Equation 4.29.

$$Sublimation = \frac{H_l}{L_v \times \rho_w} \quad \textbf{Eq. 4.29}$$

Where, $L_v = 2.834 \times 10^6 \, JKg^{-1}$. The total ablation is the summation of melt and sublimation with subtracted re-sublimation.

4.6.3. MODEL CALIBRATION/VALIDATION

In this study, the proposed model was used for glacier mass balance estimation, which constrained a large number of parameters. Some of these parameters have well-defined values that are determined by the physical processes and empirical equations. However, the other variables are strongly dependent upon the local glacial-meteorological conditions and need to be determined using parameter optimization or local information (Ragettli et al. 2013). While field observation from the Himansh AWS location was used for calibration/validation of the proposed model, we assumed that the glaciers in that basin experienced similar regional weather patterns due to close proximity (~20 km) and approximately similar mean elevation. The glacier mass balance measurement was derived from the annual field measurements to determine winter, summer, and annual mass balances following conventional field mass balance techniques (Cogley 2011). The field data obtained from AWS location was used for a one-to-one comparison of model parameters to estimate the accuracy of the proposed model. However, the mass balance and meteorological time series were analyzed against each variable using the root mean squared error (RMSE), coefficient of determination (R^2) values and Pearson's correlation (R) analysis. The main aim was to minimize RMSE and R^2 for each variable and overall annual glacier mass balance measurement.

In this study, a total of nine input parameters, i.e., T_a, T_S, SWI, e_a, precipitation gradient, P, α, cloudiness, and turbulent exchange coefficient, etc., were assigned to estimate the uncertainties in the spatial glacier mass balance estimation model. However, uncertainty caused by the subsurface layer temperature is not taken into account as it has a negligible influence on the mass balance (Oerlemans and Klok 2002). The aim of the present uncertainty analysis is to quantify the associated uncertainty in the mass balance model. However, not all potential sources of uncertainty could be considered.

4.7. RESULTS AND DISCUSSION

4.7.1. GLACIO-METEOROLOGICAL CONDITIONS

4.7.1.1. Surface and air temperature

The T_s was derived for the selected images over the period 2013–2019 based on Artis and Carnahan (1982) formulas. However, Barsi et al. (2005) have suggested that all surface temperatures are rough estimates due to the approximation of surface properties, i.e., emissivity and the fundamental errors in the atmospheric correction of the thermal band. The estimated mean T_s ranged from –12.0 ºC (2018/19) to –8.2 ºC (2017/18), with an average of –10.0 ºC for the annual studied cycle. Additionally, the monthly analysis suggested that January was the coldest month, with a mean value of –23.5 ºC, while August was the warmest month with a mean value of +3.0 ºC (Figure 4.2). The minimum T_s was experienced by the Samudra Tapu followed by the Bara Shigri glacier, whereas maximum in the Hamtah glacier.

The T_a was estimated using the multivariate linear regression model (Discussed in the methodology section) for the six hydrological years. The mean annual T_a was observed –8.1 ºC, which varied from –9.1 ºC (2018/19) to –7.1 ºC (2014/15); it shows an inter-annual variability. The mean minimum and maximum temperatures were observed in February (–20.0 ºC) and August (–1.3 ºC), respectively (Figure 4.2). Many authors have found a similar pattern of T_a over the study region (Azam et al., 2014; Mandal et al., 2016, 2015; Pratap et al., 2019; Soheb et al., 2017). For example, Azam et al. (2014) have observed that the coldest month was January and the warmest was August for the Chhota-Shigri glacier. Besides, Pratap et al. (2019) have also highlighted that the maximum T_a (11.4 ºC and 7.4 ºC) was observed in July and the minimum (–15 ºC and –15.7 ºC) in January for the Himansh and Sutri Dhaka glacier observational sites. Similarly, Sharma et al. (2016) have highlighted that the minimum temperature was observed in January and maximum in July over the Lahaul and Spiti region over 1901–2002. Moreover, the monthly T_a of each hydrological year (2013–2019) above melting point was observed between May and October. Therefore, we have considered the period from May to October as a summer/melt season, while the remaining months as a winter/non-melt season. Similar months were considered by Vincent et al. (2013) for seasonal analysis over the Chhota Shigri Glacier. In addition, results demonstrated that the qualitative pattern of T_a and T_s were highly correlated (R^2 = 0.85). Similarly, Schauwecker et al. (2015) have reported that the satellite-based T_s was well correlated (R^2 = 0.74) with the T_a over the Bara Shigri glacier.

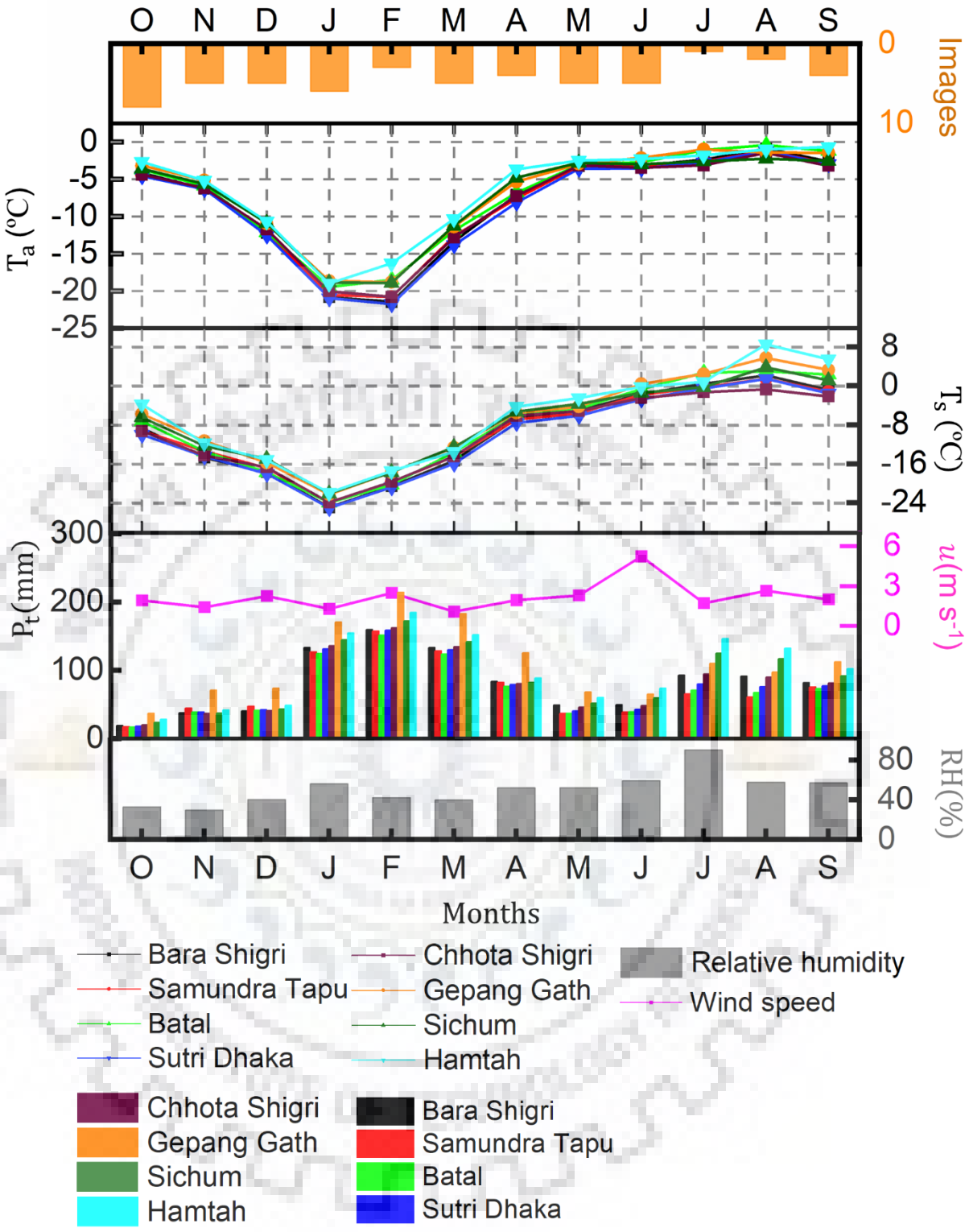

Figure 4.2. Mean monthly values of T_a, T_s, RH, u, and P_t of eight selected glaciers over six hydrological years between October 2013 and September 2019.

4.7.1.2. Relative humidity and wind speed

Both RH and *u* are the essential atmospheric variables, and it affects the H_l flux, which further supplies for sublimation/re-sublimation of the glaciers (Dadic et al. 2013). For the study area, the

minimum and maximum mean monthly RH were observed in November (29.2%) and June (89.9%), respectively. Similarly, Azam et al. (2014) highlighted that the mean monthly RH showed an increase in June and a decreasing pattern in October over the Chhota Shigri glacier. Likewise, Ramanathan (2011) demonstrated that the RH varied between 12 to 99% over the Chhota Shigri glacier. However, we observed that the mean annual RH ranged from 39.4% (2018/19) to 68.6% (2013/14), with an average of 53.3%, and its Coefficient of Variation (CV) was around 30%.

However, the mean annual *u* was 3.70 m s^{-1} based on in situ measurement, which ranged from 2.3 to 6.3 m s^{-1} that shows less variability (CV = 47 %) over the study area. In contrast, Schauwecker et al. (2015) assumed that a constant *u* (3 m s^{-1}) at the time of satellite overpass in the Bara Shigri glacier for energy balance study. Furthermore, *u* attains a maximum (5.2m s^{-1}) in June, while minimum in March (1.1 m s^{-1}). However, Mandal et al. (2020) have reported that the higher *u* was observed in winter (DJFM), whereas lower in summer season (JJAS) for the period from 1 October 2009 and 28 September 2019 recorded at the AWS located in 4863 m a.s.l. elevation over the Chhota Shigri glacier.

4.7.1.3. Total precipitation

The P_t was estimated from the ERA-5 reanalysis data for the observational period to understand the monthly distribution of precipitation over the region. In the Indian context, the ERA-5 performed better than other reanalysis products as well as revealed higher correlation (R^2= 0.85) with the IMD station data. Also, it can be used for hydrological assessment over the region (Mahto and Mishra 2019). The result showed that 70% of precipitation occurred during winter (January to March), while 15% occurred from July to September. However, this region received precipitation both from the ISM in summer and mid-latitude Westerlies in winter (Shekhar et al. 2010). Moreover, the mean annual P_t was observed 1021.8 mm with a minimum in 2015/16 (817.2 mm) and a maximum in 2013/14 (1029.7 mm). However, the yearly P_t found in 2014/15 was relatively closer to the mean annual precipitation.

4.7.2. SEASONAL CYCLE IN GLACIER SURFACE MASS BALANCE

The mean monthly of each energy balance component was calculated for the selected glaciers (Figure 4.3). It was observed that the SWN progressively increases from April (86.2 W m^{-2}) and reached a maximum in August (512 W m^{-2}). This is due to the combined effect of increasing top-of-the-atmosphere irradiation and decreasing snow albedo (Li et al. 2018b).

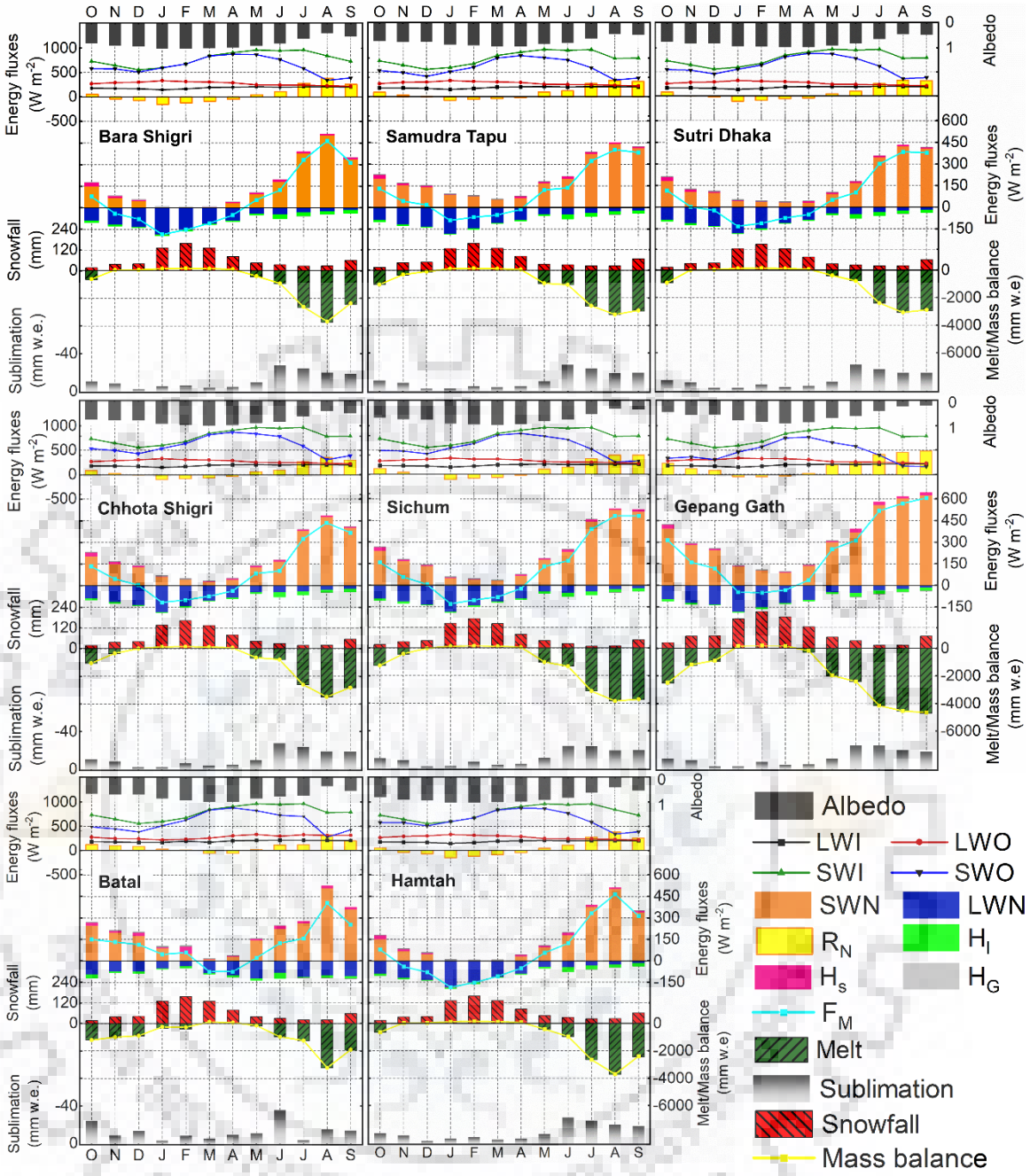

Figure 4.3. Average monthly energy and mass fluxes of the selected glacier during the six hydrological years (2013 – 2019).

Furthermore, SWN rapidly decreases after September because of the start of snowfall events that increase α. Therefore, α was observed maximum in March that shows minimum SWN. Several authors have reported that the maximum snow cover extent measured in February and March over the Chenab basin for the period 2017/18 (Randhawa and Gautam 2019; Dharpure et al. 2020). However, LWN constitutes a large amount of energy loss. The mean monthly *LWN* varied from –184.7 W m^{-2} (January) to –17.9 W m^{-2} (September), with an average of –88.6 W m^{-2}. It shows more negative in winter (November-April) than in summer (May-October).

The R_N indicates the amount of energy gained during the melt season and losses in the remaining months. The average monthly R_N was observed positive from May to October; otherwise remains negative for the rest of the year. Other than the value of H_S remains positive throughout the year; however, it attains higher value during winter as compared to summer, ranging from 2.7 W m^{-2} (March) to 26.5 W m^{-2} (October), with a mean of 10.6 W m^{-2}. However, H_l flux generally negative during the study period, which shows the sublimation, occurred around the year. It varies from –29.4 W m^{-2} (June) to –2.8 W m^{-2} (December), with an average of 11.8 W m^{-2}. The absolute value of H_S was smaller than the H_l during the melt period, whereas it is more significant for the non-melt season. Therefore, the combination of turbulent heat fluxes, i.e., H_S and H_l constitutes a surface energy reduction in melt season and source of energy gain in the non-melt season. Overall, R_N dominant for melt in the summer season while H_S dominant in the winter season. The H_G flux is the energy loss through heat conduction. The value of H_G is positive when energy is transferred towards the ground and vice versa. The H_G progressively increases (energy sink) from 0.0 or nearly negative in August (–0.75 W m^{-2}) to 5.7 W m^{-2} in January.

However, the amount of melting was estimated by considering available F_M (at the surface) greater than 0.0 W m^{-2}, which means positive F_M contribute to glacier melt. Mostly melting occurred from May to October, with a maximum value of 3.8 m w.e. in August. The glacier net melt is the summation of surface melt and sublimation or re-sublimation of the glacier. It was also observed that the selected glaciers were mainly dominated by the process of sublimation. The sublimation continuously occurred throughout the year with a maximum in winter (–2.9 mm w.e.) while minimum in summer (–26.0 mm w.e.); a similar pattern was observed by Azam et al. (2014) over the Chhota Shigri glacier. Moreover, a significant mass gain (~64%) was observed from January to April, whereas a higher mass loss during the remaining months. Several authors reported a similar pattern of mass balance over the region (Knudsen 2011; Moiwo et al. 2011).

4.7.3. INTERANNUAL VARIABILITY OF THE GLACIER MASS BALANCE

The annual energy fluxes and mass balance of the glaciers were calculated over the six hydrological years, as shown in Figure 4.4. The proposed model provides an understanding of heat transfer to the superficial glacier layer, which turned into melt when the T_s is at above 0.0 ^oC. The estimated annual glacier mass balance was –3.4 m w.e., with a loss of –3.5 m w.e. in the summer and a gain of +0.1 m w.e. in the winter. This result indicates that the H_l was intensified due to the amount of sublimation during the winter; however, it slowly increases over the snow accumulation season and rapidly ends with the melt season (Table 4.2).

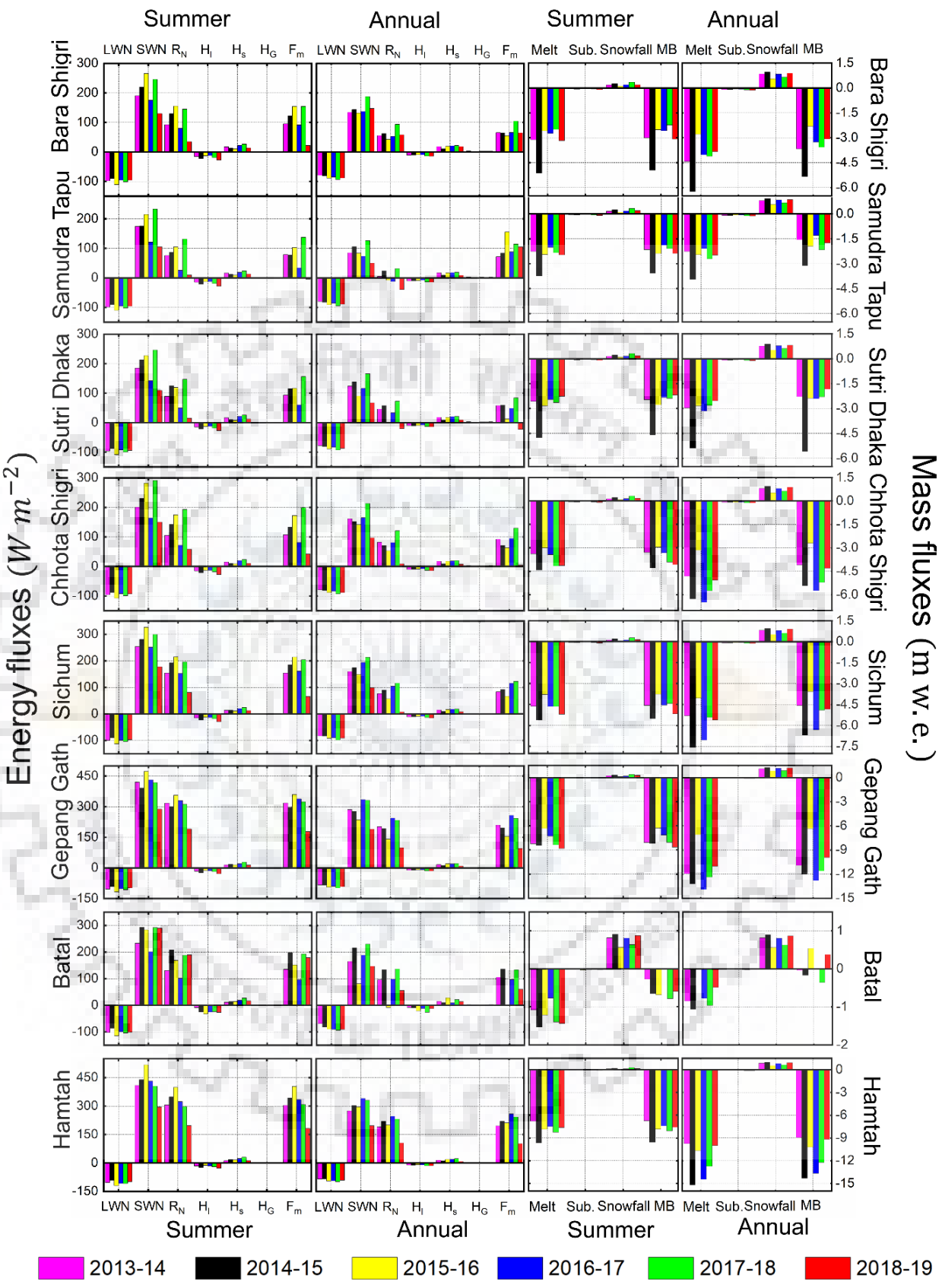

Figure 4.4. Interannual variability of energy and mass fluxes of 8 selected glaciers during six hydrological years (2013 – 2019).

Similar results were observed by Li et al. (2018) over the Qiangtang No.1 glacier in the Tibetan Plateau. The majority of surface ablation occurred in the summer season by R_N as well as H_S. However, the negative value of R_N indicates the radiative cooling of the glacier surface, whereas its positive value represents the source of heat responsible for melting. Therefore, we have mainly focused on the interannual variability of SEB during the melt season. Results indicate that the H_G flux experienced a negligible change over the six-melt seasons. The interannual ranges of SWI and LWI were 71 W m^{-2} and 13.1 W m^{-2}, respectively, over the period. While the mean annual total incoming radiation (SWI + LWI) was about 55.6 W m^{-2}.

The interannual range of SWO and LWO were 26 W m^{-2} and 99.7 W m^{-2}, respectively, with total outgoing radiation obtained 102.8 W m^{-2}. Compared to this, the mean interannual ranges of LWN and SWN were observed about 22.2 W m^{-2} and 155.7 W m^{-2}, respectively for six hydrological years. Additionally, the average of LWN and SWN were 78.4 W m^{-2} and 85.8 W m^{-2} during the study period, respectively. These results indicate that the α dominated the R_N on the interannual scale. Also, the total turbulent heat fluxes (H_s + H_l) contribute to negligible energy (–1.3 W m^{-2}) during the melt season. The H_S was observed higher than the H_l during the period. The overall melting of the entire glaciers ranged from 1.1 to 4.9 m w.e., with an average of 2.4 m w.e. The maximum melting of 3.8 m w.e. occurred in the Hamtah glacier during 2015/16 while minimum melting of 1.3 m w.e. occurred in the Samudra Tapu for the period 2017/18.

In order to analyze the spatial variability of the energy and mass fluxes over the glacier surfaces, two different date images (6 October 2017 for ablation and 31 March 2018 for accumulation period) were selected for analyzing the effectiveness of the proposed model. The spatial distribution of α, SWN, LWN, R_N, H_S, H_l, H_G fluxes, and F_M were mapped over the glacier topography for better understanding the spatial distribution of fluxes (Figure 4.5). For the selected images, the SWN varied from 0 to 821 W m^{-2}during the ablation; however, from 0 to ~459 W m^{-2} over the accumulation period. The observed variation in *SWN* mainly depends upon the topography and α of the surface.

The SWN decreases with aspects changing from south-facing to north-facing orientation, as shown in Figure 4.5**.** There was also a sharp transition between larger than 600 W $m^{-2}$and smaller than 300 W m^{-2} for the SWN. The area between these two transition values observed the majority of the steepest slope, which received less incident solar radiation. However, this region also attains a high average α as it carries permanent snow throughout the year. Additionally, the LWN and turbulent heat fluxes vary with changes in altitude. These estimated

fluxes mainly depend on the T_a, RH, and u, which all are the function of elevation. Overall, the R_N was found nearly zero or negative in the accumulation image, where high α along with low SWN and a deficit of LWN.

Table 4.2. Mean annual and seasonal energy fluxes during six hydrological years (2013 – 2019).

Variable	2013/14	2014/15	2015/16	2016/17	2017/18	2018/19
Annual average (W m^{-2} [%])						
SWI	787.9	769.7	752.8	755.3	777.5	743.5
SWO	624.5	592.9	601.6	577.3	565.6	639.5
LWI	181.9	184.6	188.7	186.2	176.0	178.3
LWO	262.8	266.9	279.9	273.3	271.3	267.8
R_N	82.5 (73%)	94.6 (81%)	60.1 (68%)	90.9 (75%)	116.6 (76%)	15.1 (37%)
H_s	16.9 (15%)	10.0 (9%)	17.9 (20%)	19.3 (16%)	20.7 (14%)	8.6 (21%)
H_l	–10.6 (9%)	–10.7 (9%)	–9.0 (10%)	–8.4 (7%)	–13.6 (9%)	–14.6 (36%)
H_G	3.0 (3%)	1.9 (2%)	1.9 (2%)	2.4 (2%)	2.3 (2%)	2.7 (7%)
F_M	91.7	95.7	70.9	104.3	126.0	11.1
Summer average (W m^{-2} [%])						
SWI	869.0	805.4	787.2	741.5	805.0	751.1
SWO	611.2	522.7	451.1	484.8	485.5	548.9
LWI	189.2	197.0	201.1	196.3	189.8	201.1
LWO	287.8	286.1	273.8	257.1	255.8	259.7
R_N	148.8 (82%)	180.2 (83%)	204.4 (90%)	128.4 (79%)	194.5 (81%)	72.7 (64%)
H_s	15.6 (9%)	13.7 (6%)	11.1 (5%)	21.3 (13%)	26.0 (11%)	12.9 (11%)
H_l	–15.1 (8%)	–22.0 (10%)	–12.2 (5%)	–12.8 (8%)	–18.5 (8%)	–27.6 (11%)
H_G	1.1 (1%)	0.2 (0%)	0.4 (0%)	0.8(1%)	1.2 (1%)	0.7 (1%)
F_M	150.4	172.1	203.6	137.7	203.2	58.7
Winter average (W m^{-2} [%])						
SWI	722.5	740.8	667.1	713.4	678.3	683.7
SWO	617.2	632.6	621.9	570.2	538.3	624.1
LWI	176.3	175.1	179.0	178.3	162.8	160.1
LWO	243.1	251.8	253.9	257.3	251.0	244.9
R_N	38.5 (57%)	31.5 (73%)	–26.3 (44%)	64.2 (71%)	51.7 (65%)	–21.0 (61%)
H_s	17.9 (26%)	7.0 (16%)	23.5 (40%)	17.7 (20%)	15.3 (19%)	5.3 (15%)
H_l	–7.1 (10%)	–1.7 (4%)	–6.7 (11%)	–4.9 (5%)	–8.7 (11%)	–4.1 (12%)
H_G	4.4 (7%)	3.2 (7%)	3.2 (5%)	3.7 (4%)	3.4 (4%)	4.2 (12%)
F_M	53.8	40.0	0.0	80.8	61.8	0.0

The spatial distribution of ablation was calculated as a function of elevation and latitudes with the proposed model over the above-selected images (Figure 4.6). The ablation model estimates the net annual mass loss that includes the melting that occurred during the snow accumulation as well as the net melting of surface ice during the melt season. Results demonstrated that the glacier melts varied from –1.9 to +0.3 m w.e. (with a mean of –0.42 m w.e.) during the ablation and from –2.1 to 0.2 m w.e. (with an average of –0.27 m w.e.) for the accumulation period. The negative sign represents the glacier mass loss, while the positive indicates the no glacier mass loss due to the available melt energy. The 2-D melt distribution shows substantial spatial variation over the period, which indicates a low melting in the upper reaches compared to higher melting in the ablation zone of the glaciers. However, a more substantial surface melt was observed near the centerline of the glaciers.

From the above-selected images, the mean mass loss due to sublimation was estimated 0.022 m for the ablation and 0.016 m in the accumulation periods. Simulated sublimation shows a distinct elevation gradient, maximized on the windward, and minimized on the leeward side of the glaciers. Therefore, it is directly proportional to u at the glacier surface. It was observed that sublimation occurred in round the year if the vapor pressure deficit exists and non-zero u. A decrease in snowfall or prolong melting period causes a significant reduction in snow accumulation and a decrease in α that enlarges the absorption of solar radiation. Therefore, the result shows a strong interrelationship between these variables and their sensitivity with the mass balance. These findings concurred with Negi et al. (2018) that discussed the rise in liquid precipitation trend over the north-western (NW) Himalayan region, which has an adverse influence on the glaciers.

4.7.4. ALTITUDINAL VARIATION IN SURFACE MELTING

The mean energy balance components were assessed at 500 m a.s.l. elevation interval over the selected glaciers (Figure 4.7). The result indicates that the LWN and H_l flux becomes less negative as it moves higher elevation, whereas the H_s flux was not consistent for all the years. Besides, the *SWN* shows a higher value at the upper elevation (> 5750 m a.s.l.) of the glaciers. However, the *SWN* was decreasing irrespective of the altitude, while the expected increases (in the higher elevation) could be contributed by the optical air mass that decreases with elevation. These patterns may be caused by the effect of shading, slope, aspect, sky obstruction, and terrain reflection. Klok and Oerlemans (2002) have demonstrated that the reflected radiation has the smallest effect (4.3%) due to nearby terrain features; however, significantly influenced by the shading (10.0%), slope, and aspect (8.5%).

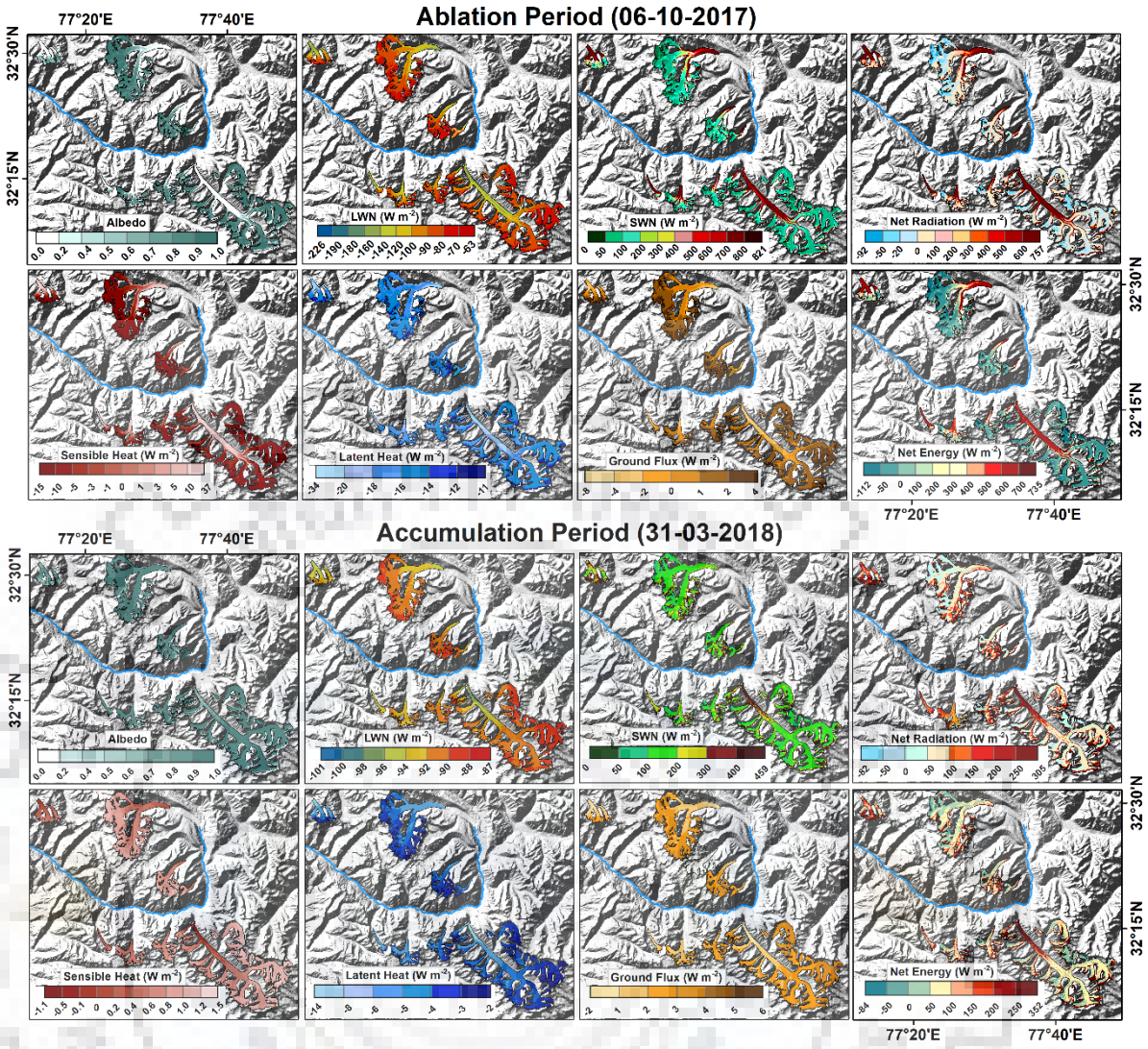

Figure 4.5. Spatial distribution of estimated energy balance components over the two selected images during the ablation (6 October 2017) and accumulation (31 March 2018) periods.

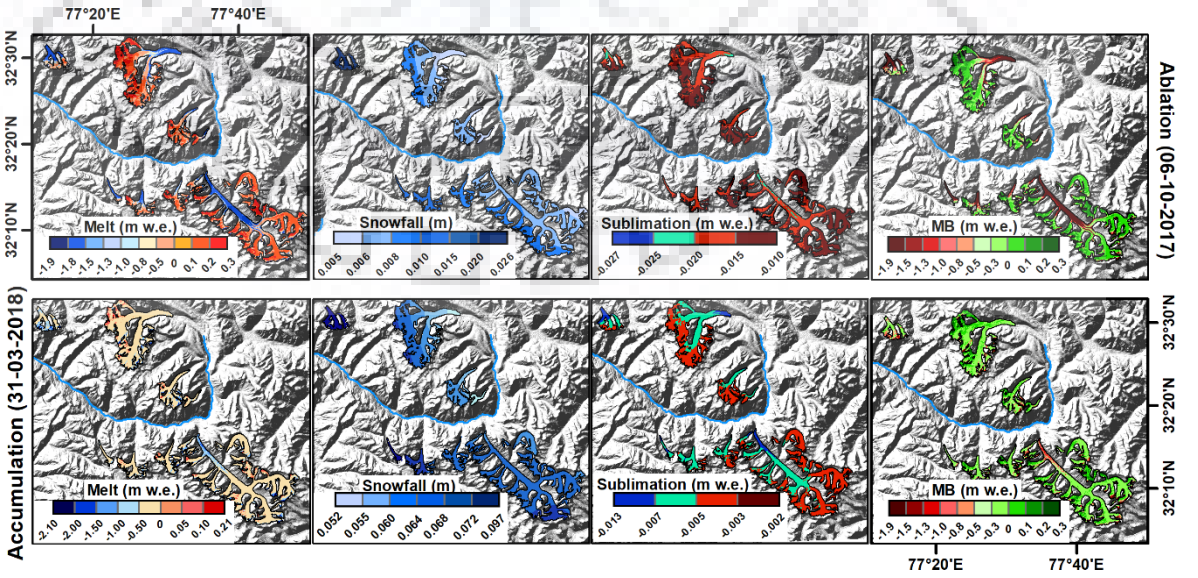

Figure 4.6. The spatial distribution of the melting, snowfall, sublimation, and mass balance of glaciers during the ablation (6 October 2017) and accumulation (31 March 2018) period.

Arnold et al. (1996) have also observed the effect of topography on the *SWN* of the Haut glacier d'Aroll in the Alps. They found that the shading reduces radiation by 5.2%, and slope and aspect decrease the shortwave reception by 14.7%. However, the H_S flux was higher than H_l flux irrespective of all the elevations. It was observed that the annual F_M (summation of all the fluxes) indicates positive at all the elevations in three hydrological years (2013/14, 2016/17 and 2017/18); however, it becomes negative for other hydrological years at the mean altitude between 5250 and 5750 m a.s.l. The negative F_M implies that there is no melting or the snow/ice pack not able to attain mass or loss in the heat.

Our studies illustrated that the surface melting of the selected glaciers ranged from –5.1 to –2.5 m w.e. that lies between 4500 to 5000 m a.s.l. However, the melting was reduced by –1.4 to –2.3 m w.e. at the lowest part of the ablation zone < 4500 m a.s.l. Also, Mandal et al. (2020) have reported that melting over the debris-covered part of the Chhota Shigri glacier was reduced by –1 to –2 m w.e. at an elevation below 4400 m a.s.l., indicating that the debris suppresses melting by insulating the ice surface from direct solar radiation. The meteorological observations on the Sutri Dhaka glacier during 2015/16 and 2016/17 showed a melting rate of –6.0 and –2.0 m w.e., respectively, between 4500 and 5000 m a.s.l. (Pratap et al. 2019). A similar ablation rate of the Chhota Shigri glacier within the same altitudinal range (4500 to 5000 m a.s.l) was observed from 2002 to 2006 (Wagnon et al. 2007).

4.7.5. MODEL VALIDATION

4.7.5.1. With observational data

To validate the proposed model, the sets of input variables were compared with the meteorological data (at half-hourly) measured at the Himansh station by NCPOR over the two separate periods- October 2015 to October 2016 and October 2017 to October 2018. The relationship between observed T_a, *SWI, SWO, LWI, LWO,* and α with the in-situ station data, which shows a good agreement with an overall R^2 ranged from 0.84 to 0.98 (no. of sample = 18) (Figure 4.8). This indicates the robustness of the model over the other existing techniques.

The comparison revealed that the computed energy fluxes were ~2.0% smaller than the measured data. This underestimation is acceptable given an overall uncertainty of $\pm$5.0 to 10.0 W m^{-2} in the point-based measurements (USEPA 2000). The T_a was calculated at a spatial scale by the multi-regression analysis, which indicates a higher correlation (R^2 = 0.95, $p < 0.001$) between modeled T_a and station temperature with an average difference of 0.1 ºC. This T_a difference corresponds to a mean difference of 1.0 - 2.0 W m^{-2} between the estimated and measured LWI.

Overall, it is concluded that the model was able to compute the modeled T_a and energy balance components at point scale. Moreover, it was able to accurately estimate the SEB and overall mass balance of the glaciers.

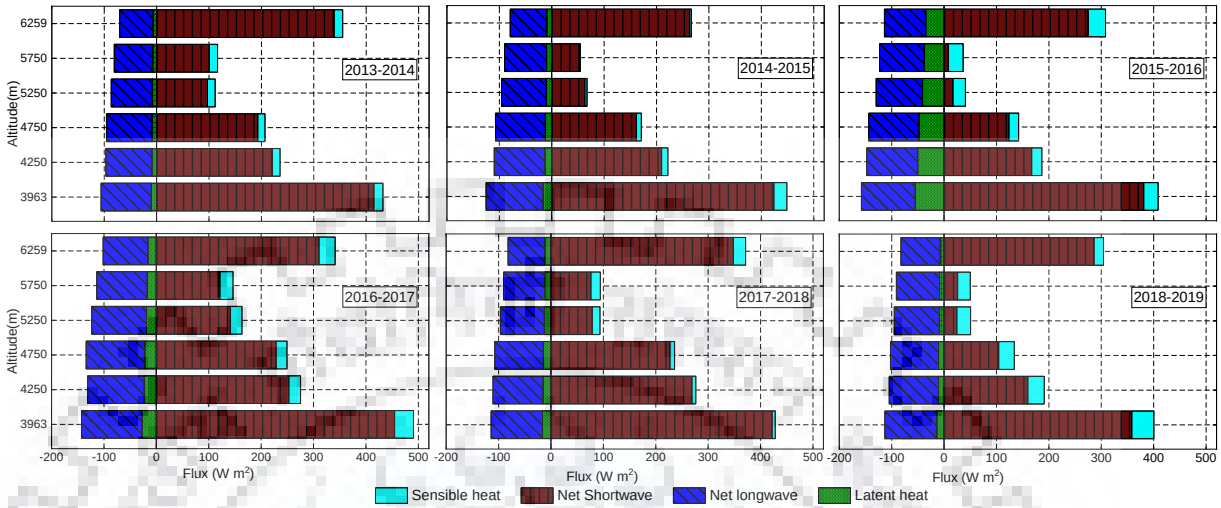

Figure 4.7. Mean annual energy fluxes (SWN, LWN, H_S and H_l) at 500 m a.s.l. intervals of six hydrological years (2013 – 2019).

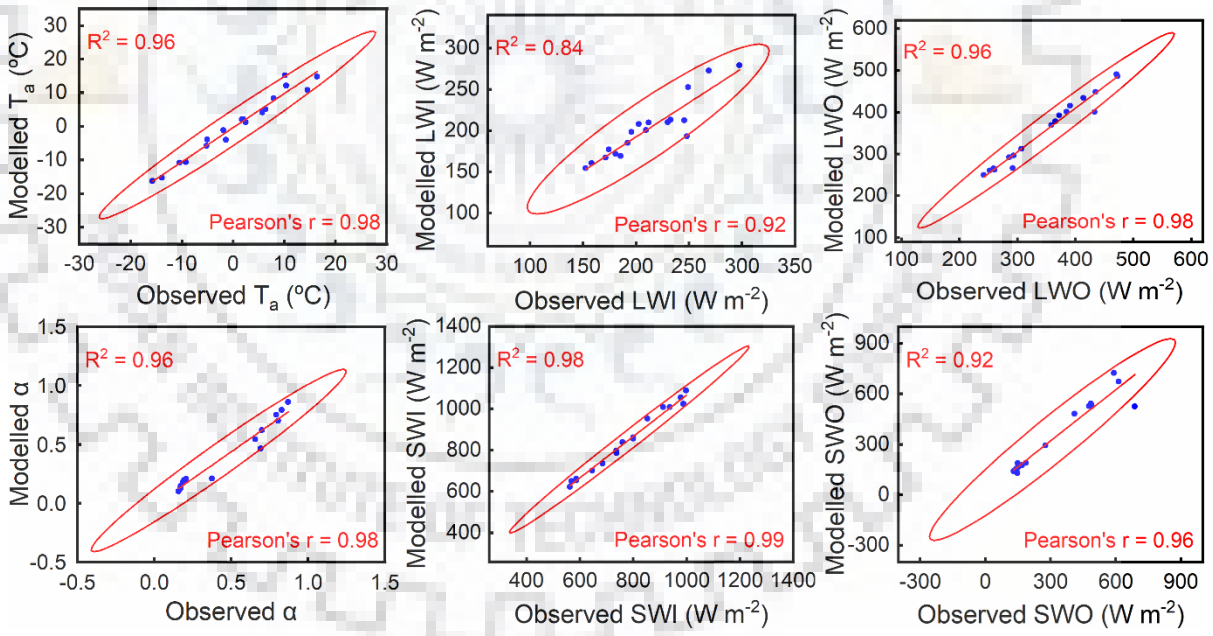

Figure 4.8. Validation between modelled and observed T_a, SWI, SWO, LWI , LWO and α over the two separate periods (October 2015 – October 2016 and October 2017 – October 2018) (no. of samples = 18).

4.7.5.2. With published literature

The energy balance components and mass balance of different glaciers obtained in this study were also compared through the published literature. The overall annual mass balance of the

Chhota Shigri glacier shows a negative mass balance with a rate of –0.4 ± 0.1 m w. e. a^{-1} for the six hydrological years. Also, the mean annual glacier mass balance was estimated as –0.35 m w. e. a^{-1} for 2013–2019, which shows a good agreement with Mandal et al. (2020) based on field data (–0.20 m w. e. a^{-1}) for the same period. They have also highlighted that the majority of the years experienced negative mass balance for the Chhota Shigri glacier over the observational period (2002–2019) except for 2004/05, 2008/11, and 2018/19. It was found that the inter-annual variability of winter and summer mass balance was relatively low (standard deviation of ±0.28 and ±0.3 m w. e. a^{-1}) between 2009 and 2019. However, in the present study, the inter-annual variability was slightly higher than the reported, which is ±0.40 m w. e. a^{-1} for the winter while ±0.48 m w. e. a^{-1} in the summer mass balance over the six hydrological years. Additionally, Azam et al. (2014) have reconstructed the annual mass balance of the Chhota Shigri glacier between 1969 and 2012 using the degree-day approach and accumulation model. They observed a steady state of the glacier between 1986 and 2000; however, it accelerated mass loss after 2000. Similarly, Vincent et al. (2013) have used the combination approach of field measurement and digital elevation differencing from satellite data, which showed a positive or near zero mass balance between 1988 and 1999. However, a slight glacier mass loss was experienced between 1988 and 2010 (–3.8 ± 2.0, corresponding to –0.17 ± 0.09 m w. e. a^{-1}).

Moreover, the Hamtah glacier showed a negative mass balance (–1.45 ± 0.15 m w. e. a^{-1}) for 2000–2012 (Sharma et al. 2020). However, the Hamtah glacier exists in the same climatic zone irrespective of the Chhota Shigri glacier, which governed similar climatic conditions and almost the same orientation. The primary difference comes with the lower maximum altitude and smaller accumulation area in comparison to the Chhota Shigri glacier (Pandey et al. 2017). Also, the retention of the meltwater in the snowpack was very limited, and the presence of supra-glacial rivulets as well as Moulin (Shukla et al. 2020). Our analysis suggested that the Hamtah glacier received the highest negative mass balance (–1.1 m w.e.) as compared to other selected glaciers.

Additionally, the Gepang Gath glacier shows a negative mass balance of –1.16 ± 0.22 m w. e. a^{-1} during 2014–2018 (Sharma et al. 2020). Similarly, Patel et al. (2017) have also witnessed the higher melting and calving of the Gepang Gath glacier in contact with the lake is probably responsible for the increased retreat of the terminus of the glacier. Kulkarni and Karyakarte (2014) have revealed the overall glacier ice loss of 19 ± 7 m between 1975 and 2011 for the Chandra basin glaciers. In the present study, the mean annual glacier-wide mass balance of the Gepang Gath was –1.0 ± 0.21 m w. e. a^{-1} during 2014–2019, which is similar to the mass balance reported by Sharma et al. (2020), within the uncertainties.

Similarly, the in-situ mean annual net mass balance for the Sutri Dhaka glacier was –0.82 $\pm$ 0.17 m w. e. a^{-1} during 2013–2017 (Sharma et al. 2020). In contrast, the present study estimated an annual mass balance of –0.74 $\pm$ 0.1 m w. e. a^{-1} over the same study period. Another study carried out by Pratap et al. (2019) revealed that the annual melting at Sutri Dhaka was –4.20 $\pm$ 0.84 for 2015/16 and –3.09 $\pm$ 0.62 m w.e. for 2016/17. Compared to this, the proposed model estimated an average melting of –3.2 m w.e. and –2.8 m w.e. for 2015/16 and 2016/17, respectively.

For the Batal glacier, Sharma et al. (2020) reported that the glacier mass balance was significantly negative (–0.47 $\pm$ 0.10 m w. e. a^{-1}) from 2013 to 2017. Similarly, the present study revealed a negative mass balance (–0.56 $\pm$ 0.60 m w. e. a^{-1}) during the same period (2013–2017). This glacier attains the second-highest melt among the selected glaciers. The Sutri Dhaka and Batal glacier come under the same climatic condition and elevation zone. However, the debris thickness shows a heterogeneous pattern in the Batal, which results in the varying spatial distribution of melting. Sharma et al. (2016) have reported that the debris cover attenuated the ice melt throughout the ablation zone, and about 90% of the ablation area was experiencing inhibited melting in the Batal glacier.

The mass balance of the Chandra basin's largest glacier (Bara Shigri) was estimated to be –0.50 $\pm$ 0.3 m w. e. a^{-1} using the proposed model. Also, the field-based mass balance was observed at about –0.57 $\pm$ 0.12 m w. e. a^{-1} during 2014–2017 (Sharma et al. 2020). This glacier is experiencing a climatically induced negative mass balance that is responsible for the terminus recession, frontal area changes, and increase in debris cover during the past few decades (Chand et al. 2017). Overall, every selected glacier for this study is a good agreement with the published literature, although discrepancies exist in the shadow-influenced area of the glaciers.

4.7.6. CORRELATION BETWEEN ENERGY FLUXES AND MASS BALANCE

To understand the relation between forcing variables and potential glacier changes, a correlation matrix was plotted between the annual glacier mass balance and the glacial-meteorological variables. Results demonstrated that it has a strong correlation among the drivers (Figure 4.9). Further, it revealed that the *u* was negatively correlated with P_t ($r = –0.88$, $p < 0.01$) and snowfall ($r = –0.84$, $p < 0.01$). Our results supported the finding of Liu et al. (2019). However, the α shows a negative correlation with land surface temperature ($r = –0.82$, $p < 0.01$) while a positive relationship with SWO ($r = 0.92$, $p < 0.01$), and a higher positive correlation ($r = 0.99$, $p < 0.01$) was observed between R_N and SWN. Therefore, it was observed that the mass balance mainly controlled by SWN. Results revealed that the shortwave flux transmittance increases as α

decreases. Similar results were demonstrated by Che et al. (2019) and suggested that the glacier mass balance is sensitive to the snow albedo and time scale.

4.7.7. UNCERTAINTIES ASSOCIATED WITH THE PROPOSED MODEL

In the proposed model, it was observed that the SWN is the main contributor to the surface energy balance during the summer season. It contributes about 56% (SWN) in total energy (F_M) available for surface melt. Therefore, changes in the amount of solar radiation over the glacier surface will be dominated by the R_N and significantly influences the SEB. The intensity of solar radiation at the surface is a function of latitude and seasons, with topographic shading, slope, and aspect controlling the spatial distribution of solar radiation (Oerlemans and Klok 2002). The topographic shading occurs when the glacier surface is obscured by the sun's position and adjacent topography. This uncertainty affects the glacier mass balance over the observation period. Furthermore, the accuracy of the parameterization of variables and mass balance from remote sensing data is greatly influenced by cloud coverage and haze. To overcome this limitation, only cloud-free images were considered for the glacier mass balance estimation.

4.7.8. SENSITIVITY ANALYSIS

In order to understand the uncertainties associated with the modeled glacier mass balance and the input variables, energy, and mass fluxes, we conducted a sensitivity analysis (Table 4.3). The sensitivity test was conducted over the 2015/16 data. When α is increased by 0.10, the value of mass balance is altered by 14.9% from the reference mass balance. Similarly, the mass balance decreases by 32.4%, when the SWI is increased by 5.0 W m^{-2}. This may be occurred due to the strong effect of α on radiation fluxes. Compared to this, the mass balance reduces by 6.1% from reference when the LWI increased by 5.0 W m^{-2}. Similarly, an increment of H_S and H_G does not affect the mass balance significantly. These mass fluxes make a possibly small contribution (5.0% for the H_S and 0.9% for the H_G) to the F_M available for melting as compared to R_N. However, H_l is more sensitive to the mass balance change as its effect in double energy loss in terms of H_l and sublimation. Accordingly, the mass balance is changed by $\pm$10.7% by an increase of 5.0 W m^{-2} H_l. Furthermore, increased/reduction in snowfall by 5.0 mm that results in the gain/loss of reference mass balance by 38.7%. The present study suggested that the total amount of energy available for melt mainly contributed by R_N (~75%) followed by H_S (15%) and H_l (8%) and H_G (2%) for the study area (Table 4.2). Analysis of relative contributors in energy balance components for melt was conducted at several other glaciers of the Himalayan region.

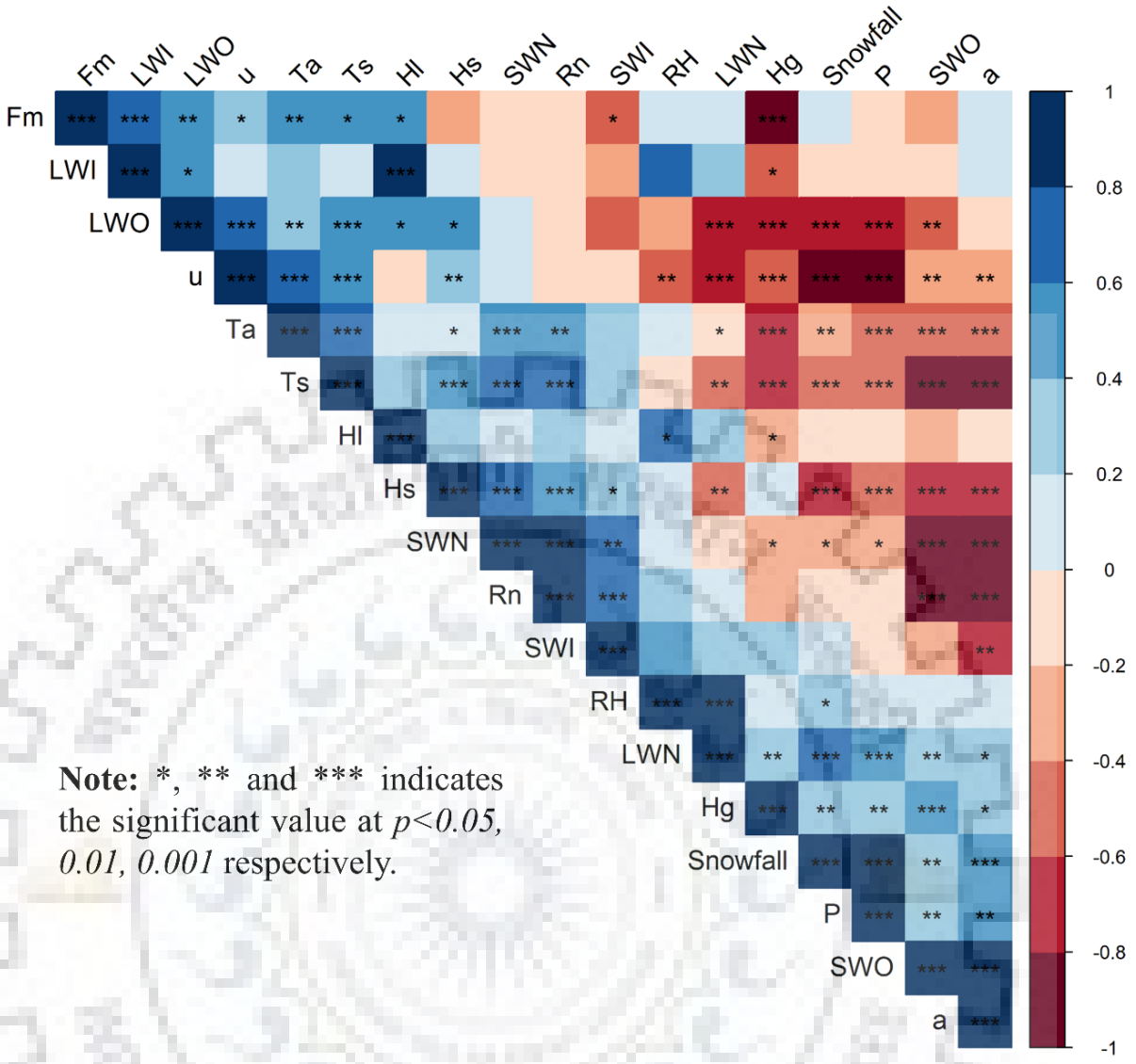

Figure 4.9. Correlation matrix between the annual glacier mass balance and the glacial-meteorological variables over six hydrological years (2013–2019).

Table 4.3. Results of sensitivity analysis of the model for the period of October 2015 to September 2016.

Input parameter	Reference case mass balance change (%)
α increased by 0.1	–14.9%
LWI increased by 5 W m^{-2}	6.1%
SWI increased by 5 W m^{-2}	–32.4%
H_l increased by 5 W m^{-2}	–10.7%
Snowfall increased by 5mm	38.7%

A study was carried out on the AX010 glacier of the Central Himalayas during 25 May – 25 September 1978, which concluded 85% contribution from R_N followed by H_S (10%) and H_l (5%)

at an elevation of 4960 m a.s.l. (Kayastha et al. 1999). Similarly, Azam et al. (2014a) observed that the energy balance over the Chhota Shigri glacier from 8 July to 5 September 2013 revealed that about 80% contribution of R_N, whereas H_S and H_l fluxes contributions were found to be 13% and 5%, respectively, at an elevation of 4670 m a.s.l. Also, a study conducted in the Glacier Parlung No. 4 of Southeast Tibetan Plateau from 21 May to 8 Sep 2009 estimated the 86% contribution of R_N followed by H_S (16%) and H_l (–1%) fluxes at an elevation of 4800 m a.s.l. (Yang et al. 2011). Another study from Zhadang glacier (Central Tibetan Plateau) revealed that radiation components contributed 82% of energy to F_M for the observation period 4 October 2009 – 15 September 2011 (Zhang et al. 2013). This was followed by 10% and 6% contributions of H_S and H_l fluxes, respectively. For the observation period 2011–2017 in the Yala glacier (Langtang Valley, Nepal), the percentage contribution of radiation to F_M ranges from 61% to 66% for the stake positions up to 5358 m a.s.l. (Acharya and Kayastha 2018). Similarly, heat conduction flux of 2% was indicated for the Zhadang Glacier and Chhota Shigri glacier with –1% for the Parlung No.4 Glacier ablation zone over the different observational periods.

4.8. CONCLUSIONS

In the Indian Himalayas, the availability of in-situ meteorological observation data is scarce, and the majority of available data are for a short duration. To overcome this limitation, a spatially distributed model of energy and mass balance fluxes was developed using the remote sensing and reanalysis data for eight selected glaciers of the Chandra basin for the period 2013–2019 hydrological years. The melting rate of the glacier was calculated from the F_M available at the surface. Since the selected glaciers are located between the high mountainous, we derived the T_a spatially using the multivariate statistical approach. The estimated results were calibrated/validated with the in-situ observations. The modeled T_a indicates a relative error of 0.02-0.05 ºC with the observed data. Also, the differences between the modeled and observed radiation fluxes were < 10.0 W m^{-2}. The amount of snow accumulation revealed discrepancies with the measured data because of the snowfall parameterization scheme is intricate as it depends on the local topography and climatic conditions. Overall, it was suggested that the model had performed well with the observation data.

Our study demonstrates that the Chandra basin glaciers were losing their mass rapidly, with a mean annual mass balance of -0.59 ± 0.12 m w. e. a^{-1} during 2013–2019. The study revealed that the maximum amount of F_M available for melt was observed during the summer season while the small or negligible amount of melt contributed for the winter season. However, the R_N is the

main source of energy which contributes about 75% of energy to F_M whereas H_S, H_l, and H_G fluxes shared 15%, 8%, and 2%, respectively.

The proposed model is useful for investigating the spatial pattern of energy and mass balance fluxes. The model results indicated that the SWN was highly variable at the glacier surface, with a maximum in the lower elevation zone and a minimum in the upper zone due to the higher α value above the snow line. It was also noted that the effect of topography and cloud cover would lead to a decrease in mass balance. Therefore, it is essential to account for the topographic effect on shortwave radiation for calculating mass balance. For this reason, slope, aspect, declination, inclination, latitude, and hour angle were considered for the estimation of SWI. The sensitivity analysis of energy balance components with the mass balance indicates that the mass balance is highly sensitive to α, and SWN. However, the mass balance was less sensitive to RH and other components.

In a future perspective, this proposed mass balance model will be useful for glacier-wide energy and mass balance at local as well as basinal scale. The utility of remote sensing data would overcome the data scarcity in the upper reaches of the Himalayan region. This model also provides a better understanding related to the future water supply in the downstream as well as the upstream region. Lastly, this spatial mass balance model will help in the reconstruction of historical and future projections of the glacier mass balance data.

CHAPTER 5

MONITORING GLACIER RETREAT/ADVANCE BY USING GEODETIC MASS BALANCE METHOD AND ITS IMPLICATION ON GLACIER HEALTH

5.1. INTRODUCTION

The Himalayan region is one of the largest mountain glacier systems outside the polar region, widespread from the Karakoram to the eastern Himalayas, covering a length of 2000km (Kääb et al. 2012). It is not only important for socio-economic aspects but also for downstream livelihoods for which glaciers act as a perennial source of freshwater (Kaser et al. 2010). Also, the Himalayan region act as a 'climatic barrier' between Central Asia and India; therefore, the glaciers of this region are the sensitive indicators to climate change (Kääb et al. 2012). Moreover, the Himalayan glaciers have gained interest across the world (Singh et al. 2011; Wester et al. 2019) because of their accelerating glacier mass loss that could potentially impact the runoff of glacier-fed rivers and then contribute to global sea-level rise (Scherler et al. 2011). Therefore, monitoring glacier characteristics and their associated changes are important using meteorological and glaciological observations (Farinotti et al. 2020b). However, only about 24 glaciers were monitored using the conventional methods (in-situ observations) that cover < 1% of the total glacierized area of the Himalayan region (Bolch et al. 2012). Moreover, such in-situ measurements of glacier changes in the Himalayan region are challenging due to complex topography and transboundary conditions (Mandal et al. 2020).

To overcome such limitations, the remote sensing data enables the monitoring of glacier changes at spatial and temporal scales. Numerous authors have already utilized remote sensing data for the mass budget estimation at a regional scale (Gardelle et al., 2013; Kumar et al., 2019; Wang et al., 2021) to local scale (Azam et al. 2014b; Vincent et al. 2018; Mandal et al. 2020). A glacier's mass budget helps to provide insight into mass gain or loss over a certain period; however, other glacier characteristics employed include the direction of glacier moving (retreating), hotspot/coldspot region on the glacier surface, and zone wise glacier movement. Several authors have quantified the glacier velocity (Heid and Kääb 2012; Tiwari et al. 2014; Shukla and Garg 2020), ice thickness (Huss and Farinotti 2012; Gantayat et al. 2014), glacier areal changes (Patel et al. 2019), and their volume estimation (Sattar et al. 2019; Pandit and Ramsankaran 2020) over different Himalayan glaciers.

To quantify the glacier surface velocity, some authors have utilized the conventional stake based methods (Ramanathan, 2011; Azam et al., 2012; Patel et al., 2021b), while many authors have used remote sensing data using the automatic sub-pixel correlation techniques (Coregistration of Optically Sensed Images and Correlation (COSI-Corr)) (Garg et al. 2017; Kaushik et al. 2020; Shukla and Garg 2020). In addition, numerous other surface velocity methods were available and applied to the Himalayan glaciers (Patel et al., 2017; Robson et al., 2018). In this study, we have utilized the COSI-Corr method for surface velocity estimation because it demonstrated higher accuracy and robustness than other sub-pixel correlation methods over the Himalayan glaciers and offered longer-term observations (Sahu and Gupta 2019; Sattar et al. 2019).

5.2. RESEARCH QUESTIONS

- **How is the glacier feature changing with time over the selected glaciers?** Are the glacier clean ice and debris coverage changed? If any, what is the contribution of surface temperature in that particular year?
- **What factors controlled the glacier surface velocity of the study area?** What are the forcing mechanisms responsible for glacier's higher velocity in the ablation zone? And how do they affect the ice thickness of the selected glaciers?
- **How does a long-term geodetic mass balance vary at the locale scale?** Is any significant change in mass observed during the study period? How is the volume of the glaciers changed over the period? What are the likely implications of glacier health and even the sensitivity of climate change?

5.3. OBJECTIVES

- Quantification of the variability of glacier wide features classification and their shift in isotherm line based on Land Surface Temperature
- Analyzing the multi-temporal satellite data for calculating the surface velocities using the sub-pixel correlation technique and their ice thickness
- Analyzing the locale scale glacier mass balance using the geodetic method and its volume change
- Assessing the uncertainties associated with glacier surface velocity and sensitivity of controlling variables related to ice thickness

5.4. STUDY AREA

The studied glaciers, i.e., Sutri Dhaka (32° 20′29′′N and 77° 34′57′′E) and Batal (32° 22′49′′N and 77° 32′05′′E) glaciers, lies in the Chandra river basin (one of the tributaries of Indus river system), western Himalayas (Figure 5.1). The selected glaciers are valley-type glaciers, oriented in the North-East direction for the ablation zone while the accumulation zone in the North for Sutri Dhaka and North-East for the Batal glaciers. The overall elevation of the selected glaciers ranged from ~4280 to 6200m above sea level (a.s.l.) based on Shuttle Radar Topographic Mission (SRTM) Digital Elevation Model (DEM) version 4.0.

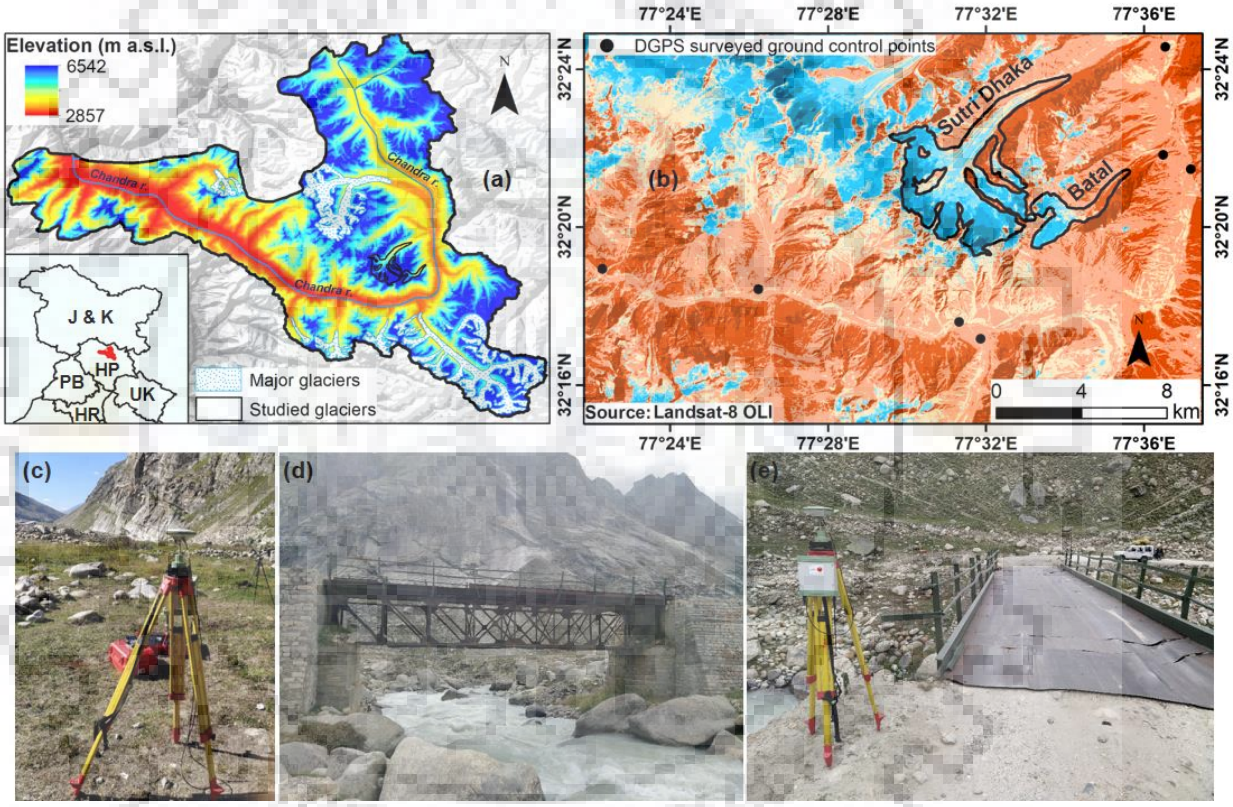

Figure 5.1. (a) Location map of the Chandra river basin and its major glaciers (b) location map of selected glaciers used in this study with Digital Global Positioning System (DGPS) surveyed locations (c-d), and some pictorial view of the field photographs of Ground Control Points (GCPs) collected during the field campaign during 22 – 30 September 2019.

According to the Geological Survey of India (GSI) inventory, the Sutri Dhaka glacier was identified with number IN 5Q212 12 058 and Batal glacier as IN 5Q212 12 054 (Sangewar and Shukla 2009). The Sutri Dhaka and Batal glaciers cover an area of 20.4 km^2 and 4.1 km^2, respectively based on the Randolph Glacier Inventory (RGI) 6.0 outline (RGI Consortium 2017). The total length of the Sutri Dhaka and Batal glaciers are 11.0 km and 6.6 km, and the mean ice

thickness is 100m and 30m, respectively (Sharma et al. 2016). The meltwater of the Batal and Sutri Dhaka glaciers meet the Chandra River from the snout at ~1.5 km and ~3.5 km, respectively. These two glaciers have similar climatic conditions and orientations, despite having varying melt conditions by controlling debris thickness over the glacier surface (Sharma et al. 2016).

Both the glaciers are situated in the northern limits of the zone influenced by the Indian Summer Monsoon (ISM) during summer and significant influence of mid-latitude western disturbances in the winter season (Sharma et al. 2016). However, the selected glaciers are dominantly influenced by western disturbances compared to ISM (Singh et al. 2019). This region also falls under the semi-arid zone with less vegetation cover due to rain shadow on the leeward side of the mountain (Pratap et al. 2019) and is highly sensitive to climate variation. The major criteria for selecting these two glaciers were their varying range of debris thickness and ablation melt rate.

5.5. DATA DESCRIPTION

This study used multispectral and multi-sensor satellite data with various multi-decadal DEMs to analyse the glacier changes and their characteristics. And field measurements were used for DEM generation as well as calibration/validation.

5.5.1. LANDSAT-8 OLI SATELLITE DATA

The Landsat-8 Operational Land Imager (OLI) datasets were acquired at a 30-m grid resolution of optical, 100-m (resampled at 30-m) of thermal, and 15-m of panchromatic bands in the selected glaciers. This data is freely available and downloadable from the United States Geological Survey (USGS) Earth Explorer (https://earthexplorer.usgs.gov/) at 16-day temporal resolution. Selection criteria for image acquisition, i.e., cloud cover < 5% or cloud-free, were applied for monitoring the glacier dynamics. The optical and thermal bands were utilized for glacier features classification along with isotherm delineation. Also, the panchromatic band was used for glacier surface velocity estimation. For this, individual ablation period (August to mid-October) images in each year were selected during 2013–2019 (25 September 2013, 28 September 2014, 30 August 2015, 03 October 2016, 20 September 2017, 22 August 2018, and 26 September 2019).

5.5.2. CARTOSAT-1 SATELLITE DATA

Cartosat-1 stereo pair data was obtained with a 2.5-m spatial resolution and 10-bit radiometric resolution, which offers along-track stereo pair data acquisition with a base-to-height ratio of 0.62 (Kumar et al. 2018b). This data has a geolocation accuracy of ~150-m without a local Ground Control Point (GCP) over the study area. However, the absolute accuracy of the DEM was enhanced with a value of ~20m by the use of the GCP points. This study includes the data for the ablation period (28 September 2009) with less cloud coverage.

5.5.3. ASTER DEM

This study utilized the AST14DMO product of Advanced Spaceborne Thermal Emission and Reflection Radiometer (ASTER) orthorectified DEM version 003, retrieved from https://search.earthdata.nasa.gov/. These data cover an area of 60 × 60 km that comprises an orthorectified image of each spectral band and DEM with a horizontal resolution of 30-m. This derived DEM was generated from the raw ASTER images by the Land Processes Distributed Active Archive Centre (LPDAAC) using the orbital ancillary data without GCP. In this study, we have acquired DEM for the ablation period **(**20 September 2020**)**, covering the selected glaciers in a tile. The necessary preprocessing was applied over the data for elevation differencing explained by Berthier *et al.* (2016).

5.5.4. SRTM DEM

The C-band and X-band radar frequencies were captured by the SRTM during 11 – 22 February 2000 (11-day mission) (Krieger et al., 2007). The SRTM-X band was processed by German Space Agency (DLR), while C-band data was distributed and processed by Jet Propulsion Laboratory (JPL). However, SRTM-C provides global coverage of the dataset while SRTM-X does not. Therefore, in this study, we have utilized the interpolated and void filled SRTM-C DEM version 4 for reliable estimation of elevation data which is freely available from https://cgiarcsi.community/data/srtm-90m-digital-elevation-database-v4-1/ with an absolute vertical accuracy of ±16 m while a relative accuracy was ±6 m over ~90% of the data (Czubski et al. 2013; Kumar et al. 2018b).

5.5.5. NASA ITS_LIVE

The Inter-Mission Time Series of Land Ice Velocity and Elevation (ITS_LIVE) project provides global low-latency measurements of glacier and ice sheet surface velocity and elevation change at 240-m spatial and a high temporal resolution (Gardner et al. 2019). This product is a set of

regional compilations of annual mean surface velocities for major glacier-covered regions from 1985 to 2018, subject to image availability and quality. The surface velocities are measured from Landsat 4, 5, 7, and 8 imagery based on the auto- Repeat Image Feature Tracking (RIFT) algorithms (Gardner et al. 2018). Data scarcity and/or low radiometric quality are significant limiting factors for many regions in the earlier product. In this study, we have used ITS_LIVE velocities from 2013 to 2018 for comparing the estimated velocity from Landsat-8 data. For comparison, the Landsat-8 based estimated velocities are resampled to match the spatial resolution of ITS_LIVE velocities. The product is available at the Jet Propulsion Laboratory (JPL) National Aeronautics and Space Administration (NASA) (https://its-live.jpl.nasa.gov/).

5.5.6. STAKE MEASUREMENTS

The stake-based surface velocity was measured from the Differential Global Positioning System (DGPS) survey carried out by National Centre for Polar and Ocean Research (NCPOR), Goa, India, during 2017/18. A total of 33 points for Sutri Dhaka and 8 locations in the Batal glacier were utilized to assess the performance of the estimated surface velocity against in-situ observations over the selected glaciers.

5.5.7. FIELD DATA

A field survey was conducted over the Chandra basin from 22 – 30 September 2019 to collect the local GCP points. This data was taken from the Leica DGPS for reliable estimation of elevation information. A total of 12 GCPs were collected over the permanent features such as bridges, guest houses, villages, etc. (Figure 5.1).

5.6. METHODOLOGY

This section describes the remote sensing data processing to assess the changing pattern of glaciers over time. Preprocessing of data is required to minimize the dimensionality error and to further enhance the data quality. This study quantified different glacier aspects, i.e., feature classification, glacier velocity, ice thickness, geodetic approach-based mass balance, and total volume change over the selected glaciers. A detailed description of each approach and its related consideration is given below:

5.6.1. GLACIER FEATURE MAPPING AND ISOTHERM DELINEATION

A semi-automatic approach was applied for glacier feature classification using multispectral Landsat data for the period 2013–2019. The shortwave infrared (SWIR) and a green band of

Landsat data were utilized for NDSI calculation due to high contrast over the tongue of a glacier. A threshold of NDSI ≥ 0.55 was used to delineate the clean ice feature over the glacier surface (Silverio and Jaquet 2005; Patel et al. 2019). Then, we have classified the remaining pixel by the use of Landsat thermal data. The Land Surface Temperature (LST) was derived from the thermal band using the emissivity approach, previously explained by several authors (Anul Haq et al. 2012; Ullah et al. 2019). Further, an average threshold of LST ≥ 3.2°C was used over the LST map in order to derive the debris pixel. The threshold value was considered based on the previous studies carried out over the Himalayan glaciers (Bhardwaj et al. 2014; Patel et al. 2019). And the value of the threshold was also highly dependent upon the date of image acquisition. After clean ice and debris classification, the remaining unclassified pixels were recognized as Ice Mixed with Debris (IMD).

5.6.2. GLACIER SURFACE VELOCITY ESTIMATION

The surface velocity was estimated by the application of an automatic cross-correlation approach to acquire the decadal characteristics of glacier change. For this, a well-established and known feature tracking toolbox, i.e., COSI-Corr (Scherler et al. 2008), was used to assess the glacier surface displacement using Landsat-8 OLI data over the Sutri Dhaka and Batal glaciers during 2013–2019. Several authors previously used this technique for glacier velocity estimation over the Himalayan region (Tiwari et al. 2014; Shukla and Garg 2020; Wu et al. 2020). Before assessing the surface displacement, the panchromatic band of Landsat data was co-registered with the common reference data set; however, there is no need for orthorectification in this data because the pan band is already orthorectified (Sahu and Gupta 2019). It was observed that this step reduces the misalignment of less than a single pixel for any pair of images (Wu et al. 2020). Then, the sub-pixel cross-correlation approach was applied at multi-temporal image pairs. It can be achieved by considering the optimum value of window size at 64 × 64 for initial and 32 × 32 for the final between master and slave images. We have considered a step size of 2 and run it for five iterative processes. Finally, the correlation between the pre- and post- images was obtained, which comprises displacement in North/South and East/West direction along with Signal-to-Noise Ratio (SNR). The final magnitude of glacier surface displacement was calculated by combining the horizontal ground displacement is expressed by Equation 5.1.

$$D = \sqrt[2]{D_{North/south}^2 + D_{East/west}^2} \qquad \textbf{Eq. 5.1}$$

After that, the value of SNR < 0.9 was used to eliminate the extreme values before the estimation of surface velocity. Many authors previously used this threshold value for improving the accuracy

of surface displacement (Quincey et al. 2015; Wu et al. 2020). Finally, the surface velocity map was generated by normalizing the displacement in 365-days for annual analysis (expressed in m yr^{-1}).

5.6.3. GLACIER ICE THICKNESS

The present study includes the calculation of ice thickness using Glen's flow laws during 2013–2019, as expressed by the following Equation 5.2 (Cuffey and Paterson 2010):

$$H = \sqrt[4]{\frac{1.5\ U_S}{A\ (f\ \rho\ g \sin\alpha)^3}} \qquad \textbf{Eq. 5.2}$$

Where, H indicates the ice thickness, A denotes the creep parameter that is highly dependent on ice temperature, grain size, and water content ($A = 2.4 \times 10^{-24}\ s^{-1}Pa^{-3}$ was considered for temperate glaciers). U_s is the surface velocity (obtained from COSI-Corr toolbox), ρ is the density of ice (ρ = 900 kg m^{-3}), g is the acceleration due to gravity (g = 9.8 m s^{-1}), α is the surface slope (in degree), and f is the shape factor that can vary from 0.6 to 1.0. Based on the literature for the Himalayan region, the value of the shape factor was considered as 0.8 (Gantayat et al. 2014; Sattar et al. 2019). And the slope was estimated using the ASTER DEM elevation contours at 100-m intervals. This method was previously used by several authors for ice thickness estimation (Farinotti et al. 2009; Huss and Farinotti, 2012; Sattar et al. 2019; Wu et al. 2020) across different glaciers of the world. The method for ice thickness is widely used due to its simplicity in concept as well as in application.

5.6.4. GEODETIC-DERIVED MASS BALANCE CALCULATION

This study comprises the utilization of various DEM extracted from different sources to quantify the elevation change over a period of time. For this, we have taken Cartosat-1 images for DEM generation using the Leica Photogrammetry Suite (LPS) toolbox inbuilt in the latest version of ERDAS Imagine 9 that covered the area of Sutri Dhaka and Batal glaciers. For that, a project file was created with datum (World Geodetic System 84 (WGS84)) and projection as Universal Transverse Mercator 43North (UTM 43N). The Cartosat-1 data includes stereo pair images ('Fore' and 'Aft') with supplied Rational Polynomial Coefficient (RPC) files used for DEM preparation. The acquired RPC file and field-collected Ground Control Points (GCPs) were collectively utilized in order to maintain the Root Mean Square Error (RMSE) less than 1.5m in the X and Y direction. After the automatic tie point generation, the image was orthorectified, and then DEM was created for the selected region.

All the DEMs were projected to a common reference system, and then the selected DEMs were co-registered with the analytical approach discussed by several authors (Kumar et al. 2019; Kumar et al. 2018). It was suggested that the horizontal shifts between DEMs may lower the standard deviation of their elevation difference. The elevation difference was modeled by subtracting the reference (SRTM) DEM with the slave by the relationship explained by Kumar et al. (2018) over the Patsio glacier. The elevation difference was measured after DEM correction and averaged within a 100-m elevation interval. The average elevation change was then multiplied by the area and density to calculate the mass balance over the entire glacier surface.

The DEM differencing was considered to be a benchmark measurement and further used to estimate the volume change (ΔV) over the observational period. The pixel-wise volume change was measured by multiplying the area of grid resolution with elevation change. For example, the ΔV can be measured by Equation 5.3:

$$\Delta V = (Elevation_{2009} - Elevation_{2000}) \times Area_{Grid\ resolution} \quad \textbf{Eq. 5.3}$$

5.7. RESULTS AND DISCUSSION

5.7.1. MAPPING OF GLACIER FEATURES

Monitoring of glacio-morphometric features and their changing pattern are essential in order to understand the impact of a warming climate on the glacier surface. Therefore, we have utilized Landsat-8 data of the ablation period to classify the glacier feature into three classes: clean ice, ice mixed with debris, and debris-covered at the spatio-temporal scale during 2013–2019 (Figure 5.2). The classified glacier features illustrate that the clean ice shows a heterogeneous pattern across the selected glaciers, which attained higher value in 2017 and lower in 2016. This changing pattern of clean ice may have occurred due to the fluctuations in snow accumulation and the prolonged melting of the glacier during the period.

Randhawa et al. (2016) have reported a significant reduction in snow cover area (SCA) during 2015/16 compared to 2010–2014 over the Chandra River basin. In the broader context, Blunden and Arndt (2017) have highlighted that 2016 was the 37th consecutive year from 1980 to 2016 for overall alpine glacier retreat across the globe. Additionally, a reduction in SCA and its duration was observed by Dharpure et al. (2020) in 2016 over the Chenab river basin. On the other hand, the year 2017 shows a reduced mean ablation rate (especially in September) on the clean ice over the Chhota Shigri glacier located in the same catchment (Mandal et al. 2020). Also,

Pratap et al. (2019) have estimated a lower negative value of mass balance in 2016/17 compared to 2015/16 over the Sutri Dhaka glacier.

Other than this, the presence of debris in glacier beds was increasing during the selected period. The majority of the debris was obtained near the snout and also in the margins of the glaciers. This expansion of debris on the glacier surface may lead to a higher melting rate only when the debris thickness is less than or equal to 2 cm (Pratap et al. 2015; Östrem 2017). Sharma et al. (2016) have mapped the distribution of debris in the Sutri Dhaka and Batal glaciers. They have revealed thick debris over the terminus of both the glacier, whereas thin debris was detected over the trunk of the Batal glacier. Therefore, the melting in the glacier trunk was higher in the Batal glacier than in the Sutri Dhaka. Our results also demonstrate that the pattern of debris significantly increased from the terminus towards the trunk of the glacier. Patel et al. (2016) have observed that the ablation zone of the Batal glacier was 90% covered with debris, out of which 35% was thick debris (> 10 cm).

A zero-degree isotherm was plotted using the time-series ablation data (LST) during 2013–2019 in order to assess the ablation potential over the glacier surface (Figure 5.3). The isotherm line was shifted towards the higher elevation with a maximum shift in 2018 with respect to 2013 in both the glaciers. This indicates that the glacier area above the isotherm was considered the accumulation zone where the snow remains persistent throughout the year (Misra et al. 2020). Therefore, the shifting isotherm indicates that the accumulation zone of these two selected glaciers was continuously changing over the period. Dhar et al. (2020) have observed that the glaciers of the Lahaul and Spiti region experienced a significant rise in elevation of Equilibrium Line Altitude (ELA) during 1980–2011.

The combined results of glacier feature classification and isotherms illustrate that the varying distribution of glacier features was closely related to the thickness of debris and climatic variability. It was also found that the Sutri Dhaka glacier shows a higher ablation rate in the previous studies (Patel et al. 2016; Pratap et al. 2019), which may be caused due to the climate variation as well as the debris thickness.

5.7.2. SURFACE VELOCITY AND ICE THICKNESS

5.7.2.1. Surface velocity

Time-series glacier surface velocities were estimated using Landsat-8 data of the ablation period during 2013–2019 (Figure 5.4).

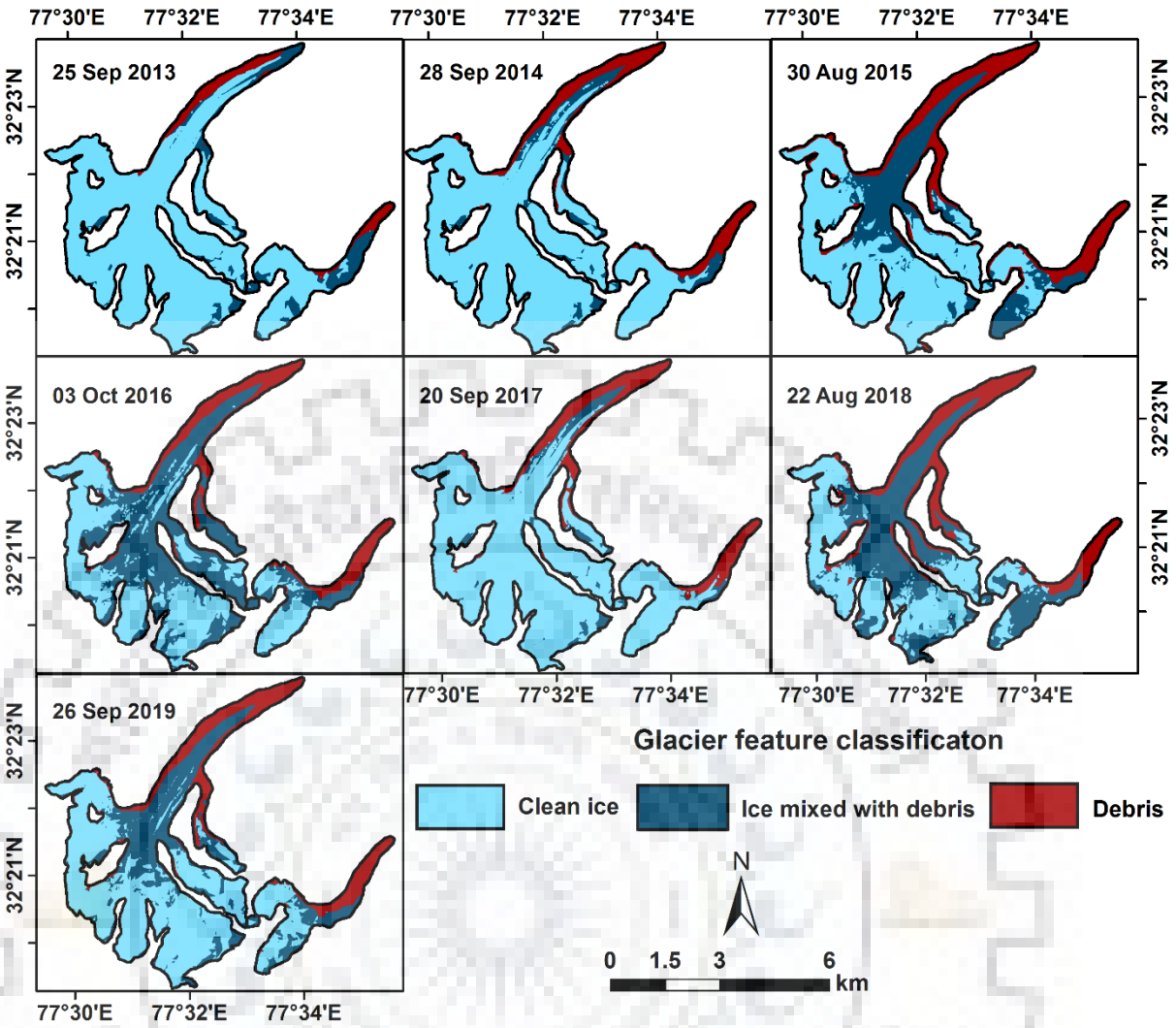

Figure 5.2. Year-wise spatial glacier features classification using multispectral data (Landsat-8) for the period 2013–2019.

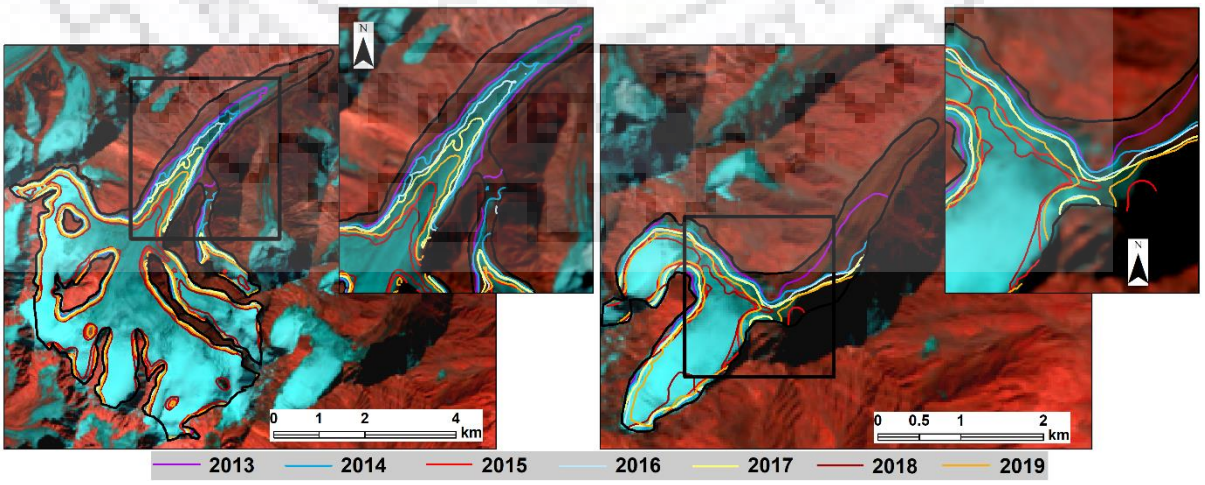

Figure 5.3. Glacier-wide yearly 0°C isotherms from 2013 to 2019 over the selected glaciers.

Results demonstrated a progressively increasing surface velocity over the central part of the Sutri Dhaka glacier, and a small pocket of high/low velocity was found in the Batal glacier in each selected year. The average velocity ranged from ~0 to 70 m yr^{-1} with a minimum in the accumulation zone while abruptly higher values in the ablation zone, and it slowly decreases over the snout. The intensity of glacier retreat was maximum in Sutri Dhaka and minimum in Batal glacier. Such a reduced surface velocity of the Batal glacier may have been caused by thick debris distribution in the ablation zone and because it has a comparatively narrow valley than the Sutri Dhaka glacier. The presence of thick debris in the glacier surface can control the glacier surface velocity, as it insulates the ice surface to be exposed to radiation (Banerjee 2017; Rounce et al. 2021). The higher value of surface velocity was attained in 2016/17, although lower in 2013/14. Patel et al. (2021b) have measured the surface velocity of Sutri Dhaka and Batal glaciers for the period 2017–2018, which shows an average velocity of 52.6 ± 17.3 m yr^{-1} and 6.2 ± 2.9 m yr^{-1}, respectively. Similarly, our results show a mean velocity of 43.9 ± 12.8 m yr^{-1} for the Sutri Dhaka and 5.68 ± 3.8 m yr^{-1} for the Batal glacier during the same observation period. Both the glaciers have experienced a lower surface velocity near the terminus, while the ablation zone has a comparative higher velocity.

Our study also indicates that when all tributaries of the Sutri Dhaka glacier converge at the trunk of the glacier, then the surface velocity is suddenly increased. This convergence of the tributaries may create shear stress and strain over the main channel as well as cause deformation, which further impacts the direction and velocity of the glacial flow (Hewitt 2007; Paul 2015). Our observation about the Sutri Dhaka glacier was well-matched with the finding of Patel et al. (2021b). The no data (pixel containing zero/error values) occurred by removing higher SNR values from the displacement images of each image pair. The higher SNR was mainly caused due to the presence of cloud cover, haze, and shadow over the terrain (Dehecq et al. 2015), which hindered the velocity information (Sahu and Gupta 2020). Therefore, we have utilized the elevation data to reduce the shadow effect and enhance the data quality.

The cross-sectional profile on the glacier surface was drawn to assess the velocity change with respect to distance (Figure 5.4). The first profile was marked near the terminus, while the other was in the ablation zone of the glaciers. The average velocity of both cross-sectional profiles in the Sutri Dhaka glacier ranged from ~2 to 35 m yr^{-1} with higher in the middle and lower along the lateral margins of the glacier. It was also noted that profile S2-S2´ experienced higher velocity than profile S1-S1´ with interannual variability over the observational period. In 2016/17, profile S2-S2´ showed a higher value after 2018/19, whereas it was lowest in profile 1.

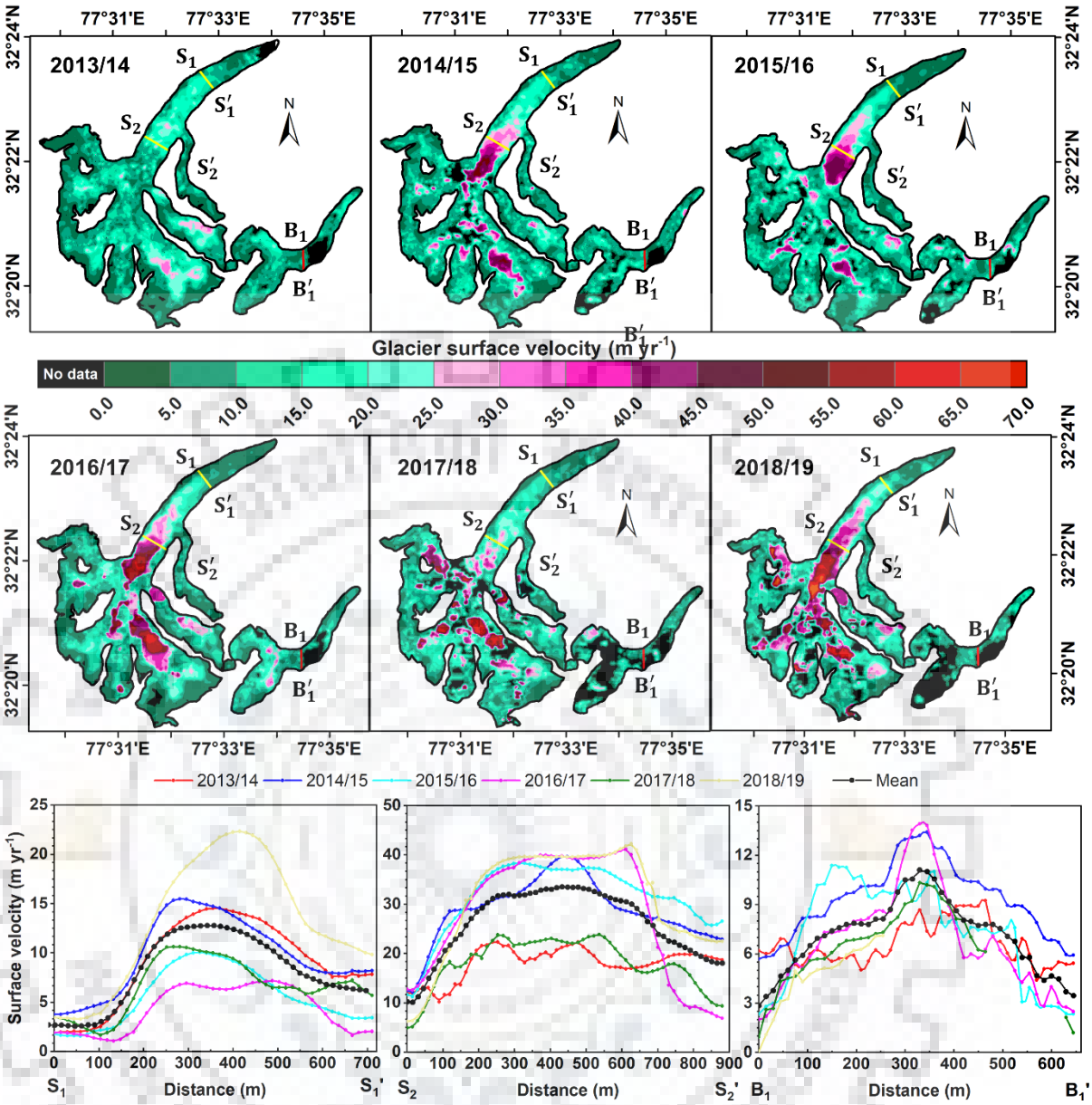

Figure 5.4. Spatio-temporal distribution of glacier surface velocity from 2013 to 2019 with cross-sectional profile over the glacier surface.

Similarly, the profile (B1-B1') of the Batal glacier indicates that the velocity was highly variable over the surface; however, maximum velocity was received at a distance of ~80-700 m (near the middle line) and minimum in the lateral margins of the glacier. A similar pattern of surface velocity in cross-sectional profiles was illustrated by several studies (Kraaijenbrink et al. 2016; Sun et al. 2017; Steiner et al. 2018). Overall, the cross-sectional profiles of both the glaciers follow a similar pattern with high and relatively constant in the middle portion of the profile; however dramatically reduced close to the glacier margins. This mainly occurred due to the basal sliding-type mechanism, which indicates that the ice flow regime is dominated by internal deformation. It follows a parabolic pattern, which was low initially and gradually increases from

margin to center. Therefore, it was noted by the visual evidence that the internal deformation influenced both glaciers compared to basal sliding.

5.7.2.2. Validation

5.7.2.2.1. With stake measurements

The DGPS collected stake locations were used to compare with the surface velocities derived from COSI-Corr over the selected glaciers for 2017/18 to assess the performance of estimated results against field observations. Results demonstrate that the estimated velocity was well-matched with the field measurements by a correlation of 0.92 and 0.89 at $p < 0.05$ for the Sutri Dhaka and Batal glaciers (Figure 5.5). The estimated velocity of the Sutri Dhaka glacier shows an underestimation with field observation data. It was also noted that the magnitude of the fluctuations in the Sutri Dhaka glacier was higher at the ablation stakes than those with accumulation area. This means that changes in observed and measured surface velocity using the COSI-Corr method, especially in the ablation stakes region, are well suited for understanding the glacier state and their reaction towards changing climate. A similar higher ablation/snout stake accuracy with remote sensing surface velocity was reported by Tiwari et al. (2014) over the Chhota Shigri glacier. In the Sutri Dhaka glacier, the stake-based and COSI-Corr estimated surface velocity shows a mean percentage change of 24.2 ± 10.7%; however, the majority of points (20 out of 33) indicate less than 15%. The percentage change in the Batal glacier was not studied because of limited stake data, as it was noticed by Ekström et al. (2018) that if the number of samples was less, then the robustness of percentage change may vary.

5.7.2.2.2. With ITS_LIVE

The estimated time-series of COSI-Corr derived surface velocity were also compared with the ITS_LIVE data product over the selected glaciers during 2013–2018 (Figure 5.6). Results demonstrate a significant correlation of 0.80 and 0.79 (at $p < 0.05$) between these two velocities for Sutri Dhaka and Batal glaciers, respectively. The peak and trough of the obtained results were well localized with the ITS_LIVE velocity data. The COSI-Corr result shows an underestimation for both the glaciers with ITS_LIVE data. An apparent underestimation of ITS_LIVE data against DGPS observation was revealed by Patel et al. (2021b) over 12 glaciers of the Chandra basin. They have also highlighted that the ITS_LIVE data shows a higher difference over the smaller glaciers, whereas it was lower for the larger glaciers. This difference in surface velocity may be occurred due to its coarser spatial resolution (240m). To reduce this difference, we have resampled the estimated velocity with the grid resolution of ITS_LIVE data before undertaking

the pixel-wise comparison. Moreover, this data was derived from the Landsat series by applying the image tracking method; therefore, it may be the reason for the well-matched comparison between these two datasets.

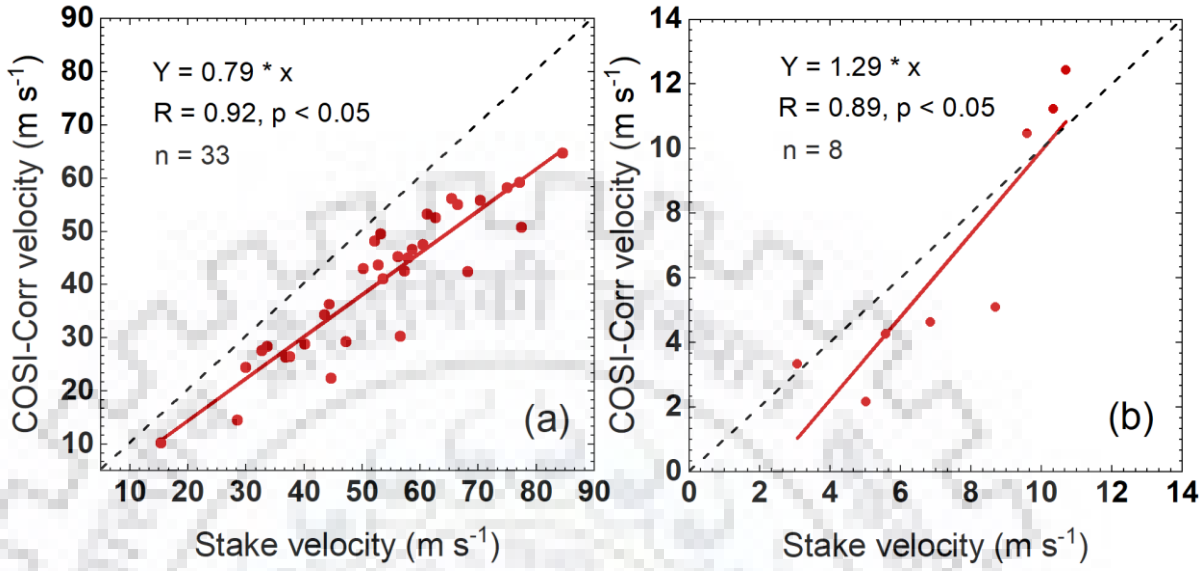

Figure 5.5. Scatter plots between stake measurements and COSI-Corr-based glacier surface velocity in the (a) Sutri Dhaka and (b) Batal glaciers.

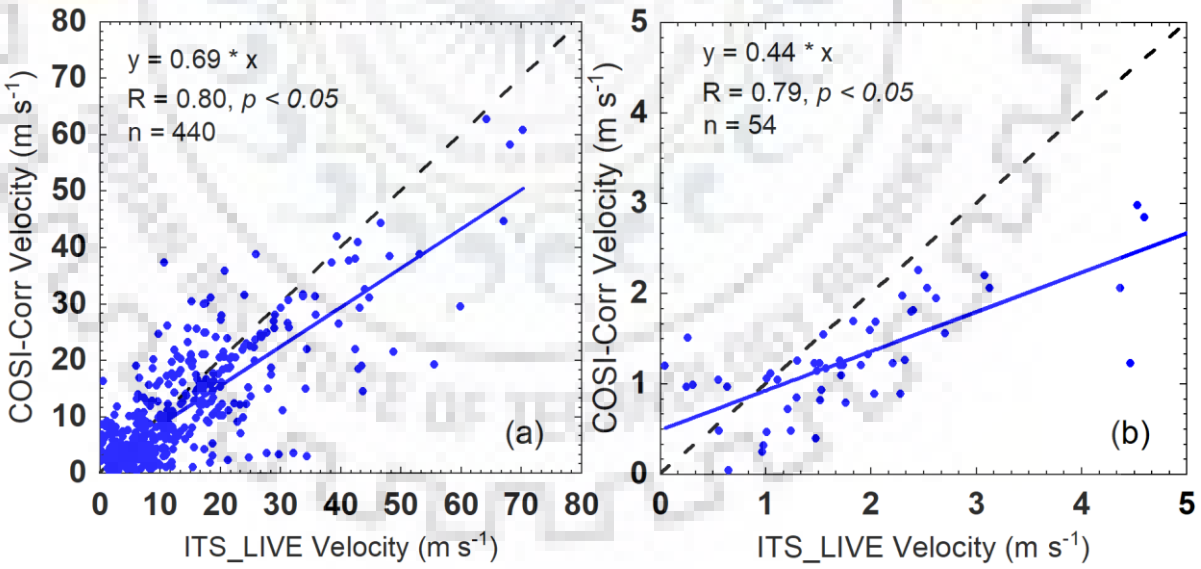

Figure 5.6. Scatter plots between ITS_LIVE and COSI-Corr-based glacier surface velocities in the (a) Sutri Dhaka and (b) Batal glaciers.

5.7.2.3. Variation in surface velocity based on terrain features

The surface velocity at different elevation zones was analyzed during 2013–2019 for monitoring the influence of altitude in changing velocity (Figure 5.7). Results demonstrate that the Sutri

Dhaka shows the maximum velocity in 4800–5000 m a.s.l. elevation zone, covering 11.9% of total glacier area, while it decreases when moving upwards and acquired minimum value in the upper elevation zone (6000–6200 m a.s.l.). Sam et al. (2018) have reported that the western Himalayas shows the higher velocity in the annual and melt period at an elevation between 4981 and 5271. Similarly, Wu et al. (2020) have experienced maximum velocity in the main trunk of the Kyagqen glacier with a range of altitude from 4800 to 5000 m a.s.l. They have also indicated that the middle elevation zones (4981–5271 m and 5271–5561 m a.s.l.) have considerably higher velocity for clean ice glaciers. On the other hand, the Batal glacier experienced maximum velocity in lower elevation, i.e., 4400–4600 m a.s.l. and minimum in 4800–5000 m a.s.l., covering 8.5% and 12.8% of the total glacier area, respectively. This indicates that the maximum velocity in the Sutri Dhaka is mainly controlled by elevation change, whereas local factors influence the Batal glacier velocity. The Batal glacier has peculiar features like detached accumulation area from the ablation zone as well as the thick debris in the ablation zone. Patel et al. (2021b) conducted a similar study that shows the surface velocity below 4700 m a.s.l for clean ice was lower than the debris-covered area.

The slope and aspect variations of the selected glaciers were examined using time-series surface velocity, which indicates that the maximum velocity was attained in 0-10° slope for the entire observational period except for 2017/18 and had a significant retreat in the South/Southwest direction over the Sutri Dhaka glacier. A similar slope pattern was observed by Singh et al., (2021a) over the glaciers of Dhauliganga, central Himalayas. In contrast, the Batal glacier experienced maximum velocity in the South/Southeast direction with a slope of > 40° across the entire period except for 2013/14 and 2015/16. A similar pattern of aspect and slope variation with surface velocity was previously illustrated by Sam et al. (2018) over the western Himalayas. It was also noticed that the South, Southeast, and southwest facing shows significant velocities than others. This probably occurred because these aspects are more prone to melting across the year, especially in the Himalayan context. Additionally, the south-facing was more susceptible to maximum snow accumulation and became more vulnerable for subsequent melting and directly received sun radiation for maximum time (Sam et al. 2018).

By analyzing the variability of surface velocity on terrain features, we can conclude that the aspect is a strong limiting factor for surface velocity change during the ablation period. It was also noticed that the aspect of higher elevation, which is not directly exposed to the sun, is not prone to high melting and may be driven by the dominance of deformational flow. On the other hand, the sun-facing aspect at all elevations can contribute to higher velocities, thus illustrating the significance of aspect on surface velocity as well as the melting. This analysis also

emphasizes that the surface velocity in each elevation zone may be controlled by the local factor that induces glacier melting and further contribute to glacier flows.

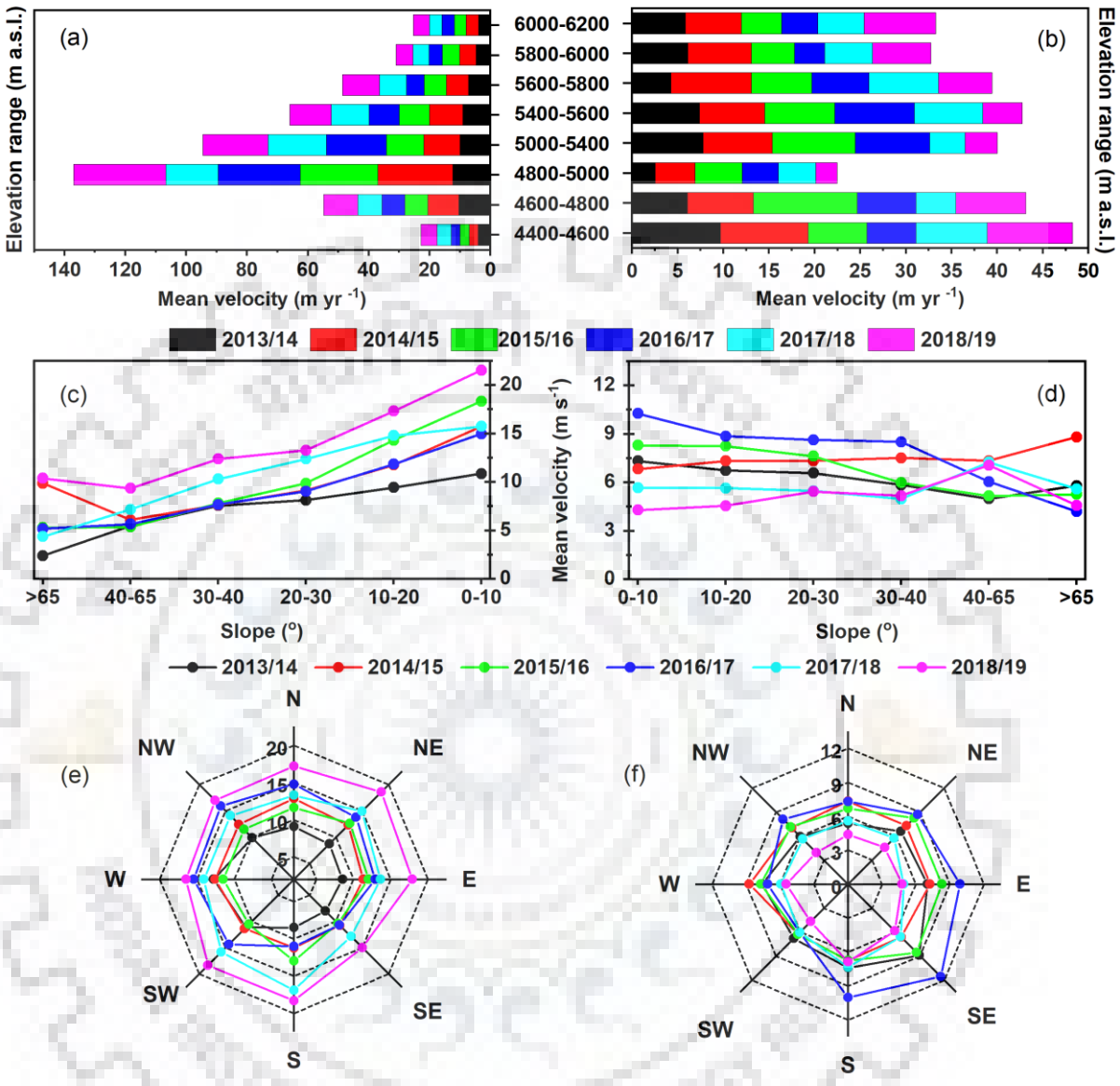

Figure 5.7. Temporal distribution of glacier surface velocity with topographical variables, (a-b) elevation, (c-d) slope, and (e-f) aspect over the Sutri Dhaka (left panel) and Batal glacier (right panel) from 2013 to 2019.

5.7.2.4. Glacier ice thickness

The spatio-temporal distribution of glacier ice thickness was quantified from 2013 to 2019 over the selected glaciers (Figure 5.8). The calculated mean ice thickness was found to be less than 250 m for the Sutri Dhaka and 180 m for the Batal glacier. It was also noted that the Batal glacier has localized pockets of high/low ice thickness across the glacier. In contrast, the Sutri Dhaka glacier observed a higher thickness in the trunk and a lower value at the snout of the glacier. This pattern of ice thickness was consistent with the modeled ice thickness (Zekollari et al. 2013;

Pandit and Ramsankaran 2020). Similarly, Wu et al. (2020) have indicated that the average ice thickness was less near the snout. It increases with altitude until ELA (or lower accumulation area), then decreases in the upper accumulation area. The years 2017/18 and 2018/19 had a higher uncertainty (no-data), mainly due to cloud presence in the 2018 image. The selection of cloud-free images was slightly difficult in the ablation period because the cloud coverage was higher in the summer than in the winter season (Sicart et al. 2016).

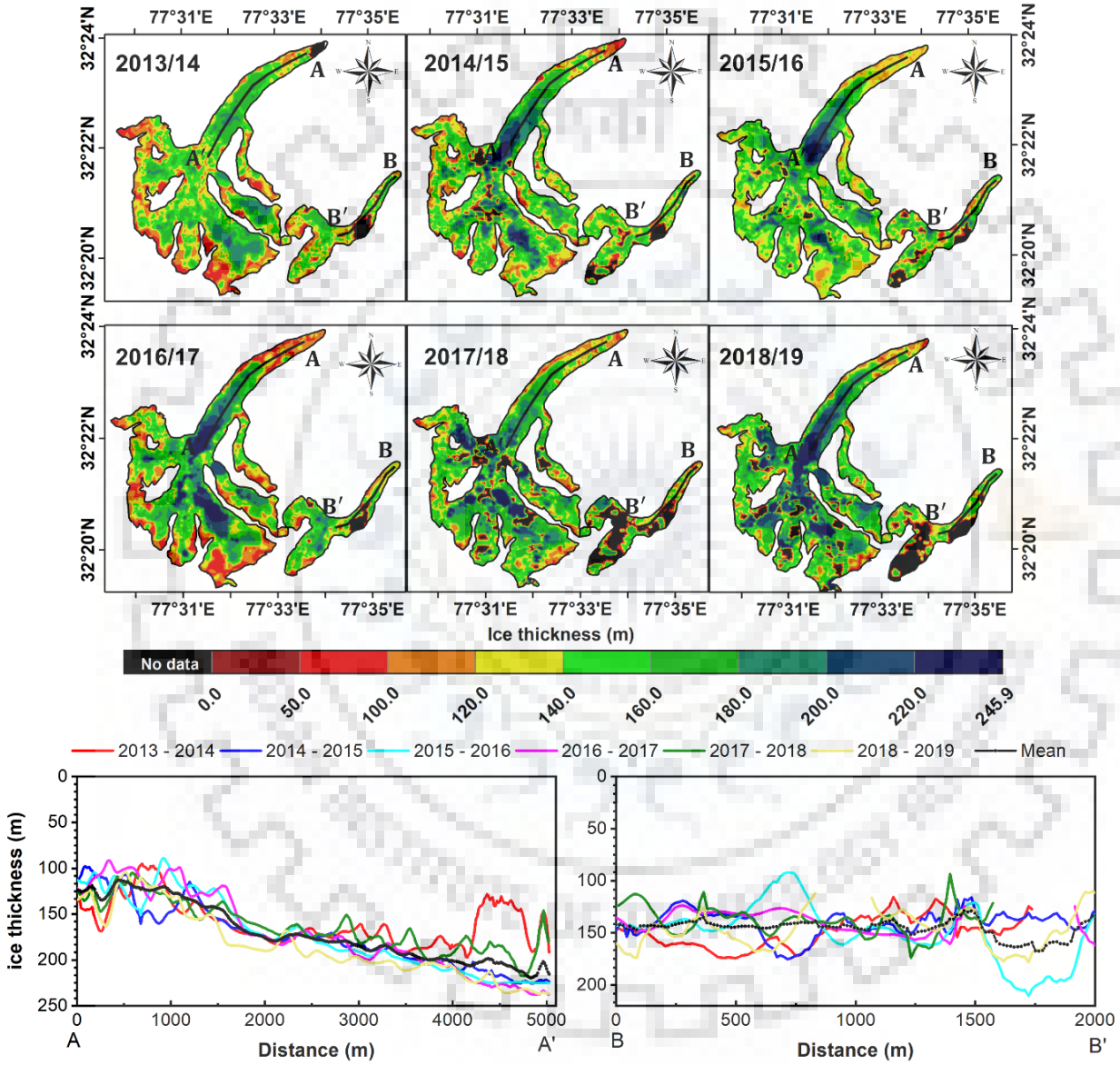

Figure 5.8. Spatial distribution of ice thickness and its longitudinal profiles over the Sutri Dhaka and Batal glaciers during 2013–2019.

The longitudinal profiles were created along the central line of the selected glaciers to quantify the lateral pattern of ice thickness over the glacier surface (Figure 5.8). In the Sutri Dhaka glacier, the ice thickness was increased when moving from snout (point A) towards the upper ablation

zone (A'). In contrast, the mean thickness profile of the Batal glacier was found highly variable with localized changes. This thickness pattern from snout to ablation may confirm that the selected glacier follows the ice thickness hypothesis, which was higher in the snout and lower in the accumulation zone. This higher ice thickness over the ablation may have occurred where the slope is smaller and critical shear stress develops, which piles up the snow and creates more ice (Cuffey and Paterson 2010).

5.7.3. GLACIER MASS BALANCE AND TOTAL VOLUME CHANGE

5.7.3.1. Glacier mass balance

Glacier-wide mass balance was calculated by the difference of co-registered DEMs (geodetic mass balance approach in two different periods (2000–2009 and 2009–2020). Results reveal a less negative mass balance (–0.03 ± 0.5 m w.e. yr^{-1}) and elevation change during 2000–2009 (Figure 5.9).

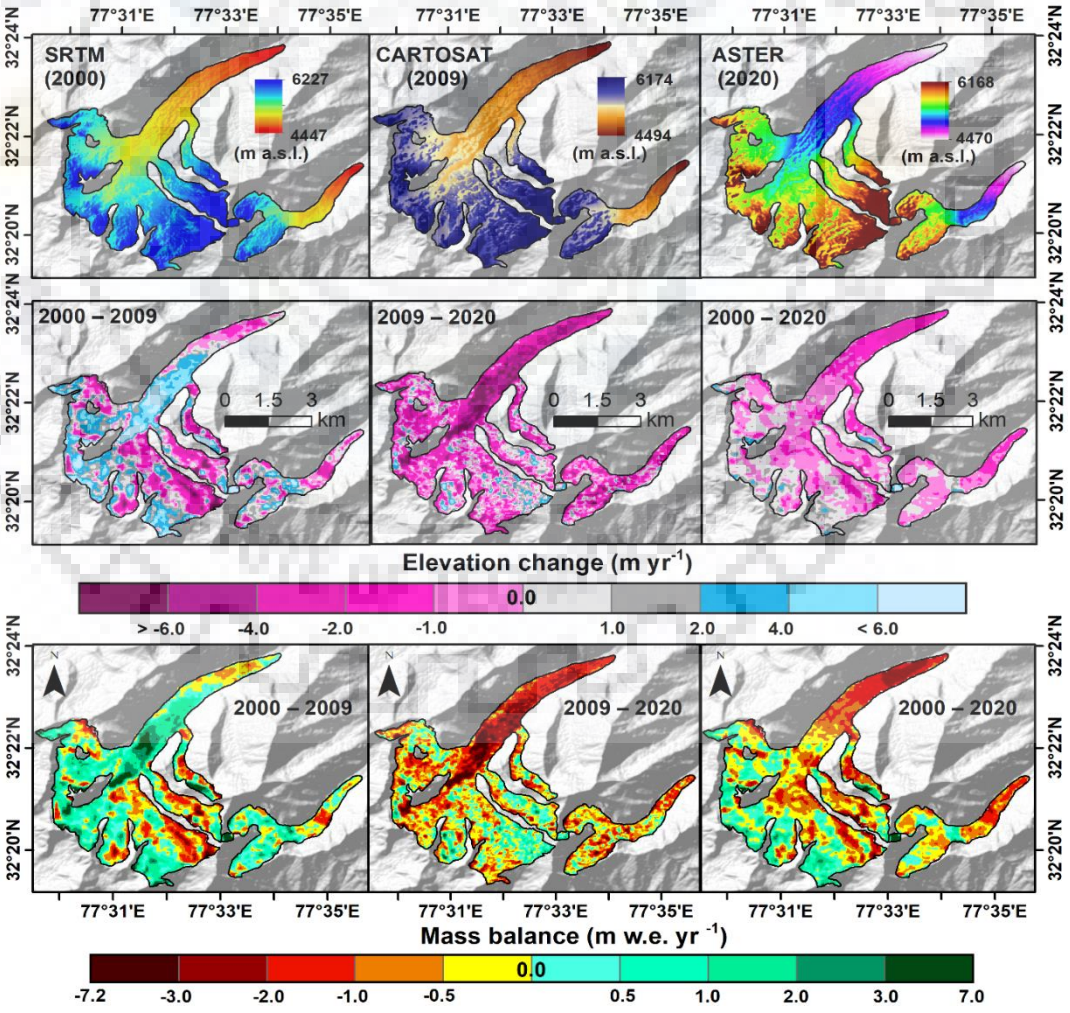

Figure 5.9. Spatial distribution of elevation change (middle) derived from various DEMs (top) and its geodetic mass balance (bottom) geodetic mass balance for two separate periods.

On the other hand, the average mass balance of these two glaciers had a mean value of –0.34 ± 0.14 m w.e. yr^{-1} during 2009–2020. These results were largely in line with previous studies that observed a mass loss ranging from –1.22 to 0.01 m w.e. between 1984 and 2012 over the Chandra basin glaciers (Tawde et al. 2017). They have also illustrated that the Sutri Dhaka and Batal glaciers come under the range of –0.60 to –0.40 m w.e. Tawde et al. (2016) have modeled the cumulative mass balance of –0.79 ± 0.34 m w.e. yr^{-1} for 12 selected glaciers in the Chandra basin from 1999/2000 to 2008/09. Also, Vincent et al. (2013) have experienced slight mass loss (–0.09 m w.e. yr^{-1}) between 1988 and 2010 over the Chhota Shigri glacier, which lies under the same basin and almost similar climatic conditions.

The negative elevation change had previously been reported by Ramsankaran et al. (2019) for 2000–2013. They have also observed that the specific mass balance rate of the Chandra basin glaciers varied from –0.83 ± 0.41 to –0.14 ± 0.07 m w.e. yr^{-1} with a mean of about –0.61 ± 0.29 m w.e. yr^{-1}. Similarly, in-situ-based mass balance estimation of the Sutri Dhaka and Batal glaciers also confirmed a –0.82 ± 0.17 m w.e. and –0.47 ± 0.10 m w.e. mass loss, respectively, from 2013 to 2017 (Sharma et al. 2020). In addition, the whole observation period (2000–2020) shows a negative mean elevation change; however, it was positive in the accumulation zone while the negative value was subtly varied (Figure 5.9). The estimated mean mass balance was –0.13 ± 0.10 m w.e. yr^{-1} between 2000 and 2020, although individual glacier change estimates varied substantially.

It should be noted that both the glaciers are located in the same climatic condition, orientation, and topographical distribution. Despite this, mass balance variation may be accounted by the disproportionate amount of debris thickness and their distribution. Sharma et al. (2016) have determined that the vertical gradient of melting rate in the ablation zone shows contrastingly opposite behavior in the selected glaciers. Other than that, the melting was higher in the Sutri Dhaka than Batal glacier because of the presence of thick debris that insulates the surface from melting (Patel et al. 2021). Based on the analysis, our conclusion is that glacier topographical changes on both basin- and local scales play an essential role in influencing the glacier mass balance pattern.

The latitude-wise mass balance distribution and glacier area were plotted over both the glaciers for the selected observation periods (2000–2009, 2009–2020, and 2000–2020) (Figure 5.10). Our results revealed that the maximum glacier area was concentrated at latitude range 32.31–33.37, which shows a negative mass balance for 2009–2020 and 2000–2020 periods over the Sutri Dhaka glacier. The Batal glacier experienced a negative mass balance during 2009–2020 across

the glacier surface, whereas a zig-zag pattern of positive/negative mass balance was found during 2000–2009. It was also noticed that the selected glaciers follow a similar pattern during both the observational periods (2009–2020 and 2000–2020) with varying mass balance. The mass balance pattern starts increasing from snout to ablation zone (~32.33 latitudes) and then suddenly decreases in the accumulation zone. A similar pattern of mass balance with latitude change was previously reported by Dussaillant et al. (2019).

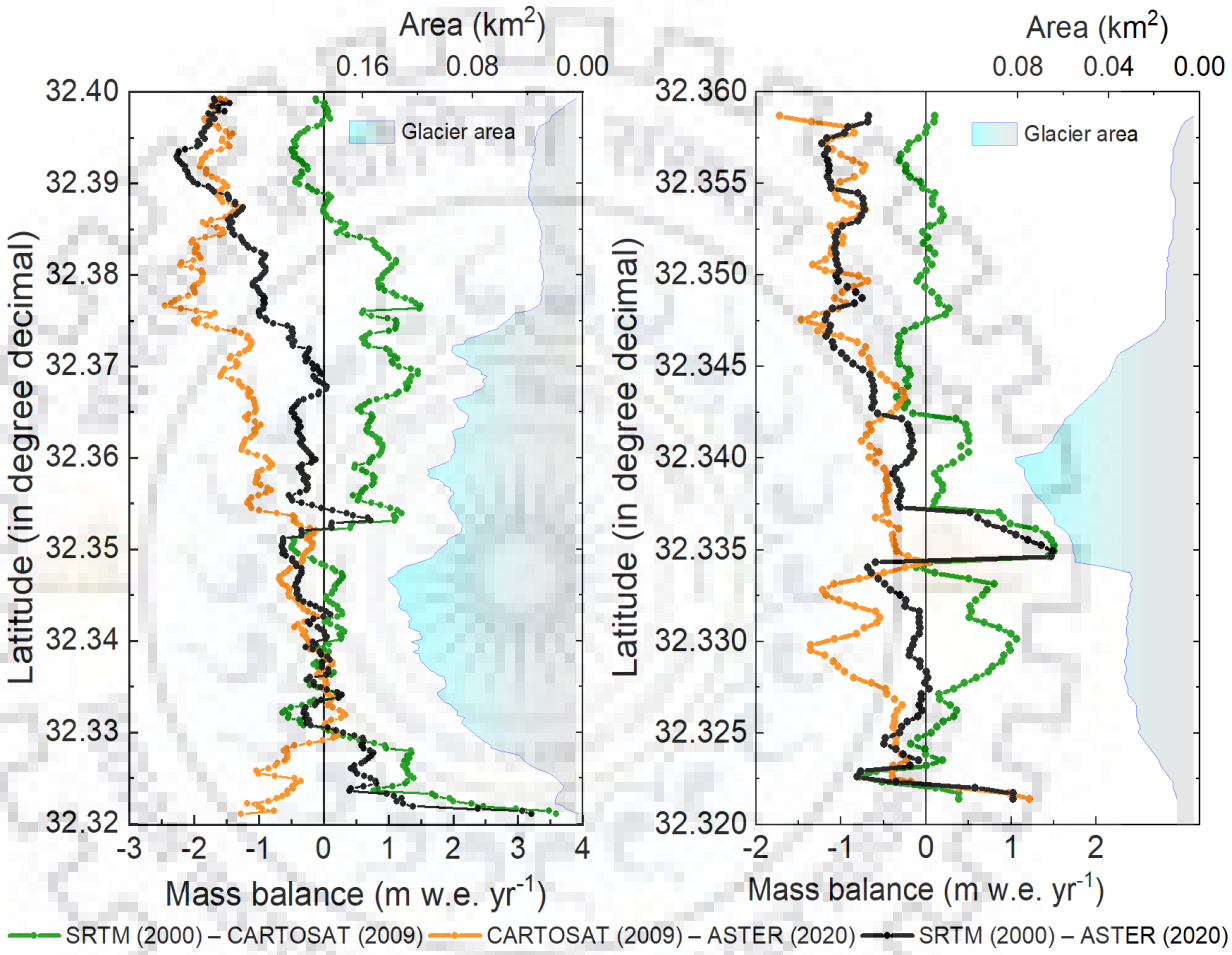

Figure 5.10. Latitude-wise mass balance distribution with its varying glacier area for the (a) Sutri Dhaka and (b) Batal glacier.

5.7.3.2. Total volume change

The glacier volume change was measured from DEM differencing (2000–2009, 2009–2020, and 2000–2020) to quantify the volume loss over a certain period (Figure 5.11). Comparison between volume change of each observation period (2000–2009 and 2009–2020) and entire study period (2000–2020) was evaluated, highlighting that the 2000–2009 period had higher ice volume than the recent period (2009–2020) for both the glaciers. The average volume change was ~ –0.13 ± 0.22 × 10^{-3} km^3yr^{-1} for the entire period (2000–2020) with significantly higher loss (–0.35 ±

0.10×10^{-3} km^3yr^{-1}) observed during 2009–2020 relative to 2000–2009 (–0.03 ± 0.28 × 10^{-3} km^3yr^{-1}).

Brahmbhatt et al. (2018) have reported the total volume change of the Chhota-Shigri glacier (located in the same river catchment), estimated as ~ $–2.0 \times 10^{-3}$ km^3yr^{-1} from 2000 to 2014. The spatial distribution of volume change suggested that the maximum loss was found between the snout and ablation zone for both the glaciers. Wu et al. (2020) noted a similar spatial distribution of volume change. However, the intensity of loss was higher in the Sutri Dhaka than the Batal glacier across all the selected periods. A similar higher volume change in clean ice glaciers than debris-covered glaciers was observed by Banerjee (2020).

5.7.4. SENSITIVITY ANALYSIS

A sensitivity test was performed over the derived ice thickness by varying the model variables and estimating the thickness change (Figure 5.12). This study has considered various ranges for different variables, depending upon their sensitivity. For example, when the slope was changed by 1°, then the thickness was varied ±8.8%. When the value of creep factor ($A = 3.24 \times 10^{-24}$ $Pa^{-3}s^{-1}$) was incremented/decremented by 0.1, then the ice thickness changed by ± 0.3%.

The sensitivity of ice thickness with respect to slope indicates that the average thickness was changed by ±3.7% when ice density was increased or decreased by 50 kg m^{-3}. Similarly, when the shape factor was changed by 0.02, the ice thickness was influenced by a factor of ±4.2%. Moreover, the sensitivity of the ice thickness model towards remotely sensed surface velocity was tested by increasing the value of 5.0 m yr^{-1}, which yields an ice thickness change of ±8.4%. This analysis shows that the ice thickness model was more sensitive to slope followed by velocity in comparison with other input variables. Therefore, the calibration of obtained results with in-situ measured surface velocity is important for reliable estimation of ice thickness distribution and its changing pattern in the future.

5.7.4. UNCERTAINTY ANALYSIS

Although remote sensing data are widely used for glacier surface velocity estimation, the quality of data can deteriorate through haze, cloud, and snow coverage, which reduces the contrast of the image and also causes information loss. However, this error can be minimized by acquiring an image with the minimum snow and cloud coverage (< 5%). The image-to-image registration and ortho-rectification of the paired images can also contribute to errors in the velocity.

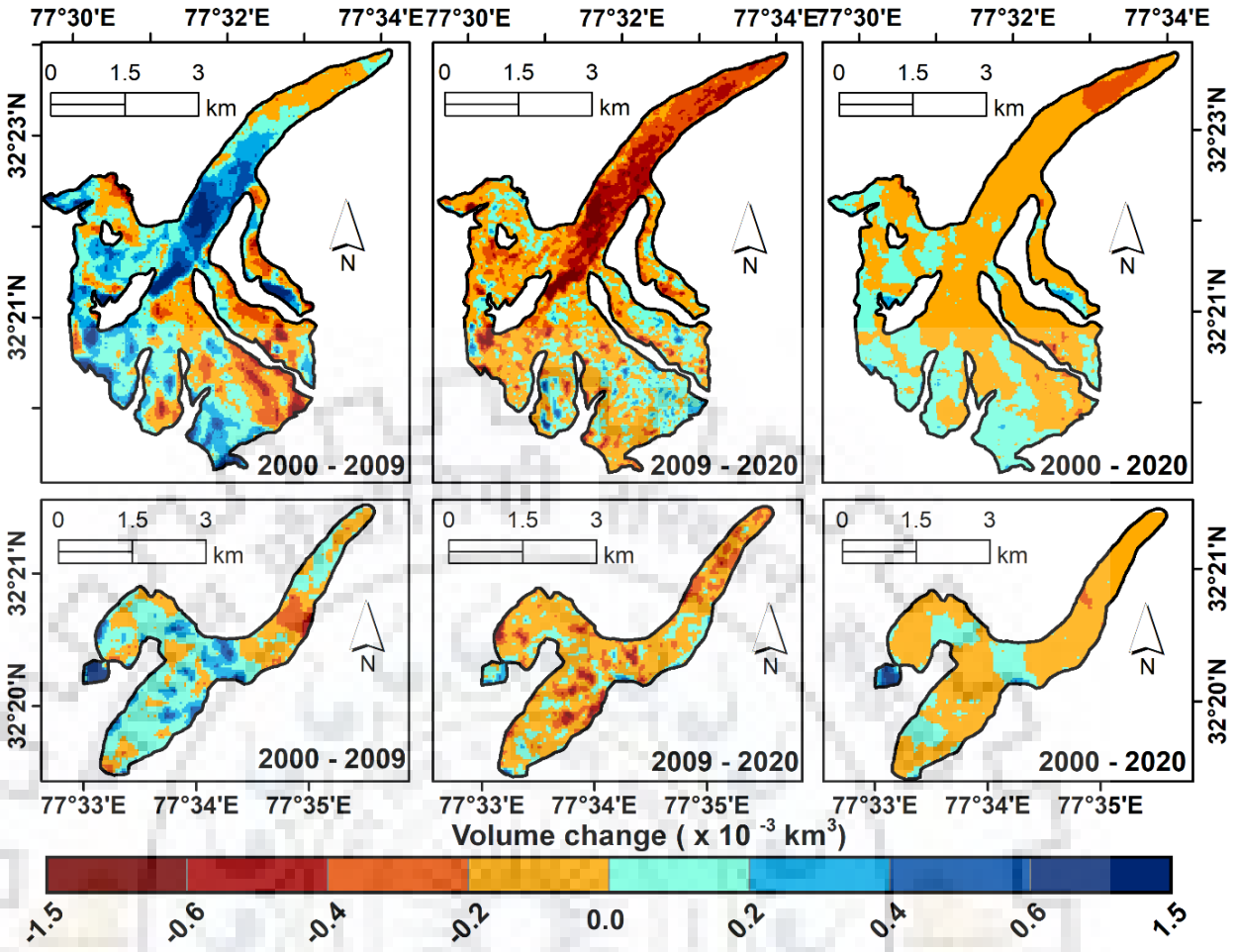

Figure 5.11. Spatial distribution of volume change over the Sutri Dhaka and Batal glacier for the selcted observational period.

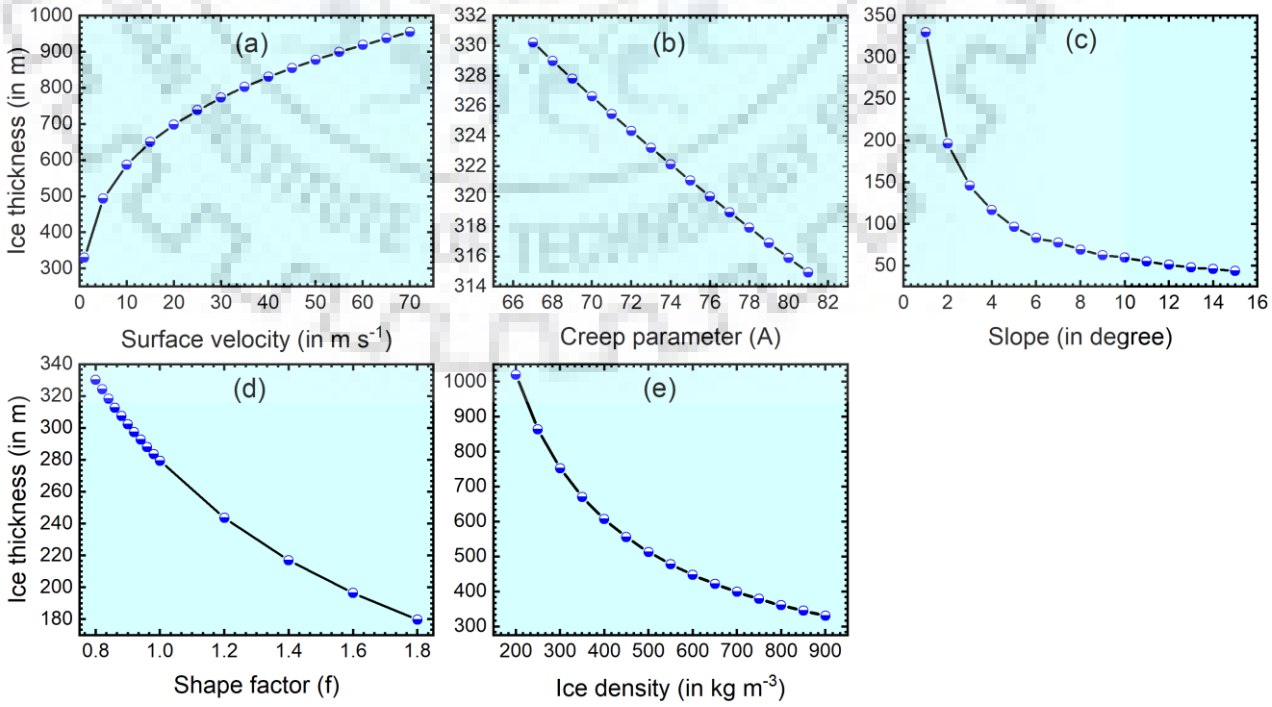

Figure 5.12. Sensitivity analysis of ice thickness by varying a model variable.

The ortho-rectification may induce horizontal shifts due to errors in the base DEM used in the analysis (Shukla and Garg 2020). These errors can be reduced if the correlated images were from the same row and path, then DEM error can only create a minimal error in the generated velocity (Heid and Kääb 2012). Moreover, this study uses Landsat data for surface velocity estimation, which was previously reported to be better for glaciological studies due to the superior image-to-image co-registration in Landsat images (Storey and Choate 2004; Heid and Kääb 2012). As per our computation, the accuracy of image correlation was ranged in order of 1/20 – 1/10 of the pixel resolution, causing an overall error of about ±1.5 m yr^{-1}. Several authors previously explained this accuracy (Tiwari et al. 2014; Shukla and Garg 2020). The computed error does not include the contribution caused by the deformation, opening, closing of crevasses, debris cover, etc. It is difficult to map these using the image-to-image correlation method. On the other hand, the estimated uncertainty of surface velocity was ranged from 0.04 to 1.20 m day^{-1} during the study period. These uncertainties of surface velocity were highly dependent upon the separation between the time of two images (pre and post).

The combined relative uncertainty for ice thickness was derived to assess the error associated with ice thickness measurement through the remote sensing approach using Equation 5.4 as given below:

$$\frac{dH}{H} = 0.25\left[\frac{dU_S}{U_S} - \frac{dA}{A} - 3\frac{df}{f} - 3\frac{d\rho}{\rho} - 3\frac{d(\sin\alpha)}{(\sin\alpha)}\right] \quad \textbf{Eq. 5.4}$$

This equation for uncertainty assessment was already applied and tested over different glaciers of the Himalayan region (Gantayat et al. 2014; Remya et al. 2019; Sattar et al. 2019). The estimated ice thickness uncertainty was ~17.8% over the selected glaciers. However, the error in shape factor, ice density, and associated uncertainty with sinα were ±4.9%, 5.8% (using 830 to 900 ice density), and ±10.1%, respectively. It was also found that the uncertainty in sinα is mainly caused by vertical inaccuracies in the DEM (Gantayat et al. 2014). The obtained uncertainties from different components and overall ice thickness were well matched with the results of many authors over the Indian Himalayas (Gantayat et al. 2014; Remya et al. 2019; Sattar et al. 2019)

5.8. CONCLUSION

A remote sensing-based multi-dimensional approach was utilized for analyzing the glacier characteristics and its mass balance over two benchmark glaciers (Sutri Dhaka and Batal) of the Chandra basin. Result demonstrates that the semi-automatic approach-based glacier feature classification suggests that the debris cover area was increased during the observational period

with significantly decreasing clean ice pixel across the glacier surface. On the other hand, the isotherm line was shifted towards the higher elevation with a maximum shift in 2018 with reference to 2013 in both the glacier. The combined glacier classification and isotherm results indicate that the debris thickness and warming climate-controlled these glaciers. The image correlation method (COSI-Corr) based glacier surface velocity reveals that the average velocity varies from ~ 0.0 to 70.0 m yr^{-1} with a minimum in the accumulation zone, relatively much higher in the upper ablation zone, then slowly decreases over the terminus of the glacier. The estimated surface velocity from COSI-Corr was validated with stake-derived velocity and compared with the NASA ITS_LIVE data. Our result shows that the estimated velocity was significantly correlated with the field-derived velocity data as well as the velocity obtained from the ITS_LIVE product for both the glaciers. The ice thickness calculated using Glen's equation revealed that the Sutri Dhaka glacier has significantly higher (up to ~250 m) thickness than the Batal glacier (up to ~180 m). Whereas the Sutri Dhaka showed a higher thickness in the trunk of the glacier, the ice thickness in Batal revealed heterogeneous patterns without a clear pattern.

Based on the geodetic mass balance approach, the estimated mean mass balance of the selected glacier was –0.03 ± 0.5, –0.34 ± 0.14, and –0.13 ± 0.10 m w.e. yr^{-1} during 2000–2009, 2009–2020, and 2000–2020, respectively, although individual glacier change estimates varied substantially. The mean volume change shows a maximum loss (–0.35 ± 0.10 × 10^{-3} km^3yr^{-1}) during 2009–2020 relative to 2000–2009 (–0.03 ± 0.28 × 10^{-3} km^3yr^{-1} whereas the entire period (2000–2020) found loss as ~ –0.13 ± 0.22 × 10^{-3} km^3yr^{-1}. A sensitivity test on estimated ice thickness by varying the model variables demonstrated that the modeled ice thickness was more sensitive to changes in slope followed by the velocity than any other variables. The present analysis demonstrates that the remote sensing data is robust and reliable to quantify the changes in glacier characteristics, velocity, and mass budget over the inaccessible region of the Himalayas.

CHAPTER 6

RESEARCH CONTRIBUTIONS AND PERSPECTIVES

6.1. ORIGINAL RESEARCH CONTRIBUTION

A central theme of this thesis is to provide a reliable quantification of glacier MB and their sensitivity to climate variation. For monitoring and modeling the glacier MB, a large part of the problem stems from the limitation of field observation due to harsh weather conditions and rugged terrain. Therefore, detailed studies on the changing pattern of glacier MB along the KH region were carried out by utilizing the remote sensing observation and calibrating/validation the model with *in situ* observations. The varying spatial scales (regional, basinal, and local) were considered in order to analyze the glacier interaction with atmospheric changes. For this, we have analyzed the spatio-temporal rainfall trend and its characteristics over the major river basin of India (Indus-Ganga-Brahmaputra). The monsoonal and annual rainfall indicates a significant decreasing trend in the eastern while increasing in the western part of the IGB basins. Therefore, the Indus basin observed a positive rainfall trend compared to the Ganga and Brahmaputra basins. Afterward, the regional scale glacier mass variation and its volume change were monitored using the twin satellite gravimetric data. The total mass change rate over the KH region was –55.0 ± 8.7 Gt yr^{-1} during 2002–2019. The GRACE-derived mass change was validated with the published MB, indicating a higher correlation (R = 0.77) over the region. Moreover, the interannual mass change in the glaciated region was also analyzed through hydro-climate data and energy fluxes.

The finding of regional glacier MB suggested that the junction of WH and CH glaciers shows higher variability (negative MB). Therefore, the Chandra basin was selected for basinal scale glacier MB modeling, a part of WH, and has sufficient field observation and published literature to validate the obtained results. To analyze the basinal MB, we have developed two-dimensional spatially distributed glacier surface energy and mass fluxes model that uses the remote sensing data and meteorological variables for modeling and *in situ* observation for calibration/validation of the modeled output. We have derived T_a spatially using the multivariate statistical approach, which indicates a relative error of 0.02 – 0.05℃ with the observed data. The relative error between the modeled and observed radiation fluxes was < 10.0 W m^{-2}. Our study revealed that the Chandra basin glaciers have been losing their mass with a mean annual MB of −0.59 ± 0.12

m w.e. a^{-1} for the six hydrological years. Results illustrated that the mean surface melt rate of the selected glaciers ranged from −5.1 to −2.5 m w.e. a^{-1}, which lies between 4500 and 5000 m a.s.l.

After analyzing the MB and surface melting, a variety of glaciers come in the vicinity of the Chandra basin, suggesting that the Sutri Dhaka and Batal are nearby glaciers; however, having contrasting behavior than other glaciers in the basin. Therefore, we have monitored the glacier feature classification, shifting in isotherm line, surface velocity, ice thickness, glacier mass balance, and volume changes of the selected glaciers for further detailed investigation at a local scale. The estimated geodetic glacier MB shows an average value of –0.03 ± 0.5, –0.34 ± 0.10, and –0.13 ± 0.14 m w.e. yr^{-1} during 2000–2009, 2009–2020, and 2000–2020, respectively. The outcomes of glacier surface velocities were validated with the stakes measured surface velocity and from other data archives of surface velocity.

6.2. FUTURE RESEARCH PERSPECTIVES

Overall, the presented studies prove the potential of various remote sensing data for monitoring and modeling glaciological processes in one of the world's major freshwater reservoir regions. It also addresses the contributing variables and their changing pattern with respect to time. The study includes the limiting factors (uncertainties) that influence the accuracy of a model and further generate an error in the observation. These outcomes could be used to establish a connection between the glacier and climate variation as well as able to assess the direct impact on the lives and livelihood of millions of population.

LIST OF PUBLICATIONS

JOURNAL PUBLICATIONS

1. **Akansha Patel,** Ajanta Goswami, Jaydeo K Dharpure, and Meloth Thamban. Rainfall variability over the Indus, Ganga, and Brahmaputra River basins: A spatio-temporal characterization. *Quaternary International Journal,* **2020,** *575-576*, pp. 280-294**.** https://doi.org/10.1016/j.quaint.2020.06.010

2. **Akansha Patel,** Ajanta Goswami, Jaydeo K Dharpure, Meloth Thamban, Anil V. Kulkarni and Parmanand Sharma. Regional mass variations and its sensitivity to climate drivers over glaciers of Karakoram and Himalayas. *GIScience & Remote Sensing Journal,* **2021,** *58(5),* pp. 670-692**.** https://doi.org/10.1080/15481603.2021.1930730

3. **Akansha Patel,** Ajanta Goswami, Jaydeo K Dharpure, Meloth Thamban, Parmanand Sharma, Anil V. Kulkarni, and Sunil Oulkar. Estimation of mass and energy balance of glaciers using a distributed energy balance model over the Chandra River basin (Western Himalaya). *Hydrological Processes Journal,* **2021**, *35(2),* pp. e14058. https://doi.org/10.1002/hyp.14058

4. **Akansha Patel,** Ajanta Goswami, Jaydeo K Dharpure, Parmanand Sharma, Lavkush Patel and Meloth Thamban. Monitoring of glacier characteristics and its mass balance using multi-dimensional approach over the glaciers of Chandra basin, western Himalaya. *Hydrological Science Journal,* **2021.** https://www.tandfonline.com/doi/full/10.1080/02626667.2022.2027950.

CONFERENCE PROCEEDINGS

1. **Akansha Patel,** Ajanta Goswami, and Meloth Thamban. Development of basinal scale glacier mass balance model: an approach based on satellite observations and energy balance components. In Proceedings of *EGU General Assembly Conference Abstracts*, Vienna, **2020**, abstract no 3425. https://doi.org/10.5194/egusphere-egu2020-3425

2. **Akansha Patel,** Ajanta Goswami, and Meloth Thamban. Spatio-temporal variability of rainfall using TRMM over the Indus, Ganga, and Brahmaputra River basins of Indian Himalayas. In Proceedings of the *Remote Sensing for Agriculture, Ecosystems, and Hydrology XXI, SPEI*; Strasbourg, France, **2019**.

3. **Akansha Patel,** Ajanta Goswami, and Meloth Thamban. Identification of temperature and rainfall hotspot across Indian major rivers basin. In Proceedings of DwD-GCRF-UKADR-DRG-UKCDR International Conference, Northumbria University Newcastle, UK, **2019**

4. **Akansha Patel** and Ajanta Goswami. Spatio-temporal Variability of Rainfall using TRMM over the Indus, Ganga, and Brahmaputra River basin of Indian Himalayas. In Proceedings of the India-UK (IUKWC) workshop; Wildlife Institute of India, Dehradun, Uttarakhand, **2018.**

BIBLIOGRAPHY

1. Abdullah T, Romshoo SA, Rashid I (2020) The satellite observed glacier mass changes over the Upper Indus Basin during 2000–2012. Sci Rep 10:1–9. https://doi.org/10.1038/s41598-020-71281-7
2. Acharya A, Kayastha RB (2018) Mass and energy balance estimation of Yala Glacier (2011-2017), Langtang Valley, Nepal. Water (Switzerland) 11:. https://doi.org/10.3390/w11010006
3. Albergel C, Dutra E, Munier S, et al (2018) ERA-5 and ERA-Interim driven ISBA land surface model simulations: Which one performs better? Hydrol Earth Syst Sci 22:3515–3532. https://doi.org/10.5194/hess-22-3515-2018
4. Allen RG., Trezza R., Tasumi M (2002) Surface energy balance algorithms for land, Advance Training and User Mannual, NASA, 1-98
5. Allen RG (1996) Assessing integrity of weather data for reference evapotranspiration estimation. J Irrig Drain Eng 122:97–106. https://doi.org/10.1061/(ASCE)0733-9437(1996)122:2(97)
6. Allen RG, Pereira LS, Raes D, et al (1998) Crop evapotranspiration - Guidelines for computing crop water requirements - FAO Irrigation and drainage paper 56 By. 1–15
7. Allen SK, Linsbauer A, Randhawa SS, et al (2016) Glacial lake outburst flood risk in Himachal Pradesh, India: an integrative and anticipatory approach considering current and future threats. Nat Hazards 84:1741–1763. https://doi.org/10.1007/s11069-016-2511-x
8. Alpert P (1986) Mesoscale indexing of the distribution of orographic precipitation over high mountains. J Clim Appl Meteorol 25:532–545. https://doi.org/10.1175/1520-0450(1986)025<0532:MIOTDO>2.0.CO;2
9. Anders AM, Roe GH, Hallet B, et al (2006) Spatial patterns of precipitation and topography in the Himalaya. Spec Pap Soc Am 398:39
10. Anul Haq M, Jain K, Menon KPR (2012) Surface Temperature Estimation of Gangotri Glacier Using Thermal Remote Sensing. ISPRS - Int Arch Photogramm Remote Sens Spat Inf Sci XXXIX-B8:115–119. https://doi.org/10.5194/isprsarchives-xxxix-b8-115-2012
11. Arnold NS, Willis IC, Sharp MJ, et al (1996) A distributed surface energy-balance model for a small valley glacier. I. Development and testing for Haut Glacier d' Arolla, Valais, Switzerland. J Glaciol 42:77–89. https://doi.org/10.3189/s0022143000030549

12. Artan G, Gadain H, Smith JL, et al (2007) Adequacy of satellite derived rainfall data for stream flow modeling. Nat Hazards 43:167–185. https://doi.org/10.1007/s11069-007-9121-6

13. Artis DA, Carnahan WH (1982) Survey of emissivity variability in thermography of urban areas. Remote Sens Environ 12:313–329. https://doi.org/10.1016/0034-4257(82)90043-8

14. As-Syakur AR, Tanaka T, Prasetia R, et al (2011) Comparison of TRMM multisatellite precipitation analysis (TMPA) products and daily-monthly gauge data over Bali. Int J Remote Sens 32:8969–8982. https://doi.org/10.1080/01431161.2010.531784

15. ASCE–EWRI (2005) The ASCE Standardized Reference Evapotranspiration Equation. ASCE–EWRI Standardization of Reference Evapo- transpiration Task Committe Rep., ASCE Reston, Va

16. Ashraf A, Batool A (2019) Evaluation of glacial resource potential for sustaining kuhl irrigation system under changing climate in the Himalayan region. J Mt Sci 16:1150–1159. https://doi.org/10.1007/s11629-018-5077-0

17. Ashraf A, Naz R, Roohi R (2012) Glacial lake outburst flood hazards in Hindukush, Karakoram and Himalayan ranges of Pakistan: Implications and risk analysis. Geomatics, Nat Hazards Risk 3:113–132. https://doi.org/10.1080/19475705.2011.615344

18. Azam MF, Wagnon P, Berthier E, et al (2018) Review of the status and mass changes of Himalayan-Karakoram glaciers. J Glaciol 64:61–74. https://doi.org/10.1017/jog.2017.86

19. Azam MF, Wagnon P, Patrick C, et al (2014a) Reconstruction of the annual mass balance of Chhota Shigri glacier, Western Himalaya, India, since 1969. Ann Glaciol 55:69–80. https://doi.org/10.3189/2014AoG66A104

20. Azam MF, Wagnon P, Ramanathan A, et al (2012) From balance to imbalance: A shift in the dynamic behaviour of Chhota Shigri glacier, western Himalaya, India. J Glaciol 58:315–324. https://doi.org/10.3189/2012JoG11J123

21. Azam MF, Wagnon P, Vincent C, et al (2014b) Processes governing the mass balance of Chhota Shigri Glacier (western Himalaya, India) assessed by point-scale surface energy balance measurements. Cryosphere 8:2195–2217. https://doi.org/10.5194/tc-8-2195-2014

22. Bahadur J (1993) The Himalayas: a third polar region. Snow glacier Hydrol Proc Int Symp Kathmandu, 1992 181–190

23. Baidya SK, Shrestha ML, Sheikh MM (2008) Trends in daily climatic extremes of Nepal. J Hydrol Meteorol 5:2008

24. Bamber JL, Westaway RM, Marzeion B, Wouters B (2018) The land ice contribution to sea level during the satellite era. Environ Res Lett 13:. https://doi.org/10.1088/1748-9326/aac2f0

25. Bandyopadhyay D, Singh G, Kulkarni A V. (2018) Glacier ice mass changes in central Himalayas during 2000-2014 using TanDEM- X data. Int Arch Photogramm Remote Sens Spat Inf Sci - ISPRS Arch 42:193–196. https://doi.org/10.5194/isprs-archives-XLII-5-193-2018

26. Bandyopadhyay D, Singh G, Kulkarni A V. (2019) Spatial distribution of decadal ice-thickness change and glacier stored water loss in the Upper Ganga basin, India during 2000–2014. Sci Rep 9:1–9. https://doi.org/10.1038/s41598-019-53055-y

27. Bandyopadhyay J (1995) Water Management in the Ganges–Brahmaputra Basin: Emerging Challenges for the 21st Century. Int J Water Resour Dev 11:411–442. https://doi.org/10.1080/07900629550042119

28. Banerjee A (2017) Brief communication: Thinning of debris-covered and debris-free glaciers in a warming climate. Cryosphere 11:133–138. https://doi.org/10.5194/tc-11-133-2017

29. Banerjee A (2020) Volume-area scaling for debris-covered glaciers. J Glaciol 5:

30. Banerjee C, Kumar DN (2018) Analyzing Large-Scale Hydrologic Processes Using GRACE and Hydrometeorological Datasets. Water Resour Manag 4409–4423. https://doi.org/10.1007/s11269-018-2070-x

31. Barnett TP, Adam JC, Lettenmaier DP (2005) Potential impacts of a warming climate on water availability in snow-dominated regions. Nature 438:303–309. https://doi.org/10.1038/nature04141

32. Barrand NE, Murray T (2006) Multivariate controls on the incidence of glacier surging in the Karakoram Himalaya. Arctic, Antarct Alp Res 38:489–498. https://doi.org/10.1657/1523-0430(2006)38[489:MCOTIO]2.0.CO;2

33. Barros AP, Joshi M, Putkonen J, Burbank DW (2000) A study of the 1999 monsoon rainfall in a mountainous region in central Nepal using TRMM products and rain gauge observations. Geophys Res Lett 27:3683–3686

34. Barsi JA, Schott JR, Palluconi FD, Hook SJ (2005) Validation of a web-based atmospheric correction tool for single thermal band instruments. Earth Obs Syst X 5882:58820E. https://doi.org/10.1117/12.619990

35. Bastiaanssen WGM (2000) SEBAL-based sensible and latent heat fluxes in the irrigated Gediz Basin, Turkey. J Hydrol 229:87–100. https://doi.org/10.1016/S0022-1694(99)00202-4

36. Bastiaanssen WGM, Pelgrum H, Wang J, et al (1998) A remote sensing surface energy balance algorithm for land (SEBAL), Part 1: Formulation. J Hydrol 212–213:213–229. https://doi.org/10.1016/S0022-1694(98)00254-6

37. Benhamrouche A, Boucherf D, Hamadache R, et al (2015) Spatial distribution of the daily precipitation concentration index in Algeria. Nat Hazards Earth Syst Sci 15:617–625. https://doi.org/10.5194/nhess-15-617-2015

38. Bera S (2017) Trend Analysis of Rainfall in Ganga Basin, India during 1901-2000. Am J Clim Chang 06:116–131. https://doi.org/10.4236/ajcc.2017.61007

39. Berger S, Bliefernicht J, Linstädter A, et al (2019) The impact of rain events on CO2 emissions from contrasting land use systems in semi-arid West African savannas. Sci Total Environ 647:1478–1489. https://doi.org/10.1016/j.scitotenv.2018.07.397

40. Berthier E, Cabot V, Vincent C, Six D (2016) Decadal region-wide and glacier-wide mass balances derived from multi-temporal aster satellite digital elevation models. Validation over the mont-blanc area. Front Earth Sci 4:1–16. https://doi.org/10.3389/feart.2016.00063

41. Bezerra BG, Silva BB da, Santos CAC dos, Bezerra JRC (2015) Actual Evapotranspiration Estimation Using Remote Sensing: Comparison of SEBAL and SSEB Approaches. Adv Remote Sens 04:234–247. https://doi.org/10.4236/ars.2015.43019

42. Bhambri R, Hewitt K, Kawishwar P, et al (2019) Ice-dams, outburst floods, and movement heterogeneity of glaciers, Karakoram. Glob Planet Change 180:100–116. https://doi.org/10.1016/j.gloplacha.2019.05.004

43. Bhambri R, Hewitt K, Kawishwar P, Pratap B (2017) Surge-type and surge-modified glaciers in the Karakoram. Sci Rep 7:1–14. https://doi.org/10.1038/s41598-017-15473-8

44. Bhardwaj A, Joshi PK, Snehmani, et al (2014) Mapping debris-covered glaciers and identifying factors affecting the accuracy. Cold Reg Sci Technol 106–107:161–174. https://doi.org/10.1016/j.coldregions.2014.07.006

45. Bharti V, Singh C, Ettema J, Turkington TAR (2016) Spatiotemporal characteristics of extreme rainfall events over the Northwest Himalaya using satellite data. Int J Climatol 36:3949–3962. https://doi.org/10.1002/joc.4605

46. Bhowmik SKR, Joardar D, Roy SS, Hatwar HR (2005) Mesoscale features of monsoon precipitation system as revealed by the objective analysis of rainfall from the use of high dense land rainfall observations. Mausam 56:543

47. Bhutiyani MR (1999) Mass-balance studies on Siachen Glacier in the Nubra valley, Karakoram Himalaya, India. J Glaciol 45:112–118. https://doi.org/10.1017/S0022143000003099

48. Bilal H, Chamhuri S, Mokhtar M Bin, Kanniah KD (2019) Recent snow cover variation in the Upper Indus Basin of Gilgit Baltistan, Hindukush Karakoram Himalaya. J Mt Sci 16:296–308. https://doi.org/10.1007/s11629-018-5201-3

49. Bisset RR, Dehecq A, Goldberg DN, et al (2020) Reversed surface-mass-balance gradients on himalayan debris-covered glaciers inferred from remote sensing. Remote Sens 12:. https://doi.org/10.3390/rs12101563

50. Blunden J, Arndt E (2017) State of the Climate in 2016, Bulletin of the American Meterological Society

51. Bolch T, Kulkarni A, Kääb A, et al (2012) The state and fate of himalayan glaciers. Science (80-) 336:310–314. https://doi.org/10.1126/science.1215828

52. Bolch T, Pieczonka T, Mukherjee K, Shea J (2017) Brief communication: Glaciers in the Hunza catchment (Karakoram) have been nearly in balance since the 1970s. Cryosphere 11:531–539. https://doi.org/10.5194/tc-11-531-2017

53. Bonekamp PNJ, de Kok RJ, Collier E, Immerzeel WW (2019) Contrasting meteorological drivers of the glacier mass balance between the Karakoram and central Himalaya. Front Earth Sci 7:1–14. https://doi.org/10.3389/feart.2019.00107

54. Bookhagen B, Burbank DW (2010) Toward a complete Himalayan hydrological budget: Spatiotemporal distribution of snowmelt and rainfall and their impact on river discharge. J Geophys Res Earth Surf 115:1–25. https://doi.org/10.1029/2009JF001426

55. Bookhagen B, Strecker MR (2008) Orographic barriers, high-resolution TRMM rainfall, and relief variations along the eastern Andes. Geophys Res Lett 35:. https://doi.org/10.1029/2007GL032011

56. Bookhagen B, Thiede RC, Strecker MR (2005) Late Quaternary intensified monsoon phases control landscape evolution in the northwest Himalaya. Geology 33:149–152

57. Brahmbhatt RM, Agrawal R, Rathore BP, et al (2018) Estimation of changes in ice thickness of Chhota Shigri glacier , Himachal Pradesh using DGPS and SRTM derived elevation profiles. J Geomatics 12:117–121

58. Braithwaite RJ (1995) Positive degree-day factors for ablation on the Greenland ice sheet studied by energy-balance Modelling. J Glaciol 41:153–160

59. Brock BW, Willis IC, Sharp MJ (2000) Measurement and parameterisation of albedo variations at Haut Glacier d ' Arolla , Switzerland. J Glaciol 46:675–688. https://doi.org/10.3189/172756506781828746

60. Brown RD, Brasnett B, Robinson D, et al (2010) Gridded North American monthly snow depth and snow water equivalent for GCM evaluation. Atmosphere-Ocean 5900:. https://doi.org/10.3137/ao.410101

61. Brun F, Berthier E, Wagnon P, et al (2017) A spatially resolved estimate of High Mountain Asia glacier mass balances from 2000 to 2016. Nat Geosci 10:668–673. https://doi.org/10.1038/ngeo2999

62. Brunetti M, Caloiero T, Coscarelli R, et al (2012) Precipitation variability and change in the Calabria region (Italy) from a high resolution daily dataset. Int J Climatol 32:57–73. https://doi.org/10.1002/joc.2233

63. Burton EJ, McKeith IG, Burn DJ, et al (2004) Cerebral atrophy in Parkinson's disease with and without dementia: A comparison with Alzheimer's disease, dementia with Lewy bodies and controls. Brain 127:791–800. https://doi.org/10.1093/brain/awh088

64. C3S CCCS (2019) C3S ERA5-Land reanalysis. In: Copernicus Clim. Chang. Serv.

65. Cao Y, Roy S Sen (2020) Spatial patterns of seasonal level trends of groundwater in India during 2002–2016. Weather 75:123–128. https://doi.org/10.1002/wea.3370

66. Chanard K, Avouac JP, Ramillien G, Genrich J (2014) Modeling deformation induced by seasonal variations of continental water in the Himalaya region: Sensitivity to Earth elastic structure. J Geophys Res Solid Earth 119:5097–5113. https://doi.org/10.1002/2013JB010451

67. Chand P, Sharma MC, Bhambri R, et al (2017) Reconstructing the pattern of the Bara Shigri Glacier fluctuation since the end of the Little Ice Age, Chandra valley, north-western Himalaya. Prog Phys Geogr 41:643–675. https://doi.org/10.1177/0309133317728017

68. Chander G, Markham B (2003) Revised Landsat-5 TM Radiometrie Calibration Procedures and Postcalibration Dynamic Ranges. IEEE Trans Geosci Remote Sens 41:2674–2677. https://doi.org/10.1109/TGRS.2003.818464

69. Che Y, Zhang M, Li Z, et al (2019) Energy balance model of mass balance and its sensitivity to meteorological variability on Urumqi River Glacier No.1 in the Chinese Tien Shan. Sci Rep 9:1–13. https://doi.org/10.1038/s41598-019-50398-4

70. Cogley JG (2011) Present and future states of Himalaya and Karakoram glaciers. Ann Glaciol 52:69–73. https://doi.org/10.3189/172756411799096277

71. Cooper M (2010) Changes in rainfall and relative humidity in river basins in northwest and central India. Pratap Singh,Vijay Kumar,T Thomas and Manohar Arora 2274:2267–2274. https://doi.org/10.1002/hyp

72. Copland L, Sylvestre T, Bishop M, et al (2011) Expanded and recently increased glacier surging in the karakoram. Arctic, Antarct Alp Res 43:503–516. https://doi.org/10.1657/1938-4246-43.4.503

73. Cosgrove WJ, Loucks DP (2015) Water management: Current and future challenges and research directions. Wyo Univ Water Resour Res Inst Water Resour Ser 51:4823–4839. https://doi.org/10.1002/2014WR016869.Received

74. Cresswell MP, Morse AP, Thomson MC, Connor SJ (1999) Estimating surface air temperatures, from meteosat land surface temperatures, using an empirical solar zenith angle model. Int J Remote Sens 20:1125–1132. https://doi.org/10.1080/014311699212885

75. Cristóbal J, Jiménez-Muñoz JC, Sobrino JA, et al (2009) Improvements in land surface temperature retrieval from the Landsat series thermal band using water vapor and air temperature. J Geophys Res Atmos 114:1–16. https://doi.org/10.1029/2008JD010616

76. Cuffey KM, Paterson WSB (2010) The physics of glaciers. Academic Press

77. Czubski K, Kozak J, Kolecka N (2013) Accuracy of SRTM-X and ASTER elevation data and its influence on topographical and hydrological modeling: Case study of the Pieniny Mts. in Poland. Int J Geoinformatics 9:7–14

78. Dadic R, Mott R, Lehning M, et al (2013) Sensitivity of turbulent fluxes to wind speed over snow surfaces in different climatic settings. Adv Water Resour 55:178–189. https://doi.org/10.1016/j.advwatres.2012.06.010

79. Dai Y, Zeng X, Dickinson RE, et al (2003) The common land model. Bull Am Meteorol Soc 84:1013–1023. https://doi.org/10.1175/BAMS-84-8-1013

80. Das A, Ghosh B., Choudhury B., et al (2009) Climate Change in Northeast India: Recent Facts and Events –Worry For Agricultural Management. ISPRS Arch XXXVIII-8/W3 Work Proc Impact Clim Chang Agric 32–37

81. Das S, Kar NS, Bandyopadhyay S (2015) Glacial lake outburst flood at Kedarnath, Indian Himalaya: a study using digital elevation models and satellite images. Nat Hazards 77:769–786. https://doi.org/10.1007/s11069-015-1629-6

82. Das S, Patel PP, Sengupta S (2016) Evaluation of different digital elevation models for analyzing drainage morphometric parameters in a mountainous terrain : a case study of the Supin – Upper Tons Basin , Indian Himalayas. Springerplus 1–38. https://doi.org/10.1186/s40064-016-3207-0

83. Davaze L, Rabatel A, Dufour A, et al (2020) Region-Wide Annual Glacier Surface Mass Balance for the European Alps From 2000 to 2016. Front Earth Sci 8:0–14. https://doi.org/10.3389/feart.2020.00149

84. De Kok RJ, Kraaijenbrink PDA, Tuinenburg OA, et al (2020) Towards understanding the pattern of glacier mass balances in High Mountain Asia using regional climatic modelling. Cryosphere 14:3215–3234. https://doi.org/10.5194/tc-14-3215-2020

85. De Kok RJ, Tuinenburg OA, Bonekamp PNJ, Immerzeel WW (2018) Irrigation as a Potential Driver for Anomalous Glacier Behavior in High Mountain Asia. Geophys Res Lett 45:2047–2054. https://doi.org/10.1002/2017GL076158

86. Dehecq A, Gourmelen N, Trouve E (2015) Deriving large-scale glacier velocities from a complete satellite archive: Application to the Pamir-Karakoram-Himalaya. Remote Sens Environ 162:55–66. https://doi.org/10.1016/j.rse.2015.01.031

87. Deka RL, Mahanta C, Pathak H, et al (2013) Trends and fluctuations of rainfall regime in the Brahmaputra and Barak basins of Assam, India. Theor Appl Climatol 114:61–71. https://doi.org/10.1007/s00704-012-0820-x

88. Dhar S, Kumar A, Rai SK (2020) Spatio-temporal disposition of Chandra basin Glaciers from 1980 to 2011, Lahaul and Spiti Himalayan Region, Himachal Pradesh, India. Int J Emerg Technol 11:1005–1012

89. Dharpure JK, Patel A, Goswami A, Kulkarni A V (2020) Spatiotemporal snow cover characterization and its linkage with climate change over the Chenab river basin , western Himalayas. GIScience Remote Sens 00:1–25. https://doi.org/10.1080/15481603.2020.1821150

90. Dimri AP, Yasunari T, Kotlia BS, et al (2016) Indian winter monsoon: Present and past. Earth-Science Rev 163:297–322. https://doi.org/10.1016/j.earscirev.2016.10.008

91. Dobhal DP, Mehta M, Srivastava D (2013) Influence of debris cover on terminus retreat and mass changes of Chorabari Glacier, Garhwal region, central Himalaya, India. J Glaciol 59:961–971. https://doi.org/10.3189/2013JoG12J180

92. Dobhal DP, Thayyen R (2008) Mass balance studies of Dokriani Glacier from 1992 to 2000 , Garhwal A rt i c l e

93. DST (2012) Status Report on Gangotri Glacier. Himal Glaciol Tech Rep 105

94. Duffie JA., Beckman WA (1989) Solar engineering of thermal processes

95. Dussaillant I, Berthier E, Brun F, et al (2019) Two decades of glacier mass loss along the Andes. Nat Geosci 12:802–808. https://doi.org/10.1038/s41561-019-0432-5

96. Dyurgerov MB, Meier MF (2005) Glaciers amd the Changing Earth System: A 2004 Snapshot. Instaar

97. Dyurgerov MB, Meier MF (1997) Mass Balance of Mountain and Subpolar Glaciers: A New Global Assessment for 1961-1990. Arct Alp Res 29:379–391. https://doi.org/10.2307/1551986

98. Ekström M, Gutmann ED, Wilby RL, et al (2018) Robustness of hydroclimate metrics for climate change impact research. WIREs Water 5:1–20. https://doi.org/10.1002/wat2.1288

99. Farinotti D, Huss M, Bauder A, et al (2009) A method to estimate the ice volume and ice-thickness distribution of alpine glaciers. J Glaciol 55:422–430. https://doi.org/10.3189/002214309788816759

100. Farinotti D, Immerzeel WW, de Kok RJ, et al (2020a) Manifestations and mechanisms of the Karakoram glacier Anomaly. Nat Geosci 13:8–16. https://doi.org/10.1038/s41561-019-0513-5

101. Farinotti D, Immerzeel WW, de Kok RJ, et al (2020b) Manifestations and mechanisms of the Karakoram glacier Anomaly. In: EGU General Assembly Conference Abstracts. pp 8–16

102. Feng X, Porporato A, Rodriguez-Iturbe I (2013) Changes in rainfall seasonality in the tropics. Nat Clim Chang 3:811–815. https://doi.org/10.1038/nclimate1907

103. Fujita K, Nuimura T (2011) Spatially heterogeneous wastage of Himalayan glaciers. Proc Natl Acad Sci 108:14011–14014. https://doi.org/10.1073/pnas.1106242108

104. Gaddam VK, Kulkarni A V., Gupta AK (2016) Estimation of glacial retreat and mass loss in Baspa basin, Western Himalaya. Spat Inf Res 24:257–266. https://doi.org/10.1007/s41324-016-0026-x

105. Gain AK, Giupponi C (2015) A dynamic assessment of water scarcity risk in the Lower Brahmaputra River Basin: An integrated approach. Ecol Indic 48:120–131. https://doi.org/10.1016/j.ecolind.2014.07.034

106. Gantayat P, Kulkarni A V, Srinivasan J (2014) Estimation of ice thickness using surface velocities and slope: Case study at Gangotri Glacier, India. J Glaciol 60:277–282. https://doi.org/10.3189/2014JoG13J078

107. García-Barrón L, Camarillo JM, Morales J, Sousa A (2015) Temporal analysis (1940-2010) of rainfall aggressiveness in the Iberian Peninsula basins. J Hydrol 525:747–759. https://doi.org/10.1016/j.jhydrol.2015.04.036

108. Gardelle J, Berthier E, Arnaud Y (2012) Slight mass gain of Karakoram glaciers in the early twenty-first century. Nat Geosci 5:1–4. https://doi.org/10.1038/ngeo1450

109. Gardelle J, Berthier E, Arnaud Y, Kääb A (2013) Region-wide glacier mass balances over the Pamir-Karakoram-Himalaya during 1999-2011. Cryosphere 7:1263–1286. https://doi.org/10.5194/tc-7-1263-2013

110. Gardner AS, Fahnestock MA, Scambos TA (2019) ITS_LIVE Regional Glacier and Ice Sheet Surface Velocities. Data Arch Natl Snow Ice Data Cent 5:2018–2020

111. Gardner AS, Moholdt G, Cogley JG, et al (2013) A reconciled estimate of glacier contributions to sea level rise: 2003 to 2009. Science (80-) 340:852–857. https://doi.org/10.1126/science.1234532

112. Gardner AS, Moholdt G, Scambos T, et al (2018) Increased West Antarctic and unchanged East Antarctic ice discharge over the last 7 years. Cryosphere 12:521–547. https://doi.org/10.5194/tc-12-521-2018

113. Garg PK, Shukla A, Tiwari RK, Jasrotia AS (2017) Assessing the status of glaciers in part of the Chandra basin, Himachal HimalayaA multiparametric approach. Geomorphology 284:99–114. https://doi.org/10.1016/j.geomorph.2016.10.022

114. Garrison JD, Adler GP (1990) Estimation of precipitable water over the United States for application to the division of solar radiation into its direct and diffuse components. Sol Energy 44:225–241. https://doi.org/10.1016/0038-092X(90)90151-2

115. Gilany N, Iqbal J (2020) Geospatial analysis and simulation of glacial lake outburst flood hazard in Shyok Basin of Pakistan. Environ Earth Sci 79:1–24. https://doi.org/10.1007/s12665-020-8867-y

116. Greuell W (1992) Hintereisferner, Austria: mass-balance reconstruction and numerical modelling of the historical length variations. J Glaciol 38:233–244. https://doi.org/10.1017/S0022143000003646

117. Guhathakurta P, Rajeevan M (2008) Trends in the rainfall pattern over India. Int J Climatol 2029:2011–2029. https://doi.org/10.1002/joc

118. Gunter BC, Riva REM, Urban T, et al (2008) Evaluation of GRACE and ICESat Mass Change Estimates Over Antarctica. In: Gravity , Geoid and Earth Observation. pp 23–27

119. Guo J, Mu D, Liu X, et al (2016) Water Storage Changes over the Tibetan Plateau Revealed by GRACE Mission. Acta Geophys 64:463–476. https://doi.org/10.1515/acgeo-2016-0003

120. Gupta M, Srivastava PK, Islam T, Ishak AM Bin (2014) Evaluation of TRMM rainfall for soil moisture prediction in a subtropical climate. Environ Earth Sci 71:4421–4431. https://doi.org/10.1007/s12665-013-2837-6

121. Gurgiser W, Marzeion B, Nicholson L, et al (2013) Modeling energy and mass balance of shallap glacier, Peru. Cryosphere 7:1787–1802. https://doi.org/10.5194/tc-7-1787-2013

122. Haeberli W (2016) Brief communication: On area- and slope-related thickness estimates and volume calculations for unmeasured glaciers. Cryosph Discuss 1–18. https://doi.org/10.5194/tc-2015-222

123. Haeberli W, Schaub Y, Huggel C (2017) Increasing risks related to landslides from degrading permafrost into new lakes in de-glaciating mountain ranges. Geomorphology 293:405–417. https://doi.org/10.1016/j.geomorph.2016.02.009

124. Hartmann H, Buchanan H (2014) Trends in extreme precipitation events in the indus River Basin and flooding in Pakistan. Atmos - Ocean 52:77–91. https://doi.org/10.1080/07055900.2013.859124

125. Hasson S, Lucarini V, Pascale S, Böhner J (2014) Seasonality of the hydrological cycle in major South and Southeast Asian river basins as simulated by PCMDI/CMIP3 experiments. Earth Syst Dyn 5:67–87. https://doi.org/10.5194/esd-5-67-2014

126. Heid T, Kääb A (2012) Evaluation of existing image matching methods for deriving glacier surface displacements globally from optical satellite imagery. Remote Sens Environ 118:339–355. https://doi.org/10.1016/j.rse.2011.11.024

127. Hewitt K (2007) Tributary glacier surges: An exceptional concentration at Panmah Glacier, Karakoram Himalaya. J Glaciol 53:181–188. https://doi.org/10.3189/172756507782202829

128. Himanshu SK, Pandey A, Yadav B (2017) Assessing the applicability of TMPA-3B42V7 precipitation dataset in wavelet-support vector machine approach for suspended sediment load prediction. J Hydrol 550:103–117. https://doi.org/10.1016/j.jhydrol.2017.04.051

129. Hirabayashi Y, Kanae S, Emori S, et al (2010) Global projections of changing risks of floods and droughts in a changing climate Global projections of changing risks of floods and droughts in a changing climate. Atmos Environ 37–41

130. Hock R (2005) Glacier melt : a review on processes and their modelling. Prog Phys Geogr 3:362–391

131. Hock R (2003) Temperature index melt modelling in mountain areas. J Hydrol 282:104–115. https://doi.org/10.1016/S0022-1694(03)00257-9

132. Hock R (1999) A distributed temperature-index ice- and snowmelt model including potential direct solar radiation. J Glaciol 45:101–111. https://doi.org/10.3189/s0022143000003087

133. Hock R, Bliss A, Marzeion BEN, et al (2019a) GlacierMIP-A model intercomparison of global-scale glacier mass-balance models and projections. J Glaciol 65:453–467. https://doi.org/10.1017/jog.2019.22

134. Hock R, Holmgren B (2005) A distributed surface energy-balance model for complex topography and its application to Storglaciären, Sweden. J Glaciol 51:25–36. https://doi.org/10.3189/172756505781829566

135. Hock R, Kootstra DS, Reijmer C (2007) Deriving glacier mass balance from accumulation area ratio on Storglaciären, Sweden. IAHS-AISH Publ 1946:163–170

136. Hock R, Rasul G, Adler C, et al (2019b) High Mountain Areas

137. Huffman GJ, Bolvin DT, Nelkin EJ, et al (2007) The TRMM Multisatellite Precipitation Analysis (TMPA): Quasi-Global, Multiyear, Combined-Sensor Precipitation Estimates at Fine Scales. J Hydrometeorol 8:38–55. https://doi.org/10.1175/JHM560.1

138. Huintjes E, Neckel N, Hochschild V, Schneider C (2015) Surface energy and MAss balance at Purogangri ice cap, central Tibetan Plateau, 2001-2011. J Glaciol 61:1048–1060. https://doi.org/10.3189/2015JoG15J056

139. Huss M (2013) Density assumptions for converting geodetic glacier volume change to mass change. Cryosph 7:877–887. https://doi.org/10.5194/tc-7-877-2013

140. Huss M, Farinotti D (2012) Distributed ice thickness and volume of all glaciers around the globe. J Geophys Res Earth Surf 117:1–10. https://doi.org/10.1029/2012JF002523

141. Huss M, Hock R (2015) A new model for global glacier change and sea-level rise. Front Earth Sci 3:1–22. https://doi.org/10.3389/feart.2015.00054

142. Immerzeel WW, Droogers P, de Jong SM, Bierkens MFP (2009) Large-scale monitoring of snow cover and runoff simulation in Himalayan river basins using remote sensing. Remote Sens Environ 113:40–49. https://doi.org/10.1016/j.rse.2008.08.010

143. Immerzeel WW, Pellicciotti F, Bierkens MFP (2013) Rising river flows throughout the twenty-first century in two Himalayan glacierized watersheds. Nat Geosci 6:742–745. https://doi.org/10.1038/ngeo1896

144. Immerzeel WW, Van Beek LPH, Bierkens MFP (2010) Climate change will affect the asian water towers. Science (80-) 328:1382–1385. https://doi.org/10.1126/science.1183188

145. IPCC (2014) Climate Change 2014 Part A: Global and Sectoral Aspects

146. Jacob T, Wahr J, Pfeffer WT, Swenson S (2012) Recent contributions of glaciers and ice caps to sea level rise. Nature 482:514–518. https://doi.org/10.1038/nature10847

147. Jamandre CA, Narisma GT (2013) Spatio-temporal validation of satellite-based rainfall estimates in the Philippines. Atmos Res 122:599–608. https://doi.org/10.1016/j.atmosres.2012.06.024

148. Jiao J, Zhang Y, Bilker-Koivula M, et al (2020) Interannual glacier and lake mass changes over Scandinavia from GRACE. Geophys J Int 221:2126–2141. https://doi.org/10.1093/gji/ggaa146

149. Jin S, Zhang TY, Zou F (2017) Glacial density and GIA in Alaska estimated from ICESat, GPS and GRACE measurements. J Geophys Res Earth Surf 122:76–90. https://doi.org/10.1002/2016JF003926

150. Kääb A, Berthier E, Nuth C, et al (2012) Contrasting patterns of early twenty-first-century glacier mass change in the Himalayas. Nature 488:495–498. https://doi.org/10.1038/nature11324

151. Kääb A, Leinss S, Gilbert A, et al (2018) Massive collapse of two glaciers in western Tibet in 2016 after surge-like instability. Nat Geosci 11:114–120. https://doi.org/10.1038/s41561-017-0039-7

152. Kääb A, Treichler D, Nuth C, Berthier E (2015) Brief Communication: Contending estimates of 2003-2008 glacier mass balance over the Pamir-Karakoram-Himalaya. Cryosphere 9:557–564. https://doi.org/10.5194/tc-9-557-2015

153. Karki R, ul Hasson S, Schickhoff U, et al (2017) Rising precipitation extremes across Nepal. Climate 5:1–25. https://doi.org/10.3390/cli5010004

154. Kaser G, Großhauser M, Marzeion B (2010) Contribution potential of glaciers to water availability in different climate regimes. 2010:. https://doi.org/10.1073/pnas.1008162107

155. Kaushik S, Rafiq M, Joshi PK, Singh T (2020) Examining the glacial lake dynamics in a warming climate and GLOF modelling in parts of Chandra basin, Himachal Pradesh, India. Sci Total Environ 714:136455. https://doi.org/10.1016/j.scitotenv.2019.136455

156. Kayastha RB, Ohata T, Ageta Y (1999) Application of a mass-balance model to a Himalayan glacier. J Glaciol 45:559–567

157. Kelkar U, Narula KK, Sharma VP, Chandna U (2008) Vulnerability and adaptation to climate variability and water stress in Uttarakhand State, India. Glob Environ Chang 18:564–574. https://doi.org/10.1016/j.gloenvcha.2008.09.003

158. Khadka N, Zhang G, Thakuri S (2018) Glacial Lakes in the Nepal Himalaya : Inventory and Decadal Dynamics (1977-2017). Remote Sens 1913. https://doi.org/10.3390/rs10121913

159. King O, Bhattacharya A, Bhambri R, Bolch T (2019) Glacial lakes exacerbate Himalayan glacier mass loss. Sci Rep 9:1–9. https://doi.org/10.1038/s41598-019-53733-x

160. Klok EJ, Oerlemans J (2002) Model study of the spatial distribution of the energy and mass balance of Morteratschgletscher, Switzerland. J Glaciol 48:505–518. https://doi.org/10.3189/172756502781831133

161. Knudsen EM (2011) Modeling of the potential effect of Himalayan glacier melting on water availability. University of Bergen

162. Kothawale DR, Rajeevan M (2016) Monthly, Seasonal and Annual Rainfall Time Series for All-India, Homogeneous Regions and Meteorological Subdivisions: 1871-2016. 02:1871–2016

163. Kraaijenbrink P, Meijer SW, Shea JM, et al (2016) Seasonal surface velocities of a Himalayan glacier derived by automated correlation of unmanned aerial vehicle imagery. Ann Glaciol 57:103–113. https://doi.org/10.3189/2016AoG71A072

164. Krakauer NY, Lakhankar T, Dars GH (2019) Precipitation trends over the Indus basin. Climate 7:1–20. https://doi.org/10.3390/cli7100116

165. Krieger G, Moreira A, Fiedler H, et al (2007) TanDEM-X: A satellite formation for high-resolution radar interferometry. Proc Int Radar Symp 45:3317–3341

166. Kripalani RH, Kulkarni A (2001) Monsoon rainfall variations and teleconnections over South and East Asia. Int J Climatol 21:603–616. https://doi.org/10.1002/joc.625

167. Kripalani RH, Kumar P (2004) Northeast monsoon rainfall variability over south peninsular India vis-à-vis the Indian Ocean dipole mode. Int J Climatol 24:1267–1282. https://doi.org/10.1002/joc.1071

168. Krishnan R, Sanjay J, Gnanaseelan C, et al (2020) Assessment of climate change over the Indian region. Springer Singapore

169. Kulkarni A V, Karyakarte Y (2014) Observed changes in Himalayan glaciers. Curr Sci 106:237–244. https://doi.org/10.18520/cs/v106/i2/237-244

170. Kumar A, Gupta AK, Bhambri R, et al (2018a) Assessment and review of hydrometeorological aspects for cloudburst and flash flood events in the third pole region (Indian Himalaya). Polar Sci 18:1–16. https://doi.org/10.1016/j.polar.2018.08.004

171. Kumar A, Negi HS, Kumar K, et al (2019a) Quantifying mass balance of East-Karakoram glaciers using geodetic technique. Polar Sci 19:24–39. https://doi.org/10.1016/j.polar.2018.11.005

172. Kumar A, Negi HS, Kumar K, et al (2018b) Estimation of recent changes in thickness and mass balance of the Patsio glacier in the Great Himalayan region using geodetic technique and ancillary data. Geocarto Int 0:1–17. https://doi.org/10.1080/10106049.2018.1506506

173. Kumar P, Saharwardi MS, Banerjee A, et al (2019b) Snowfall Variability Dictates Glacier Mass Balance Variability in Himalaya-Karakoram. Sci Rep 9:1–9. https://doi.org/10.1038/s41598-019-54553-9

174. Kumar V, Jain SK (2010) Trends in seasonal and annual rainfall and rainy days in Kashmir Valley in the last century. Quat Int 212:64–69. https://doi.org/10.1016/j.quaint.2009.08.006

175. Kumar V, Jain SK, Singh Y (2010) Analyse des tendances pluviométriques de long terme en Inde. Hydrol Sci J 55:484–496. https://doi.org/10.1080/02626667.2010.481373

176. Latif M, Syed FS, Hannachi A (2017) Rainfall trends in the South Asian summer monsoon and its related large-scale dynamics with focus over Pakistan. Clim Dyn 48:3565–3581. https://doi.org/10.1007/s00382-016-3284-3

177. Lettenmaier DP, Wood EF, Wallis JR (1994) Hydro-climatological trends in the continental United States, 1948-88. J. Clim. 7:586–607

178. Li F, Jackson TJ, Kustas WP, et al (2004) Deriving land surface temperature from Landsat 5 and 7 during SMEX02/SMACEX. Remote Sens Environ 92:521–534. https://doi.org/10.1016/j.rse.2004.02.018

179. Li G, Wang ZS, Huang N (2018a) A Snow Distribution Model Based on Snowfall and Snow Drifting Simulations in Mountain Area. J Geophys Res Atmos 123:7193–7203. https://doi.org/10.1029/2018JD028434

180. Li S, Yao T, Yang W, et al (2018b) Glacier Energy and Mass Balance in the Inland Tibetan Plateau: Seasonal and Interannual Variability in Relation to Atmospheric Changes. J Geophys Res Atmos 123:6390–6409. https://doi.org/10.1029/2017JD028120

181. Lillesand TM, Kiefer RW, Chipman JW (2015) Remote Sensing and Image Interpretation, Seventh Ed. John Wiley & Sons, Hoboken, USA

182. Lin H, Li G, Cuo L, et al (2017) A decreasing glacier mass balance gradient from the edge of the Upper Tarim Basin to the Karakoram during 2000-2014. Sci Rep 7:1–9. https://doi.org/10.1038/s41598-017-07133-8

183. Lin S, Moore NJ, Messina JP, et al (2012) Evaluation of estimating daily maximum and minimum air temperature with MODIS data in east Africa. Int J Appl Earth Obs Geoinf 18:128–140. https://doi.org/10.1016/j.jag.2012.01.004

184. Lin X, Wen J, Liu Q, et al (2020) Spatiotemporal variability of land surface Albedo over the Tibet Plateau from 2001 to 2019. Remote Sens 12:1–18. https://doi.org/10.3390/rs12071188

185. Liu Y, Wang N, Zhang J, Wang L (2019) Climate change and its impacts on mountain glaciers during 1960–2017 in western China. J Arid Land 11:537–550. https://doi.org/10.1007/s40333-019-0025-6

186. Livada I, Asimakopoulos DN (2005) Individual seasonality index of rainfall regimes in Greece. Clim Res 28:155–161. https://doi.org/10.3354/cr028155

187. Long D, Yang Y, Wada Y, et al (2015) Deriving scaling factors using a global hydrological model to restore GRACE total water storage changes for China's Yangtze River Basin. Remote Sens Environ 168:177–193. https://doi.org/10.1016/j.rse.2015.07.003

188. Lutz AF, Immerzeel WW, Shrestha AB, Bierkens MFP (2014) Consistent increase in High Asia's runoff due to increasing glacier melt and precipitation. Nat Clim Chang 4:587–592. https://doi.org/10.1038/nclimate2237

189. Machiwal D, Kumar S, Dayal D, Mangalassery S (2017) Identifying abrupt changes and detecting gradual trends of annual rainfall in an Indian arid region under heightened rainfall rise regime. Int J Climatol 37:2719–2733. https://doi.org/10.1002/joc.4875

190. Mahto SS, Mishra V (2019) Does ERA-5 Outperform Other Reanalysis Products for Hydrologic Applications in India? J Geophys Res Atmos 124:9423–9441. https://doi.org/10.1029/2019JD031155

191. Manatsa D, Chingombe W, Matarira CH (2008) The impact of the positive Indian Ocean dipole on Zimbabwe droughts Tropical climate is understood to be dominated by. Int J Climatol 2029:2011–2029. https://doi.org/10.1002/joc

192. Mandal A, Ramanathan A, Angchuk T, et al (2016) Unsteady state of glaciers (Chhota Shigri and Hamtah) and climate in Lahaul and Spiti region, western Himalayas: a review of recent mass loss. Environ Earth Sci 75:1–12. https://doi.org/10.1007/s12665-016-6023-5

193. Mandal A, Ramanathan A, Azam MF, et al (2020) Understanding the interrelationships among mass balance, meteorology, discharge and surface velocity on Chhota Shigri Glacier over 2002–2019 using in situ measurements. J Glaciol 66:727–741. https://doi.org/10.1017/jog.2020.42

194. Mandal A, Ramanathan A, Farooq Azam M, et al (2015) Annual and seasonal mass balances of Chhota Shigri Glacier (benchmark glacier, Western Himalaya), India. EGU Gen Assem Conf Abstr 17:14078

195. Marzeion B, Champollion N, Haeberli W, et al (2017) Observation-Based Estimates of Global Glacier Mass Change and Its Contribution to Sea-Level Change. Surv Geophys 38:105–130. https://doi.org/10.1007/s10712-016-9394-y

196. Matsuo K, Heki K (2010) Time-variable ice loss in Asian high mountains from satellite gravimetry. Earth Planet Sci Lett 290:30–36. https://doi.org/10.1016/j.epsl.2009.11.053

197. Maurer JM, Schaefer JM, Rupper S, Corley A (2019) Acceleration of ice loss across the Himalayas over the past 40 years. Sci Adv 5:. https://doi.org/10.1126/sciadv.aav7266

198. Meredith M, Sommerkorn S, Cassotta S, et al (2019) Polar regions

199. Miller JD, Immerzeel WW, Rees G (2012) Climate Change Impacts on Glacier Hydrology and River Discharge in the Hindu Kush–Himalayas. Mt Res Dev 32:461–467. https://doi.org/10.1659/mrd-journal-d-12-00027.1

200. Milly PCD, Dunne KA, Vecchia A V. (2005) Global pattern of trends in streamflow and water availability in a changing climate. Nature 438:347–350. https://doi.org/10.1038/nature04312

201. Milner AM, Khamis K, Battin TJ, et al (2017) Glacier shrinkage driving global changes in downstream systems. Proc Natl Acad Sci U S A 114:9770–9778. https://doi.org/10.1073/pnas.1619807114

202. Ming J, Wang Y, Du Z, et al (2015) Widespread albedo decreasing and induced melting of Himalayan snow and ice in the early 21st century. PLoS One 10:. https://doi.org/10.1371/journal.pone.0126235

203. Misra A, Kumar A, Bhambri R, et al (2020) Topographic and climatic influence on seasonal snow cover: Implications for the hydrology of ungauged Himalayan basins, India. J Hydrol. https://doi.org/10.2166/nh.2005.0014

204. Mittal N, Mishra A, Singh R, Kumar P (2014) Assessing future changes in seasonal climatic extremes in the Ganges river basin using an ensemble of regional climate models. Clim Change 123:273–286. https://doi.org/10.1007/s10584-014-1056-9

205. Mohamed AA, Odindi J, Mutanga O (2017) Land surface temperature and emissivity estimation for Urban Heat Island assessment using medium- and low-resolution space-borne sensors: A review. Geocarto Int 32:455–470. https://doi.org/10.1080/10106049.2016.1155657

206. Moholdt G, Nuth C, Hagen JO, Kohler J (2010) Recent elevation changes of Svalbard glaciers derived from ICESat laser altimetry. Remote Sens Environ 114:2756–2767. https://doi.org/10.1016/j.rse.2010.06.008

207. Moiwo JP, Yang Y, Li H, et al (2009) Comparison of GRACE with in situ hydrological measurement data shows storage depletion in Hai River Basin, Northern China. Water SA 35:663–670. https://doi.org/10.4314/wsa.v35i5.49192

208. Moiwo JP, Yang Y, Tao F, et al (2011) Water storage change in the Himalayas from the Gravity Recovery and Climate Experiment (GRACE) and an empirical climate model. Water Resour Res 47:1–13. https://doi.org/10.1029/2010WR010157

209. Muhammad S, Tian L, Khan A (2019) Early twenty-first century glacier mass losses in the Indus Basin constrained by density assumptions. J Hydrol 574:467–475. https://doi.org/10.1016/j.jhydrol.2019.04.057

210. Mukherjee K, Bhattacharya A, Pieczonka T, et al (2018) Glacier mass budget and climate reanalysis data indicate a climatic shift around 2000 in Lahaul-Spiti, western Himalaya. Clim Change 148:219–233. https://doi.org/10.1007/s10584-018-2185-3

211. Mukhopadhyay B, Khan A (2015) A reevaluation of the snowmelt and glacial melt in river flows within Upper Indus Basin and its significance in a changing climate. J Hydrol 527:119–132. https://doi.org/10.1016/j.jhydrol.2015.04.045

212. Munro DS (1989) Surface roughness and bulk heat transfer on a glacier: comparison with eddy correlation. J Glaciol 35:343–348. https://doi.org/10.1017/S0022143000009266

213. Naidu C V., Durgalakshmi K, Krishna KM, et al (2009) Is summer monsoon rainfall decreasing over India in the global warming era? J Geophys Res Atmos 114:1–16. https://doi.org/10.1029/2008JD011288

214. NASA (2009) ASTER Global DEM Validation. lpdaac usgs gov4 accessed 28 July 2009 28

215. National Research Council (2012) Himalayan Glaciers: Climate change , wtaer resources and water security

216. Neckel N, Kropáček J, Bolch T, Hochschild V (2014) Glacier mass changes on the Tibetan Plateau 2003-2009 derived from ICESat laser altimetry measurements. Environ Res Lett 9:. https://doi.org/10.1088/1748-9326/9/1/014009

217. Negi HS, Kanda N, Shekhar MS, Ganju A (2018) Recent wintertime climatic variability over the North West Himalayan cryosphere. Curr Sci 114:760–770. https://doi.org/10.18520/cs/v114/i04/760-770

218. Negi HS, Kumar A, Kanda N, et al (2020) Status of glaciers and climate change of East Karakoram in early twenty-first century. Sci Total Environ 753:141914. https://doi.org/10.1016/j.scitotenv.2020.141914

219. Nepal S, Shrestha AB (2015) Impact of climate change on the hydrological regime of the Indus, Ganges and Brahmaputra river basins: a review of the literature. Int J Water Resour Dev 31:201–218. https://doi.org/10.1080/07900627.2015.1030494

220. Nie Y, Pritchard HD, Liu Q, et al (2021) Glacial change and hydrological implications in the Himalaya and Karakoram. Nat Rev Earth Environ 2:91–106. https://doi.org/10.1038/s43017-020-00124-w

221. O'Neel S, Hood E, Arendt A, Sass L (2014) Assessing streamflow sensitivity to variations in glacier mass balance. Clim Change 123:329–341. https://doi.org/10.1007/s10584-013-1042-7

222. Oerlemans J (2001) Glaciers and climate change. CRC Press

223. Oerlemans J, Anderson B, Hubbard A, et al (1998) Modelling the response of glaciers to climate warming. Clim Dyn 14:267–274. https://doi.org/10.1007/s003820050222

224. Oerlemans J, Klok EJ (2002) Energy Balance of a Glacier Surface: Analysis of Automatic Weather Station Data from the Morteratschgletscher, Switzerland. Arctic, Antarct Alp Res 34:477. https://doi.org/10.2307/1552206

225. Ohmura A (2001) Physical basis for the temperature-based melt-index method. J Appl Meteorol 40:753–761. https://doi.org/10.1175/1520-0450(2001)040<0753:PBFTTB>2.0.CO;2

226. Oke TR (1987) Boundary layer climates, 2nd edn. Taylor & Francis e-Library

227. Oliver JE (1980) Monthly precipitation distribution: A comparative index. Prof Geogr 32:300–309. https://doi.org/10.1111/j.0033-0124.1980.00300.x

228. Östrem G (2017) Ice Melting under a Thin Layer of Moraine , and the Existence of Ice Cores in Moraine Ridges. Geogr Ann 4422:228230. https://doi.org/10.1080/20014422.1959.11907953

229. Pandey P, Ali SN, Ramanathan AL, et al (2017) Regional representation of glaciers in Chandra Basin region, western Himalaya, India. Geosci Front 8:841–850. https://doi.org/10.1016/j.gsf.2016.06.006

230. Pandit A, Ramsankaran R (2020) Modeling ice thickness distribution and storage volume of glaciers in Chandra Basin, western Himalayas. J Mt Sci 17:2011–2022. https://doi.org/10.1007/s11629-019-5718-y

231. Partal T, Kahya E (2006) Trend analysis in Turkish precipitation data. Hydrol Process 20:2011–2026. https://doi.org/10.1002/hyp.5993

232. Patel A, Dharpure JK, Snehmani, Ganju A (2017a) Estimating surface ice velocity on Chhota Shigri glacier from satellite data using Particle Image Velocimetry (PIV) technique. Geocarto Int 6049:1–13. https://doi.org/10.1080/10106049.2017.1404142

233. Patel A, Prajapati R, Dharpure JK, et al (2019) Mapping and monitoring of glacier areal changes using multispectral and elevation data: A case study over Chhota-Shigri glacier. Earth Sci Informatics 12:489–499. https://doi.org/10.1007/s12145-019-00388-x

234. Patel LK, Sharma P, Laluraj CM, et al (2017b) A geospatial analysis of Samudra Tapu and Gepang Gath glacial lakes in the Chandra Basin, Western Himalaya. Nat Hazards 86:1275–1290. https://doi.org/10.1007/s11069-017-2743-4

235. Patel LK, Sharma P, Singh AT, et al (2021) Spatial surface velocity pattern in the glaciers of Chandra Basin, Western Himalaya. Geocarto Int 0:1–18. https://doi.org/10.1080/10106049.2021.1920627

236. Patel LK, Sharma P, Thamban M, et al (2016) Debris control on glacier thinning—a case study of the Batal glacier, Chandra basin, Western Himalaya. Arab J Geosci 9:309. https://doi.org/10.1007/s12517-016-2362-5

237. Pattanaik DR, Kalsi SR, Hatwar HR (2005) Evolution of convection anomalies over the Indo-Pacific region in relation to Indian monsoon rainfall. Mausam 56:811

238. Paul F (2015) Revealing glacier flow and surge dynamics from animated satellite image sequences: Examples from the Karakoram. Cryosphere 9:2201–2214. https://doi.org/10.5194/tc-9-2201-2015

239. Paul F, Kotlarski S (2010) Forcing a distributed glacier mass balance model with the regional climate model REMO. Part II: Downscaling strategy and results for two swiss glaciers. J Clim 23:1607–1620. https://doi.org/10.1175/2009JCLI3345.1

240. Paul F, Machguth H, Hoelzle M, et al (2008) Alpine-wide distributed glacier mass balance modelling: a tool for assessing future glacier change? Darkening Peaks Glacial Retreat Sci Soc Context 111–125. https://doi.org/10.5167/uzh-8177

241. Pechlivanidis IG, Arheimer B, Donnelly C, et al (2017) Analysis of hydrological extremes at different hydro-climatic regimes under present and future conditions. Clim Change 141:467–481. https://doi.org/10.1007/s10584-016-1723-0

242. Pelto MS, Riedel J (2001) Spatial and temporal variations in annual balance of North Cascade glaciers, Washington 1984-2000. Hydrol Process 15:3461–3472. https://doi.org/10.1002/hyp.1042

243. Prasetia R, As-syakur AR, Osawa T (2013) Validation of TRMM Precipitation Radar satellite data over Indonesian region. Theor Appl Climatol 112:575–587

244. Pratap B, Dobhal DP, Bhambri R, et al (2016) Four decades of glacier mass balance observations in the Indian Himalaya. Reg Environ Chang 16:643–658. https://doi.org/10.1007/s10113-015-0791-4

245. Pratap B, Dobhal DP, Mehta M, Bhambri R (2015) Influence of debris cover and altitude on glacier surface melting: A case study on Dokriani Glacier, central Himalaya, India. Ann Glaciol 56:9–16. https://doi.org/10.3189/2015AoG70A971

246. Pratap B, Sharma P, Patel L, et al (2019) Reconciling high glacier surface melting in summer with air temperature in the semi-arid zone of Western Himalaya. Water (Switzerland) 11:1–18. https://doi.org/10.3390/w11081561

247. Prihodko L, Goward SN (1997) Estimation of air temperature from remotely sensed surface observations. Remote Sens Environ 60:335–346. https://doi.org/10.1016/S0034-4257(96)00216-7

248. Pritchard DMW, Forsythe N, O'Donnell G, et al (2020) Multi-physics ensemble snow modelling in the western Himalaya. Cryosphere 14:1225–1244. https://doi.org/10.5194/tc-14-1225-2020

249. Prudhomme C, Reed DW (1998) Relationships between extreme daily precipitation and topography in a mountainous region: A case study in Scotland. Int J Climatol 18:1439–1453. https://doi.org/10.1002/(SICI)1097-0088(19981115)18:13<1439::AID-JOC320>3.0.CO;2-7

250. Quincey DJ, Glasser NF, Cook SJ, Luckman A (2015) Heterogeneity in Karakoram glacier surges. J Geophys Res Earth Surf 120:1288–1300. https://doi.org/10.1002/2015JF003515

251. Ragettli S, Immerzeel WW, Pellicciotti F (2016) Contrasting climate change impact on river flows from high-altitude catchments in the Himalayan and Andes Mountains. Proc Natl Acad Sci U S A 113:9222–9227. https://doi.org/10.1073/pnas.1606526113

252. Ragettli S, Pellicciotti F, Bordoy R, Immerzeel WW (2013) Sources of uncertainty in modeling the glaciohydrological response of a Karakoram watershed to climate change. Water Resour Res 49:6048–6066. https://doi.org/10.1002/wrcr.20450

253. Raj J (2014) Uttarakhand Action Plan on Climate Change: Transforming Crisis into Opportunity

254. Rajeevan M, Bhate J (2008) A High Resolution Daily Gridded Rainfall Data Set (1971-2005) for Mesoscale Meteorological Studies

255. Rajendran K, Kitoh A, Srinivasan J, et al (2012) Monsoon circulation interaction with Western Ghats orography under changing climate: Projection by a 20-km mesh AGCM. Theor Appl Climatol 110:555–571. https://doi.org/10.1007/s00704-012-0690-2

256. Ramanathan AL (2011) Status Report on Chhota Shigri Glacier (Himachal Pradesh)

257. Ramsankaran R, Pandit A, Parla A (2019) Decadal estimates of surface mass balance for glaciers in chandra basinj, western Himalayas, India-A geodetic Approach. In: Climate Change Signals and Response

258. Randhawa SS., Gautam N (2019) Assessment of Spatial Distribution of Seasonal Snow Cover During the Year 2018-19 in Himachal Pradesh Using Space Data

259. Randhawa SS, Rathore BP, Ishant R (2016) Assessment of seasonal snow cover variation during the year 2015-16 in Himachal Pradesh using space data

260. Rathore LS, Attri SD, Jaswal AK (2013) State Level Climate Change Trends in India

261. Reager JT, Gardner AS, Famiglietti JS, et al (2016) A decade of sea level rise slowed by climate-driven hydrology. Science (80-) 351:699–703. https://doi.org/10.1126/science.aad8386

262. Reid TD, Brock BW (2010) An energy-balance model for debris-covered glaciers including heat conduction through the debris layer. J Glaciol 56:903–916. https://doi.org/10.3189/002214310794457218

263. Remya SN, Kulkarni A V., Pradeep S, Shrestha DG (2019) Volume estimation of existing and potential glacier lakes, Sikkim Himalaya, India. Curr Sci 116:620–627. https://doi.org/10.18520/cs/v116/i4/620-627

264. RGI Consortium (2017) Randolph Glacier Inventory – A Dataset of Global Glacier Outlines: Version 6.0. echnical Report, Glob L Ice Meas from Space, Color USA Digit Media 1–14. https://doi.org/https://doi.org/10.7265/N5-RGI-60

265. Richardson SD, Reynolds JM (2000) An overview of glacial hazards in the Himalayas. Quat Int 65–66:31–47. https://doi.org/10.1016/S1040-6182(99)00035-X

266. Richey AS, Thomas BF, Lo M-H, et al (2015) Quantifying renewable groundwater stress with GRACE. Water Resour Res 51:1–22. https://doi.org/10.1002/2015WR017349.Received

267. Robson BA, Nuth C, Nielsen PR, et al (2018) Spatial variability in patterns of glacier change across the manaslu range, central himalaya. Front Earth Sci 6:1–19. https://doi.org/10.3389/feart.2018.00012

268. Rodell M, Chen J, Kato H, et al (2007) Estimating groundwater storage changes in the Mississippi River basin (USA) using GRACE. Hydrogeol J 15:159–166. https://doi.org/10.1007/s10040-006-0103-7

269. Rodell M, Famiglietti JS (2002) The potential for satellite-based monitoring of groundwater storage changes using GRACE: The High Plains aquifer, Central US. J Hydrol 263:245–256. https://doi.org/10.1016/S0022-1694(02)00060-4

270. Rodell M, Houser PR (2004) Updating a land surface model with MODIS-derived snow cover. J Hydrometeorol 5:1064–1075

271. Rodell M, Houser PR, Jambor U, et al (2004) The Global Land Data Assimilation System. Am Meteorol Soc

272. Rodell M, Velicogna I, Famiglietti JS (2009) Satellite-based estimates of groundwater depletion in India. Nature 460:999–1002. https://doi.org/10.1038/nature08238

273. Rosenzweig C, Iglesius A, Yang XB, et al (2001) Climate change and extreme weather events. Glob Chang Hum Heal 2:90–104

274. Rounce DR, Hock R, McNabb RW, et al (2021) Distributed Global Debris Thickness Estimates Reveal Debris Significantly Impacts Glacier Mass Balance. Geophys Res Lett 48:. https://doi.org/10.1029/2020GL091311

275. Rui H, Beaudoing HK (2018) README Document for GLDAS Version 2 Data Products. Goddard Earth Sci Data Inf Serv Cent (GES DISC) 1–32. https://doi.org/http://hydro1.sci.gsfc.nasa.gov/data/s4pa/GLDAS/GLDAS_NOAH10_M.2.0/doc/README_ GLDAS2.pdf

276. Rupper S, Roe G (2008) Glacier changes and regional climate: A mass and energy balance approach. J Clim 21:5384–5401. https://doi.org/10.1175/2008JCLI2219.1

277. Sahu R, Gupta RD (2019) SURFACE VELOCITY DYNAMICS OF SAMUDRA TAPU GLACIER , INDIA FROM 2013 TO 2017 USING LANDSAT-8 DATA. ISPRS Ann Photogramm Remote Sens Spat Inf Sci IV:10–11

278. Sahu R, Gupta RD (2020) Snow Cover Analysis in Chandra Basin ofWestern Himalaya from 2001 to 2016. Springer Singapore

279. Sakai A, Nuimura T, Fujita K, et al (2015) Climate regime of Asian glaciers revealed by GAMDAM glacier inventory. Cryosphere 9:865–880. https://doi.org/10.5194/tc-9-865-2015

280. Sam L, Bhardwaj A, Kumar R, et al (2018) Heterogeneity in topographic control on velocities of Western Himalayan glaciers. Sci Rep 8:12843. https://doi.org/10.1038/s41598-018-31310-y

281. Sanchez-Moreno JF, Mannaerts CM, Jetten V (2014) Applicability of satellite rainfall estimates for erosion studies in small offshore areas: A case study in Cape Verde Islands. Catena 121:365–374. https://doi.org/10.1016/j.catena.2014.05.029

282. SANDRP (2013) Uttarakhand Flood Disaster : Role of Human Actions

283. Sangewar C V., Shukla SP (2009) Inventory of the Himalayan Glaciers: a contribution to the International Hydrological Programme. An updated edition. In: Kolkata: Geological Survey of India (Special Publication 34). pp 0254–0436

284. Sattar A, Goswami A, Kulkarni A V., Das P (2019) Glacier-surface velocity derived ice volume and retreat assessment in the dhauliganga basin, central himalaya – A remote sensing and modeling based approach. Front Earth Sci 7:1–15. https://doi.org/10.3389/feart.2019.00105

285. Sattar A, Goswami A, Kulkarni A V, Emmer A (2020) Lake evolution, hydrodynamic outburst flood modeling and sensitivity analysis in the central himalaya: A case study. Water (Switzerland) 12:1–19. https://doi.org/10.3390/w12010237

286. Schauwecker S, Rohrer M, Huggel C, et al (2015) Remotely sensed debris thickness mapping of Bara Shigri Glacier, Indian Himalaya. J Glaciol 61:675–688. https://doi.org/10.3189/2015JoG14J102

287. Scherler D, Bookhagen B, Strecker MR (2011) Spatially variable response of Himalayan glaciers to climate change affected by debris cover. Nat Geosci 4:156–159. https://doi.org/10.1038/ngeo1068

288. Scherler D, Leprince S, Strecker MR (2008) Glacier-surface velocities in alpine terrain from optical satellite imagery-Accuracy improvement and quality assessment. Remote Sens Environ 112:3806–3819. https://doi.org/10.1016/j.rse.2008.05.018

289. Sekertekin A, Bonafoni S (2020) Land surface temperature retrieval from Landsat 5, 7, and 8 over rural areas: Assessment of different retrieval algorithms and emissivity models and toolbox implementation. Remote Sens 12:. https://doi.org/10.3390/rs12020294

290. Shamsudduha M, Taylor RG, Longuevergne L (2012) Monitoring groundwater storage changes in the highly seasonal humid tropics: Validation of GRACE measurements in the Bengal Basin. Water Resour Res 48:1–12. https://doi.org/10.1029/2011WR010993

291. Sharma P, Patel LK, Ravindra R, et al (2016) Role of debris cover to control specific ablation of adjoining batal and sutri dhaka glaciers in chandra basin (Himachal Pradesh) during peak ablation season. J Earth Syst Sci 125:459–473. https://doi.org/10.1007/s12040-016-0681-2

292. Sharma P, Patel LK, Singh AT, et al (2020) Glacier Response to Climate in Arctic and Himalaya During Last Seventeen Years: A Case Study of Svalbard, Arctic and Chandra

Basin, Himalaya. In: Goel PS, Ravindra R, Chattopadhyay S (eds) Climate Change and the White World. Springer, pp 139–156

293. Shean DE, Bhushan S, Montesano P, et al (2020) A Systematic, Regional Assessment of High Mountain Asia Glacier Mass Balance. Front Earth Sci 7:1–19. https://doi.org/10.3389/feart.2019.00363

294. Shekhar MS, Chand H, Kumar S, et al (2010) Climate-change studies in the western Himalaya. Ann Glaciol 51:105–112. https://doi.org/10.3189/172756410791386508

295. Shrestha AB, Aryal R (2011) Climate change in Nepal and its impact on Himalayan glaciers. Reg Environ Chang 11:65–77. https://doi.org/10.1007/s10113-010-0174-9

296. Shrestha AB, Wake CP, Mayewski PA, Dibb JE (2000) Precipitation fluctuations in the Himalaya and its vicinity: An analysis based on temperature records from Nepal. Int J Clim 20:317–327. https://doi.org/doi:10.1175/1520-0442(1999)012<2775:MTTITH>2.0.CO;2

297. Shrestha ABA, Agrawal NNK, Alfthan B, et al (2015) The Himalayan Climate and Water Atlas: Impact of climate change on water resources in five of Asia's major river basins. ICIMOD, GRID-Arendal and CICERO

298. Shrestha D, Singh P, Nakamura K (2012) Spatiotemporal variation of rainfall over the central Himalayan region revealed by TRMM Precipitation Radar. J Geophys Res Atmos 117:1–14. https://doi.org/10.1029/2012JD018140

299. Shukla A, Garg PK (2020) Spatio-temporal trends in the surface ice velocities of the central Himalayan glaciers, India. Glob Planet Change 190:103187. https://doi.org/10.1016/j.gloplacha.2020.103187

300. Shukla A, Garg PK, Srivastava S (2018) Evolution of glacial and high-altitude lakes in the Sikkim, Eastern Himalaya over the past four decades (1975-2017). Front Environ Sci 6:1–19. https://doi.org/10.3389/fenvs.2018.00081

301. Shukla SP, Mishra R, Kumar A (2020) Glacier Melt Water Characteristics of Hamtah Glacier, Lahaul and Spiti District, Himachal Pradesh, India. In: Goel PS, Ravindra R, Chattopadhyay S (eds) Climate Change and the White World. pp 169–186

302. Sicart JE, Espinoza JC, Quéno L, Medina M (2016) Radiative properties of clouds over a tropical Bolivian glacier: seasonal variations and relationship with regional atmospheric circulation. Int J Climatol 36:3116–3128. https://doi.org/10.1002/joc.4540

303. Sicart JE, Hock R, Ribstein P, et al (2011) Analysis of seasonal variations in mass balance and meltwater discharge of the tropical Zongo Glacier by application of a distributed energy balance model. J Geophys Res Atmos 116:1–18. https://doi.org/10.1029/2010JD015105

304. Silverio W, Jaquet JM (2005) Glacial cover mapping (1987-1996) of the Cordillera Blanca (Peru) using satellite imagery. Remote Sens Environ 95:342–350. https://doi.org/10.1016/j.rse.2004.12.012

305. Singh AT, Rahaman W, Sharma P, et al (2019) Moisture sources for precipitation and hydrograph components of the Sutri Dhaka Glacier basin, western Himalayas. Water (Switzerland) 11:. https://doi.org/10.3390/w11112242

306. Singh DK, Thakur PK, Naithani BP, Dhote PR (2021) Spatio-temporal analysis of glacier surface velocity in dhauliganga basin using geo-spatial techniques. Environ Earth Sci 80:1–16. https://doi.org/10.1007/s12665-020-09283-x

307. Singh P, Bengtsson L (2004) Hydrological sensitivity of a large Himalayan basin to climate change. Hydrol Process 18:2363–2385. https://doi.org/10.1002/hyp.1468

308. Singh P, Kumar N (1997) Impact assessment of climate change on the hydrological response of a snow and glacier melt runoff dominated Himalayan river. J Hydrol 193:316–350

309. Singh SP, Bassignana-Khadka I, Karky BS, et al (2011) Climate change in the Hindu Kush-Himalayas: the state of current knowledge

310. Soheb M, Ramanathan A, Angchuk T, et al (2020) Mass-balance observation, reconstruction and sensitivity of Stok glacier, Ladakh region, India, between 1978 and 2019. J Glaciol. https://doi.org/10.1017/jog.2020.34

311. Soheb M, Ramanathan A, Mandal A, et al (2018) Wintertime surface energy balance of a high-altitude seasonal snow surface in Chhota Shigri glacier basin, Western Himalaya. Geol Soc Spec Publ 462:155–168. https://doi.org/10.1144/SP462.10

312. Stanley T, Kirschbaum DB, Pascale S, Kapnick S (2020) Extreme precipitation in the Himalayan landslide hotspot. Adv Glob Chang Res 69:1087–1111. https://doi.org/10.1007/978-3-030-35798-6_31

313. Steiner JF, Kraaijenbrink PDA, Jiduc SG, Immerzeel WW (2018) Brief communication: The Khurdopin glacier surge revisited - Extreme flow velocities and formation of a dammed lake in 2017. Cryosphere 12:95–101. https://doi.org/10.5194/tc-12-95-2018

314. Stisen S, Sandholt I (2010) Evaluation of remote-sensing-based rainfall products through predictive capability in hydrological runoff modelling. Hydrol Process 24:879–891. https://doi.org/10.1002/hyp.7529

315. Storey JC, Choate MJ (2004) Landsat-5 bumper-mode geometric correction. IEEE Trans Geosci Remote Sens 42:2695–2703. https://doi.org/10.1109/TGRS.2004.836390

316. Strassberg G, Scanlon BR, Rodell M (2007) Comparison of seasonal terrestrial water storage variations from GRACE with groundwater-level measurements from the High Plains Aquifer (USA). Geophys Res Lett 34:1–5. https://doi.org/10.1029/2007GL030139

317. Sun Y, Jiang L, Liu L, et al (2017) Spatial-temporal characteristics of glacier velocity in the central Karakoram revealed with 1999-2003 Landsat-7 ETM+ pan images. Remote Sens 9:. https://doi.org/10.3390/rs9101064

318. Sutterley TC, Velicogna I, Hsu CW (2020) Self-Consistent Ice Mass Balance and Regional Sea Level From Time-Variable Gravity. Earth Sp Sci 7:. https://doi.org/10.1029/2019EA000860

319. Swinbank WC (1963) Long-wave radiation from clear skies. Q J R Meteorol Soc 89:339–348. https://doi.org/10.1002/qj.49708938105

320. Tak S, Keshari AK (2020) Investigating mass balance of Parvati glacier in Himalaya using satellite imagery based model. Sci Rep 10:12211. https://doi.org/10.1038/s41598-020-69203-8

321. Tasumi M (2005) Progress in operational estimation of regional evapotranspiration using satellite imagery

322. Tawde SA, Kulkarni A V., Bala G (2016) Estimation of glacier mass balance on a basin scale: An approach based on satellite-derived snowlines and a temperature index model. Curr Sci 111:1977–1989. https://doi.org/10.18520/cs/v111/i12/1977-1989

323. Tawde SA, Kulkarni A V., Bala G (2017) An estimate of glacier mass balance for the Chandra basin, western Himalaya, for the period 1984-2012. Ann Glaciol 58:99–109. https://doi.org/10.1017/aog.2017.18

324. Tayal S, Sarkar SK (2019) Climate Change impacts on Himalayan glaciers and implications on energy security of the country. TERI Discuss Pap

325. Teodoro PE, Delgado RC, Oliveira-Junior JF, et al (2018) Incoming Longwave Radiation Evaluation for the Legal Amazon Using HadRM3 and Geostatistic Theoretical Models. Floresta e Ambient 25:. https://doi.org/10.1590/2179-8087.009416

326. Thayyen RJ, Dimri AP, Kumar P, Agnihotri G (2013) Study of cloudburst and flash floods around Leh, India, during August 4-6, 2010. Nat Hazards 65:2175–2204. https://doi.org/10.1007/s11069-012-0464-2

327. Thomas BF, Famiglietti JS, Landerer FW, et al (2017) GRACE Groundwater Drought Index: Evaluation of California Central Valley groundwater drought. Remote Sens Environ 198:384–392. https://doi.org/10.1016/j.rse.2017.06.026

328. Tiwari RK, Gupta RP, Arora MK (2014) Estimation of surface ice velocity of Chhota-Shigri glacier using sub-pixel ASTER image correlation. Curr Sci 106:853–859

329. Tiwari VM, Wahr J, Swenson S (2009) Dwindling groundwater resources in northern India, from satellite gravity observations. Geophys Res Lett 36:1–5. https://doi.org/10.1029/2009GL039401

330. Todd J, Christoffersen P, Zwinger T, et al (2019) Sensitivity of a calving glacier to ice-ocean interactions under climate change: New insights from a 3-d full-stokes model. Cryosphere 13:1681–1694. https://doi.org/10.5194/tc-13-1681-2019

331. Trenberth KE (2011) Changes in precipitation with climate change. Clim Res 47:123–138. https://doi.org/10.3354/cr00953

332. Ullah S, Ahmad K, Sajjad RU, et al (2019) Analysis and simulation of land cover changes and their impacts on land surface temperature in a lower Himalayan region. J Environ Manage 245:348–357. https://doi.org/10.1016/j.jenvman.2019.05.063

333. USEPA (2000) Meteorological Monitoring Guidance for Regulatory Modeling Applications. Epa-454/R-99-005 171

334. Varikoden H, Samah AA, Babu CA (2010) Spatial and temporal characteristics of rain intensity in the peninsular Malaysia using TRMM rain rate. J Hydrol 387:312–319

335. Vijay S, Braun M (2016) Elevation change rates of glaciers in the Lahaul-Spiti (Western Himalaya, India) during 2000-2012 and 2012-2013. Remote Sens 8:1–16. https://doi.org/10.3390/rs8121038

336. Vincent C, Ramanathan A, Wagnon P, et al (2013) Balanced conditions or slight mass gain of glaciers in the Lahaul and Spiti region (northern India, Himalaya) during the nineties preceded recent mass loss. Cryosph 7:569–582. https://doi.org/10.5194/tc-7-569-2013

337. Vincent C, Soruco A, Azam F, et al (2018) A non-linear statistical model for extracting a climatic signal from glacier mass-balance measurements". J Geophys Res Earth Surf. https://doi.org/10.1029/2018JF004702

338. Vrieling A, Sterk G, de Jong SM (2010) Satellite-based estimation of rainfall erosivity for Africa. J Hydrol 395:235–241. https://doi.org/10.1016/j.jhydrol.2010.10.035

339. Wagnon P, Linda A, Arnaud Y, et al (2007) Four years of mass balance on Chhota Shigri Glacier, Himachal Pradesh, India, a new benchmark glacier in the western Himalaya. J Glaciol 53:603–611. https://doi.org/10.3189/002214307784409306

340. Wagnon P, Vincent C, Arnaud Y, et al (2013) Seasonal and annual mass balances of Mera and Pokalde glaciers (Nepal Himalaya) since 2007. Cryosphere 7:1769–1786. https://doi.org/10.5194/tc-7-1769-2013

341. Wallinga J, Van De Wal SWR (1998) Sensitivity of Rhonegletscher, Switzerland, to climate change: Experiments with a one-dimensional flowline model. J Glaciol 44:383–393. https://doi.org/10.1017/S0022143000002719

342. Wang Q, Yi S, Chang L, Sun W (2017) Large-Scale Seasonal Changes in Glacier Thickness Across High Mountain Asia. Geophys Res Lett 44:10,427-10,435. https://doi.org/10.1002/2017GL075300

343. Wang Q, Yi S, Sun W (2021) Continuous Estimates of Glacier Mass Balance in High Mountain Asia Based on ICESat-1,2 and GRACE/GRACE Follow-On Data. Geophys Res Lett 48:. https://doi.org/10.1029/2020GL090954

344. Wang R, Liu S, Shangguan D, et al (2019) Spatial heterogeneity in glacier mass-balance sensitivity across High Mountain Asia. Water (Switzerland) 11:1–21. https://doi.org/10.3390/w11040776

345. Wastlhuber R, Hock R, Kienholz C, Braun M (2017) Glacier changes in the Susitna Basin, Alaska, USA, (1951-2015) using GIS and remote sensing methods. Remote Sens 9:1–17. https://doi.org/10.3390/rs9050478

346. Watkins MM, Wiese DN, Yuan D-N, et al (2015) Improved methods for observing Earth's time variable mass distribution with GRACE using spherical cap mascons. J Geophys Res Solid Earth 3782–3803. https://doi.org/10.1002/2015JB012608.Received

347. Wester P, Mishra A, Mukherji A, et al (2019) The Hindu Kush Himalaya Assessment. Springer Nature Switzerland

348. WGMS (2020) Fluctuations of Glaciers Database. In: World Glacier Monit. Serv. Zurich, Switz.

349. Wiese DN, Landerer FW, Watkins MM (2016) Quantifying and reducing leakage errors in the JPL RL05M GRACE mascon solution. Water Resour Res 52:7490–7502. https://doi.org/10.1002/2016WR019344

350. Wolf AT, Yoffe SB, Giordano M (2003) International waters: Identifying basins at risk. Water Policy 5:29–60. https://doi.org/10.2166/wp.2003.0002

351. Wouters B, Gardner AS, Moholdt G (2019) Global glacier mass loss during the GRACE satellite mission (2002-2016). Front Earth Sci 7:1–11. https://doi.org/10.3389/feart.2019.00096

352. Wu K, Liu S, Zhu Y, et al (2020) Dynamics of glacier surface velocity and ice thickness for maritime glaciers in the southeastern Tibetan Plateau. J Hydrol 590:125527. https://doi.org/10.1016/j.jhydrol.2020.125527

353. Wu Q, Si B, He H, Wu P (2019) Determining Regional-Scale Groundwater Recharge with GRACE and GLDAS. Remote Sens 11:154. https://doi.org/10.3390/rs11020154

354. Yang P, Xia J, Zhan C, et al (2017) Monitoring the spatio-temporal changes of terrestrial water storage using GRACE data in the Tarim River basin between 2002 and 2015. Sci Total Environ 595:218–228. https://doi.org/10.1016/j.scitotenv.2017.03.268

355. Yang W, Guo X, Yao T, et al (2011) Summertime surface energy budget and ablation modeling in the ablation zone of a maritime Tibetan glacier. J Geophys Res Atmos 116:1–11. https://doi.org/10.1029/2010JD015183

356. Yatagai A, Kamiguchi K, Arakawa O, et al (2012) Aphrodite constructing a long-term daily gridded precipitation dataset for Asia based on a dense network of rain gauges. Bull Am Meteorol Soc 93:1401–1415. https://doi.org/10.1175/BAMS-D-11-00122.1

357. Yeşilırmak E, Atatanır L (2016) Spatiotemporal variability of precipitation concentration in western Turkey. Nat Hazards 81:687–704. https://doi.org/10.1007/s11069-015-2102-2

358. Yi S, Song C, Heki K, et al (2019) Substantial meltwater contribution to the Brahmaputra revealed by satellite gravimetry. Cryosph Discuss 2:1–23. https://doi.org/10.5194/tc-2019-211

359. Yi S, Sun W (2014) Evaluation of glacier changes in high-mountain Asia based on 10 year GRACE RL05 models. J Geophys Res Solid Earth 119:2504–2517. https://doi.org/10.1002/2015JB012028.Received

360. Yin J, Gentine P, Zhou S, et al (2018) Large increase in global storm runoff extremes driven by climate and anthropogenic changes. Nat Commun 9:. https://doi.org/10.1038/s41467-018-06765-2

361. Yu J, Zhang G, Yao T, et al (2016) Developing daily cloud-free snow composite products from MODIS terra-aqua and IMS for the tibetan plateau. IEEE Trans Geosci Remote Sens 54:2171–2180. https://doi.org/10.1109/TGRS.2015.2496950

362. Yu W, Yang Y-C, Savitsky A, et al (2013a) Future Climate Scenarios for the Indus Basin. The Indus Basin of Pakistan 77–93. https://doi.org/10.1596/9780821398746_ch04

363. Yu W, Yang Y-C, Savitsky A, et al (2013b) Hydrology and Glaciers in the Upper Indus Basin. In: The Indus Basin of Pakistan. pp 57–76

364. Yue S, Hashino M (2003) Long term trends of annual and monthly precipitation in Japan. J Am Water Resour Assoc 39:587–596. https://doi.org/10.1111/j.1752-1688.2003.tb03677.x

365. Zekollari H, Huybrechts P, Fürst JJ, et al (2013) Calibration of a higher-order 3-D ice-flow model of the Morteratsch glacier complex, Engadin, Switzerland. Ann Glaciol 54:343–351. https://doi.org/10.3189/2013AoG63A434

366. Zemp M, Frey H, Gärtner-Roer I, et al (2015) Historically unprecedented global glacier decline in the early 21st century. J Glaciol 61:745–762. https://doi.org/10.3189/2015JoG15J017

367. Zemp M, Hoelzle M, Haeberli W (2009) Six decades of glacier mass-balance observations: A review of the worldwide monitoring network. Ann Glaciol 50:101–111. https://doi.org/10.3189/172756409787769591

368. Zemp M, Huss M, Thibert E, et al (2019) Global glacier mass changes and their contributions to sea-level rise from 1961 to 2016. Nature 568:382–386. https://doi.org/10.1038/s41586-019-1071-0

369. Zhang G, Kang S, Fujita K, et al (2013) Energy and mass balance of Zhadang glacier surface, central Tibetan Plateau. J Glaciol 59:137–148. https://doi.org/10.3189/2013JoG12J152

370. Zhu T, Ringler C (2012) Climate change impacts on water availability and use in the Limpopo River Basin. Water (Switzerland) 4:63–84. https://doi.org/10.3390/w4010063

371. Ziegler AD, Wasson RJ, Bhardwaj A, et al (2014) Pilgrims, progress, and the political economy of disaster preparedness - the example of the 2013 Uttarakhand flood and Kedarnath disaster. Hydrol Process 28:5985–5990. https://doi.org/10.1002/hyp.10349